

INNOVATIVE RADIOPHARMACEUTICALS IN ONCOLOGY AND NEUROLOGY

EDITED BY : Françoise Kraeber-Bodéré, Jacques Barbet, Michel Chérel
and Denis Guilloteau

PUBLISHED IN: Frontiers in Medicine





frontiers

Frontiers Copyright Statement

© Copyright 2007-2017 Frontiers Media SA. All rights reserved.

All content included on this site, such as text, graphics, logos, button icons, images, video/audio clips, downloads, data compilations and software, is the property of or is licensed to Frontiers Media SA ("Frontiers") or its licensees and/or subcontractors. The copyright in the text of individual articles is the property of their respective authors, subject to a license granted to Frontiers.

The compilation of articles constituting this e-book, wherever published, as well as the compilation of all other content on this site, is the exclusive property of Frontiers. For the conditions for downloading and copying of e-books from Frontiers' website, please see the Terms for Website Use. If purchasing Frontiers e-books from other websites or sources, the conditions of the website concerned apply.

Images and graphics not forming part of user-contributed materials may not be downloaded or copied without permission.

Individual articles may be downloaded and reproduced in accordance with the principles of the CC-BY licence subject to any copyright or other notices. They may not be re-sold as an e-book.

As author or other contributor you grant a CC-BY licence to others to reproduce your articles, including any graphics and third-party materials supplied by you, in accordance with the Conditions for Website Use and subject to any copyright notices which you include in connection with your articles and materials.

All copyright, and all rights therein, are protected by national and international copyright laws.

The above represents a summary only. For the full conditions see the Conditions for Authors and the Conditions for Website Use.

ISSN 1664-8714

ISBN 978-2-88945-174-6

DOI 10.3389/978-2-88945-174-6

About Frontiers

Frontiers is more than just an open-access publisher of scholarly articles: it is a pioneering approach to the world of academia, radically improving the way scholarly research is managed. The grand vision of Frontiers is a world where all people have an equal opportunity to seek, share and generate knowledge. Frontiers provides immediate and permanent online open access to all its publications, but this alone is not enough to realize our grand goals.

Frontiers Journal Series

The Frontiers Journal Series is a multi-tier and interdisciplinary set of open-access, online journals, promising a paradigm shift from the current review, selection and dissemination processes in academic publishing. All Frontiers journals are driven by researchers for researchers; therefore, they constitute a service to the scholarly community. At the same time, the Frontiers Journal Series operates on a revolutionary invention, the tiered publishing system, initially addressing specific communities of scholars, and gradually climbing up to broader public understanding, thus serving the interests of the lay society, too.

Dedication to quality

Each Frontiers article is a landmark of the highest quality, thanks to genuinely collaborative interactions between authors and review editors, who include some of the world's best academicians. Research must be certified by peers before entering a stream of knowledge that may eventually reach the public - and shape society; therefore, Frontiers only applies the most rigorous and unbiased reviews.

Frontiers revolutionizes research publishing by freely delivering the most outstanding research, evaluated with no bias from both the academic and social point of view.

By applying the most advanced information technologies, Frontiers is catapulting scholarly publishing into a new generation.

What are Frontiers Research Topics?

Frontiers Research Topics are very popular trademarks of the Frontiers Journals Series: they are collections of at least ten articles, all centered on a particular subject. With their unique mix of varied contributions from Original Research to Review Articles, Frontiers Research Topics unify the most influential researchers, the latest key findings and historical advances in a hot research area! Find out more on how to host your own Frontiers Research Topic or contribute to one as an author by contacting the Frontiers Editorial Office: researchtopics@frontiersin.org

INNOVATIVE RADIOPHARMACEUTICALS IN ONCOLOGY AND NEUROLOGY

Topic Editors:

Françoise Kraeber-Bodéré, University Hospital of Nantes, France

Jacques Barbet, Arronax GIP, Saint-Herblain, France

Michel Chérel, University of Nantes, France

Denis Guilloteau, University François Rabelais of Tours, France



FDG-PET maximum-intensity-projection image recorded in a patient with mantle cell lymphoma. Metabolic tumor volume quantification was extracted from segmented foci represented in red.

Image by Clément Bailly

The aim of this Research Topic was to assemble a series of articles describing basic, preclinical and clinical research studies on radiopharmaceuticals and nuclear medicine. The articles were written by attendees of the third Nuclear Technologies for Health Symposium (NTHS, 10th-11th March 2015, Nantes, France) under the auspices of the IRON LabEx (Innovative Radiopharmaceuticals in Oncology and Neurology Laboratory of Excellence). This French network, gathering approximately 160 scientists from 12 academic research teams (Funded by “investissements d’Avenir”), fosters transdisciplinary projects between teams with expertise in chemistry, radiochemistry, radiopharmacy, formulation, biology, nuclear medicine and medical physics. The 13 articles within this resulting eBook present a series of comprehensive reviews and original research papers on multimodality imaging and targeted radionuclide therapy; illustrating the different facets of studies currently conducted in these domains.

Citation: Kraeber-Bodéré, F., Barbet, J., Chérel, M., Guilloteau, D., eds. (2017). Innovative Radiopharmaceuticals in Oncology and Neurology. Lausanne: Frontiers Media. doi: 10.3389/978-2-88945-174-6

Table of Contents

05 Editorial: Innovative Radiopharmaceuticals in Oncology and Neurology

Jacques Barbet, Nicolas Arlicot, Marie-Hélène Gaugler, Michel Chérel,
Denis Guilloteau and Françoise Kraeber-Bodéré

Chapter A: Multimodality Imaging

Section 1: Preclinical Testing

08 Assessment of the Protection of Dopaminergic Neurons by an $\alpha 7$ Nicotinic Receptor Agonist, PHA 543613, Using [^{18}F]LBT-999 in a Parkinson's Disease Rat Model

Sophie Sérrière, Aurélie Doméné, Johnny Vercouillie, Céline Mothes, Sylvie Bodard,
Nuno Rodrigues, Denis Guilloteau, Sylvain Routier, Guylène Page and Sylvie Chalon

Section 2: Clinical Studies

15 Assessment of Lymph Nodes and Prostate Status Using Early Dynamic Curves with ^{18}F -Choline PET/CT in Prostate Cancer

Cédric Mathieu, Ludovic Ferrer, Thomas Carlier, Mathilde Colombié, Daniela Rusu,
Françoise Kraeber-Bodéré, Loïc Campion and Caroline Rousseau

21 Clinical and Survival Impact of FDG PET in Patients with Suspicion of Recurrent Ovarian Cancer: A 6-Year Follow-up

Daniela Rusu, Thomas Carlier, Mathilde Colombié, Dorothée Goulon,
Vincent Fleury, Nicolas Rousseau, Dominique Berton-Rigaud, Isabelle Jaffre,
Françoise Kraeber-Bodéré, Loïc Campion and Caroline Rousseau

Section 3: Comprehensive Reviews

29 Story of Rubidium-82 and Advantages for Myocardial Perfusion PET Imaging

Jean-François Chatal, François Rouzet, Ferid Haddad, Cécile Bourdeau,
Cédric Mathieu and Dominique Le Guludec

36 Focus on the Controversial Aspects of ^{64}Cu -ATSM in Tumoral Hypoxia Mapping by PET Imaging

Mathilde Colombié, Sébastien Gouard, Mathieu Frindel, Aurélien Vidal,
Michel Chérel, Françoise Kraeber-Bodéré, Caroline Rousseau and Mickaël Bourgeois

43 Imaging Modalities to Assess Oxygen Status in Glioblastoma

Aurélien Corroyer-Dulmont, Ararat Chakhoyan, Solène Collet, Lucile Durand,
Eric T. MacKenzie, Edwige Petit, Myriam Bernaudin, Omar Touzani and
Samuel Valable

Chapter B: Targeted Radionuclide Therapy

Section 1: *In vitro* Development

50 *Development of Biocompatible and Functional Polymeric Nanoparticles for Site-Specific Delivery of Radionuclides*

Nicolas Lepareur, Loleh Leal E Costa, Maëva Bocqué, Clément Blondelle, Clément Ruello, Marie Desjulets, Nicolas Noiret and Sandrine Cammas-Marion

59 *Alpha Particles Induce Autophagy in Multiple Myeloma Cells*

Jean-Baptiste Gorin, Sébastien Gouard, Jérémie Ménager, Alfred Morgenstern, Frank Bruchertseifer, Alain Faivre-Chauvet, Yannick Guilloux, Michel Chérel, François Davodeau and Joëlle Gaschet

Section 2: Preclinical Testing

70 *Improvement of the Targeting of Radiolabeled and Functionalized Liposomes with a Two-Step System Using a Bispecific Monoclonal Antibody (Anti-CEA × Anti-DTPA-In)*

Aurore Rauscher, Mathieu Frindel, Holisoa Rajerison, Sébastien Gouard, Catherine Maurel, Jacques Barbet, Alain Faivre-Chauvet and Marie Mouglin-Degraef

79 *Therapeutic Efficacy of Alpha-RIT Using a ²¹³Bi-Anti-hCD138 Antibody in a Mouse Model of Ovarian Peritoneal Carcinomatosis*

Aurélien Derrien, Sébastien Gouard, Catherine Maurel, Marie-Hélène Gaugler, Frank Bruchertseifer, Alfred Morgenstern, Alain Faivre-Chauvet, Jean-Marc Classe and Michel Chérel

89 *Single-Dose Anti-CD138 Radioimmunotherapy: Bismuth-213 Is More Efficient than Lutetium-177 for Treatment of Multiple Myeloma in a Preclinical Model*

Nolwenn Fichou, Sébastien Gouard, Catherine Maurel, Jacques Barbet, Ludovic Ferrer, Alfred Morgenstern, Frank Bruchertseifer, Alain Faivre-Chauvet, Edith Bigot-Corbel, François Davodeau, Joëlle Gaschet and Michel Chérel

Section 3: Clinical Studies

100 *Pharmacokinetics and Dosimetry Studies for Optimization of Pretargeted Radioimmunotherapy in CEA-Expressing Advanced Lung Cancer Patients*

Caroline Bodet-Milin, Ludovic Ferrer, Aurore Rauscher, Damien Masson, Latifa Rbah-Vidal, Alain Faivre-Chauvet, Evelyne Cerato, Caroline Rousseau, José Hureauux, Olivier Couturier, Pierre-Yves Salaün, David M. Goldenberg, Robert M. Sharkey, Françoise Kraeber-Bodéré and Jacques Barbet



Editorial: Innovative Radiopharmaceuticals in Oncology and Neurology

Jacques Barbet^{1,2,3,4}, Nicolas Arlicot^{5,6,7}, Marie-Hélène Gaugler^{1,2,3}, Michel Chérel^{1,2,3,8}, Denis Guilloteau^{5,6,7} and Françoise Kraeber-Bodéré^{1,2,3,8,9*}

¹Centre Régional de Recherche en Cancérologie Nantes/Angers (CRCNA), UMR892 Inserm, Nantes, France, ²6299 CNRS, Nantes, France, ³Université de Nantes, Nantes, France, ⁴GIP Arronax, Saint-Herblain, France, ⁵UMR Inserm U930, Tours, France, ⁶Université François Rabelais, Tours, France, ⁷CHRU de Tours, Hôpital Bretonneau, Tours, France, ⁸Service de Médecine Nucléaire, Institut de Cancérologie de l'Ouest, Saint-Herblain, France, ⁹Service de Médecine Nucléaire, CHU de Nantes, Nantes, France

Keywords: radiopharmaceuticals, targeted radionuclide therapy, multimodality imaging, theranostic, PET imaging, pretargeted radioimmunotherapy

Editorial on the Research Topic

Innovative Radiopharmaceuticals in Oncology and Neurology

Personalized medicine is presented as the future of patient care. Nuclear Medicine will play a major role in the selection of patients for targeted therapies and in early therapy assessment with the investigation of phenotypes and functions using sensitive and specific SPECT and PET imaging techniques and theranostic approaches. Nuclear Medicine is already a key in the development of new therapies and targeted radionuclide therapy provides efficacious treatment modalities against cancer. An incredible amount of innovation is related to the use of a variety of radionuclides, new or improved multimodality imaging devices, and numbers of recently marketed radiopharmaceuticals in all medical domains and particularly cardiology, neurology, and oncology.

In this context, a network of laboratories and Nuclear Medicine departments, the IRON Laboratory of Excellence (Labex), has been set as part of the French “Investissements d’Avenir” program to help translating innovative radiopharmaceuticals into clinical testing by a multidisciplinary approach from the production of radionuclides using cyclotrons, to basic studies of targets and ligands, clinical trials, and assessment of the societal impacts of innovation in medicine in neurology and oncology. To foster communication between scientists, inside the Labex and with the international community, a series of highly specialized international “Nuclear Technologies for Health Symposia” has been organized annually, with the most recent edition, the third, held in Nantes, France, on March 10–11, 2015.

Plenary lectures given by distinguished speakers (Hank Kung, Philadelphia, PA, USA, Tom Bäck, Gothenburg, Sweden, Otto Boerman, Nijmegen, The Netherlands, Franck Bruchertseifer, Karlsruhe, Germany, and Claire Tabouret-Viaud, Geneva, Switzerland) addressed the state of the arts and new developments in the use of radioactivity and radiopharmaceuticals for multimodality imaging and therapy. The latest achievements in clinical nuclear medicine, science, and technology were discussed during interactive oral and poster sessions.

Selected talks were organized in four sessions: innovative tracers in neurology: from bench to bedside, multimodality imaging, theranostic in nuclear medicine, and targeted radionuclide therapy.

After the meeting, 12 papers were published in the Nuclear Medicine topic open by *Frontiers in Medicine*. These papers are representative of current research and development in Nuclear Medicine.

OPEN ACCESS

Edited and Reviewed by:

Jean-Pierre Pouget,
French Institute of Health and
Medical Research, France

*Correspondence:

Françoise Kraeber-Bodéré
francoise.bodere@chu-nantes.fr

Specialty section:

This article was submitted to
Nuclear Medicine,
a section of the journal
Frontiers in Medicine

Received: 09 November 2016

Accepted: 21 December 2016

Published: 11 January 2017

Citation:

Barbet J, Arlicot N, Gaugler M-H,
Chérel M, Guilloteau D and
Kraeber-Bodéré F (2017) Editorial:
Innovative Radiopharmaceuticals in
Oncology and Neurology.
Front. Med. 3:74.
doi: 10.3389/fmed.2016.00074

In a review article, Chatal et al. discussed the interest of ^{82}Rb PET for heart diseases, especially in obese patients and in women with large breasts. A great advantage of ^{82}Rb PET is its capacity to accurately measure myocardial blood flow and coronary reserve. ^{82}Rb has a very short half-life (75 sec) and is obtained from an $^{82}\text{Sr}/^{82}\text{Rb}$ generator. A major limitation for this technology is the low worldwide production of ^{82}Sr , but the situation is improving with new production facilities, including Arronax, becoming active, increased production yields, and approval of new generator/infuser systems.

Another radionuclide that attracts interest is ^{64}Cu , a PET emitter with a longer half-life (12.7 h). ^{64}Cu may be used to label peptides and antibodies. Another potential application is the mapping of tumor hypoxia using ^{64}Cu -ATSM, as discussed by Colombié et al. Hypoxic cells are more resistant to chemotherapy and to external beam radiation therapy. Delivering increased radiation doses to tumor hypoxic areas delineated by PET imaging could improve response. However, there is some controversy about the actual cause of increased ^{64}Cu -ATSM in tumor tissues. Corroyer-Dulmont et al. made a rather comprehensive review of the various methods that may be used to assess oxygenation/hypoxia, focusing on glioblastoma: other PET tracers such as ^{18}F Fluoromisonidazole (^{18}F FMISO) as well as many other imaging approaches, including MRI. They conclude that PET imaging may be the most relevant tool to characterize hypoxia in glioblastoma.

PET imaging is also useful in neurodegenerative diseases with the new tracers of amyloid plaques and in stroke with tracers of neuroinflammation. The objective of the paper by Sérière et al. was to evaluate the effects of a new agonist of $\alpha 7\text{R}$ on striatal dopaminergic neurodegeneration and neuroinflammation in a rat model of Parkinson Disease by PET imaging with ^{18}F LBT-999 to quantify the striatal dopamine transporter. Thanks to the use of preclinical PET imaging, they could conclude that an $\alpha 7\text{R}$ agonist may be beneficial for the treatment of Parkinson Disease.

In cancer diseases, ^{18}F FDG and ^{18}F fluorocholine are the most commonly used tracers in clinical practice. In a retrospective study, Rusu et al. evaluated the contribution of ^{18}F FDG PET to the clinical management and survival outcome of patients suspected of recurrent ovarian carcinoma. They showed that early diagnosis of recurrent ovarian cancer by PET had a significant impact on treatment planning and predicted patient outcome. In prostate cancer, Mathieu et al. reported interest of dynamic PET/CT image acquisition with ^{18}F fluorocholine to define pelvic lymph node or prostate pathological status.

Nuclear Medicine is also therapy. This has been known for many years, with the use of ^{131}I in the treatment of thyroid cancer. Tracking other cancers remains a challenge, but progress is made. New radioactive therapeutic agents are designed to improve response and survival, while minimizing side-effects. Locoregional injection of radioactive microparticles is in use in hepatic cancers. Encapsulation of radionuclides in nanoparticles that could be injected systemically has been proposed as a way to increase the radioactive load and reduce exposure of normal tissues. Lepareur and coworkers described non-toxic nanoparticles, able to release their load in a controlled way. They

prepared biodegradable and biocompatible pegylated nanoparticles loaded with a lipophilic $^{99\text{m}}\text{Tc}$ -labeled tracer that may be labeled by ^{188}Re for therapy (Lepareur et al.). Targeting similar nanoparticles is also explored by Rauscher et al., who develop pegylated liposomes labeled with ^{111}In and $^{125/131}\text{I}$ for pretargeted radioimmunotherapy, using a bispecific monoclonal antibody recognizing a tumor antigen and a small molecular weight tag attached to the surface of the liposomes. Immunospecific tumor targeting was demonstrated *in vitro* and *in vivo* in a mouse model.

With small radiolabeled molecules, clinical proofs of concept have been obtained for a variety of pretargeting methods in single photon imaging, PET imaging, and therapy. The key is the bispecific pretargeting agent and the optimization of the pretargeting protocol. Bodet-Milin et al. studied a new class of bispecific antibodies in a phase I radioimmunotherapy trial (<http://ClinicalTrials.gov/NCT01221675>) to optimize pretargeting parameters. The best dosing parameters were a short pretargeting delay (24 h) and a high bispecific molar dose.

A promising avenue for cancer therapy is the use of alpha-particle emitters. Alpha particles have very short tracks (usually less than 100 μm) and a very high cytotoxic potential even against radioresistant tumor cells in hypoxic area. ^{223}Ra , a bone targeting agent, has been recently approved for symptomatic metastatic prostate cancer therapy. Antibodies may be used to target other alpha-emitting radionuclides. Here, ^{213}Bi has been targeted to multiple myeloma, in a syngeneic mouse model, by means of an anti-CD138 antibody. Fichou et al. demonstrated that ^{213}Bi is much more effective than ^{177}Lu . The higher efficacy in such disseminated diseases has been presented as the major interest and the best rationale for the use of alpha emitters in therapy, but this is one of the first direct comparisons. In the same model, Gorin et al. showed that autophagy is a prominent cell death mechanism with ^{213}Bi . Derrien et al. confirmed the efficacy of locally delivered antibodies labeled with ^{213}Bi in an ovarian cancer model and proposed combination with hyperthermic intraperitoneal chemotherapy in an attempt to treat advanced disease.

AUTHOR CONTRIBUTIONS

Substantial contributions to the conception or design of the work; or the acquisition, analysis, or interpretation of data for the work: JB, NA, M-HG, MC, DG, FK-B. Drafting the work or revising it critically for important intellectual content: JB, NA, M-HG, MC, DG, FK-B. Final approval of the version to be published: JB, NA, M-HG, MC, DG, FK-B. Agreement to be accountable for all aspects of the work in ensuring that questions related to the accuracy or integrity of any part of the work are appropriately investigated and resolved: JB, NA, M-HG, MC, DG, FK-B.

FUNDING

This work has been supported in part by grants from the French National Agency for Research called “Investissements d’Avenir” Labex IRON no ANR-11-LABX-0018-01 and Equipex ArronaxPlus no ANR-11-EQPX-0004.

Conflict of Interest Statement: The authors declare that the research was conducted in the absence of any commercial or financial relationships that could be construed as a potential conflict of interest.

The handling Editor declared a shared affiliation, though no other collaboration, with the authors and states that the process nevertheless met the standards of a fair and objective review.

Copyright © 2017 Barbet, Arlicot, Gaugler, Chérel, Guilloteau and Kraeber-Bodéré. This is an open-access article distributed under the terms of the Creative Commons Attribution License (CC BY). The use, distribution or reproduction in other forums is permitted, provided the original author(s) or licensor are credited and that the original publication in this journal is cited, in accordance with accepted academic practice. No use, distribution or reproduction is permitted which does not comply with these terms.



Assessment of the protection of dopaminergic neurons by an $\alpha 7$ nicotinic receptor agonist, PHA 543613 using [^{18}F]LBT-999 in a Parkinson's disease rat model

Sophie Sérrière¹, Aurélie Doméné¹, Johnny Vercouillie¹, Céline Mothes², Sylvie Bodard¹, Nuno Rodrigues³, Denis Guilloteau^{1,4}, Sylvain Routier³, Guylène Page⁵ and Sylvie Chalon^{1*}

OPEN ACCESS

Edited by:

Alain Faivre-Chauvet,
University of Nantes, France

Reviewed by:

Jan Booij,
Academic Medical Center,
Netherlands
Susanne Asenbaum-Nan,
NÖ Landeskliniken-Holding, Austria
Puja Panwar Hazari,
Institute of Nuclear Medicine and
Allied Sciences, India

*Correspondence:

Sylvie Chalon,
UMR INSERM U930, Université
François Rabelais de Médecine,
10 Boulevard Tonnellé,
Tours 37032, France
sylvie.chalon@univ-tours.fr

Specialty section:

This article was submitted to Nuclear
Medicine, a section of the journal
Frontiers in Medicine

Received: 10 June 2015

Accepted: 17 August 2015

Published: 02 September 2015

Citation:

Sérrière S, Doméné A, Vercouillie J, Mothes C, Bodard S, Rodrigues N, Guilloteau D, Routier S, Page G and Chalon S (2015) Assessment of the protection of dopaminergic neurons by an $\alpha 7$ nicotinic receptor agonist, PHA 543613 using [^{18}F]LBT-999 in a Parkinson's disease rat model. *Front. Med.* 2:61. doi: 10.3389/fmed.2015.00061

¹ UMR INSERM U930, Université François Rabelais, Tours, France, ² Laboratoires Cyclopharma, Tours, France, ³ UMR CNRS 7311, Institut de Chimie Organique et Analytique, Université d'Orléans, Orléans, France, ⁴ CHRU de Tours, Hôpital Bretonneau, Tours, France, ⁵ EA3808 – CiMoTheMA, Université de Poitiers, Poitiers, France

The inverse association between nicotine intake and Parkinson's disease (PD) is well established and suggests that this molecule could be neuroprotective through anti-inflammatory action mediated by nicotinic receptors, including the $\alpha 7$ -subtype ($\alpha 7\text{R}$). The objective of this study was to evaluate the effects of an agonist of $\alpha 7\text{R}$, PHA 543613, on striatal dopaminergic neurodegeneration and neuroinflammation in a rat model of PD induced by 6-hydroxydopamine (6-OHDA) lesion. Adult male Wistar rats were lesioned in the right striatum and assigned to either the PHA group ($n = 7$) or the Sham group ($n = 5$). PHA 543613 hydrochloride at the concentration of 6 mg/kg (PHA group) or vehicle (Sham group) was intra-peritoneally injected 2 h before 6-OHDA lesioning and then at days 2, 4, and 6 post-lesion. Positron emission tomography (PET) imaging was performed at 7 days post-lesion using [^{18}F]LBT-999 to quantify the striatal dopamine transporter (DAT). After PET imaging, neuroinflammation was evaluated in same animals *in vitro* through the measurement of the microglial activation marker 18 kDa translocator protein (TSPO) by quantitative autoradiography with [^3H]PK-11195. The DAT density reflecting the integrity of dopaminergic neurons was significantly decreased while the intensity of neuroinflammation measured by TSPO density was significantly increased in the lesioned compared to intact striatum in both groups. However, these both modifications were partially reversed in the PHA group compared to Sham. In addition, a significant positive correlation between the degree of lesion and the intensity of neuroinflammation was evidenced. These findings indicate that PHA 543613 exerts neuroprotective effects on the striatal dopaminergic neurons associated with a reduction in microglial activation in this model of PD. This reinforces the hypothesis that an $\alpha 7\text{R}$ agonist could provide beneficial effects for the treatment of PD.

Keywords: autoradiography, dopamine transporter, 6-hydroxydopamine, neuroinflammation, PET, TSPO

Abbreviations: $\alpha 7\text{R}$, $\alpha 7$ nicotinic receptor; CE, cerebellum; IST, intact striatum; LST, lesioned striatum; SUV, standard uptake value; SUVr, standard uptake value ratio to CE.

Introduction

Parkinson's disease (PD) is the second most common age-related neurodegenerative disorder after Alzheimer's disease. It is characterized by the relatively selective death of dopaminergic neurons in the substantia nigra pars compacta leading to a striatal dopamine deficit (1). PD is mainly sporadic and is usually accompanied by motor symptoms, such as bradykinesia, rigidity, postural instability, and resting tremor, although a rising occurrence of non-motor symptoms is now recognized (2). Currently, the treatment of PD is only symptomatic and no efficient neuroprotective or disease modifying approaches are available. The search for such curative treatments requires to explore various molecular pathways involved in order to focus on drugs able to block or curb disease progression. One neuropathological feature of PD is the occurrence of neuroinflammatory processes, which manifests in part through the activation of microglial cell and astrocytes in the substantia nigra (3–5). Regulating neuroinflammation appears therefore to be a potential therapeutic approach; however, despite promising results obtained with different anti-inflammatory drugs in animal models (6, 7), clinical studies have been disappointing (8).

As previously described in the peripheral nervous system (9), it has been shown that downregulation of the microglial activation can be induced through the activation of $\alpha 7$ nicotinic receptors ($\alpha 7$ Rs) harbored by microglial cells (10). $\alpha 7$ Rs are the acetylcholine nicotinic receptors most represented, with the $\alpha 4\beta 2$ subtype, in mammalian brain and have several pharmacological characteristics, such as a high permeability to calcium, low sensitivity to acetylcholine, and high affinity for α -bungarotoxin (11). They are localized both on neurons (12) and glial cells (13). Besides their effects on neurotransmission, $\alpha 7$ Rs are involved in the modulation of neuroinflammatory processes, and agonists of these receptors are more efficient than acetylcholine at inhibiting the inflammatory signaling and production of pro-inflammatory cytokines from immune cells (14). In addition, several studies conducted in animal models support the idea that drugs acting at nicotinic acetylcholine receptors may be beneficial for PD (15). In particular, it has recently been suggested that the beneficial effect on the dopaminergic function observed with the $\alpha 7$ R agonist ABT-107 could be linked to a reduction of the glutamate excitotoxicity leading to the promotion of neuronal integrity (16).

In this study, we used a selective agonist of $\alpha 7$ R, PHA 543613 (17, 18), in a rat model of PD induced by unilateral striatal administration of 6-hydroxydopamine (6-OHDA) to investigate whether this compound has a protective effect on dopaminergic neurons through an anti-inflammatory mechanism. For this aim, we measured the striatal dopamine transporter (DAT) by *in vivo* positron emission tomography (PET) imaging using the fluorinated derivative of PE2I, (*E*)-*N*-(4-fluorobut-2-enyl)2 β -carbomethoxy-3 β -(4'-tolyl)nortropane or LBT-999 that we previously developed (19, 20). The neuroinflammation was evaluated through the density of the 18 kDa translocator protein (TSPO) using a quantitative autoradiographic method with the reference ligand of TSPO [3 H]PK-11195, which has been widely used in rodent and human brains (21–24).

Materials and Methods

Animals

All procedures were conducted in accordance with the European Community Council Directive 2010/63/EU for laboratory animal care and the experimental protocol was validated by the Regional Ethical Committee (Authorization N°00434.02). Experiments were carried out on adult male Wistar rats (CERJ, France) weighing 290–300 g at the beginning of experiments. Animals were housed in groups of two per cage in a temperature ($21 \pm 1^\circ\text{C}$) and humidity ($55 \pm 5\%$) controlled environment under a 12-h light/dark cycle, with food and water available *ad libitum*.

6-OHDA Lesion

The experimental design was performed according to a previously described procedure (25). Twenty minutes before surgery, rats were injected intra-peritoneally with pargyline (50 mg/kg, Sigma, Saint-Quentin Fallavier, France). Rats were anesthetized with isoflurane (4%, 500 mL/min) and placed on a stereotaxic apparatus (Stoelting, Phymep, Paris, France) and maintained under isoflurane 2.5% (500 mL/min) during surgery. The skull was exposed and small holes were made with a dental drill. Lesion was carried out by unilateral intra-striatal injection of 6-OHDA hydrochloride (1 mg/mL, Tocris Bioscience, Bristol, UK). A total of 10 μg of 6-OHDA was administered in two areas of the right striatum (1 mg/mL in 0.01% ascorbic acid, pH 4.5, i.e., 5 μg in 5 μL for each area) with a Hamilton syringe (gage 25, Hamilton, Massy, France) at a flow rate of 1 $\mu\text{L}/\text{min}$. Coordinates from bregma were AP = +0.5 mm, L = -2.5 mm, P = -5 mm, and AP = -0.5 mm, L = -4 mm, P = -5 mm according to Paxinos and Watson atlas (26). The needle was left in place for 4 min after injection and then removed slowly to optimize toxin diffusion. After surgery, the rats were given buprenorphine (0.05 mg/kg sub-cutaneously) for postoperative pain and were allowed to recover from surgery for 7 days before being subjected to the imaging experiments.

Treatment with the $\alpha 7$ Receptor Agonist PHA 543613

PHA 543613 hydrochloride (Tocris Bioscience, Bristol, UK; 17, 18) was dissolved in sterile water and intra-peritoneally injected at the concentration of 6 mg/kg (300 $\mu\text{L}/300\text{ g}$ body weight) 2 h before 6-OHDA lesioning and then at days 2, 4, and 6 post-lesion (cumulative dose of 24 mg/kg). Twelve rats were included in this study and separated into two groups as follows: seven lesioned rats received the treatment (PHA group) and five lesioned rats received intra-peritoneally injection of vehicle at the same time points (Sham group).

Preparation of the Tracer

No-carrier-added [^{18}F]LBT-999 was prepared as previously described (27). The tracer was produced via direct nucleophilic substitution from its chloro analog by adding 3 mg of the precursor in 1 mL of DMSO to the dry [^{18}F] KF/K_{2.2.2} complex. After heating at 165°C for 10 min, the mixture was cooled and purified by HPLC (Alltima, C18, 250 \times 10 mm, 5 μm column) using ammonium acetate 0.1M/acetonitrile 4/6 as the mobile phase at

a 4 mL/min flow rate. In these conditions, time retention was 13.5 min. The desired fraction was collected, diluted in water, and the [^{18}F]LBT-999 was trapped on a *t*-C18 light SepPak cartridge. The cartridge was rinsed with 5 mL of injectable water, and the [^{18}F]LBT-999 was eluted with 0.5 mL of ethanol. Formulation was completed by the addition of 3.5 mL of NaCl 0.9%. Quality control was performed by HPLC (Alltima, C18, 250 \times 4.6 mm, 5 μm column) using ammonium acetate 0.1M/Acetonitrile 3/7. [^{18}F]LBT-999 was obtained with a radiochemical purity >98% and with a mean specific activity of 65 ± 10 GBq/ μmol .

PET Imaging and Data Analyses

Positron emission tomography imaging was performed at 7 days post-lesion. Acquisitions were made on a microPET eXplore VISTA-CT system (GE Healthcare, France) which has an effective axial/trans axial field of view (FOV) of 4.8/6.7 cm, a spatial resolution less than 2 mm and a sensitivity above 2.5% in the whole FOV. Animals were anesthetized with isoflurane (Baxter, France), at 4–5% in O_2 for induction and then 1.5–2% during scanning. For imaging, each rat was placed on a thermo-regulated bed (Minerve, France) in the prone position with a nose cone. The brain was positioned on the center of the FOV. Before PET acquisition, a 5-min computed tomography (CT) scan was acquired for attenuation correction. A bolus injection of 37 MBq/300 g body weight of [^{18}F]LBT-999 in saline was administered into the tail vein. During PET acquisition, the respiratory rate and body temperature were monitored and kept as constant as possible. Each acquisition lasted 50 min and PET list-mode scans were rebinned into 27 frames: 4 10-s frames followed by 4 20-s frames, 4 60-s frames, 14 180-s frames, and 1 120-s frame. Each PET scan was corrected for random, scatter, and attenuation, and the images were reconstructed using a 2-D OSEM algorithm (GE Healthcare, France) into voxels of 0.3875 mm \times 0.3875 mm \times 0.775 mm. All images were analyzed using PMOD (3.403, PMOD Technologies, Zurich, Switzerland, www.pmod.com). The PET-corrected images were used for standard uptake value (SUV) calculations. For each PET scan, data were summed over the first 5 min after radiotracer injection to create a pseudo perfusion image. This image reflects the initial flow-dependent activity and was registered with the CT image through a known hardware registration (PET to CT transformation). CT scans were also recorded using a rat brain magnetic resonance imaging template (MRI-Template) (PMOD) (28) and a rat brain MRI-Template to CT transformation was saved. All PET images, after checking for potential head movements, were co-registered in a single interpolation to the Schiffer rat brain MRI-Template by a combination of these two transformations (MRI-Template to CT, and PET to CT transformations). The inverse combined transformation was calculated. The Schiffer MRI-template was processed in the PET space images using the inverse transformation applied on the originals dynamic PET data and statistics for the regions of interest (ROIs) were extracted. PET images were analyzed with the ROIs for the left striatum (i.e., intact striatum, IST), right striatum (i.e., lesioned striatum, LST), and cerebellum (CE). In this study, the standard uptake value ratio (SUVr) was used as quantitative criterions. All SUVrs were calculated using the CE as the reference region.

Autoradiographic Study

After the PET scan, rats were humanely killed by decapitation under light isoflurane anesthesia, and their brains were carefully removed on ice for autoradiographic experiments according to Ref. (25). Brains were frozen in isopentane cooled at -35°C and stored at -80°C . Coronal brain sections 20- μm thick were cut with a cryostat (CM 3050S, Leica, Germany) at -20°C , collected on gelatinized slides and stored at -80°C for at least 4 days. A total of six sections per brain were studied for each animal. The density of TSPO binding sites was measured by *in vitro* autoradiographic experiments using [^3H]PK-11195 (specific activity 3.06 GBq/ μmol ; Perkin Elmer, Norwalk, CT, USA) at 1 nmol/L in a 50-mmol/L Tris-HCl buffer pH 7.4. Brain sections were allowed to equilibrate at room temperature (RT) for 3 h, then were incubated with 1 nmol/L [^3H]PK-11195 in 50 mmol/L Tris-HCl buffer pH 7.4 at RT for 60 min. Non-specific binding was assessed in the presence of 1 $\mu\text{mol/L}$ PK-11195 (Sigma Aldrich, France). Sections were rinsed twice in ice cold buffer (4°C) for 5 min, then briefly in distilled water at 4°C and dried at RT. Dry sections were made conductive by an application of metal electric tape (3M, Euromedex) on the free side and then placed in the gas chamber of the β -imagerTM 2000 (Biospace Lab, Paris, France). Acquisitions were collected for 4 h. Two anatomical ROIs, i.e., the LST and IST were selected manually and identified in Paxinos and Watson atlas (26). Using the β -vision software (Biospace Lab, Paris, France), the level of bound radioactivity was directly determined by counting the number of β -particles emitted from the delineated area. The radioligand signal in the ROIs was measured for each rat and expressed as counts per minute per square millimeter (cpm/ mm^2). Specific binding was determined by subtracting non-specific binding from total binding. Radioactivity was quantified using an image analyzer (M3-vision Biospace Instruments, France). The percentage increase of TSPO binding in LST vs. IST was calculated as:

$$\frac{[\text{LST} - \text{IST}]}{\text{IST}} * 100$$

Statistical Analysis

For PET imaging and autoradiographic studies, results were expressed as mean \pm mean standard error (SEM). Comparisons between the binding in the LST and IST were performed using the Wilcoxon test one-tailed. To compare the two groups of rats (PHA vs. Sham), a Mann-Whitney test was used. The level of significance was $p \leq 0.05$. Correlation between PET imaging and autoradiography was estimated by using a one-tailed Spearman test (GraphPad Instat, GraphPad Software, San Diego, CA, USA). The level of significance was $p \leq 0.05$. Statistical analyses were performed using the GraphPad Prism software version 5.

Results

Animals

No physiological issues and no difference in body weight were observed between animals in the PHA and Sham groups (weight on the day of lesion: 300 ± 4 vs. 297 ± 6 g, respectively; weight at day 7 post-lesion: 313 ± 5 vs. 301 ± 6 g, respectively).

PET Imaging

Positron emission tomography images are presented in **Figure 1**. After [^{18}F]LBT-999 injection, a progressive accumulation of radioactivity was observed mainly in the IST (**Figure 1A**). Static PET images revealed that accumulation of [^{18}F]LBT-999 on the lesioned striatum was greater in PHA rats than in Sham rats (**Figures 1B,C**).

The time activity curves (**Figure 2A**) showed a rapid uptake of [^{18}F]LBT-999 in the ROIs (i.e., the IST, LST, and CE) after intravenous bolus injection. In the CE, the uptake decreased rapidly and remained low and stable after 20 min post-injection in both groups (SUV in the PHA group: 0.97 ± 0.06 , and 0.99 ± 0.08 in the Sham group). The uptake remained high and stable in the IST in both groups (SUV in the PHA group: 3.99 ± 0.33 , and 3.84 ± 0.31 in the Sham group). By contrast, the values observed in the LST were reduced in comparison to those in the IST in both groups (SUV in the PHA group: 1.41 ± 0.19 , and 0.98 ± 0.11 in the Sham group).

The analysis of SUVr to CE (**Figure 2B**) showed a significant reduction in the LST compared to the IST, both in the PHA (1.58 ± 0.23 vs. 4.34 ± 0.42 , $p < 0.05$ Wilcoxon test) and Sham (0.99 ± 0.07 vs. 3.94 ± 0.37 , $p < 0.05$ Wilcoxon test) groups. These SUVr were similar in the IST in both groups (PHA: 4.34 ± 0.42 and Sham: 3.94 ± 0.37), whereas in the LST the SUVr was slightly higher in the PHA than in the Sham group (1.58 ± 0.23 and 0.99 ± 0.07 , respectively). In addition, the percentage of decrease

in the SUVr (which reflects the intensity of the lesion) was significantly lower in the PHA group compared to the Sham group (64.6 ± 2.9 vs. $73.7 \pm 3.7\%$, $p < 0.05$, Mann-Whitney test) (**Figure 2C**).

Autoradiographic Study

The TSPO density was evaluated on adjacent brain sections by [^3H]PK-11195 binding in the IST and LST from each rat in both groups as illustrated in **Figure 3A**. The specific binding of [^3H]PK-11195 (**Figure 3B**) in the IST was low and similar between the PHA and Sham groups (1.53 ± 0.18 and 1.40 ± 0.29 cpm/mm 2 , respectively). In the LST of both groups, this binding was significantly increased (PHA group: 3.69 ± 0.32 vs. 1.53 ± 0.18 cpm/mm 2 in the IST $p < 0.05$ Wilcoxon test; Sham group: 4.85 ± 0.29 vs. 1.40 ± 0.06 cpm/mm 2 in the IST, $p < 0.05$ Wilcoxon test). However, this increase was significantly lower in the PHA group than in the Sham group (24% lower, $p < 0.05$, Mann-Whitney test). In addition, as shown in **Figure 3C**, the percent of increase of TSPO binding in LST vs. IST was significantly lower in the PHA group compared to the Sham group (157.5 ± 30.9 vs. $262.2 \pm 20.6\%$, $p < 0.05$, Mann-Whitney test).

Correlation Between PET Imaging and Autoradiography

The correlation between PET imaging results (expressed as the degree of lesion, i.e., % tracer binding in LST vs. IST) and

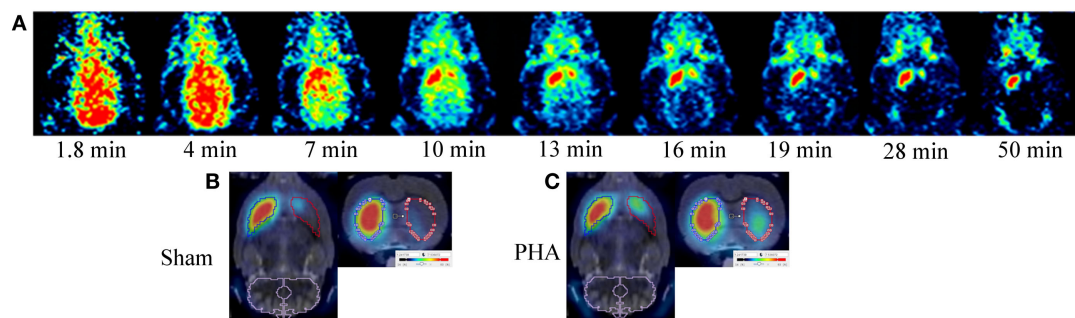


FIGURE 1 | PET brain images with [^{18}F]LBT-999. (A) Coronal PET images in a 6-OHDA lesioned rat with [^{18}F]LBT-999 from 1.8 to 50 min after bolus injection of the tracer. PET brain static sagittal and coronal images with [^{18}F]LBT-999 co-registered with the MRI-Template in a Sham rat (**B**) and in a PHA rat (**C**).

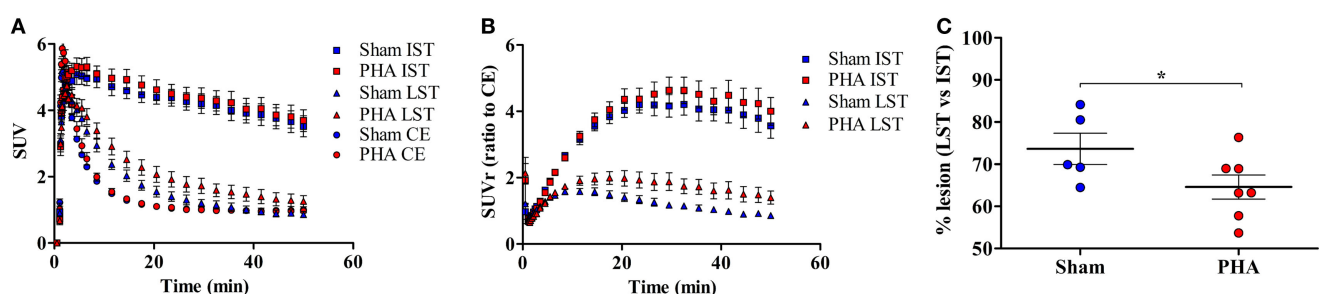
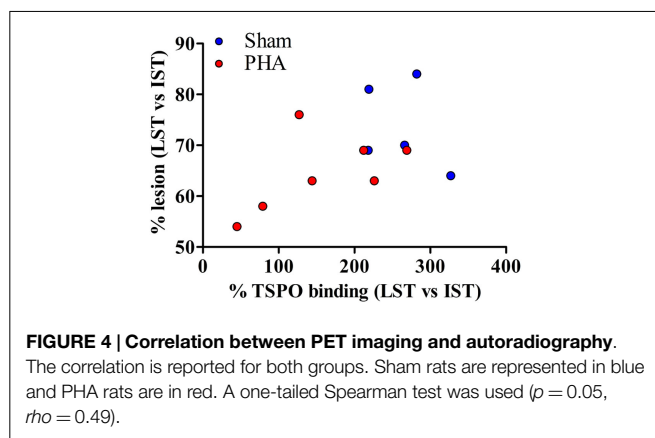
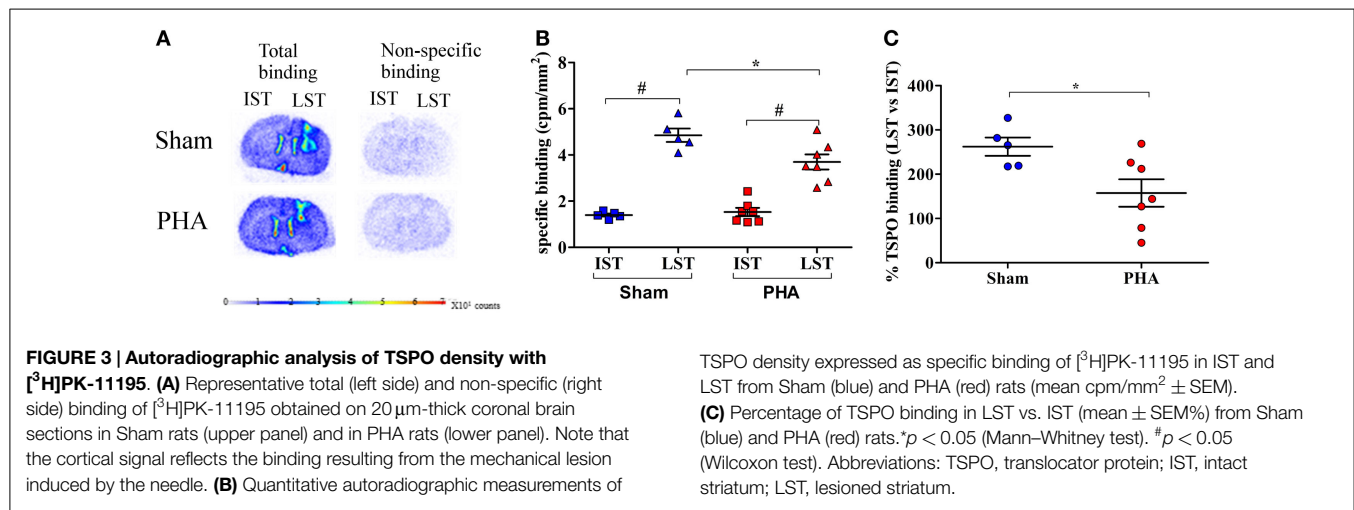


FIGURE 2 | Quantitative results from PET brain images with [^{18}F]LBT-999. (A) Mean-time activity curves of [^{18}F]LBT-999 SUVs in the IST, LST, and CE, in Sham (blue) and PHA (red) rats. (**B**) Mean-time activity curves of SUVr to CE of tracer accumulation in IST and LST in Sham (blue) and PHA (red)

rats. (**C**) Percentage of lesion in Sham (blue) and PHA (red) rats. * $p < 0.05$ compared with Sham (Mann-Whitney test). Abbreviations: CE: cerebellum, IST: intact striatum, LST: lesioned striatum, SUV: standard uptake value, SUVr: standard uptake value ratio to CE.



autoradiography (expressed as a percent of neuroinflammation, i.e., % TSPO binding in LST vs. IST) is shown in **Figure 4**. The degree of lesion measured by PET imaging was positively correlated with the intensity of neuroinflammation (*p* = 0.05, *rho* = 0.49).

Discussion

To date, no treatment has been recognized as useful neuroprotective approach for PD. Neuroinflammation is believed to be a key pathophysiological mechanism that could be targeted to achieve neuroprotection (29). A number of epidemiological and experimental evidence have converged to demonstrate a neuroprotective effect of nicotine in PD (30), involving particularly the α7-subtype of nicotinic receptors (31). Interestingly, this effect could be at least partly mediated by the modulation of neuroinflammation affected by these receptors (11). On this basis, we evaluated in this study the effects of a potent agonist of α7R, PHA 543613, on the neurodegeneration of dopaminergic neurons and associated microglial activation in a rat model of PD.

To date, little is known on the potential effects of α7R agonists in PD. As we aimed to induce a potential neuroprotective effect, we used a partial lesion model which corresponds to an early symptomatic stage of PD (32, 33).

Because the striatal DAT has proven to be a marker that correlates with the level of dopaminergic denervation (30, 34), we studied the integrity of striatal dopaminergic nerve endings using PET imaging with the fluorinated derivative of PE2I, (*E*)-*N*-(4-fluorobut-2-enyl)2β-carbomethoxy-3β-(4'-tolyl)nortropine or LBT-999 that we previously developed (19, 20). We recently demonstrated the ability of [¹⁸F]LBT-999 to quantify *in vivo* the DAT in the rat brain with high reproducibility, sensitivity, and specificity (27). In addition, this tracer has proven useful in a rat model of PD to quantify the lesions and as a treatment for cell restoration (35).

In order to evaluate the effects of PHA on neuroinflammation, we measured the density of the 18 kDa TSPO in the brain of PD rats after exploration by PET imaging. Indeed, the inflammatory reaction in the brain involves the activation of microglia (36) leading to a dramatic increase in the expression of the TSPO which can thus be considered as a sensitive biomarker of this activation (37, 38). We used a quantitative autoradiographic method with the reference ligand of TSPO [³H]PK-11195, which has been widely used in rodent and human brains (21–24).

Our PET experiment showed that at 7 days after 6-OHDA lesion, the specific accumulation of [¹⁸F]LBT-999 in the striatum, measured as the SUVR to CE as reference region, was high and similar on the intact side of all animals, and reduced on the lesioned side, as expected. However, we observed that the degree of lesion of dopaminergic neurons on the lesioned side, calculated as the percentage of tracer binding in the lesioned vs. intact striatum was slightly but significantly reduced in the PHA-treated group compared to Sham group (64 vs. 74% lesion, respectively). These results are in agreement with a partial neuroprotective effect of the α7R agonist on dopaminergic nerve endings. It is known that PHA 543613 is a potent and selective α7R agonist (17, 18), which has been shown to reduce induced brain edema in a mouse model through the inhibition of GSK-3β (39, 40). Similarly, PHA 568487, an α7R agonist closely related to PHA 543613, has been shown to reduce the severity of an ischemic stroke (41).

In rodent models of PD, neuroprotective effects have already been described with different α7R agonists, i.e., DMXBA (42), PNU-282987 (43) and more recently ABT-107 (16). In several of

these studies microglial activation was reduced by treatment with $\alpha 7R$ agonists, but the effects on neuroinflammatory parameters were observed at much earlier time's post-lesion than the effects on dopaminergic parameters (42, 43). We demonstrated herein a strong relationship between the effects of the $\alpha 7R$ agonist on the dopaminergic neurons integrity and on neuroinflammation, because $\alpha 7R$ agonist treatment reduced both dopaminergic neuron loss and microglial activation in the same animal. This is reinforced by the fact that we showed a significant positive correlation between the decrease of [^{18}F]LBT-999 accumulation and [3H]PK-11195 binding, which confirms that the upregulation of TSPO is directly correlated with the degree of neuronal damage (38).

Taking into account the small number of animals studied, our present findings can be considered as preliminary. In addition, several complementary experiments such as the evaluation of dopaminergic neuron integrity through TH immunostaining, behavioral tests assessing the dopaminergic function, and different experimental designs with various doses and administration points would be performed to confirm our findings. Nevertheless,

we showed that *in vivo* PET exploration in rodent models can be useful to evaluate different neuroprotective approaches using a variety of pharmacological compounds and experimental designs. In this field, the use of the TSPO PET tracer [^{18}F]DPA-714 in parallel to PET tracers of neurodegeneration would be of great value in rodent models of neurodegenerative disease, as recently done (44).

Our findings indicate that PHA 543613, a high affinity and selective $\alpha 7R$ agonist, partially preserved the integrity of striatal dopaminergic nerve endings and reduced neuroinflammation in 6-OHDA-lesioned rats. This reinforces the hypothesis that $\alpha 7R$ agonists may be beneficial in PD.

Acknowledgments

The research leading to these results has received funding from the European Union's Seventh Framework Programme (FP7/2007-2013) under grant agreement n°278850 (INMiND) and from Labex IRON (ANR-11-LABX-18-01). We thank the Laboratoires Cyclopharma for providing fluor-18.

References

- Dauer W, Przedborski S. Parkinson's disease: mechanisms and models. *Neuron* (2003) 39:889–909. doi:10.1016/S0896-6273(03)00568-3
- Ferrer I, Lopez-Gonzalez I, Carmona M, Dalfo E, Pujol A, Martinez A. Neurochemistry and the non-motor aspects of PD. *Neurobiol Dis* (2012) 46:508–26. doi:10.1016/j.nbd.2011.10.019
- McGeer PL, Itagaki S, Boyes BE, McGeer EG. Reactive microglia are positive for HLA-DR in the substantia nigra of Parkinson's and Alzheimer's disease brains. *Neurology* (1988) 38:1285–91. doi:10.1212/WNL.38.8.1285
- Hartmann A, Hunot S, Hirsch EC. Inflammation and dopaminergic neuronal loss in Parkinson's disease: a complex matter. *Exp Neurol* (2003) 184:561–4. doi:10.1016/j.expneurol.2003.08.004
- Lee JK, Tran T, Taney MG. Neuroinflammation in Parkinson's disease. *J Neuroimmune Pharmacol* (2009) 4:419–29. doi:10.1007/s11481-009-9176-0
- Aubin N, Curet O, Deffois A, Carter C. Aspirin and salicylate protect against MPTP-induced dopamine depletion in mice. *J Neurochem* (1998) 71:1635–42. doi:10.1046/j.1471-4159.1998.71041635.x
- Teismann P, Ferger B. Inhibition of the cyclooxygenase isoenzymes COX-1 and COX-2 provide neuroprotection in the MPTP-mouse model of Parkinson's disease. *Synapse* (2001) 39:167–74. doi:10.1002/1098-2396(200102)39:2<167::AID-SYN8>3.0.CO;2-U
- Tansey MG, Goldberg MS. Neuroinflammation in Parkinson's disease: its role in neuronal death and implications for therapeutic intervention. *Neurobiol Dis* (2010) 37:510–8. doi:10.1016/j.nbd.2009.11.004
- Wang H, Yu M, Ochani M, Amella CA, Tanovic M, Susarla S, et al. Nicotinic acetylcholine receptor $\alpha 7$ subunit is an essential regulator of inflammation. *Nature* (2003) 421:384–8. doi:10.1038/nature01339
- Shytle RD, Mori T, Townsend K, Vendrame M, Sun N, Zeng J, et al. Cholinergic modulation of microglial activation by $\alpha 7$ nicotinic receptors. *J Neurochem* (2004) 89:337–43. doi:10.1046/j.1471-4159.2004.02347.x
- Connejero-Goldberg C, Davies P, Ulloa L. Alpha7 nicotinic acetylcholine receptor: a link between inflammation and neurodegeneration. *Neurosci Biobehav Rev* (2008) 32:693–706. doi:10.1016/j.neubiorev.2007.10.007
- Jensen AA, Frolund B, Liljefors T, Krogsgaard-Larsen P. Neuronal nicotinic acetylcholine receptors: structural revelations, target identifications, and therapeutic inspirations. *J Med Chem* (2005) 48:4705–45. doi:10.1021/jm040219e
- Gahring LC, Persiyanov K, Dunn D, Weiss R, Meyer EL, Rogers SW. Mouse strain-specific nicotinic acetylcholine receptor expression by inhibitory interneurons and astrocytes in the dorsal hippocampus. *J Comp Neurol* (2004) 468:334–46. doi:10.1002/cne.1094
- De Longe WJ, Ulloa L. The alpha7 nicotinic acetylcholine receptor as a pharmacological target for inflammation. *Br J Pharmacol* (2007) 151:915–29. doi:10.1038/sj.bjp.0707264
- Quik M, Campos C, Grady SR. Multiple CNS nicotinic receptors mediate L-dopa-induced dyskinesias: studies with parkinsonian nicotinic receptor knock-out mice. *Biochem Pharmacol* (2013) 86:1153–62. doi:10.1016/j.bcp.2013.06.027
- Bordia T, McGregor M, Papke RL, Decker MW, McIntosh JM, Quik M. The $\alpha 7$ nicotinic receptor ABT-107 protects against nigrostriatal damage in rats with unilateral 6-hydroxydopamine lesions. *Exp Neurol* (2015) 263:277–84. doi:10.1016/j.expneurol.2014.09.015
- Wishka DG, Walker DP, Yates KM, Reitz SC, Jia S, Myers JK, et al. Discovery of N-[(3R,5R)-1-azabicyclo[2.2.2]oct-3-yl][2,3-c]pyridine-5-carboxamide, an agonist of the $\alpha 7$ nicotinic acetylcholine receptor, for the potential treatment of cognitive deficits in schizophrenia: synthesis and structure-activity relationship. *J Med Chem* (2006) 49:4425–36. doi:10.1021/jm0602413
- Acker BA, Jacobsen EJ, Rogers BN, Wishka DG, Reitz SC, Piotrowski DW. Discovery of N-[(3R,5R)-1-azabicyclo[3.2.1]oct-3-yl]furo-[2,3-c]pyridine-5-carboxamide an agonist of the $\alpha 7$ nicotinic acetylcholine receptor: in vitro and in vivo activity. *Bioorg Med Chem* (2008) 18:3611–5. doi:10.1016/j.bmcl.2008.04.070
- Chalon S, Hall H, Saba W, Garreau L, Dollé F, Halldin C, et al. Pharmacological characterization of (E)-N-(4-fluorobut-2-enyl)-2beta-carbomethoxy-3beta-(4'-tolyl)nortropane (LBT-999) as a highly promising fluorinated ligand for the dopamine transporter. *J Pharmacol Exp Ther* (2006) 317:147–52. doi:10.1124/jpet.105.096792
- Dollé F, Helfenbein J, Hinnen F, Mavel S, Mincheva Z, Saba W, et al. One-step radiosynthesis of [^{18}F]LBT-999: a selective radioligand for the visualization of the dopamine transporter with PET. *J Labelled Comp Radiopharm* (2007) 50:716–23. doi:10.1002/jlcr.1412
- Doble A, Malgouiri C, Daniel M, Daniel N, Imbault F, Basbaum A, et al. Labelling of peripheral-type benzodiazepine binding sites in human brain with [3H]PK 11195: anatomical and subcellular distribution. *Brain Res Bull* (1987) 18:49–64. doi:10.1016/0361-9230(87)90033-5
- Dubois A, Bénavidès J, Peny B, Duverger D, Fage D, Gotti B, et al. Imaging of primary and remote ischaemic and excitotoxic brain lesions. An autoradiographic study of peripheral type benzodiazepine binding sites in the rat and cat. *Brain Res* (1988) 445:77–90. doi:10.1016/0006-8993(88)91076-1
- Myers R, Manjil LG, Cullen BM, Price GW, Frackowiak RS, Cremer JE. Macrophage and astrocyte populations in relation to [3H]PK-11195 binding in rat cerebral cortex following a local ischaemic lesion. *J Cereb Blood Flow Metab* (1991) 11:314–22. doi:10.1038/jcbfm.1991.64

24. Miller TR, Wetter JB, Jarvis MF, Bitner RS. Spinal microglial activation in rat models of neuropathic and osteoarthritic pain: an autoradiographic study using [³H]PK11195. *Eur J Pain* (2013) **17**:692–703. doi:10.1002/j.1532-2149.2012.00232.x
25. Maia S, Arlicot N, Vierron E, Bodard S, Vergote J, Guilloteau D, et al. Longitudinal and parallel monitoring of neuroinflammation and neurodegeneration in a 6-hydroxydopamine rat model of Parkinson's disease. *Synapse* (2012) **66**:573–83. doi:10.1002/syn.21543
26. Paxinos G, Watson C. *The Rat Brain in Stereotaxic Coordinates*. 6th ed. San Diego, CA: Elsevier Academic Press (2007).
27. Sérière S, Tauber C, Vercouillie J, Guilloteau D, Deloye JB, Garreau L, et al. In vivo PET quantification of the dopamine transporter in rat brain with [¹⁸F]LBT-999. *Nucl Med Biol* (2014) **41**:106–13. doi:10.1016/j.nucmedbio.2013.09.007
28. Schiffer WK, Mirrione MM, Dewey SL. Optimizing experimental protocols for quantitative behavioral imaging with 18F-FDG in rodents. *J Nucl Med* (2007) **48**:277–87.
29. Athauda D, Foltynie T. The ongoing pursuit of neuroprotective therapies in Parkinson disease. *Nat Rev Neurol* (2015) **11**:25–40. doi:10.1038/nrneurol.2014.226
30. Quik M, O'Neill M, Perez XA. Nicotine neuroprotection against nigrostriatal damage: importance of the animal model. *Trends Pharmacol Sci* (2007) **28**:229–35. doi:10.1016/j.tips.2007.03.001
31. Quik M, Perez XA, Bordia T. Nicotine as a potential neuroprotective agent for Parkinson's disease. *Mov Disord* (2012) **27**:947–57. doi:10.1002/mds.25028
32. Björklund A, Rosenblad C, Winkler C, Kirik D. Studies on neuroprotective and regenerative effects of GDNF in a partial lesion model of parkinson's disease. *Neurobiol Dis* (1997) **4**:186–200. doi:10.1006/nbdi.1997.0151
33. Kirik D, Rosenblad C, Björklund A. Characterization of behavioral and neurodegenerative changes following partial lesions of the nigrostriatal dopamine system induced by intrastratial 6-hydroxydopamine in the rat. *Exp Neurol* (1998) **152**:259–77. doi:10.1006/exnr.1998.6848
34. Brooks DJ, Pavese N. Imaging biomarkers in Parkinson's disease. *Prog Neurobiol* (2011) **95**:614–28. doi:10.1016/j.pneurobio.2011.08.009
35. Grealish S, Diguët E, Kirkeby A, Mattson B, Heuer A, Bramouille Y, et al. Human ESC-derived dopamine neurons show similar preclinical efficacy and potency to fetal neurons when grafted in a rat model of Parkinson's disease. *Cell Stem Cell* (2014) **15**:653–65. doi:10.1016/j.stem.2014.09.017
36. Kreutzberg GW. Microglia: a sensor for pathological events in the CNS. *Trends Neurosci* (1996) **19**:312–8. doi:10.1016/0166-2236(96)10049-7
37. Papadopoulos V, Baraldi M, Guilarte TR, Knudsen TB, Lacapère JJ, Lindemann P, et al. Translocator protein (18 kDa): new nomenclature for the peripheral-type benzodiazepine receptor based on its structure and molecular function. *Trends Pharmacol Sci* (2006) **27**:402–9. doi:10.1016/j.tips.2006.06.005
38. Chen MK, Guilarte TR. Translocator protein 18 kDa (TSPO): molecular sensor of brain injury and repair. *Pharmacol Ther* (2008) **118**:1–17. doi:10.1016/j.pharmthera.2007.12.004
39. Krafft PR, Altay O, Rolland WB, Duri K, Lekic T, Tang J, et al. $\alpha 7$ nicotinic acetylcholine receptor agonism confers neuroprotection through GSK-3 β inhibition in a mouse model of intracerebral hemorrhage. *Stroke* (2012) **43**:844–50. doi:10.1161/STROKEAHA.111.639989
40. Krafft PR, Caner B, Klebe D, Rolland WB, Tang J, Zhang JH. PHA-543613 preserves blood-brain barrier integrity after intracerebral hemorrhage in mice. *Stroke* (2013) **44**:1743–7. doi:10.1161/STROKEAHA.111.000427
41. Han Z, Shen F, He Y, Degos V, Camus M, Maze M, et al. Activation of $\alpha 7$ nicotinic acetylcholine receptor reduces ischemic stroke injury through reduction of pro-inflammatory macrophages and oxidative stress. *PLoS One* (2014) **9**:e105711. doi:10.1371/journal.pone.0105711
42. Suzuki S, Kaamata J, Matsushita T, Matsumura A, Hisahara S, Takata K, et al. 3-[(2,4-dimethoxy)benzylidene]-anabaseine dihydrochloride protects against 6-hydroxydopamine-induced parkinsonian neurodegeneration through $\alpha 7$ nicotinic acetylcholine receptor stimulation in rats. *J Neurosci* (2013) **33**:462–71. doi:10.1002/jnr.23160
43. Stuckenholz V, Bacher M, Balzer-Geletzer M, Alvarez-Fischer D, Oertel WH, Dodel RC, et al. The $\alpha 7$ nAChR agonist PNU-282987 reduces inflammation and MPTP-induced nigral dopaminergic cell loss in mice. *J Parkinsons Dis* (2013) **3**:161–72. doi:10.3233/JPD-120157
44. Sérière S, Tauber C, Vercouillie J, Mothes C, Pruckner C, Guilloteau D, et al. Amyloid load and translocator protein 18 kDa in APPswePS1-dE9 mice: a longitudinal study. *Neurobiol Aging* (2015) **36**:1639–52. doi:10.1016/j.neurobiolaging.2014.11.023

Conflict of Interest Statement: The authors declare that the research was conducted in the absence of any commercial or financial relationships that could be construed as a potential conflict of interest.

Copyright © 2015 Sérière, Doméné, Vercouillie, Mothes, Bodard, Rodrigues, Guilloteau, Routier, Page and Chalon. This is an open-access article distributed under the terms of the Creative Commons Attribution License (CC BY). The use, distribution or reproduction in other forums is permitted, provided the original author(s) or licensor are credited and that the original publication in this journal is cited, in accordance with accepted academic practice. No use, distribution or reproduction is permitted which does not comply with these terms.



Assessment of lymph nodes and prostate status using early dynamic curves with ^{18}F -choline PET/CT in prostate cancer

Cédric Mathieu^{1,2*}, Ludovic Ferrer^{3,4}, Thomas Carlier^{2,3}, Mathilde Colombié¹, Daniela Rusu¹, Françoise Kraeber-Bodéré^{1,2,3}, Loïc Campion⁵ and Caroline Rousseau^{1,3}

¹ Department of Nuclear Medicine, ICO Cancer Center, Saint Herblain, France, ² Department of Nuclear Medicine, University Hospital, Nantes, France, ³ Centre Régional de Recherche en Cancérologie Nantes/Angers, U892, CNRS UMR 6299, INSERM, Nantes, France, ⁴ Department of Medical Physics, ICO Cancer Center, Saint Herblain, France, ⁵ Department of Statistics, ICO Cancer Center, Saint Herblain, France

OPEN ACCESS

Edited by:

Thierry M. L. B. Vander Borgh, CHU Dinant Godinne, Belgium

Reviewed by:

Maria Mathew D'Souza, Institute of Nuclear Medicine and Allied Sciences, India
Baljinder Singh, Post Graduate Institute of Medical Education and Research, India

*Correspondence:

Cédric Mathieu, Department of Nuclear Medicine, ICO Cancer Center, Boulevard Jacques Monod, Saint Herblain 44805, France
cedric.mathieu@chu-nantes.fr

Specialty section:

This article was submitted to Nuclear Medicine, a section of the journal Frontiers in Medicine

Received: 29 April 2015

Accepted: 27 August 2015

Published: 09 September 2015

Citation:

Mathieu C, Ferrer L, Carlier T, Colombié M, Rusu D, Kraeber-Bodéré F, Campion L and Rousseau C (2015) Assessment of lymph nodes and prostate status using early dynamic curves with ^{18}F -choline PET/CT in prostate cancer.
Front. Med. 2:67.
doi: 10.3389/fmed.2015.00067

Introduction: Dynamic image acquisition with ^{18}F -Choline [fluorocholine (FCH)] PET/CT in prostate cancer is mostly used to overcome the bladder repletion, which could obstruct the loco-regional analysis. The aim of our study was to analyze early dynamic FCH acquisitions to define pelvic lymph node or prostate pathological status.

Material and methods: Retrospective analysis was performed on 39 patients for initial staging ($n = 18$), or after initial treatment ($n = 21$). Patients underwent 10-min dynamic acquisitions centered on the pelvis, after injection of 3–4 MBq/kg of FCH. Whole-body images were acquired about 1 h after injection using a PET/CT GE Discovery LS (GE-LS) or Siemens Biograph mCT (mCT). Maximum and mean SUV according to time were measured on nodal and prostatic lesions. SUV_{mean} was corrected for partial volume effect (PVEC) with suitable recovery coefficients. The status of each lesion was based on histological results or patient follow-up (>6 months). A Mann–Whitney test and ANOVA were used to compare mean and receiver operating characteristic (ROC) curve analysis.

Results: The median PSA was 8.46 ng/mL and the median Gleason score was 3 + 4. Ninety-two lesions (43 lymph nodes and 49 prostate lesions) were analyzed, including 63 malignant lesions. In early dynamic acquisitions, the maximum and mean SUV were significantly higher, respectively, on mCT and GE-LS, in malignant versus benign lesions ($p < 0.001$, $p < 0.001$). Mean SUV without PVEC, allowed better discrimination of benign from malignant lesions, in comparison with maximum and mean SUV (with PVEC), for both early and late acquisitions. For patients acquired on mCT, area under the ROC curve showed a trend to better sensitivity and specificity for early acquisitions, compared with late acquisitions (SUVmax AUC 0.92 versus 0.85, respectively).

Conclusion: Assessment of lymph nodes and prostate pathological status with early dynamic imaging using PET/CT FCH allowed prostate cancer detection in situations where proof of malignancy is difficult to obtain.

Keywords: ^{18}F -choline, prostate cancer, dynamic curves, early acquisition, pathological status

Introduction

Prostate cancer is the most common cancer in men over 50 years, and the third highest cause of death by cancer. Initial staging is reserved for tumors with intermediate or high risk according to the D'Amico classification (1). Recurrence of prostate cancer after treatment is common and occurs in 20–50% of cases at 10 years after radical prostatectomy, and in 30–40% after radiotherapy (2, 3). Management of biological relapse after curative treatment is a real diagnostic and therapeutic challenge. Hormone therapy is currently the standard palliative treatment and resistance inevitably occurs after 2–5 years (4).

In patients with intermediate or high risk, local extension, nodal, or bone metastasis, have major prognostic and therapeutic implications (4). Bone scans are recommended for patients at intermediate or high risk of progression. MRI has a major role for local extension, or location of prostate cancer after negative biopsies (5–7). Abdominal and pelvic CT can be used in order to highlight nodal metastases (8). However, imaging is supplanted by extent lymphadenectomy, which is recommended before prostatectomy or radiotherapy for intermediate and high risk prostate cancer to precisely evaluate the nodal status (9). The sentinel lymph node technique is being evaluated to guide surgeons to ensure optimal quality of dissection (10).

In prostate cancer, fluorocholine (FCH) PET/CT is indicated as an alternative to FDG PET/CT relevant to mitotic and choline kinase activities (11, 12). FCH is a highly sensitive and specific radiopharmaceutical for the initial staging of prostate cancer (intermediate or high risk tumors), or suspicion of recurrence (13–16). In most cases, PET/CT is performed in two phases (17). The first is a kinetic step centered on the pelvis to achieve the regional analysis before bladder repletion. The second consists of whole-body image acquisition 1 h post-injection.

The aim of our study was to evaluate the potential benefit of early kinetic FCH PET/CT for discriminating malignant from benign lymph node or prostate lesions, whose status has been proven by histological analysis or patient follow-up.

Materials and Methods

Population

Retrospective analyses were performed on patients with histologically proven prostatic adenocarcinoma and explored for initial staging or biochemical recurrence. Recurrence was defined as two consecutive PSA values of 0.2 ng/mL and above after radical prostatectomy, or three consecutive increasing PSA values above the previous PSA nadir measured at 3-month interval after radiotherapy. Patients had at least one focal FCH uptake in pelvic lymph nodes or in the prostate. All patients had an initially negative or equivocal conventional imaging, including bone scan, CT, and/or MRI. For each patient, we collected age, serum PSA, date of initial diagnosis, Gleason score, topography of prostate cancer, initial treatment, and time to recurrence. We obtained informed consent from all patients allowing the use of their clinical data for research purposes under a protocol approved in our institution.

Acquisition and Interpretation of PEC/CT

After 6 h of fasting, 3–4 MBq/kg of FCH were injected when starting PET/CT acquisition. Acquisition was realized in two phases. First a 10-min kinetic acquisition in list mode centered on the pelvis was acquired, followed by whole-body image acquisition at 60 min. Examinations were performed on two different PET/CT instruments, a GE Discovery LS (GE-LS) (GE Medical System, Waukesha WI, USA) and a Siemens Biograph mCT 40 (mCT) (Siemens, Erlanger, Germany). Images were reconstructed by iterative OSEM reconstruction with two iterations and 28 subsets associated with a 2D Gaussian filter (FWHM 5.45 mm) for GE-LS and OP-OSEM-PSF TOF with 3 iterations and 21 subsets associated with a 3D Gaussian filter (2 mm FWHM) for mCT.

Maximum and mean standard uptake values (SUV_{max} and SUV_{mean}) were measured on late images in every prostatic or pelvic nodal lesion. Dynamic curves were built for each lesion, measuring the SUV_{max} and SUV_{mean} every minute in the first 10 min. To delineate the tumor contours, we used a system-specific contrast-oriented algorithm proposed by Nestle (18), using the following formula:

$$\text{SUV}_{\text{threshold}} = (k \times \text{SUV}_{\text{max}}) + \text{SUV}_{\text{background}}$$

The $\text{SUV}_{\text{background}}$ was defined as the SUV_{mean} in the gluteus maximus, and k was a system-specific constant determined by phantom acquisitions for each PET/CT camera. A correction of partial volume effect (PVEC) on SUV_{mean} was performed with suitable recovery coefficients (19).

Gold Standard and Statistical Analyses

Lymph node or prostate lesions preferentially confirmed by histology were considered (prostatectomy results, lymph node dissection, or prostate biopsies). In other cases, concordant imaging (CT or MRI) or PSA decrease after targeted radiotherapy was also used to confirm lesion status. FCH uptake in the inguinal region was interpreted as reactive inflammatory lymph node as described in the literature (20). For patients with prostatic histological proof (biopsy or resection), the agreement between PET images and histology was evaluated by comparison with the detailed histological report. Statistical analysis consisted of a comparison of repeated averages between benign and malignant lesions using an ANOVA for early acquisitions. For late acquisitions, the SUV of benign and malignant lesions were compared by comparing averages (non-parametric Mann–Whitney test). SUV between the end of the early acquisition (10 min) and the late acquisition (60 min) was compared using a paired t -test. Early and late acquisitions were compared using a receiver operating characteristic (ROC) curve, only for patients acquired on mCT ($n = 71$). The tests were performed bilaterally with a limit of 5% significance ($p \leq 0.05$). The software used was SPSS 18 and Stata 13.1.

Results

Patients and Lesions

We identified 39 patients from September 2008 to January 2014 with FCH uptake in 49 prostatic and 43 nodal lesions. Median

age was 73 years and median PSA at PET time was 8.46 ng/mL (2.02–172.6). Among the 21 patients with biochemical recurrence, initial treatment was a prostatectomy for 38% (8/21) of them, and the median time to recurrence was 54.8 months (12–195). The median PSA doubling time was 8.2 months (1.7–24.7). Four patients were treated with hormone therapy at the time of PET (10.2%). Patient characteristics are presented in **Table 1**.

Within the 39 patients explored, 19 patients (49%) had isolated prostatic lesions, 8 (20%) isolated nodal lesions, and 12 (31%) had both. Histological results were available for 96.7% (30/31) of patients with prostatic lesions and for 40% (8/20) of patients with nodal lesions (lymph node dissection). For one patient with histologically unconfirmed prostatic lesions, PSA decrease after targeted radiotherapy was considered as a proof of disease. For the 12 patients with histologically unproven lymph node lesions, malignancy was assessed by a concordant imaging between CT and MRI in five cases (25%), PSA decrease after targeted radiotherapy in three cases (15%) or inguinal lymph node location in four cases (20%). Lesion characteristics are presented in **Table 2**.

TABLE 1 | Description of patient characteristics ($n = 39$).

	Initial staging $n = 18$ (Min–Max)	Recurrence $n = 21$ (Min–Max)
Median age (years)	70.5 (51–78)	74 (55–84)
Median PSA at PET (ng/mL)	11.5 (3.5–172.6)	5.23 (2.02–14.95)
Gleason score		
6	3	5
7	9	13
8–9	6	2
Unknown	0	1
Initial stage		
T1	7	3
T2	6	10
T3	3	5
Unknown	2	3
Previous treatment		
S	NA	2
S + R		5
S + HT		1
R		10
R + HT		1
HT		2

S, surgery; S + R, Surgery + Radiotherapy; R + HT, Radiotherapy + Hormone Therapy; HT, hormone therapy; NA, not applicable.

TABLE 2 | Description of lesion characteristics ($n = 92$) in the 39 patients.

	Prostatic lesions number (%)		Nodal lesions number (%)	
	Per patient analysis	Per lesion analysis	Per patient analysis	Per lesion analysis
Number	31	49	20	43
Histological proof	30 (97%)	48 (98%)	8 (40%)	14 (33%)
Concordant imaging	0 (0%)	0 (0%)	5 (25%)	14 (33%)
PSA decrease after RTE	1 (3%)	1 (2%)	3 (15%)	7 (16%)

RTE, radiotherapy.

Within the 49 prostatic lesions, 38 were malignant (77.6%), and 28 (57.1%) were identified in patients referred for initial staging. Forty-three nodal lesions were explored, 25 were malignant (58.1%) and 18 (41.8%) were identified in patients referred for initial staging. The location of the 25 malignant lymph nodes was as follows: common iliac for 5 (20%), external iliac for 14 (56%), internal iliac for 2 (8%), obturator fossa for 1 (4%), and pre-sacral for 3 (12%). Benign lymph nodes were found in the common iliac area for one (6%), external iliac for five (28%), and inguinal node for 12 (66%).

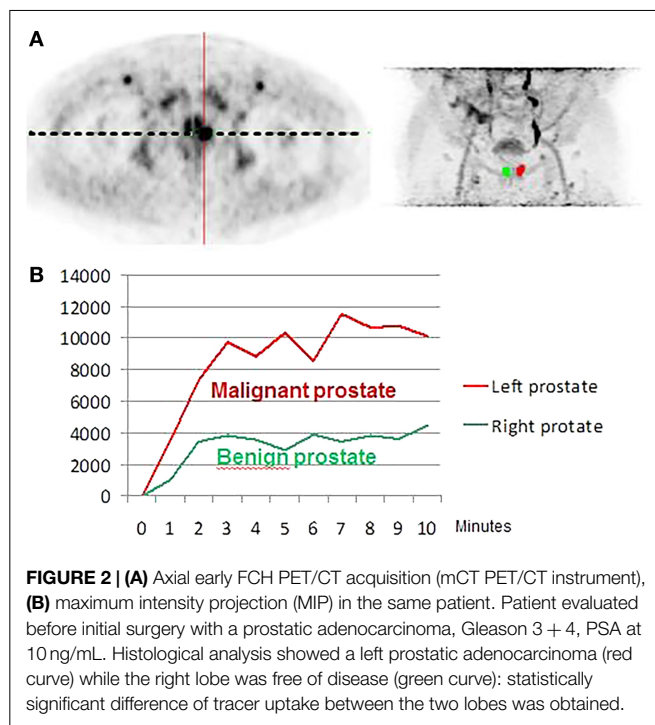
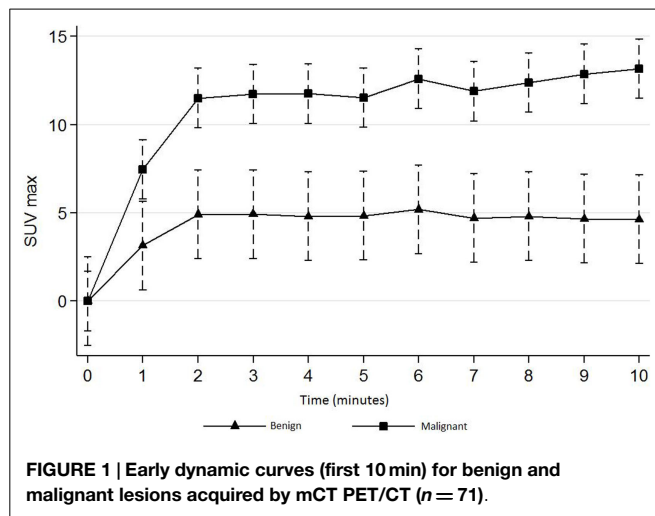
Early Kinetic of Lymph Node and Prostate Lesions

The mean SUV_{max} on the early dynamic acquisitions was significantly higher for malignant versus benign lesions, respectively, on mCT ($n = 71$) and on GE-LS ($n = 21$) ($p < 0.001$ and $p < 0.001$). Malignant lesions showed intense FCH uptake, with a maximum level of SUV_{max} almost reached at the second minute post-injection, followed by a plateau. Benign lesions showed a less intense uptake. The mean SUV_{max} in the plateau was, respectively, on mCT and on GE-LS about 12 and 8 for malignant lesions and 5 and 3 for benign lesions (**Figures 1 and 2**). The results were confirmed with SUV_{mean} with significantly higher FCH uptake in malignant lesions (with and without PVEC).

Analysis of 60 min Post-Injection Images and Comparison to the Early Kinetic Results

On mCT ($n = 71$), the mean SUV_{max} in the late acquisition was significantly higher in malignant lesions versus benign lesions, 11.1 versus 3.8 ($p < 0.001$), and also on LS-GE PET ($n = 21$) 8 versus 2.7 ($p < 0.001$). There was a significant decrease of the average SUV_{max} between the end of the early acquisition and late acquisition of 13% for malignant lesions (12.8 versus 11.1, $p < 0.001$), and 19% for benign lesions (4.7 versus 3.8, $p = 0.02$).

On mCT ($n = 71$), the optimal SUV threshold that maximized both sensitivity and specificity in early acquisitions was obtained at 8 min post-injection. SUV_{max} ROC curve analysis showed better area under the curve (AUC) for the early acquisition at 8 min versus late acquisition (**Figure 3**) (0.92 versus 0.85, respectively). In the early acquisitions, SUV_{mean} displayed the best AUC in comparison with SUV_{max} and SUV_{mean} with PVEC (0.97 versus 0.92 and 0.91, respectively). The same results were found for late acquisitions with a superiority of SUV_{mean} without PVEC. Optimal threshold and data for SUV_{mean} with and without PVEC are summarized in **Table 3**.



Discussion

We conducted a retrospective study with early dynamic acquisitions of FCH PET/CT in patients explored for initial staging or suspicion of recurrence of prostate cancer. To the best of our knowledge, this is the first study to assess the kinetic uptake of the radiopharmaceutical with 1 min step images to discriminate benign from malignant lesions, and explore the potential benefit that could be provided by PVEC correction for SUV_{mean} .

There are few published data on the contribution of dynamic acquisitions, and most involve small cohorts of patients. While it is known that an initial dynamic acquisition is useful in differentiating prostatic lesions from the urinary tract (21), the

optimal image acquisition time remains uncertain. For prostatic lesions, Kwee et al. (17) conducted a prospective study in 26 patients with an early whole-body imaging at 7 min post-injection associated with a step on the pelvis 1 h post-injection. They showed that benign lesions could be quickly differentiated from malignant lesions with higher uptake and an increased SUV_{max} by 14% over time. Because they built a curve with two independent measurements of SUV, they could not precisely define the time to reach maximum activity. Steiner et al. (22) in a retrospective study of 15 lesions in 11 patients achieved a FCH PET/CT in 3 phases (dynamic 10 min, immediately followed by a whole body and a late acquisition on pelvis at 1 h post-injection). They found that benign lesions could be quickly differentiated from malignant lesions, which show higher uptake and an increasing SUV_{max} until the 14th minute. In our study, the dynamic acquisition in list mode allowed us to determine a maximum activity reached in about the third minute post-injection, followed by an initial plateau and a discrete reduction of SUV, especially for benign lesions.

Dynamic acquisitions with choline labeled with ^{18}F Fluorine are more appropriate than with ^{11}C Carbon, because of the short half-life of ^{11}C Carbon (20 min). However, a prospective study using ^{11}C -Choline in 56 patients performed with two successive whole-body acquisitions at about 3–5 and 20 min post-injection, demonstrated dual phase acquisition was useful in distinguishing benign from malignant lesions (23). Nevertheless, they used a different radiopharmaceutical and they did not acquire dynamic, therefore making comparisons to our study difficult.

The behavioral differences between malignant and benign lesions, whether for prostatic or nodal lesions, encourage the use of ROC curves to define optimal thresholds to discriminate the lesions. For prostatic lesions, Kwee et al. (17) found an AUC of 0.81 at 7 min and 0.92 for late acquisition at 1 h, without defining a threshold. Oprea-Lager et al. (20) only examined nodal lesions, with an AUC of 0.93 at 30 min for the SUV_{max} and 0.92 for the SUV_{mean} . They determined thresholds for lymph nodes at 2.32 and 1.66 on late acquisitions for SUV_{max} and SUV_{mean} , respectively. In our study, we found similar AUC using SUV_{max} for early and late acquisitions (0.92 and 0.85, respectively). Our optimal SUV_{max} thresholds were 6.1 and 4.3 on early and late acquisitions, respectively, which allowed a sensitivity of 89.8 and 77.5%, and a specificity of 90.9 and 77.3%. We observed superior performance for SUV_{mean} than SUV_{max} , for both early and late acquisitions. We also observed a better AUC for the early acquisition at 8 min versus late acquisition. Few studies explored the use of SUV_{mean} , especially for response to therapy studies with a high impact of PVE correction. Nevertheless, a precise and robust delineation of tumor functional volume as used in our study, this index seems more relevant than SUV_{max} . SUV_{max} provides only very limited information relating to radiotracer accumulation, and no information on the associated tumor uptake distribution or the overall tumor functional volume (24). A meta-analysis showed better repeatability performance of SUV_{mean} versus SUV_{max} and could explain the differences observed (25).

We acknowledge that our study has some limitations. First, our acquisitions used two different generation PET/CT

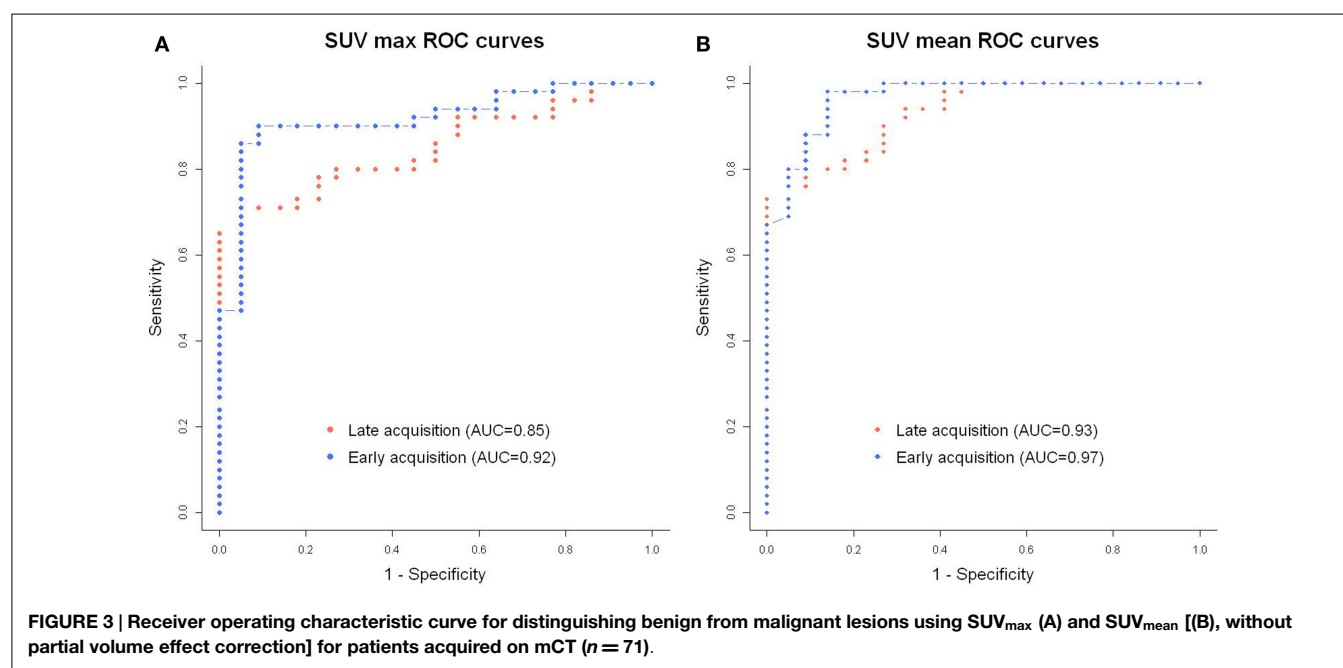


TABLE 3 | Optimal threshold of SUV for distinguishing benign from malignant lesions using SUV_{max} and SUV_{mean} for patients acquired on mCT ($n = 71$).

	Acquisition	Optimal threshold	AUC	Sensitivity (%)	Specificity (%)	Accuracy (%)
SUV_{max}	Early	6.1	0.92	89.8	90.9	90.1
	Late	4.3	0.85	77.5	77.3	77.5
SUV_{mean}	Early	2.5	0.97	98	86.4	94.4
	Late	2.4	0.93	89.8	72.7	84.5
SUV_{mean} (PVEC)	Early	5.1	0.91	87.8	81.8	85.9
	Late	5.0	0.87	83.7	72.7	80.3

instruments. This resulted in significant differences in detection sensitivity, making it impossible to compare patients acquired on the two different PET/CT systems. Second, as our study was based on patients where the malignant or benign status of lesions was proven, the enrollment was limited but equally important compared to other literature studies. For prostate lesions, we obtained a high rate of histological proof; 96.7% of patients had prostate lesions proven by biopsy or prostatectomy. For lymph node involvement, histological results were obtained for only 40% of patients, which was partially due to the difficulty in proposing systematic lymph node dissection based on PET/CT results. On the other hand, it was difficult to intraoperatively identify lymph node lesions detected by PET/CT because most of the time FCH positive lymph nodes did not correspond to morphologically increased node volume. Oprea-Lager et al. reported the same difficulties in obtaining proof for suspected malignant lymph nodes (20).

References

- Heidenreich A, Bastian PJ, Bellmunt J, Bolla M, Joniau S, van der Kwast T, et al. EAU guidelines on prostate cancer. Part 1: screening, diagnosis, and local treatment with curative intent-update 2013. *Eur Urol* (2014) **65**:124–37. doi:10.1016/j.eururo.2013.09.046

Conclusion

Assessment of lymph nodes and prostate pathological status with early PET/CT FCH dynamic curves was successful in prostate cancer where proof of malignancy is difficult to obtain. In addition to avoiding bladder repletion, dynamic early acquisitions demonstrated intense and stable FCH uptake from the first minutes post-injection, and discriminated benign from malignant lesions either in prostate or in lymph nodes. SUV_{mean} without correction of PVEC and early acquisitions may perform better than maximum SUV_{max} and late acquisitions, but larger studies are warranted.

Acknowledgments

This work has been supported in part by grants from the French National Agency for Research called “Investissements d’Avenir” Labex IRON no. ANR-11-LABX-0018-01.

- Aus G, Abbou CC, Bolla M, Heidenreich A, Schmid H-P, van Poppel H, et al. EAU guidelines on prostate cancer. *Eur Urol* (2005) **48**:546–51. doi:10.1016/j.eururo.2005.06.001
- Seltzer MA, Barbaric Z, Beldegrun A, Naitoh J, Dorey F, Phelps ME, et al. Comparison of helical computerized tomography, positron emission tomography and monoclonal antibody scans for evaluation of lymph node metastases in

- patients with prostate specific antigen relapse after treatment for localized prostate cancer. *J Urol* (1999) **162**:1322–8. doi:10.1097/00005392-199910000-00021
4. Heidenreich A, Bastian PJ, Bellmunt J, Bolla M, Joniau S, van der Kwast T, et al. EAU guidelines on prostate cancer. Part II: treatment of advanced, relapsing, and castration-resistant prostate cancer. *Eur Urol* (2014) **65**:467–79. doi:10.1016/j.eururo.2013.11.002
 5. Bjurlin MA, Meng X, Le Nobin J, Wysock JS, Lepor H, Rosenkrantz AB, et al. Optimization of prostate biopsy: the role of MRI targeted biopsy in detection, localization, and risk assessment. *J Urol* (2014) **192**(3):648–58. doi:10.1016/j.juro.2014.03.117
 6. Murphy G, Haider M, Ghai S, Sreeharsha B. The expanding role of MRI in prostate cancer. *AJR Am J Roentgenol* (2013) **201**:1229–38. doi:10.2214/AJR.12.10178
 7. Park JJ, Kim CK, Park SY, Park BK, Lee HM, Cho SW. Prostate cancer: role of pretreatment multiparametric 3-T MRI in predicting biochemical recurrence after radical prostatectomy. *AJR Am J Roentgenol* (2014) **202**:W459–65. doi:10.2214/AJR.13.11381
 8. Hövels AM, Heesakkers RAM, Adang EM, Jager GJ, Strum S, Hoogeveen YL, et al. The diagnostic accuracy of CT and MRI in the staging of pelvic lymph nodes in patients with prostate cancer: a meta-analysis. *Clin Radiol* (2008) **63**:387–95. doi:10.1016/j.crad.2007.05.022
 9. Bastide C, Beuzebec P, Cormier L, Fromont G, Hennequin C, Mongiat-Artus P, et al. Recommandations en onco-urologie 2013 du CCAFU: cancer de la prostate. *Prog Urol* (2013) **23**:S67–101. doi:10.1016/S1166-7087(13)70048-4
 10. Rousseau C, Rousseau T, Campion L, Lacoste J, Aillet G, Potiron E, et al. Laparoscopic sentinel lymph node versus hyperextensive pelvic dissection for staging clinically localized prostate carcinoma: a prospective study of 200 patients. *J Nucl Med* (2014) **55**:753–8. doi:10.2967/jnumed.113.129023
 11. Jadvar H. Prostate cancer: PET with 18F-FDG, 18F- or 11C-acetate, and 18F- or 11C-choline. *J Nucl Med* (2011) **52**:81–9. doi:10.2967/jnumed.110.077941
 12. DeGrado TR, Baldwin SW, Wang S, Orr MD, Liao RP, Friedman HS, et al. Synthesis and evaluation of (18F)-labeled choline analogs as oncologic PET tracers. *J Nucl Med* (2001) **42**:1805–14.
 13. Evangelista L, Zattoni F, Guttilla A, Saladini G, Zattoni F, Colletti PM, et al. Choline PET or PET/CT and biochemical relapse of prostate cancer: a systematic review and meta-analysis. *Clin Nucl Med* (2013) **38**:305–14. doi:10.1097/RLU.0b013e3182867f3c
 14. Beheshti M, Imamovic L, Broinger G, Vali R, Waldenberger P, Stoiber F, et al. 18F choline PET/CT in the preoperative staging of prostate cancer in patients with intermediate or high risk of extracapsular disease: a prospective study of 130 patients. *Radiology* (2010) **254**:925–33. doi:10.1148/radiol.09090413
 15. Krause BJ, Souvatzoglou M, Treiber U. Imaging of prostate cancer with PET/CT and radioactively labeled choline derivatives. *Urol Oncol* (2013) **31**:427–35. doi:10.1016/j.urolonc.2010.08.008
 16. Picchio M, Briganti A, Fanti S, Heidenreich A, Krause BJ, Messa C, et al. The role of choline positron emission tomography/computed tomography in the management of patients with prostate-specific antigen progression after radical treatment of prostate cancer. *Eur Urol* (2011) **59**:51–60. doi:10.1016/j.eururo.2010.09.004
 17. Kwee SA, Wei H, Sesterhenn I, Yun D, Coel MN. Localization of primary prostate cancer with dual-phase 18F-fluorocholine PET. *J Nucl Med* (2006) **47**:262–9.
 18. Nestle U, Kremp S, Schaefer-Schuler A, Sebastian-Welsch C, Hellwig D, Rube C, et al. Comparison of different methods for delineation of 18F-FDG PET-positive tissue for target volume definition in radiotherapy of patients with non-small cell lung cancer. *J Nucl Med* (2005) **46**:1342–8.
 19. Gallivanone F, Canevari C, Gianolli L, Salvatore C, Della Rosa PA, Gilardi MC, et al. A partial volume effect correction tailored for 18F-FDG-PET oncological studies. *Biomed Res Int* (2013) **2013**:780458. doi:10.1155/2013/780458
 20. Oprea-Lager DE, Vincent AD, van Moorselaar RJ, Gerritsen WR, Van den Eertwegh AJ, Eriksson J, et al. Dual-phase PET-CT to differentiate (18F) fluoromethylcholine uptake in reactive and malignant lymph nodes in patients with prostate cancer. *PLoS One* (2012) **7**:e48430. doi:10.1371/journal.pone.0048430
 21. Mohsen Beheshti WL. PET imaging of prostate cancer using radiolabeled choline. *PET Clin* (2009) **4**:173–84. doi:10.1016/j.cpet.2009.06.003
 22. Steiner C, Vees H, Zaidi H, Wissmeyer M, Berrebi O, Kossovsky MP, et al. Three-phase 18F-fluorocholine PET/CT in the evaluation of prostate cancer recurrence. *Nuklearmedizin* (2009) **48**(1):1–9.
 23. Garcia JR, Cuberas G, Riera E, Soler M, Moragas M, Lomeña F. Dual-phase 11C-choline PET/computed tomography in the early evaluation of prostate cancer recurrence. *Nucl Med Commun* (2015) **36**:8–15. doi:10.1097/MNM.0000000000000207
 24. Visvikis D, Hatt M, Tixier F, Cheze Le Rest C. The age of reason for FDG PET image-derived indices. *Eur J Nucl Med Mol Imaging* (2012) **39**:1670–2. doi:10.1007/s00259-012-2239-0
 25. De Langen AJ, Vincent A, Velasquez LM, van Tinteren H, Boellaard R, Shankar LK, et al. Repeatability of 18F-FDG uptake measurements in tumors: a meta-analysis. *J Nucl Med* (2012) **53**:701–8. doi:10.2967/jnumed.111.095299

Conflict of Interest Statement: The authors declare that the research was conducted in the absence of any commercial or financial relationships that could be construed as a potential conflict of interest.

Copyright © 2015 Mathieu, Ferrer, Carlier, Colombié, Rusu, Kraeber-Bodéré, Campion and Rousseau. This is an open-access article distributed under the terms of the Creative Commons Attribution License (CC BY). The use, distribution or reproduction in other forums is permitted, provided the original author(s) or licensor are credited and that the original publication in this journal is cited, in accordance with accepted academic practice. No use, distribution or reproduction is permitted which does not comply with these terms.

Clinical and survival impact of FDG PET in patients with suspicion of recurrent ovarian cancer: a 6-year follow-up

Daniela Rusu^{1*}, Thomas Carlier^{2,3}, Mathilde Colombié^{1,2}, Dorothée Goulon¹, Vincent Fleury¹, Nicolas Rousseau¹, Dominique Berton-Rigaud⁴, Isabelle Jaffre⁵, Françoise Kraeber-Bodéré^{1,2,3}, Loïc Campion^{2,6} and Caroline Rousseau^{1,2}

¹ Nuclear Medicine Unit, ICO Cancer Center, Saint-Herblain, France, ² CNRS UMR 6299, Centre Régional de Recherche en Cancérologie Nantes-Angers (CRCNA), INSERM U892, Nantes, France, ³ Nuclear Medicine, University Hospital Nantes, Nantes, France, ⁴ Oncology Unit, ICO Cancer Center, Saint-Herblain, France, ⁵ Oncologic Surgery Unit, ICO Cancer Center, Saint-Herblain, France, ⁶ Statistics Unit, ICO Cancer Center, Saint-Herblain, France

OPEN ACCESS

Edited by:

Jean-Pierre Pouget,
INSERM, France

Reviewed by:

Robert James Mairs,
University of Glasgow, UK
Maria Mathew D'Souza,
Institute of Nuclear Medicine and
Allied Sciences, India

*Correspondence:

Daniela Rusu,
ICO Cancer Center, Boulevard
Jacques Monod, 44805
Saint-Herblain, France
daniela.rusu@ico.unicanter.fr

Specialty section:

This article was submitted to Nuclear
Medicine, a section of the journal
Frontiers in Medicine

Received: 29 May 2015

Accepted: 01 July 2015

Published: 22 July 2015

Citation:

Rusu D, Carlier T, Colombié M,
Goulon D, Fleury V, Rousseau N,
Berton-Rigaud D, Jaffre I,
Kraeber-Bodéré F, Campion L and
Rousseau C (2015) Clinical and
survival impact of FDG PET in patients
with suspicion of recurrent ovarian
cancer: a 6-year follow-up.
Front. Med. 2:46.
doi: 10.3389/fmed.2015.00046

Background: The aim of this retrospective study was to evaluate the contribution of fluorine-18-fluoro-deoxyglucose (FDG) positron emission tomography (PET) to the clinical management and survival outcome of patients (pts) suspected of recurrent ovarian carcinoma, with the hypothesis that early diagnosis of recurrent ovarian cancer may improve overall survival (OS).

Methods: Fifty-three FDG PET/CT scans were retrospectively analyzed for 42 pts. CT and PET/CT findings were confirmed by imaging and clinical follow-up, and/or pathology, which were considered as the gold standard diagnosis. The treatment plan based on CT staging was compared with that based on PET/CT findings. Medical records were reviewed for pts characteristics, progression-free survival (PFS), and OS. PFS and OS were analyzed using the Cox proportional hazards regression model.

Results: The final diagnosis of recurrence was established pathologically ($n = 16$), or by a median clinical follow-up of 6.5 years (range 0.5–7.5) after the PET/CT ($n = 37$). PET/CT provided a higher detection sensitivity (92.2%, 47/51) than CT (60.8%, 31/51) ($p < 0.001$). Globally, PET/CT modified the treatment plan in 56.6% (30/53) and in 65.2% (15/23) when the CT was negative prior to PET/CT. In 30 cases, those benefited from a modified treatment plan, these changes led to the intensification of a previous treatment procedure in 83.3% (25/30), and to a reduction in the previous treatment procedure in 16.6% of cases (5/30). The Cox regression multivariate analysis showed that the number of lesions visualized by CT and presence of lung lesions detected by PET/CT were significantly associated with PFS ($p = 0.002$ and $p = 0.035$, respectively).

Conclusion: On account of its impact on treatment planning, and especially in predicting patient outcome, FDG PET is a valuable diagnostic tool for cases of suspected ovarian cancer recurrence.

Keywords: ovarian cancer, recurrence, PET/CT, 18F-FDG, survival outcome

Introduction

Ovarian cancer has the highest mortality of all gynecological cancers (1). Ovarian carcinoma is usually diagnosed at a late stage due to the paucity and insidious onset of symptoms (2). Despite high-response rates after initial treatment, 20–30% of patients with early-stage disease (stage IA-IIA), and up to 75% of patients with advanced disease (IIB-IV) present with recurrence within 2 years (3). Follow-up protocols usually consist of a physical examination, evaluation of the serum tumor marker (CA125), and morphological imaging techniques, such as ultrasound (US), computed tomography, and/or magnetic resonance imaging (MRI). However, these methods suffer certain limitations. Physical examination may be imprecise, and elevated values of CA 125 are sensitive for the early detection of active disease but do not localize the site of recurrence (4). In addition, conventional imaging (CI) techniques based on anatomical modifications, such as the identification of a new abnormal lesion or changes in the size of a known lesion, may have limited accuracy in the detection of tumor recurrence. Moreover, CT and MRI imaging (either soon after treatment or at later stages) are of limited value for optimally differentiating a recurrence signal from a post-surgical status, or due to their inability to detect normal-sized lymph node metastases (5).

Positron emission tomography (PET) with fluorine-18-fluorodeoxyglucose (FDG) has been proposed as a way of overcoming these limitations. It has been found to be highly sensitive for detecting recurrent ovarian cancer, especially in patients with an unexplained elevation of serum tumor markers. It offers the combined benefits of anatomical and functional imaging, and has been used to localize areas of increased FDG with improved anatomical specificity, and to exclude disease in sites of residual structural abnormality (6). A recent study evaluated the clinical impact of FDG PET upon treatment strategy, and found that accurate localization of ovarian cancer recurrence impacts both patient outcome and treatment strategy (7). The purpose of this study was to assess the clinical and therapeutic impact of FDG PET in women who were suspected of ovarian cancer recurrence.

Materials and Methods

Patient Population

Patients included retrospectively were of over 18 years of age, with histologically proven ovarian cancer that was suspected of recurrence, and had been treated in our institution between 2006 and 2010. All patients of the institution received written information on the possibility of use of their medical data in retrospective studies. After initial diagnosis, the patients were monitored by physical examination, CA 125 assay, and CT every 6 months over a 5-year period. Recurrent disease was suspected following abnormal examination results and/or symptoms suggestive of recurrence, equivocal results on CI, and/or the isolated elevated serum tumor marker (CA 125). PET scans were acquired only if recurrence was suspected from the different criteria described above. The International Federation of Gynecology and Obstetrics (FIGO) classification was used for clinical staging (8). A minimum of

6 months follow-up after the post-treatment PET scan was also an inclusion criterion for this study.

CT Imaging

CT images were obtained using a Hi-speed CT scanner (GE Medical Systems, Milwaukee, WI, USA). Patients fasted for ≥ 4 h before CT imaging. Scans were acquired in the craniocaudal direction, between the diaphragm and the perineum. After a series of unenhanced sections, all patients received intravenous bolus injection of contrast medium (Omnipaque 300™, GE Healthcare, Vélizy-Villacoublay, France) at a rate of 2.5–3 mL/s and a volume of 75–90 mL. The Hi-Speed CT scanner generated contiguous slices measuring 5 mm in thickness and reconstruction interval was 1.25 mm.

PET/CT Scanning

Scanning, from the patient's head to the pelvic floor with their arm held above their head, was performed using a Siemens Biograph mCT40 fitted with a 20 cm axial field of view, true of flight (TOF) feature, and in-plane resolution of 4.4 mm in full width at half maximum (Siemens, Knoxville, TN, USA). Images were reconstructed with Ultra HD and TOF (3 iterations, 21 subsets). Patients fasted for at least 4 h before PET acquisition. Fasting blood glucose, which had to be <7 mmol/L, was checked prior to injection of 3 MBq/kg of FDG. Intravenous injection was followed by a tracer-uptake period of approximately 60 min, during which patients remained seated in a quiet room. Low dose-unenhanced CT was performed for localization and attenuation correction. The reformatted, transverse, coronal, and sagittal views were used for interpretation.

Qualitative Imaging Analysis

CT and PET/CT clinical reports were collected and retrospectively analyzed. All PET/CT images were interpreted independently by two nuclear medicine physicians. The observers were aware of the clinical data and findings obtained with other anatomic imaging modalities. When abnormal FDG uptake was observed, its exact anatomical location was indicated on the CT scans. On PET images, the presence of a relapse tumor was suspected when accumulation of FDG was moderately to markedly increased, in comparison with that of comparable normal contralateral structures or surrounding tissues, excluding physiological bowel and urinary activity.

For both ethical and practical reasons, not every suspected involved lesion was evaluated by histology. A gold standard reference was therefore established based on histology and 6 months follow-up data (significant tumor progression on clinical examination or on CT according to RECIST Criteria). True-positive results corresponded to an abnormal image by an imaging method (CT or PET/CT) confirmed by histopathology or follow-up. For example, foci that were detected by PET/CT, which were not histologically examined, were considered to be true-positives if the disease became obvious upon clinical observation or with the imaging methods during the follow-up. A negative finding on an imaging method was considered to be false-negative if positive by histopathology or follow-up. Indeed, a negative finding on an imaging method that was detected by another imaging method

and confirmed by histopathology or by a clinical or imaging progression was considered to be false-negative. True-negative results corresponded to the absence of an abnormality by an imaging method, confirmation by a negative tissue biopsy, or lack of recurrence during the follow-up. For example, when no abnormality was found by PET/CT, or when no intervention was performed, the result was considered to be a true-negative if no disease was identified by other imaging studies or by clinical observation during 6 months follow-up. Finally, an abnormal result on an imaging method was considered to be false-positive if negative by histopathology or by follow-up. Suspicious involved lymph nodes were followed by CT although their size initially was not enough RECIST 1.1 criteria. Indeed, their development after treatment or not treatment has defined their status.

Statistical Analysis

Results are expressed as mean values \pm SD or median (range) in the case of small group sizes. Qualitative variables were compared using the Pearson test or the Fisher exact test where necessary (small sample size). Paired qualitative variables were compared using the Mac Nemar test. Quantitative variables were compared using the Student's *t*-test or the Mann-Whitney *U* test where necessary. Survival curves were calculated by means of the Kaplan-Meier method and compared by a log rank test. Multivariate analysis was performed by means of a Cox regression model. Analyses were performed using SAS 9.1 (SAS Institute Inc., Cary, NC, USA) and Stata/SE 10 (StataCorp LP, College Station, TX, USA). All tests were performed at a two-sided significance level of $\alpha = 0.05$.

Results

Patient Characteristics

We retrospectively evaluated 42 patients, with a median age of 45.5 years (35–81). For these patients, 53 PET/CT were performed. Patient characteristics are described in **Table 1**. All patients, except one, had a high risk of relapse. The recurrence was suspected due to abnormal results by CI in 30/53 PET/CT (56.6%) and an isolated elevated serum tumor marker CA 125 was observed in 23/47 PET/CT (48.9%). Recurrence was histopathologically confirmed in 30% (16/53) of cases, or by clinical follow-up for other patients, with a median clinical follow-up of 6.5 years (range 0.5–7.5) after PET/CT. PET/CT scans were not repeated during the follow-up even in cases of negative PET/CT results. Only CT or MRI was repeated. The median delay between PET/CT and initial treatment was 2.72 years (range 0.2–21.1).

Imaging Results

Table 2 shows the patient-based performance of whole-body PET/CT and CI. Whole-body PET/CT provided higher sensitivity and accuracy compared to CI ($p < 0.001$), especially with a sensitivity of 92.2% for PET/CT compared to 60.8% for CI. The four PET/CT false-negative results were local recurrences, all of which were also negative by CT.

For patients with elevated tumor marker CA125 ($n = 47$), the sensitivity of PET/CT was 91.3% (42/47), compared to 50% (23/46) for CI. PET/CT accurately diagnosed a recurrent disease

TABLE 1 | Patient characteristics before each FDG PET (53 examinations).

Characteristics	Value
Number of patients	42
Number of FDG PET	53
Median years (range)	59.3 (35.1–81)
Tumor histology	
Adenocarcinoma	37
Borderline	3
Serous	1
Granulosa cells	1
FIGO stage	
II	1
III	41
CA 125 level before FDG PET (Normal $< 1.5 \mu\text{g/L}$)	
Positive	47
Negative	6
Time from previous treatment (months)	
Median (range)	33 (2–253)

TABLE 2 | Performance of FDG PET/CT and conventional imaging to detect recurrence of ovarian cancer.

Performances	PET/CT whole body	Conventional imaging	<i>p</i>
<i>N</i>	53		
True-positive (<i>n</i>)	47	31	
True-negative (<i>n</i>)	2	0	
False-positive (<i>n</i>)	0	2	
False-negative (<i>n</i>)	4	20	
Sensitivity (%)	92.2	60.8	< 0.001
Specificity (%)	100	–	0.333
PPV (%)	100	93.9	0.167
NPV (%)	33.3	–	0.046
Accuracy (%)	92.5	52.8	0.01

TABLE 3 | Frequency of abnormal FDG PET findings by the site of involvement.

Sites of recurrence	Frequency
Lymph nodes	38 (71.7%)
Supradiaphragmatic	5
Supra and infradiaphragmatic	12
Pelvis	7 (13.2%)
Liver	10 (18.9%)
Bone	2 (3.7%)
Lung	4 (7.5%)
Peritoneal lesion	16 (30.2%)

in 91.5% of patients (43/47) compared to 48.9% (23/47) by CI ($p < 0.001$). The most frequent site of recurrence was in the lymph nodes (as described in **Table 3**; **Figure 1**).

Clinical Impact of PET/CT

Table 4 summarizes the changes in patient management based on PET/CT results. The confirmation of recurrence sites by biopsy was not considered as a modified treatment plan. Therefore, the therapeutic strategy was modified in 30/53 (56.6%) cases, and in 65.2% (15/23) when CI was negative. In 30 cases, those benefited from a modified treatment plan, these changes led to the use of a previously unplanned therapeutic procedure in all cases, to the

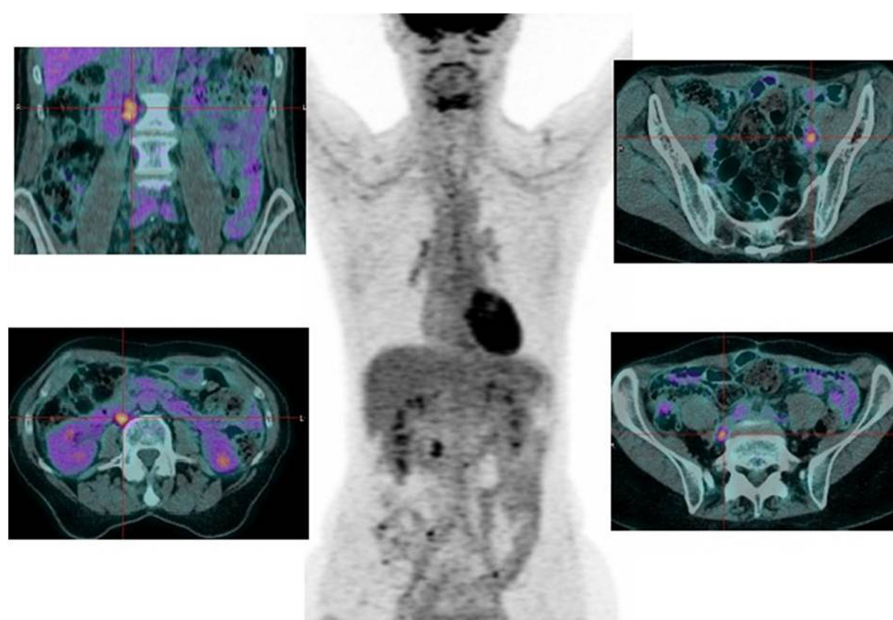


FIGURE 1 | Seventy-two-year-old patient suspected of pelvic recurrence of ovarian cancer. The CT was negative and CA125 normal (12 U/mL for $N < 35$), but with increasing kinetic. PET/CT found nodal retroperitoneal and pelvic abnormalities.

TABLE 4 | Changes in patient management based on the PET/CT results.

Treatment proposed before PET FDG	Therapeutic strategy decided after PET FDG
11 (Surgery)	7 (Chemotherapy) 1 (Surgery and chemotherapy) 1 (Extended surgery) 2 (Surveillance)
3 (Chemotherapy)	2 (Surgery) 1 (Surveillance)
1 (Radiotherapy)	1 (Chemotherapy)
15 (Surveillance)	13 (Chemotherapy) 1 (Surgery) 1 (Surgery and chemotherapy)

intensification of a previous treatment procedure in 83.3% (25/30) of cases, and to a reduction in previous treatment procedures in 16.6% of cases (5/30). In true-positive cases, the treatment showed decreases lesions size (for lesion without possible biopsy by ethics), decreases of biomarker with treatment, decreases of not significant nodes size with RECIST 1.1 but positive for PET/CT and sometimes appearance of significant lesions on CT (whereas PET/CT was earlier positive) in case of non-responders to treatment.

Survival Analysis

The impact of several variables on patient survival [progression-free and overall survival (OS)] were analyzed: age, increased CA125, the number of CT lesions, the number of PET/CT lesions, and semi-quantitative indexes, such as SUVmax, SUVmean, SUVpeak, and total lesion glycolysis (TLG).

Lung lesions detected by FDG or abnormal CT were predictive of progression free survival (PFS) (**Figure 2**). The PFS was better not only for patients with PET findings with lung foci ($p = 0.035$) but also for patients with abnormal CT than with normal CT ($p = 0.002$), as described in **Table 5**. The 1-year PFS was 42.9% for patients with PET findings without lung lesions, and 0% with lung metastases ($p = 0.049$).

Bone or lung lesions detected only by FDG PET were predictive of OS, whereas CI was not contributive (**Figure 3**). The OS was better for patients with PET findings without FDG foci corresponding to lung or bone metastasis (unknown by CI) than with PET findings, with lung foci ($p = 0.034$) or with bone foci ($p = 0.020$), as described in **Table 6**. The 1-year OS was 90.2% in patients with PET findings without bone lesions, and 50.0% with bone metastases.

Discussion

To our knowledge, this study is the first of its kind to extensively follow-up suspected recurrent ovarian carcinoma by PET/CT imaging, with the goal of determining prognostic factors for disease-free and OS, as well as the clinical impact of FDG PET in this indication. There are two major findings in this current study: (1) the absence of lung recurrence sites by PET/CT imaging was independent and prognostic of a good PFS (42% 1-year PFS) and (2) the absence of bone lesions by whole-body FDG PET was an independent and robust prognostic factor (90.2% 1-year OS).

Of all the variables analyzed (age, CA 125, number of target lesions on CT, abnormalities on CT, number of target lesions on PET/CT, abnormalities on PET/CT, lymph node, peritoneal, liver, pelvis, lung, or bone metastases, as well as semi-quantitative indexes, such as SUVmax, SUVmean, SUVpeak, and TLG), lung

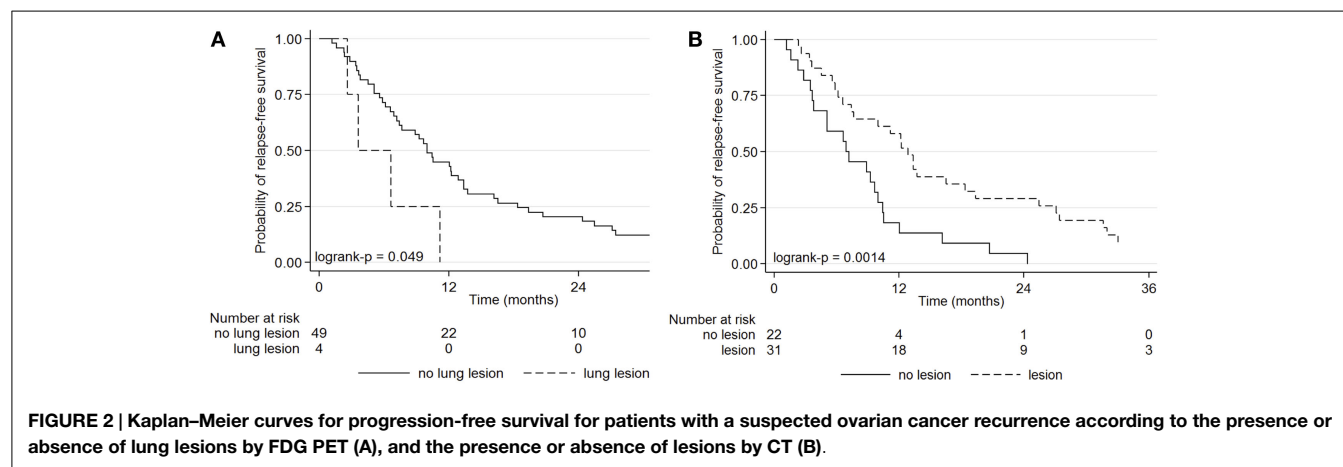


TABLE 5 | Uni- and multivariate analyses for the determination for factors prognostic of progression-free survival (PFS) in recurrent ovarian cancer.

Parameters	Univariate analysis		Multivariate analysis	
	HR (95% CI)	p-Value	HR (95% CI)	p-Value
Age	0.99 (0.96–1.02)	0.514	–	–
CA 125 > 35 vs. ≤35	2.47 (0.86–7.09)	0.093	–	–
FDG PET foci				
>0 vs. 0	0.79 (0.33–1.87)	0.590	–	–
Lung lesion >0 vs. 0	2.77 (0.96–7.96)	0.059	3.14 (1.08–9.11)	0.035
CT foci 0 vs. >0	0.39 (0.21–0.71)	0.002	2.68 (1.45–4.96)	0.002
SUVmax	1.01 (0.95–1.06)	0.891	–	–
SUVmean	1.02 (0.94–1.10)	0.680	–	–
SUVpeak	1.01 (0.95–1.08)	0.676	–	–
TLG	1.00 (0.99–1.00)	0.804	–	–

lesions detected only by PET/CT were significantly associated with PFS, while bone or lung metastases detected only by PET/CT were associated with OS. The semi-quantitative index of PET/CT has no prognostic value in our study. One possible explanation is the heterogeneity of the population studied, with one or more relapses per patient, different types of treatments, and different disease resistance to treatment. The results of our study are consistent with that of Hebel et al. (9). They did not find any significant association between SUVmax and the specific survival in patients with a positive PET/CT scan, nor a significant difference between the SUVmax of the most intense lesion or the number of suspicious lesions on PET/CT scan between patients who responded or not to therapy. On the contrary, the study of Sala et al. showed a possible prognostic role for SUVmax (10). For patients with low-grade serous ovarian cancer, the TLG could be prognostic for survival after relapse, according to a study by Takeuchi (11). In their study, multiple recurrence was associated with poorer PFS than single-lesion recurrence, while CA 125 and SUVmax were not significant predictors of PFS or OS. For our group of patients, TLG was not associated with either disease-free survival or OS (12). In the study by Levy et al., CA 125 level of recurrence and the pattern of CA 125 elevation were significantly associated with PFS and OS by univariate analysis, while in the multivariate analysis increases in CA 125 above normal levels was an independent predictor of PFS and of OS (Levy). In our study, CA 125 had no prognostic value.

Sala et al. found that the number, size, and SUVmax of recurrent ovarian cancer lesions in the peritoneum and distant lymph nodes were significantly associated with OS and PFS [Sala 8]. The recent study of Kim et al. found that the platinum-free interval, type of second-line treatment, metabolic tumor volume, and TLG were all significant prognostic factors for post-relapse survival (13).

According to clinical guidelines, when recurrence is suspected, the second step after the determination of CA 125 levels is the CT scan (14–16), with MRI as an alternative if the CT is contraindicated (17). However, several studies have shown the diagnostic superiority of PET/CT over CT. There are some limitations of PET/CT, including the non-specific nature of tracer-uptake, which can accumulate in sites of inflammation and infection, which may be detected as false-positive (18). In addition, PET/CT has a limited ability to detect small lesions, particularly for those <5 mm, with a false-negative rate of 5–10% (19, 20). PET/CT resolution is currently around 4 mm, and even with technical improvements, it cannot drop below 2 mm because the free path of a positron will always leave doubt as to its place of origin (21). Sometimes, the fusion of PET and CT images is not perfect, because of the physiological digestive peristalsis. False-negative results are possible in clear cell and mucinous ovarian cancer, and in necrotic or cystic lesions (22–24). Thus, in a prospective study, Risum et al. evaluated the sensitivity and specificity of US, CT, and PET/CT in the diagnosis of recurrence in 60 patients (25). While the specificity was the same (90%) for the three tests, sensitivity was 97% for PET/CT, 81% for CT, and 66% for US. In addition, PET/CT was superior to single recurrence detection and found recurrence in 50% of patients with negative CT and multifocal recurrence in 42% of cases with isolated recurrence on CT. The meta-analysis of Gu et al., who compared the CA 125, PET, PET/CT, and MRI for the diagnosis of recurrent ovarian cancer in 882 patients found a higher sensitivity for PET/CT (91%) and greater specificity for CA 125 (5). The retrospective study of Antunovic et al. showed better sensitivity (82 vs. 69%), specificity (87 vs. 47%), and accuracy (83 vs. 66%) of PET/CT compared to CI, and better sensitivity compared to CA 125 (83 vs. 59%). Furthermore, the sensitivity of the PET/CT was not affected in this tumor differentiation study (26). PET/CT combined with contrast iodine injection was superior in the detection of recurrence compared to PET/CT without injection in the study by Kitajima

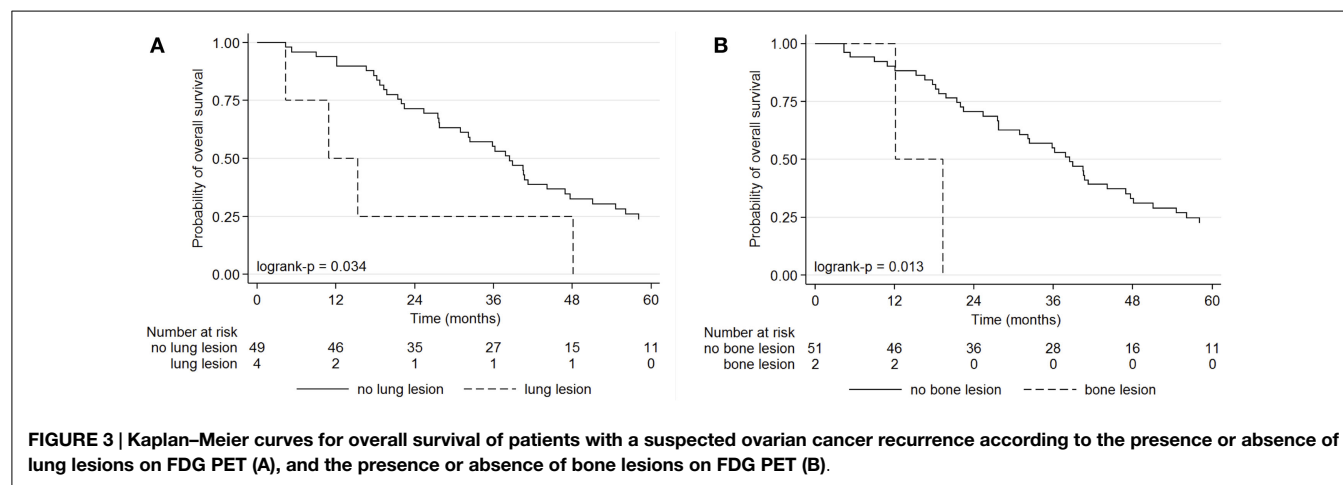


TABLE 6 | Uni- and multivariate analyses for the determination of factors prognostic for overall survival (OS) in recurrent ovarian cancer.

Parameters	Univariate analysis		Multivariate analysis	
	HR (95% CI)	p-Value	HR (95% CI)	p-Value
Age	1.02 (0.98–1.04)	0.298	–	–
CA 125 > 35 vs. ≤35	1.67 (0.59–4.70)	0.970	–	–
FDG PET foci				
>0 vs. 0	1.15 (1.02–1.29)	0.023	–	–
Lung lesion >0 vs. 0	2.93 (1.03–8.34)	0.044	3.12 (1.09–8.89)	0.034
Bone lesion >0 vs. 0	5.53 (1.22–25.12)	0.027	6.09 (1.33–27.83)	0.020
CT foci >0 vs. 0	0.63 (0.34–1.15)	0.129	–	–
SUVmax	1.02 (0.97–1.07)	0.415	–	–
SUVmean	1.00 (0.92–1.10)	0.904	–	–
SUVpeak	1.03 (0.97–1.09)	0.308	–	–
TLG	1.00 (0.99–1.00)	0.196	–	–

et al. (121 patients), with a sensitivity of 87 vs. 78% (27). Contrast iodine injections were not performed in our PET/CT analysis. The diagnostic value of PET/CT in our study (sensitivity 97.5%, 47 patients) was similar to that of MRI in the study of Sanli et al. (28), and even better for the detection of peritoneal carcinomatosis lesions of between 0.5 and 2 cm ($p < 0.05$). PET/CT has good sensitivity in detecting lymph node metastases (29), especially supra-diaphragmatic lesions (30). In our study, in 71.7% of cases, there were lymph nodes metastases, with 32% of cases with supra-diaphragmatic lesions. A negative FDG PET/CT has a high-negative predictive value (9). The results of our study are comparable to the literature, with a good performance of PET/CT (Table 7) (5, 6, 9, 11, 23, 25, 26, 28, 31, 32). Our study found a significant impact of PET/CT in the management of recurrent ovarian cancer (Table 8). The therapeutic procedures were changed in 30/53 of our cases (56.6%), which is comparable with the previously published studies of Bilici – 51.6%, Ebina – 58.4%, Fulham – 58.9%, Hebel – 69%, and Rousseau – 71.5% (6, 7, 9, 33, 34).

Despite its high accuracy (80%) in the diagnosis of ovarian cancer recurrence (35), CA 125 has its limits. While a normal value cannot exclude the presence of disease, an increase of CA 125, even in normal limits, can predict recurrence. According to a study of Bhosale et al., PET/CT detected recurrence in 58% of

TABLE 7 | Sensitivity of PET/CT in the detection of recurrent ovarian cancer: comparison with previously published data.

Studies	No. pts	Sensitivity PET/CT (%)
Gu et al. (5)	882	91
Gouhar et al. (23)	39	90
Rubini et al. (31)	79	85
Hebel et al. (9)	48	97
Takeuki et al. (11)	48	94
Risum et al. (25)	60	97
Antunovic et al. (26)	121	82
Sanli et al. (28)	47	97.5
Sari et al. (32)	34	96.1
Bilici et al. (6)	60	95
Our study	42	92.2

TABLE 8 | Impact of PET/CT in the management of recurrent ovarian cancer: comparison with previously published data.

Studies	No. pts	Change of treatment (%)
Fulham et al. (7)	90	58.9
Hebel et al. (9)	48	69
Bilici et al. (6)	60	51.6
Rousseau et al. (33)	34	71.5
Ebina et al. (34)	44	58.4
Our study	42	56.6

cases when CA125 was normal, while 31% of patients with normal CA 125 and negative CT had ovarian cancer recurrence confirmed by histology (36). Furthermore, high values cannot differentiate local recurrence from distant metastases (14, 31). It is the role of imagery, and especially PET/CT, to answer that question.

Our study has several limitations. First, it is a retrospective study with potential inherent biases, and further prospective studies are needed to confirm the results. Second, the ideal gold standard for any analysis is histological confirmation ($n = 16/53$). However, clinical follow-up ($n = 37/53$) is also a valid way to evaluate diagnostic accuracy and response to therapy, but it would have been unethical to investigate all PET/CT detected foci using invasive procedures. Finally, the number of patients in the study was relatively small and it warranted the necessity to gather

patients for survival analysis in order to retain a valid and strong power by statistical analysis.

Conclusion

In recurrent ovarian carcinoma suspected by elevated CA 125 serum levels and normal or dubious CT, FDG PET/CT provides staging information that more accurately stratifies prognostic risk in recurrence ovarian cancer when compared with CT alone. There is also a strong evidence to support the use of PET/CT not only for the detection of recurrent ovarian cancer but also

to confirm recurrence from the point of view of the therapeutic outcome (choice of treatment). Nonetheless, further evaluations appear necessary.

Acknowledgments

This work has been supported by grants from the French National Agency for Research called “Investissements d’Avenir,” Labex IRON no. ANR-11-LABX-0018-01 and Equipex ArronaxPlus no. ANR-11-EQPX-0004.

References

- Coward JIG, Middleton K, Murphy F. New perspectives on targeted therapy in ovarian cancer. *Int J Womens Health* (2015) **4**(7):189–203. doi:10.2147/IJWH.S52379
- Bharwani N, Reznick R, Rockall AG. Ovarian cancer management: the role of imaging and diagnostic challenges. *Eur J Radiol* (2011) **78**:41–51. doi:10.1016/j.ejrad.2010.11.039
- Palma MD, Gregorian M, Fiduccia P, Evangelista L, Cervino AR, Saladini G, et al. PET/CT imaging in gynecologic malignancies: a critical overview of its clinical impact and our retrospective single center analysis. *Crit Rev Oncol Hematol* (2012) **83**:84–98. doi:10.1016/j.critrevonc.2011.10.002
- Goonewardene TI, Hall MR, Rustin GJ. Management of asymptomatic patients on follow-up for ovarian cancer with rising CA-125 concentrations. *Lancet Oncol* (2007) **8**:813–21. doi:10.1016/S1470-2045(07)70273-5
- Gu P, Pan LL, Wu SQ, Sun L, Huang G. CA 125, PET alone, PET-CT, CT and MRI in diagnosing recurrent ovarian carcinoma: a systematic review and meta-analysis. *Eur J Radiol* (2009) **71**:164–74. doi:10.1016/j.ejrad.2008.02.019
- Bilici A, Ustaoglu BB, Seker M, Canpolat N, Tekinsoy B, Salepci T, et al. Clinical value of FDG PET/CT in the diagnosis of suspected recurrent ovarian cancer: is there an impact of FDG PET/CT on patient management? *Eur J Nucl Med Mol Imaging* (2010) **37**:1259–69. doi:10.1007/s00259-010-1416-2
- Fulham MJ, Carter J, Baldey A, Hicks RJ, Ramshaw JE, Gibson M. The impact of PET-CT in suspected recurrent ovarian cancer: a prospective multi-centre study as part of the Australian PET data collection project. *Gynecol Oncol* (2009) **112**:462–8. doi:10.1016/j.ygyno.2008.08.027
- Prat J; FIGO Committee on Gynecologic Oncology. Staging classification for cancer of the ovary, fallopian tube and peritoneum. *Int J Gynaecol Obstet* (2014) **124**(1):1–5. doi:10.1016/j.ijgo.2013.10.001
- Hebel B, Behrendt FF, Heinzl A, Krohn T, Mottaghy FM, Bauerschlag DO, et al. Negative 18F-2-fluorodeoxyglucose PET/CT predicts good cancer specific survival in patients with a suspicion of recurrent ovarian cancer. *Eur J Radiol* (2014) **83**:436–67. doi:10.1016/j.ejrad.2013.12.006
- Sala E, Kataoka M, Pandit-Taskar N, Ishill N, Mironov S, Moskowitz CS, et al. Recurrent ovarian cancer: use of contrast-enhanced CT and PET/CT to accurately localise tumor recurrence and to predict patients’ survival. *Radiology* (2010) **257**:125–34. doi:10.1148/radiol.10092279
- Takeuchi S, Lucchini M, Schmeler KM, Coleman RL, Gershenson DM, Munsell ME, et al. Utility of 18F-FDG PET/CT in follow-up of patients with low-grade serous carcinoma of the ovary. *Gynecol Oncol* (2014) **133**:100–4. doi:10.1016/j.ygyno.2014.02.008
- Carlier T, Campion L, Rusu D, Colombié M, Goulon D, Kraeber-Bodéré F, et al. Correlation and usefulness of textural metrics in ovarian carcinoma using PET imaging: preliminary results. *Eur J Nucl Med Mol Imaging* (2014) **41**:S366.
- Kim CY, Jeong SY, Chong GO, Son SH, Jung JH, Kim DH, et al. Quantitative metabolic parameters measured on F-18 FDG PET/CT predict survival after relapse in patients with relapsed epithelial ovarian cancer. *Gynecol Oncol* (2015) **136**(3):498–504. doi:10.1016/j.ygyno.2014.12.032
- Musto A, Rampin L, Nanni C, Marzola MC, Fanti S, Rubello D. Present and future of PET and PET/CT in gynaecologic malignancies. *Eur J Radiol* (2011) **78**:12–20. doi:10.1016/j.ejrad.2009.12.035
- Gadducci A, Cosio S. Surveillance of patients after initial treatment of ovarian cancer. *Crit Rev Oncol Hematol* (2009) **71**:43–52. doi:10.1016/j.critrevonc.2008.12.008
- Musto A, Grassetto G, Marzola MC, Rampin L, Chondrogiannis S, Maffione AM, et al. Management of epithelial ovarian cancer from diagnosis to restaging: an overview of the role of imaging techniques with particular regard to the contributions of 18F-FDG PET/CT. *Nucl Med Commun* (2014) **35**(6):588–97. doi:10.1097/MNM.0000000000000091
- Fischerova D, Burgetova A. Imaging techniques for the evaluation of ovarian cancer. *Best Pract Res Clin Obstet Gynaecol* (2014) **28**:697–720. doi:10.1016/j.bpobgyn.2014.04.006
- Son H, Khan SM, Rahaman J, Cameron KL, Prasad-Hayes M, Chuang L, et al. Role of FDG PET/CT in staging of recurrent ovarian cancer. *Radiographics* (2011) **31**(2):569–83. doi:10.1148/rg.312105713
- Prakash P, Cronin CG, Blake MA. Role of PET/CT in ovarian cancer. *AJR Am J Roentgenol* (2010) **194**:W464–70. doi:10.2214/AJR.09.3843
- Zwarthoed C, Bereder JM, Viau P, Grangeon C, Maurel F, Darcourt J, et al. TEP au 18 FDG et carcinose péritonéale d’origine ovarienne: valeurs diagnostique et pronostique avant chimio-hyperthermie intra-péritonéale. *Med Nucl* (2014) **38**:398–407. doi:10.1016/j.mednuc.2014.05.006
- Taïeb S, Kolesnikov-Gauthier H, Chevalier A, Leblanc E. Imagerie post-thérapeutique des cancers de l’ovaire. *Imagerie de la Femme* (2013) **23**:15–20. doi:10.1016/j.femme.2013.01.001
- Grant P, Sakelliset C, Jacene HA. Gynecologic oncologic imaging with PET/CT. *Semin Nucl Med* (2014) **44**:461–78. doi:10.1053/j.semnuclmed.2014.06.005
- Gouhar GK, Siam S, Sadek SM, Ahmed RA. Prospective assessment of 18F-FDG PET/CT in detection of recurrent ovarian cancer. *Egypt J Radiol Nucl Med* (2013) **44**:913–22. doi:10.1016/j.ejrm.2013.08.005
- Du XI, Jiang T, Sheng XG, Li QS, Wang C, Yu H. PET/CT scanning guided intensity-modulated radiotherapy in treatment of recurrent ovarian cancer. *Eur J Radiol* (2012) **81**:3551–6. doi:10.1016/j.ejrad.2012.03.016
- Risum S, Hogdall C, Markova E, Berthelsen AK, Loft A, Jensen F, et al. Influence of 2-(18F) fluoro-2-deoxy-d-glucose positron emission tomography/computed tomography on recurrent ovarian cancer diagnosis and on selection of patients for secondary cytoreductive surgery. *Int J Gynecol Cancer* (2009) **19**(4):600–4. doi:10.1111/IGC.0b013e3181a3cc94
- Antunovic L, Cimitan M, Borsatti E, Baresic T, Sorio R, Giorda G, et al. Revisiting the clinical value of 18F-FDG PET/CT in detection of recurrent epithelial ovarian carcinoma. *Clin Nucl Med* (2012) **37**(8):184–8. doi:10.1097/RLU.0b013e31825b2583
- Kitajima K, Ueno Y, Suzuki K, Kita M, Ebina Y, Yamada H, et al. Low-dose non-enhanced CT versus full-dose contrast-enhanced CT in integrated PET/CT scans for diagnosing ovarian cancer recurrence. *Eur J Radiol* (2012) **81**:3557–62. doi:10.1016/j.ejrad.2012.03.020
- Sanli Y, Turkmen C, Bakir B, Iyibozkurt C, Ozel S, Has D, et al. Diagnostic value of PET/CT is similar to that of conventional MRI and even better for detecting small peritoneal implants in patients with recurrent ovarian cancer. *Nucl Med Commun* (2012) **33**(5):509–15. doi:10.1097/MNM.0b013e32834fc5bf
- Yuan Y, Gu ZX, Tao XF, Liu SY. Computed tomography, magnetic resonance imaging, and positron emission tomography or positron emission tomography/computer tomography for detection of metastatic lymph nodes in patients with ovarian cancer: a meta-analysis. *Eur J Radiol* (2012) **81**:1002–6. doi:10.1016/j.ejrad.2011.01.112
- Dragosavac S, Derchain S, Caserta NMG, De Souza G. Staging recurrent ovarian cancer with 18 FDG PET/CT. *Oncol Lett* (2013) **5**:593–7. doi:10.3892/ol.2012.1075

31. Rubini G, Altini C, Notaristefano A, Merenda N, Rubini D, Stabile Ianora AA, et al. Role of 18F-FDG PET/CT in diagnosing peritoneal carcinomatosis in the restaging of patient with ovarian cancer as compared to contrast enhanced CT and tumor marker CA-12. *Rev Esp Med Nucl Imagen Mol* (2014) **33**(1):22–7. doi:10.1016/j.remnm.2013.06.008
32. Sari O, Kaya B, Kara PO, Celik C, Ozbek O, Serdengecti M. The role of FDG-PET/CT in ovarian cancer patients with high tumor markers or suspicious lesion on contrast-enhanced CT in evaluation of recurrence and/or in determination of intraabdominal metastases. *Rev Esp Med Nucl Imagen Mol* (2012) **31**(1):3–8. doi:10.1016/j.remnm.2011.03.008
33. Rousseau C, Pallardy A, Campion L, Bourbouloux E, Bodet-Milin C, Sagan C, et al. Clinical Impact of FDG-PET in the suspicion of recurrent ovarian carcinoma based on elevated tumor marker serum levels. *J Nucl Med* (2007) **48**(2):86.
34. Ebina Y, Watari H, Kaneuchi M, Takeda M, Hosaka M, Kudo M, et al. Impact of FDG PET in optimizing patient selection for cytoreductive surgery in recurrent ovarian cancer. *Eur J Nucl Med Mol Imaging* (2014) **41**:446–51. doi:10.1007/s00259-013-2610-9
35. Palomar A, Nanni C, Castelucci P, Ambrosini V, Montini GC, Allegri V, et al. Value of FDG PET/CT in patients with treated ovarian cancer and raised CA125 serum levels. *Mol Imaging Biol* (2012) **14**:123–9. doi:10.1007/s11307-010-0468-9
36. Bhosale P, Peungjesada S, Wei W, Schmeler K, Rohren E, Macapinlac HA, et al. Clinical utility of positron emission tomography/computed tomography in the evaluation of suspected recurrent ovarian cancer in the setting of normal CA 125 levels. *Int J Gynecol Cancer* (2010) **6**:936–44. doi:10.1111/IGC.0b013e3181e82a7f

Conflict of Interest Statement: The authors declare that the research was conducted in the absence of any commercial or financial relationships that could be construed as a potential conflict of interest.

Copyright © 2015 Rusu, Carlier, Colombié, Goulon, Fleury, Rousseau, Berton-Rigaud, Jaffre, Kraeber-Bodéré, Campion and Rousseau. This is an open-access article distributed under the terms of the Creative Commons Attribution License (CC BY). The use, distribution or reproduction in other forums is permitted, provided the original author(s) or licensor are credited and that the original publication in this journal is cited, in accordance with accepted academic practice. No use, distribution or reproduction is permitted which does not comply with these terms.



Story of rubidium-82 and advantages for myocardial perfusion PET imaging

Jean-François Chatal^{1*}, François Rouzet², Ferid Haddad¹, Cécile Bourdeau¹,
Cédric Mathieu³ and Dominique Le Guludec²

¹ Groupement d'Intérêt Public Arronax, University of Nantes, Saint-Herblain, France, ² UMR 1148, Department of Nuclear Medicine, Bichat Hospital, Assistance Publique Hôpitaux de Paris, DHU FIRE (Fibrosis, Inflammation, Remodeling in Cardiovascular, Respiratory and Renal Diseases), Paris-Diderot University, Paris, France, ³ Department of Nuclear Medicine, Nantes University Hospital, Nantes, France

OPEN ACCESS

Edited by:

Denis Guilloteau,
Université de Tours and CHRU Tours,
France

Reviewed by:

Flavia Groppi,
Università degli Studi di Milano, Italy
Ulli Köster,
Institut Laue-Langevin, France

*Correspondence:

Jean-François Chatal,
GIP Arronax, 1, rue Arronax,
BP 10112, 44817 Saint-Herblain
Cedex, France
chatal@arronax-nantes.fr

Specialty section:

This article was submitted to Nuclear
Medicine, a section of the journal
Frontiers in Medicine

Received: 16 June 2015

Accepted: 26 August 2015

Published: 11 September 2015

Citation:

Chatal J-F, Rouzet F, Haddad F,
Bourdeau C, Mathieu C and
Le Guludec D (2015) Story of
rubidium-82 and advantages for
myocardial perfusion PET imaging.
Front. Med. 2:65.
doi: 10.3389/fmed.2015.00065

Rubidium-82 has a long story, starting in 1954. After preclinical studies in dogs showing that myocardial uptake of this radionuclide was directly proportional to myocardial blood flow (MBF), clinical studies were performed in the 80s leading to an approval in the USA in 1989. From that time, thousands of patients have been tested and their results have been reported in three meta-analyses. Pooled patient-based sensitivity and specificity were, respectively, 0.91 and 0.90. By comparison with ^{99m}Tc-SPECT, ⁸²Rb PET had a much better diagnostic accuracy, especially in obese patients with body mass index ≥ 30 kg/m² (85 versus 67% with SPECT) and in women with large breasts. A great advantage of ⁸²Rb PET is its capacity to accurately quantify MBF. Quite importantly, it has been recently shown that coronary flow reserve is associated with adverse cardiovascular events independently of luminal angiographic severity. Moreover, coronary flow reserve is a functional parameter particularly useful in the estimate of microvascular dysfunction, such as in diabetes mellitus. Due to the very short half-life of rubidium-82, the effective dose calculated for a rest/stress test is roughly equivalent to the annual natural exposure and even less when stress-only is performed with a low activity compatible with a good image quality with the last generation 3D PET scanners. There is still some debate on the relative advantages of ⁸²Rb PET with regard to ^{99m}Tc-SPECT. For the last 10 years, great technological advances substantially improved performances of SPECT with its accuracy getting closer to this of ⁸²Rb/PET. Currently, the main advantages of PET are its capacity to accurately quantify MBF and to deliver a low radiation exposure.

Keywords: rubidium-82, myocardial perfusion, PET imaging

Introduction

The story of medical use of rubidium goes back in 1954 when Love et al. showed that the biological behavior of rubidium was comparable to the one of potassium and that its myocardial muscle uptake was proportional to blood flow in coronary arteries (1). Following this paper, several preclinical studies have been performed mainly in dogs and using different radionuclides of rubidium until the early 80s when the first injection in humans took place (2). During the 80s, a few clinical studies, including hundreds of patients, demonstrated the good diagnostic accuracy of ⁸²Rb/PET, which was higher than the one obtained with ^{99m}Tc/SPECT (3, 4). Subsequently, a generator ⁸²Sr/⁸²Rb (CardioGen-82®) was approved in 1989 and delivered in the USA by Bracco Diagnostics, Inc., for clinical use.

At that time, the number of PET cameras, their technological performances, and the production capacities of strontium-82 were limited, explaining a slow progression of this technology in the USA. However, despite this limitation, thousands of patients were tested with PET using rubidium-82 allowing three meta-analyses to be performed.

During the last 10 years, with the increased number of PET/CT systems and the higher strontium-82 production capabilities, the number of patients injected with rubidium-82 in the USA dramatically grew even if it still represents a small percentage by comparison with the use of ^{99m}Tc -sestamibi and ^{99m}Tc -tetrofosmin. Moreover, for the last 10 years, great technological advances have been introduced, including semiconductor detector SPECT scanners, novel collimator design, and novel iterative reconstruction methods allowing to substantially improve count sensitivity and image resolution. Consequently, the diagnostic accuracy of ^{99m}Tc /SPECT got closer to this of ^{82}Rb /PET, opening a large debate on the advantages of one technique with regard to the other.

The latest clinical developments zeroed in on the high prognostic value of quantification using PET and allowing to accurately measure myocardial blood flow (MBF) and coronary reserve. Even if there are no real technical limitations to such measurements with SPECT it will take some years before their potential clinical validation (5). Finally, the level of radiation dose is an important parameter to be taken into consideration due to the high number of patients to be tested and the repetition of imaging in the same patients. The aforementioned technological advances allowed to significantly reduce radiation doses with both ^{99m}Tc /SPECT and ^{82}Rb /PET even if the latter delivers the smallest dose (6).

Preclinical Studies

Beta- and gamma-emitting rubidium-86 was first used because its long 18.7 days half-life enabled to perform long-lasting kinetic studies. In 1959, Love et al. showed, in 19 dogs, that myocardial uptake of this radionuclide was directly proportional to MBF (7). These results were confirmed 2 years later in 26 dogs by Levy et al. (8).

More than a decade later, Nishiyama et al. compared optimal settings of scintillation camera with ^{201}Tl (T1/2: 73.1 h, γ : 167 keV), ^{43}K (T1/2: 22.2 h, γ : 373 keV), ^{129}Cs (T1/2: 32.06 h, γ : 372 keV), and ^{81}Rb , a positron-emitting radioisotope with a half-life of 4.6 h (9). Thallium-201 was considered as the best suited with the available equipment at that time and cesium-129 was next best. High-energy photons from ^{81}Rb largely made it impossible to obtain an interpretable image without the addition of more shielding.

In 1979, Yano et al. compared several ion-exchange columns to be used in an automated $^{82}\text{Sr}/^{82}\text{Rb}$ generator for testing in man (10).

Finally, in 1982, Selwyn et al. examined the relation between myocardial perfusion and rubidium-82 uptake during acute ischemia in six dogs after coronary stenosis and in five volunteers and five patients with coronary artery disease. Myocardial tomograms, recorded at rest and after exercise in the volunteers showed homogeneous uptake in reproducible and repeatable

scans. An absolute mean decrease of $36 \pm 14\%$ in regional myocardial uptake was found after exercise in the patients with coronary artery disease (2).

Clinical Studies

Meta-Analyses of PET Studies

Since the approval by FDA in the USA in 1989, a vast amount of clinical studies have been performed, including thousands of patients. Results have been analyzed in three meta-analyses published in 2008 and 2012 (Table 1). Pooled patient-based sensitivity and specificity were, respectively, 0.91 and 0.90. These excellent results should be tempered by some limitations and biases inherent to meta-analyses. There was heterogeneity between studies in scanning protocols and prevalence stenosis with invasive coronary angiography. Moreover, baseline characteristics, such as gender or disease prevalence, were different between patient populations resulting in a cautious interpretation.

For a long time, PET studies have been performed with two-dimensional cameras needing to inject a relatively high activity of rubidium-82 (40 mCi for stress-only) and resulting in non-negligible radiation exposure. The accuracy, outcomes, and cost-effectiveness of 3D PET technology using a low activity of 20 mCi were recently evaluated in seven centers (14). Through an effective standardization and quality assurance program, the image interpretation was highly repeatable in involved centers.

Meta-Analyses of SPECT Studies

A much larger number of 227 studies using ^{99m}Tc /SPECT and including more than 14,500 patients have been considered in 7 meta-analyses published between 1998 and 2012 (Table 2). Pooled patient-based sensitivity and specificity were, respectively, 0.88 and 0.67. The same limitations as with PET studies were applied to SPECT studies.

Comparison Between PET and SPECT

Myocardial perfusion imaging is a real challenge in overweight or obese patients and in women with large breasts due to attenuation artifacts, resulting in decreased specificity using ^{99m}Tc SPECT. PET imaging has improved specificity owing to better spatial resolution, coincidence detection, and accurate attenuation correction.

Bateman et al. compared ^{99m}Tc SPECT in 112 patients with ^{82}Rb PET in 112 patients (20). They showed a much better diagnostic accuracy using PET, in obese patients with body mass index (BMI)

TABLE 1 | Results of meta-analyses with ^{82}Rb PET.

Number of studies/patients	Patient-based sensitivity	Patient-based specificity	Reference
11/1175	0.93 (0.85–0.96)	0.90 (0.75–1.00)	(11)
11/NS ^a	0.84 (0.81–0.87)	0.81 (0.74–0.87)	(12)
6/843	0.91 (0.86–0.96)	0.93 (0.60–1.00)	(13)
28/2018	0.91	0.90	

NS, not specified.

^aPooled results.

TABLE 2 | Results of meta-analyses with ^{99m}Tc SPECT.

Number of studies/patients	Patient-based sensitivity	Patient-based specificity	Reference
20/3474	0.90 (0.89–0.90)	0.77 (0.72–0.83)	(15)
27/3237	0.87 ^a	0.64 ^a	(16)
44/2837	0.89 (0.82–0.90)	0.75 (0.65–0.75)	(17)
10/651	0.88 ^a	0.67 ^a	(18)
13/2922	0.81 ^a	0.65 ^a	(19)
105/NS	0.88 (0.88–0.89)	0.61 (0.59–0.62)	(12)
8/1410	0.85 (0.72–0.97)	0.82 (0.76–0.92)	(13)
227/14531	0.88 (0.81–0.90)	0.67 (0.61–0.82)	

NS, not specified.

^aPooled results.

$\geq 30 \text{ kg/m}^2$ (85 versus 67% with SPECT). However, it should be noted that SPECT was performed at that time without attenuation correction. With the introduction of iterative reconstruction, SPECT is now performed with attenuation correction, which may correct some artifacts and improve diagnostic accuracy in the obese population but with a decrease of sensitivity. A recent study reported on the value of ^{82}Rb PET in 2687 obese patients with BMI $\geq 30 \text{ kg/m}^2$ by comparison with 2047 overweight patients (BMI: $25.0\text{--}30.0 \text{ kg/m}^2$) and 1303 normal patients (BMI: $<25.0 \text{ kg/m}^2$). Interestingly, the results showed the same prognostic value irrespective of BMI (21).

In the future, ^{82}Rb PET should be compared to contemporary ^{99m}Tc SPECT using the last technological advances in the same overweight or obese patients to confirm or not the higher prognostic value of PET to SPECT.

As aforementioned, a large number of clinical studies have been performed using PET and SPECT in different populations of patients allowing to group the results in meta-analyses with the possibility of biases in interpretation of these results.

The most informative comparison between PET and SPECT should be in the same population of patients injected with both radiopharmaceuticals. Such comparisons have been made a long time ago at the time of approval of rubidium-82 in the USA in three studies, including a total of 433 patients (22–24). In fact, these studies used thallium-201 for SPECT, which has been replaced by technetium-99m. Quite recently, a comparison of both modalities has been performed in a small cohort of 27 patients using the most recent hybrid imaging technology, which included CT-based attenuation correction for SPECT and PET (25). ^{82}Rb /PET imaging was performed as a second-line test when previous gated rest/stress ^{99m}Tc /SPECT with or without attenuation correction was non-conclusive. In this clinical situation, there were much fewer non-conclusive results with PET than with SPECT. Image quality and interpretive confidence were higher with PET than with SPECT even when SPECT was performed with attenuation correction.

Dosimetric Studies

Radiation dosimetry of rubidium-82 has been recently estimated in 10 healthy volunteers using the OLINDA/EXM 1.0 dosimetry software (26). Using different methodological approach, the estimates were discrepant with the results previously reported. The highest absorbed dose was delivered to the kidneys but remaining

at a quite acceptable level of 1.3 cGy for 2220 MBq (60 mCi) of injected activity. The effective dose calculated for a rest/stress test with an injected activity of $2 \text{ MBq} \times 1480 \text{ MBq}$ ($2 \text{ mCi} \times 40 \text{ mCi}$) was 3.7 mSv that is roughly equivalent to the annual natural exposure.

In 2015, Dorbala et al. reported on the way to reduce radiation dose with myocardial SPECT and PET imaging (6). Considering the use of last generation of 3D PET scanners and software allowing to inject half activity of rubidium-82 ($2 \text{ MBq} \times 740 \text{ MBq}$ or $2 \text{ mCi} \times 20 \text{ mCi}$) for a preserved image quality, the calculated effective dose was 1.26 mSv for rest or stress. In the clinical situation of stress-only 3D PET with MBF estimate, the radiation dose would be at an acceptable level of around 1 mSv . This is half of the radiation dose with ^{99m}Tc -sestamibi or tetrofosmin using last generation of scanners.

Quantification Studies

The clinical use of quantitative MBF assessment with ^{82}Rb /PET started at the end of the previous decade in the USA. In 2009, El Fakhri et al. demonstrated, in 22 subjects including patients with known coronary artery disease or healthy volunteers, that the measurement of absolute quantitation of MBF was feasible, reproducible, and accurate (27). Two years later, Ziadi et al. prospectively evaluated the prognostic value of coronary flow reserve using ^{82}Rb /PET in 704 patients and compared the results with semi-quantitative assessment using summed stress scores (28). They showed that quantitative myocardial flow reserve (MFR) was a good predictor of adverse cardiac events independent of the summed stress scores. The same added prognostic value of blood flow quantitation was confirmed 2 years later by Farhad et al. in 351 patients (29).

Several software packages are available for quantification of MBF. A study (RUBY-10) compared them in 48 patients from 10 centers and showed that, using the most common kinetic model, they may be used interchangeably (30).

The value of quantification of absolute MBF using rubidium-82 has been studied in 140 patients after heart transplant and for whom the prognosis depends on allograft vasculopathy (31). It was clearly shown that mean MFR was a significant predictor of future adverse events.

The great interest of blood flow quantification has been documented in diabetes mellitus (32). Among diabetic patients without coronary artery disease, those with impaired coronary reserve had cardiac event rates comparable to those with prior coronary artery disease, whereas those with preserved coronary reserve had cardiac event rates comparable to those of non-diabetics. Moreover, it has been recently shown that “global coronary flow reserve is associated with adverse cardiovascular events independently of luminal angiographic severity and modifies the effect of early revascularization” (33). The angiographic severity was evaluated using the coronary artery disease prognostic index. This important result documents the complementary but distinct association of functional and anatomic coronary abnormalities. A significant interaction was shown between coronary flow reserve and revascularization strategy, which could have large implications in the future for therapeutic strategy.

One other cardiac PET perfusion tracer, ^{13}N -ammonia, has been approved in the USA and is being clinically used at a relatively modest level. Its positron range is favorable resulting in a good image resolution and the myocardial extraction fraction is also favorable but its short physical half-life of 9.96 min requires an onsite cyclotron, which is a great limitation for a routine clinical use. Another PET radiotracer, ^{18}F -flurpiridaz is currently undergoing a clinical phase III evaluation and is quite promising after its potential approval. It could then be a real competitor to ^{82}Rb . A recent excellent review described in depth the characteristics of all PET perfusion radiotracers (34).

Advantages

Daily Availability of Rubidium-82 in Nuclear Cardiology Departments

Like with all generators, rubidium-82 is daily available in a department of nuclear medicine after elution of the column loaded with strontium-82 (Table 3). Such elution can be repeated every 10 min making possible to inject up to 10–15 patients per day depending on the availability of a dedicated cardiac PET/CT and of patient recruitment rate. A $^{82}\text{Sr}/^{82}\text{Rb}$ generator can currently be used for 28–42 days according to the loaded strontium-82 activity. It can be expected that this use will be extended to 60 days in a near future allowing to increase the number of tested patients with the same generator and consequently to decrease the cost of rubidium-82 examination for each patient.

Easy Interpretation of Images due to High Count Density

The count density and the uniformity of distribution of rubidium-82 in the myocardium are higher with PET than with SPECT using technetium-99m, even using the last technological advances of both techniques (25). Consequently, the interpretative confidence and interreader agreement are higher with PET leading to a higher accuracy. PET cameras do not need the use of collimators, resulting in higher sensitivity and spatial resolution (35).

Measurement of Myocardial Blood Flow and Coronary Reserve

Interpretation of SPECT and PET images is visual or semi-quantitative and based on relative uptake. Myocardial areas with the highest uptake are supposed to be supplied by non-obstructive coronary arteries while those with decreased uptake during stress are considered as being supplied by obstructive arteries. A stenosis with a luminal diameter around 50% may be undetected by this visual interpretation. Moreover, patients with subclinical coronary ischemia or microvascular diffuse disease may present only

a mild heterogeneous or even homogeneous myocardial uptake. Finally, in the situation of three-vessel coronary disease, a reduction of myocardial uptake may be balanced in all coronary arteries, resulting in a homogeneous left ventricle myocardium at stress (Figure 1).

The measurements of absolute MBF in milliliter per gram per minute and MFR, which is the maximum increase in blood flow above the normal resting volume, allows to complete the field of application of conventional perfusion imaging by identifying sub-clinical coronary ischemia and characterizing extent and severity in multi-vessel disease. Moreover, it has been clearly shown during the last years that the measurement of hyperemic MBF and MFR using PET/CT may predict, better than other parameters, the occurrence of hard cardiac events.

Today, there is no doubt that absolute myocardial perfusion quantification has been fully validated using PET/CT with ^{82}Rb or ^{13}N . There is a great debate about the same possibility using $^{99\text{m}}\text{Tc}$ /SPECT. In a quite recent editorial, Garcia considered the current situation taking into account the most recent technological advances in instrumentation and quantification software (5). New heart-centered SPECT systems have a high count sensitivity and iterative reconstruction enables an efficient correction of attenuation, scatter, and resolution changes with depth. In 2013, Ben-Haim et al. (36) showed the feasibility of measuring MBF and MFR with SPECT. Today, it can be stated that there is no real limitation to the quantification of MBF and MBF reserve with SPECT. The first results on clinical efficacy using conventional SPECT/CT systems have been reported (37) but these preliminary results should be confirmed in large studies and it will take some years before full validation for clinical use. Today, there is no doubt that only PET technology allows to measure rapidly and accurately the MBF.

Low Radiation Exposure for Patients

Given the high and still increasing number of patients who have myocardial perfusion imaging all over the world each year, the radiation exposure for patients and medical staff is a real concern and should be reduced at the lowest level compatible with a good image quality.

Effective radiation dose is directly related to the physical half-life of the radiopharmaceutical, its biodistribution and injected activity. In this respect, the very short half-life of ^{82}Rb of 1.26 min in comparison of 6 h of $^{99\text{m}}\text{Tc}$ is quite favorable for a low radiation dose, especially if new technologies enable to substantially decrease injected activity. For a long time, using 2D imaging mode, injected activity of rubidium-82 for rest and stress was 1480 MBq (40 mCi), resulting in an estimated dose of 2.5 and 5 mSv, respectively (6). Shifting from 2D to 3D imaging mode allowed to inject half activity (740 MBq or 20 mCi) for the same image quality and then to reduce the dose to 1.3 mSv for stress or rest and even to <1 mSv using new estimates of rubidium-82 dose (26). Such a dose is acceptable when compared to an average natural annual radiation dose of about 3 mSv. Stress-only PET 3D imaging, allowing to measure hyperemic MBF with <1 mSv, would be the preferred strategy for risk stratification if this measurement is clinically validated with regard to the measurement of myocardial blood reserve, which needs both stress and rest tests.

TABLE 3 | Advantages and disadvantages of the use of ^{82}Rb PET myocardial imaging.

Advantages	Disadvantages
Quantification++	Cost++
Good interpretative confidence	Lack of dedicated cardiac PET cameras
Favorable dosimetry	Limited capacity of strontium production
Good diagnostic accuracy	

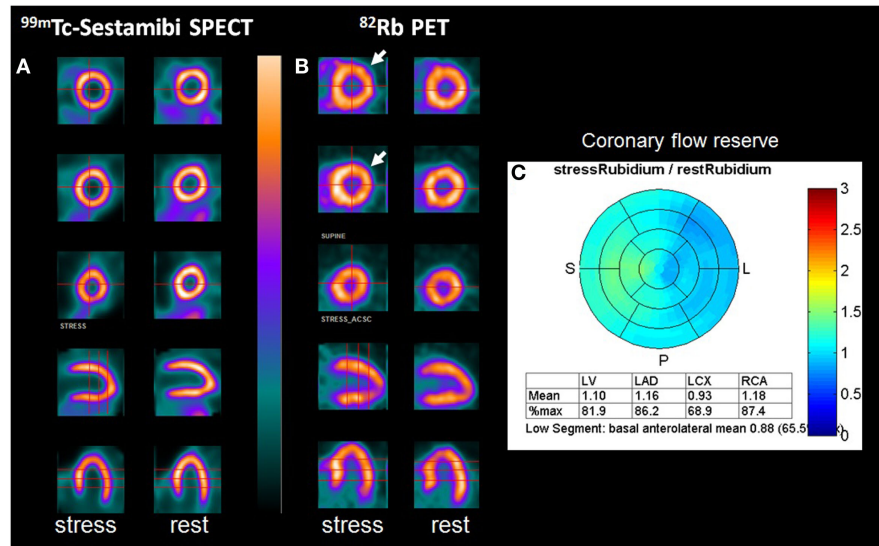


FIGURE 1 | A 56-year-old woman with a history of obesity (BMI: 31.2 cm/kg²), hypertension, hyperlipemia, and type 2 diabetes complicated of retinopathy and renal failure. The patient was referred to the Nuclear Medicine department for detection of coronary artery disease and underwent both Tc-99m-sestamibi SPECT (D-SPECT, Spectrum Dynamics, Haifa) and rubidium-82 PET/CT (Discovery 690 VCT, GEMS, Buc, France) as part of a clinical trial. SPECT (93% of the predicted maximal heart rate, no symptoms, EKG positive) was normal with a homogeneous uptake of the tracer both at stress and at rest (A). ⁸²Rb PET performed after Dipyridamole infusion showed a mild decrease of the tracer uptake in the lateral wall (arrow), completely reversible at rest, raising the suspicion of ischemia in the territory of the circumflex artery (B). This hypothesis was then confirmed by quantitative data derived from myocardial blood flow measurement with a coronary steal phenomenon in the same territory [coronary flow reserve (CFR) < 1; (C)]. In addition, the CFR was markedly decreased (< 1.5) in the territory of both the left descending artery and the right coronary artery, suggesting the presence of significant stenosis of these two coronary arteries. The coronary angiography confirmed the diagnosis of three-vessel disease and the patient underwent surgical revascularization. This case report underlines the greatest sensitivity of ⁸²Rb PET over SPECT in the setting of balanced ischemia, in relation with the ability to perform absolute quantification of myocardial blood flow.

By comparison, effective radiation doses are higher with ^{99m}Tc-based radiopharmaceuticals partially owing to the longer half-life of this radionuclide with regard to rubidium-82. Using the most recent advances in cardiac SPECT technology allowing to inject half activity for the same image quality [148–444 MBq (4–12 mCi)], the estimated doses are 2.3 and 8 mSv for rest/stress with ^{99m}Tc sestamibi and 2.0 and 6.1 mSv with ^{99m}Tc-tetrofosmin (6). Stress-only SPECT 3D imaging would deliver twice higher effective dose than with stress-only PET 3D imaging even if such dose remains moderate.

A recent study reported on projected population cancer risks in the USA using myocardial perfusion scintigraphy (38). The authors considered estimated effective doses ranging from 9 mSv for stress-only technetium-99m to 35 mSv for a rest/stress dual-isotope study associating thallium-201 and technetium-99m and using conventional SPECT equipment. For rubidium-82 PET imaging, they considered an estimated effective dose of 15 mSv for a rest/stress test using an injected activity of 1480–2250 MBq and a 2D PET camera. Cancer risk projection models were based on the National Research Council Biological Effects of Ionizing Radiation VII report assuming a linear relationship with radiation exposure. In these conditions and considering the 9.1 million tests performed each year in the USA, the number of additional future cancers would be about 7400. This number should be viewed with great caution because, from the time of Berrington's publication, estimated effective doses have been substantially decreased with the use of most advanced instrumentation allowing to dramatically decrease injected activities.

Considering the lower injected activity, which is now possible with 3D SPECT and PET cameras, which results in low effective doses, the number of additional and supposed cancers should be significantly lowered. Finally, the risk/benefit ratio should be taken into consideration for each individual patient before performing a myocardial perfusion test and the lowest activity should be injected compatible with a good image quality leading to an accurate diagnosis.

Limitations

Cost

Currently, the cost for one test with rubidium-82 is higher than with a ^{99m}Tc-labeled radiopharmaceutical even in the favorable situation of a nuclear cardiology center with a high recruitment rate (Table 3). In the USA, sestamibi-^{99m}Tc is currently reimbursed at about \$70 per dose, usually using 2 doses. However, in the hospital setting, the entire procedure including the drug is paid at \$1139. Rubidium-82 is reimbursed at approximately \$250 per dose. In the hospital setting, the entire procedure is reimbursed \$1286.

This relative low cost of technetium-99m is partly due to the fact that Mo-99/Tc-99m is not paid at full cost which explains some of the problems encountered nowadays with aging reactors and the difficulties to build new ones. Consequently, the use of rubidium-82 should be, at least at short term, limited to patients who are unable to complete exercise stress test, who are obese or who had a previous equivocal and non-conclusive SPECT test. Moreover,

rubidium-82 should be used, despite its cost, when MBF and coronary flow reserve quantitation are required, for example, in patients with multi-vessel coronary disease.

Some new high-energy cyclotrons will be installed shortly and will enable to extend strontium-82 availability, and then provide generators in a cost effective model.

Limited Number and Availability of PET 3D Systems

To be as cost-effective as possible with a $^{82}\text{Sr}/^{82}\text{Rb}$ generator, it is necessary to test a high number of patients before its expiration date (presently 28–42 days) but this situation needs to have available a dedicated cardiac PET/CT camera. In Europe, where a $^{82}\text{Sr}/^{82}\text{Rb}$ generator has not been approved yet, there is no such dedicated PET/CT cameras and the conventional PET/CT cameras are mainly used in oncology with fluorodeoxyglucose (FDG). A minimum of 8–10 patients are tested each day with this radiopharmaceutical and up to a maximum of 15–20 patients. Consequently, a quite limited number of patients could be injected with rubidium-82 per day making each test relatively expensive. This situation reinforces the fact that, at the beginning, Rb-82 will be probably limited to selective cases (see Cost). It will take probably a few years before some dedicated cardiac PET/CT cameras are available in large cardiology centers with a recruitment rate warranting such equipment.

Perspectives

Strontium-82, which is the parent nucleus of rubidium-82, is produced using proton beam interacting on a target containing stable rubidium. To be economically viable, an accelerator with proton beam of energy higher than 70 MeV and intensity $>100\ \mu\text{A}$ must be used. There are only few places in the world where such accelerators are available: Brookhaven National Laboratory (BNL-USA), Los Alamos National Laboratory (LANL-USA), iThemba labs (South Africa), INR (Russia), Triumf (Canada), and Arronax (France). These accelerators are not dedicated facilities and only part of the beam time is devoted to this production. Recently, based on the success of the first prototype of a 70 MeV machine built by a commercial cyclotron provider and installed in Nantes (France), several private companies are considering the use of such commercial cyclotron for strontium-82 production. Zevacor (USA) is one of them and CDNM (Russia) is the other one. In parallel, a 70 MeV cyclotron is being installed at Legnaro (Italy) for research purpose but one of the

two available beam lines may be used for radionuclide production. This indicates that the availability of strontium-82 in the future will be higher allowing to secure the supply chain and enlarge the use of this radionuclide to other countries (at the moment only north America is using it routinely), especially in Europe.

From a technological point of view, another advance will enlarge strontium-82 production, which is the use of rubidium metal target instead of the rubidium chloride target. With such change, higher yields can be obtained at the price of a more technical radiochemical process.

Finally, several designs of strontium-82/rubidium-82 generators are being studied and may reach the market in the future. This will allow to get generators with extended lifetime (up to 60 days) or lower activity which will better fit the need of users.

Conclusion

There is no doubt that the advantages of $^{82}\text{Rb}/\text{PET}$ myocardial imaging have been clearly documented since its routine clinical use after approval in the USA nearly 30 years ago. For a long time, its accuracy was significantly better than that obtained with the SPECT/ $^{99\text{m}}\text{Tc}$ technology particularly in obese or overweight patients and women with large breasts due to attenuation correction artifacts. With the most recent hybrid SPECT imaging technology, the situation changed, leading to an improved specificity of $^{99\text{m}}\text{Tc}/\text{SPECT}$. Currently, the main advantage of $^{82}\text{Rb}/\text{PET}$ is its capacity to accurately measure the MBF and flow reserve. Even if such measurement is technologically feasible with $^{99\text{m}}\text{Tc}/\text{SPECT}$, it will take some years before potential validation. Finally, given the very short physical half-life of rubidium-82, the radiation exposure rate with this radionuclide is significantly lower than with technetium-99m. Using 3D hybrid PET system, it is possible to inject low activities of rubidium-82 while maintaining a good image quality. The radiation exposure rate is then acceptable and inferior to natural exposure.

It can be anticipated that in the future $^{82}\text{Rb}/\text{PET}$ and $^{99\text{m}}\text{Tc}/\text{SPECT}$ will continue to be used according availability of hybrid cameras and radionuclides.

Acknowledgments

This work has been supported in part by grants from the French National Agency for Research called “Investissements d’Avenir” Equipex ArronaxPlus no. ANR-11-EQPX-0004.

References

1. Love WD, Romney RB, Burch GE. A comparison of the distribution of potassium and exchangeable rubidium in the organs of the dog, using rubidium. *Circ Res* (1954) 2:112–22. doi:10.1161/01.RES.2.2.112
2. Selwyn AP, Allan RM, L’Abbate A, Horlock P, Camici P, Clark J, et al. Relation between regional myocardial uptake of rubidium-82 and perfusion: absolute reduction of cation uptake in ischemia. *Am J Cardiol* (1982) 50:112–21. doi:10.1016/0002-9149(82)90016-9
3. Gould KL, Goldstein RA, Mullani NA, Kirkeeide RL, Wong WH, Tewson TJ, et al. Noninvasive assessment of coronary stenoses by myocardial perfusion imaging during pharmacologic coronary vasodilation. VIII. Clinical feasibility of positron cardiac imaging without a cyclotron using generator-produced rubidium-82. *J Am Coll Cardiol* (1986) 7:775–89. doi:10.1016/S0735-1097(86)80336-9
4. ACNP/SNM Task Force on Clinical PET. Positron emission tomography: clinical status in the United States in 1987. *J Nucl Med* (1988) 29:1136–43.
5. Garcia EV. Are SPECT measurements of myocardial blood flow and flow reserve ready for clinical use? *Eur J Nucl Med Mol Imaging* (2014) 41:2291–3. doi:10.1007/s00259-014-2924-2
6. Dorbala S, Blankstein R, Skali H, Park M-A, Fantony J, Mauceri C, et al. Approaches to reducing radiation dose from radionuclide myocardial perfusion imaging. *J Nucl Med* (2015) 56:592–9. doi:10.2967/jnumed.112.115097
7. Love WD, Burch GE. Influence of the rate of coronary plasma flow on the extraction of Rb86 from coronary blood. *Circ Res* (1959) 7:24–30. doi:10.1161/01.RES.7.1.24

8. Levy MN, Martins De Oliveira J. Regional distribution of myocardial blood flow in the dog as determined by Rb86. *Circ Res* (1961) 9:96–8. doi:10.1161/01.RES.9.1.96
9. Nishiyama H, Sodd VJ, Adolph RJ, Saenger EL, Lewis JT, Gabel M. Intercomparison of myocardial imaging agents: 201Ti, 129Cs, 43K, and 81Rb. *J Nucl Med* (1976) 17:880–9.
10. Yano Y, Budinger TF, Chiang G, O'Brien HA, Grant PM. Evaluation and application of alumina-based Rb-82 generators charged with high levels of Sr-82/85. *J Nucl Med* (1979) 20:961–6.
11. Nandalur KR, Dwamena BA, Choudhri AF, Nandalur SR, Reddy P, Carlos RC. Diagnostic performance of positron emission tomography in the detection of coronary artery disease: a meta-analysis. *Acad Radiol* (2008) 15:444–51. doi:10.1016/j.acra.2007.08.012
12. Jaarsma C, Leiner T, Bekkers SC, Crijns HJ, Wildberger JE, Nagel E, et al. Diagnostic performance of noninvasive myocardial perfusion imaging using single-photon emission computed tomography, cardiac magnetic resonance, and positron emission tomography imaging for the detection of obstructive coronary artery disease: a meta-analysis. *J Am Coll Cardiol* (2012) 59:1719–28. doi:10.1016/j.jacc.2011.12.040
13. Mc Ardle BA, Dowsley TF, deKemp RA, Wells GA, Beanlands RS. Does rubidium-82 PET have superior accuracy to SPECT perfusion imaging for the diagnosis of obstructive coronary disease?: a systematic review and meta-analysis. *J Am Coll Cardiol* (2012) 60:1828–37. doi:10.1016/j.jacc.2012.07.038
14. Renaud JM, Mylonas I, McArdle B, Dowsley T, Yip K, Turcotte E, et al. Clinical interpretation standards and quality assurance for the multicenter PET/CT trial rubidium-ARMI. *J Nucl Med* (2014) 55:58–64. doi:10.2967/jnumed.112.117515
15. O'Keefe JH, Barnhart CS, Bateman TM. Comparison of stress echocardiography and stress myocardial perfusion scintigraphy for diagnosing coronary artery disease and assessing its severity. *Am J Cardiol* (1995) 75:25D–34D. doi:10.1016/S0002-9149(99)80399-3
16. Fleischmann KE, Hunink MG, Kuntz KM, Douglas PS. Exercise echocardiography or exercise SPECT imaging? A meta-analysis of diagnostic test performance. *JAMA* (1998) 280:913–20. doi:10.1001/jama.280.10.913
17. Kim C, Kwok YS, Heagerty P, Redberg R. Pharmacologic stress testing for coronary disease diagnosis: a meta-analysis. *Am Heart J* (2001) 142:934–44. doi:10.1067/mhj.2001.119761
18. Imran MB, Pálkás A, Picano E. Head-to-head comparison of dipyridamole echocardiography and stress perfusion scintigraphy for the detection of coronary artery disease: a meta-analysis. Comparison between stress echo and scintigraphy. *Int J Cardiovasc Imaging* (2003) 19:23–8. doi:10.1023/A:1021746515555
19. Mowatt G, Vale L, Brazzelli M, Hernandez R, Murray A, Scott N, et al. Systematic review of the effectiveness and cost-effectiveness, and economic evaluation, of myocardial perfusion scintigraphy for the diagnosis and management of angina and myocardial infarction. *Health Technol Assess* (2004) 8:iii–iv, 1–207. doi:10.3310/hta8300
20. Bateman TM, Heller GV, McGhie AI, Friedman JD, Case JA, Bryngelson JR, et al. Diagnostic accuracy of rest/stress ECG-gated Rb-82 myocardial perfusion PET: comparison with ECG-gated Tc-99m sestamibi SPECT. *J Nucl Cardiol* (2006) 13:24–33. doi:10.1016/j.nuclcard.2005.12.004
21. Chow BJW, Dorbala S, Di Carli MF, Merhige ME, Williams BA, Veledar E, et al. Prognostic value of PET myocardial perfusion imaging in obese patients. *JACC Cardiovasc Imaging* (2014) 7:278–87. doi:10.1016/j.jcmg.2013.12.008
22. Stewart RE, Schwaiger M, Molina E, Popma J, Gacioc GM, Kalus M, et al. Comparison of rubidium-82 positron emission tomography and thallium-201 SPECT imaging for detection of coronary artery disease. *Am J Cardiol* (1991) 67:1303–10. doi:10.1016/0002-9149(91)90456-U
23. Go RT, Marwick TH, MacIntyre WJ, Saha GB, Neumann DR, Underwood DA, et al. A prospective comparison of rubidium-82 PET and thallium-201 SPECT myocardial perfusion imaging utilizing a single dipyridamole stress in the diagnosis of coronary artery disease. *J Nucl Med* (1990) 31:1899–905.
24. Marwick TH, Go RT, MacIntyre WJ, Saha GB, Underwood DA. Myocardial perfusion imaging with positron emission tomography and single photon emission computed tomography: frequency and causes of disparate results. *Eur Heart J* (1991) 12:1064–9.
25. Flotats A, Bravo PE, Fukushima K, Chaudhry MA, Merrill J, Bengel FM. 82Rb PET myocardial perfusion imaging is superior to 99mTc-labelled agent SPECT in patients with known or suspected coronary artery disease. *Eur J Nucl Med Mol Imaging* (2012) 39:1233–9. doi:10.1007/s00259-012-2140-x
26. Senthamizhchelvan S, Bravo PE, Esaias C, Lodge MA, Merrill J, Hobbs RF, et al. Human biodistribution and radiation dosimetry of 82Rb. *J Nucl Med* (2010) 51:1592–9. doi:10.2967/jnumed.110.077669
27. El Fakhri G, Kardan A, Sitek A, Dorbala S, Abi-Hatem N, Lahoud Y, et al. Reproducibility and accuracy of quantitative myocardial blood flow assessment with (82)Rb PET: comparison with (13)N-ammonia PET. *J Nucl Med* (2009) 50:1062–71. doi:10.2967/jnumed.104.007831
28. Ziadi MC, Dekemp RA, Williams KA, Guo A, Chow BJW, Renaud JM, et al. Impaired myocardial flow reserve on rubidium-82 positron emission tomography imaging predicts adverse outcomes in patients assessed for myocardial ischemia. *J Am Coll Cardiol* (2011) 58:740–8. doi:10.1016/j.jacc.2011.01.065
29. Farhad H, Dunet V, Bachelard K, Allenbach G, Kaufmann PA, Prior JO. Added prognostic value of myocardial blood flow quantitation in rubidium-82 positron emission tomography imaging. *Eur Heart J Cardiovasc Imaging* (2013) 14:1203–10. doi:10.1093/ehjci/jet068
30. Nesterov SV, Deshayes E, Scigrà R, Settimo L, Declercq JM, Pan X-B, et al. Quantification of myocardial blood flow in absolute terms using (82)Rb PET imaging: the RUBY-10 Study. *JACC Cardiovasc Imaging* (2014) 7:1119–27. doi:10.1016/j.jcmg.2014.08.003
31. Mc Ardle BA, Davies RA, Chen L, Small GR, Ruddy TD, Dwivedi G, et al. Prognostic value of rubidium-82 positron emission tomography in patients after heart transplant. *Circ Cardiovasc Imaging* (2014) 7:930–7. doi:10.1161/CIRCIMAGING.114.002184
32. Murthy VL, Naya M, Foster CR, Gaber M, Hainer J, Klein J, et al. Association between coronary vascular dysfunction and cardiac mortality in patients with and without diabetes mellitus. *Circulation* (2012) 126:1858–68. doi:10.1161/CIRCULATIONAHA.112.120402
33. Taqueti VR, Hachamovitch R, Murthy VL, Naya M, Foster CR, Hainer J, et al. Global coronary flow reserve is associated with adverse cardiovascular events independently of luminal angiographic severity and modifies the effect of early revascularization. *Circulation* (2015) 131:19–27. doi:10.1161/CIRCULATIONAHA.114.011939
34. Maddahi J, Packard RRS. Cardiac PET perfusion tracers: current status and future directions. *Semin Nucl Med* (2014) 44:333–43. doi:10.1053/j.semnuclmed.2014.06.011
35. Valenta I, Schindler TH. 82Rb PET/CT: entering a new area of myocardial perfusion imaging? *Eur J Nucl Med Mol Imaging* (2012) 39:1231–2. doi:10.1007/s00259-012-2154-4
36. Ben-Haim S, Murthy VL, Breault C, Allie R, Sitek A, Roth N, et al. Quantification of myocardial perfusion reserve using dynamic SPECT imaging in humans: a feasibility study. *J Nucl Med* (2013) 54:873–9. doi:10.2967/jnumed.112.109652
37. Hsu B, Chen F-C, Wu T-C, Huang W-S, Hou P-N, Chen C-C, et al. Quantitation of myocardial blood flow and myocardial flow reserve with 99mTc-sestamibi dynamic SPECT/CT to enhance detection of coronary artery disease. *Eur J Nucl Med Mol Imaging* (2014) 41:2294–306. doi:10.1007/s00259-014-2881-9
38. Berrington de Gonzalez A, Kim K-P, Smith-Bindman R, McAreavey D. Myocardial perfusion scans: projected population cancer risks from current levels of use in the United States. *Circulation* (2010) 122:2403–10. doi:10.1161/CIRCULATIONAHA.110.941625

Conflict of Interest Statement: The authors declare that the research was conducted in the absence of any commercial or financial relationships that could be construed as a potential conflict of interest.

Copyright © 2015 Chatal, Rouzet, Haddad, Bourdeau, Mathieu and Le Guludec. This is an open-access article distributed under the terms of the Creative Commons Attribution License (CC BY). The use, distribution or reproduction in other forums is permitted, provided the original author(s) or licensor are credited and that the original publication in this journal is cited, in accordance with accepted academic practice. No use, distribution or reproduction is permitted which does not comply with these terms.



Focus on the controversial aspects of ^{64}Cu -ATSM in tumoral hypoxia mapping by PET imaging

Mathilde Colombié¹, Sébastien Gouard², Mathieu Frindel², Aurélien Vidal³, Michel Chérel^{1,2}, Françoise Kraeber-Bodéré^{1,2,4}, Caroline Rousseau^{1,2†} and Mickaël Bourgeois^{2,3,4*†}

¹ Institut de Cancérologie de l'Ouest, Saint-Herblain, France, ² CRCNA, INSERM, Université de Nantes, Nantes, France, ³ GIP ARRONAX, Saint-Herblain, France, ⁴ Service de Médecine Nucléaire – CHU de Nantes, Nantes, France

OPEN ACCESS

Edited by:

Anil Kumar Mishra,
Defence Research and Development
Organisation, India

Reviewed by:

Zhen Cheng,
Stanford University, USA
Baljinder Singh,
PGIMER Chandigarh, India

*Correspondence:

Mickaël Bourgeois,
CRCNA, Université de Nantes,
8 quai Moncousu, BP70721,
Nantes Cedex 1 44007, France
bourgeois@arronax-nantes.fr

[†] Caroline Rousseau and
Mickaël Bourgeois have contributed
equally to this work.

Specialty section:

This article was submitted to Nuclear
Medicine, a section of the journal
Frontiers in Medicine

Received: 25 June 2015

Accepted: 10 August 2015

Published: 24 August 2015

Citation:

Colombié M, Gouard S, Frindel M,
Vidal A, Chérel M, Kraeber-Bodéré F,
Rousseau C and Bourgeois M (2015)
Focus on the controversial aspects
of ^{64}Cu -ATSM in tumoral hypoxia
mapping by PET imaging.
Front. Med. 2:58.
doi: 10.3389/fmed.2015.00058

Mapping tumor hypoxia is a great challenge in positron emission tomography (PET) imaging as the precise functional information of the biological processes is needed for many effective therapeutic strategies. Tumor hypoxia has been widely reported as a poor prognostic indicator and is often associated with tumor aggressiveness, chemo- and radio-resistance. An accurate diagnosis of hypoxia is a challenge and is crucial for providing accurate treatment for patients' survival benefits. This challenge has led to the emergence of new and novel PET tracers for the functional and metabolic characterization of tumor hypoxia non-invasively. Among these tracers, copper semicarbazone compound [^{64}Cu]-diacetyl-bis(N^4 -methylthiosemicarbazone) (= ^{64}Cu -ATSM) has been developed as a tracer for hypoxia imaging. This review focuses on ^{64}Cu -ATSM PET imaging and the concept is presented in two sections. The first section describes its *in vitro* development and pre-clinical testing and particularly its affinity in different cell lines. The second section describes the controversial reports on its specificity for hypoxia imaging. The review concludes that ^{64}Cu -ATSM – more than a hypoxic tracer, exhibits tracer accumulation in tumor, which is linked to the redox potential and reactive oxygen species. The authors concluded that ^{64}Cu -ATSM is a marker of over-reduced cell state and thus an indirect marker for hypoxia imaging. The affinity of ^{64}Cu -ATSM for over-reduced cells was observed to be a complex phenomenon. And to provide a definitive and convincing mechanism, more *in vivo* studies are needed to prove the diagnostic utility of ^{64}Cu -ATSM.

Keywords: cancer, [^{64}Cu]-ATSM, hypoxia, positron emission tomography, reactive oxygen species, radiopharmaceutical

Introduction

Tumor hypoxia is a common and important feature of the tumoral microenvironment, and a well-known consequence of an inadequate supply of dioxygen (O_2) in a wide range of malignant solid tumors. This hypoxic phenomenon is mainly linked to the imbalance between the high rate of cell proliferation potential during the carcinogenesis process compared to the more slower neoangiogenesis. Despite the difference between biochemists (O_2^- limited electron transport in mitochondria) and physiologists (reduced O_2 availability due to a decreased O_2 partial pressure) definition, the hypoxia clinical aspect with a limited oxygen delivery to the aerobic neoplastic and

stromal cells is frequently observed in various tumor type with very low oxygen levels where the partial pressure in oxygen is <5 versus 40–60 mmHg in normal tissues (1).

The origin of hypoxia regions in human tumors was postulated by Thomlinson and Gray in 1955s with some observation based on the diminution of the oxygen diffusion with the blood supply distance (2). This limited diffusion of oxygen at distance (about 100 μm) of capillary blood vessels is at the origin of a chronic diffusion hypoxia. In parallel, an acute perfusion hypoxia closest to the capillary vessel was observed. This acute event was the consequence of functionally and structurally defective vascular network in tumor (overdilated, hyperpermeable, tortuous, and disrupted), combined with the high-interstitial pressure of the extracellular matrix, which compress the vessel and reduce the blood flow.

From physiopathological aspect, hypoxia is heterogenous in time and in space and not only accounts for tissue necrosis but also a strong impact on tumor biology and has several bad prognostic for patient clinical outcome. In fact, during the tumor malignant growth, hypoxic area is correlated with an increased genetic instability and more aggressive phenotype which conduct to a strongly associated tumor metastasis risk. Likewise, hypoxia causes unequivocally some resistances to cancers treatments. It has been known from many years that hypoxic condition could cause an intrinsic chemoresistance (by different mechanisms like diminution of the drug concentration in relation with the blood vessel distance, loss of sensitivity to p53-mediated apoptosis, or diminution of cell proliferation by metabolic stress) and generate a resistance to killing by ionizing radiation [diminution of the free radical damage on the intracellular reactive oxygen species (ROS) during hypoxia event].

During 1990s, interest in overcoming the problem of the radiation resistance of hypoxic cells in tumors was rekindled by the use of commercially available oxygen electrode (mostly known as “Eppendorf electrode”), which permit to measure oxygen partial pressure levels (pO_2) in human tumors. However, this method presents some major drawbacks because it is an invasive technique limited to accessible tumors with sufficient size with a risk of tissue disruption and is known to present a large inter-observer variability. In addition to this direct measurement of pO_2 , an other invasive method based on biopsy coupled to cytological coloration with nitroimidazole compounds (like pimonidazole or EF5) or coupled to immunohistochemical analysis of various hypoxia markers proteins [like hypoxia inducing factors-1 α (HIF-1 α) or carbonic anhydrase IX (CAIX)]. In recent decades, investigations into alternative, non-invasive imaging methods for measuring pO_2 have been studied and the use of positron emission tomography (PET) has led to a number of promising positron emitters radiopharmaceuticals. Among the different tumor hypoxia PET radiotracers, the innovative [^{64}Cu]-diacetyl-bis(N^4 -methylthiosemicarbazone) ($=$ [^{64}Cu]-ATSM) presented in **Figure 1** raises questions about its real target in tumor hypoxia process and presents some controversial aspects.

Cu-ATSM *In vitro* Results

An ideal hypoxia imaging agent should have a high membrane permeability for easy access to intracellular mitochondria and a

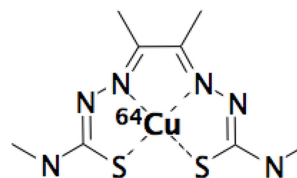


FIGURE 1 | [^{64}Cu]-diacetyl-bis(N^4 -methylthiosemicarbazone) ($=$ [^{64}Cu]-ATSM).

low redox potential to confer stability in normal tissue, but it should be able to be reduced by mitochondria with abnormally high electron concentrations in hypoxic cells. After numerous studies on nitroimidazole compounds for their selective accumulation in hypoxic tumors, as well as in ischemic tissue (3, 4), Cu-ATSM a lipophilic molecule, with high membrane permeability and low redox potential, was presented by Fujiyabashi et al. as a possible hypoxia imaging agent in occluded rat heart model (5). Cu-ATSM was reduced by hypoxic but not by normal mitochondria and Cu-ATSM retention was inversely correlated with accumulation of ^{201}Tl , a relative myocardial blood flow marker. Different schemas were proposed in the literature (6–8) but, to date, there is a consensus that *in vitro* Cu-ATSM undergoes bioreductive trapping under hypoxic conditions. After cellular entry, Cu(II)-ATSM is reduced to an unstable Cu(I)-ATSM species, a process inducing dissociation of the metal complex and subsequent irreversible trapping of Cu(I) within the cellular copper metabolic processes (9). A simplified mechanism of the reaction of Cu(II)-ATSM with cells reported that the lipophilic molecule may be diffuse into the cells by combined passive and facilitated (protein-carrier-mediated) mechanisms with no evidence to support a role for copper-transporter 1 (Ctr1) in accumulation of the compound (10). In hypoxic cells, Cu-ATSM reacted with thiol groups or redox-active proteins with NADH as a required enzymatic cofactor. The reduced, charged form is less lipophilic and retained in the cell, providing opportunity for it to be reoxidized in the normoxic cell (11). Protonation of the reduced form at the N3 and N6 positions will lead to the complex dissociating and the copper will be irreversibly trapped in the hypoxic cell (**Figure 2**). R could be a thiol, such as glutathione, or a thiol group of a redox-active protein. Cellular trapping of the copper is dependent on oxygen, pH, and NADH (12). Early on, Burgman et al. indicated considerable variation in ^{64}Cu accumulation following incubation with ^{64}Cu -ATSM among different cell lines (prostate carcinoma, fibrosarcoma, breast adenocarcinoma, and squamous cell carcinoma) with regard to uptake kinetics, maximum accumulation, and their dependence on oxygen conditions (8).

Recently, different authors explored the relationship between Cu-ATSM and some characteristics of cancer cells. First, Liu et al. showed that *in vitro* cells highly expressing multi-drug resistance (MDR1) had significantly decreased Cu-ATSM retention and enhanced efflux. Knockdown of MDR1 expression significantly enhanced the Cu-ATSM retention and decreased the efflux in MDR1-positive cells (13). Then, Yoshii et al. showed that ^{64}Cu -ATSM accumulated in rich regions of CD133 $^{+}$ cells with

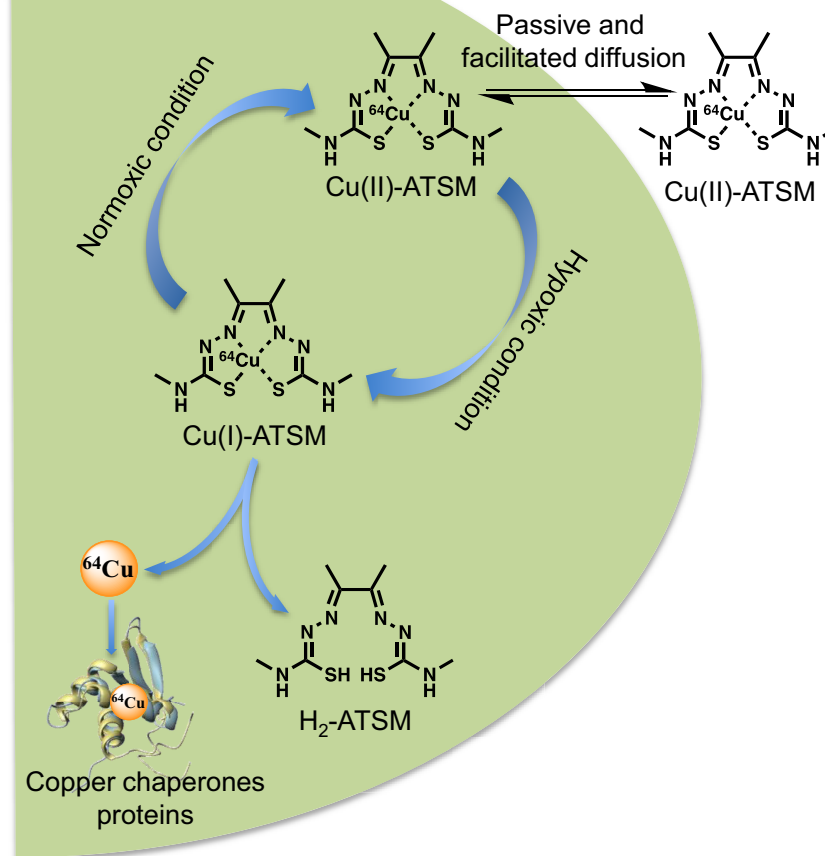


FIGURE 2 | Overview of the cellular ^{64}Cu -ATSM uptake and retention mechanisms. In hypoxic condition, the Cu(II)-ATSM (oxidation level of copper-64 is +II) is reduced to Cu(I)-ATSM (oxidation level of copper-64 is +I) then the complex became instable and free copper-64 is trapped and accumulate in intracellular copper chaperones proteins.

characteristics of cancer stem cells. Therefore, ^{64}Cu -ATSM could be a potential imaging or therapy agent for rich regions of CD133^+ cells, associated with cancer stem cells, within tumors (14). The same team was interested in the evaluation of Cu-ATSM as an indicator of intracellular overreduced states in mitochondrial disorders using cell lines with mitochondrial dysfunction, even under normoxia. Study results showed that Cu-ATSM would be a promising marker of intracellular overreduced states for disorders with mitochondrial dysfunction, such as Parkinson's disease and Alzheimer disease (15).

Still on the fact that Cu-ATSM is not a PET hypoxia marker in all tumors, Vavere et al. focused on the relationship between Cu-ATSM hypoxia and fatty acid synthase (FAS) expression in prostate cancer cell lines (16). The physiological significance of the fatty acid synthesis pathway in prostate cancers is in the harnessing of its oxidizing power for improving redox balance (i.e., lower NADH/NAD^+ ratios) despite oxygen-limiting (hypoxic) conditions. This team demonstrated that in the FAS tumor line, the lower-than-average redox potential caused reduction and trapping of Cu-ATSM in both hypoxic and normoxic areas (16).

Then, Cu-ATSM translation to the hypoxia imaging of prostate cancer may be limited by the overexpression of FAS associated with prostatic malignancies.

Cu-ATSM *In vivo* Results

The current knowledge on the tumor microenvironment shows a great number of metabolic circumstances and therefore a high variability in hypoxia tumor status with different physiopathological process.

One of the first ^{64}Cu -ATSM pre-clinical study in tumor hypoxia imaging has used a mice bearing EMT6 breast carcinoma cell line, which has shown an heterogeneous uptake of the radio-tracer (intense uptake was observed in 15–30% of the tumor) supposed to be correlated with the hypoxic area of the tumor (11). Other pre-clinical study in tumor hypoxia imaging has used an epidermoid rabbit tumor, which is known to present a high glycolytic/high hexokinase rate with high anaerobic glycolysis pathway (high lactic acid production and high NADPH ratio) (17). This study showed a major accumulation of ^{64}Cu -ATSM

around the outer rim of the tumor masses where the histological cell biology showed active, viable, and expected hypoxic cells (18).

More recently, the affinity of ^{64}Cu -ATSM for viable and hypoxic cells was confirmed with the comparison of the regional distribution between ^{64}Cu -ATSM and other prominent radiopharmaceuticals in tumor metabolic status determination field: ^{18}F -MISO, ^{18}F -FLT, and ^{18}F -FDG. The characterization of the *in vivo* behavior of ^{64}Cu -ATSM indicate a very strong correlation with classical hypoxia (^{18}F -MISO) and proliferation (^{18}F -FLT) PET radiotracer ($r^2 = 0.864$ and 0.829 , respectively) but not correlate with the ^{18}F -FDG metabolic PET radiotracer ($r^2 = 0.08$) (19).

In the same way, a rat graft tumor model of prostate adenocarcinoma and human squamous cell carcinoma showed a good correlation between the uptake of ^{18}F -MISO and ^{64}Cu -ATSM when imaged at later times after injection (20). Effectively, it appeared that the intratumoral distribution of ^{64}Cu -ATSM exhibited a significant evolution between the early (1–2 h after injection) and late (16–20 h after injection) imaging time. An additional experience with direct pO_2 measurement was broadly consistent with the hypothesis that the spatial distribution of ^{18}F -MISO and ^{64}Cu -ATSM at later times reflected tumor hypoxia. A similar study indicated that for early images, the distribution of Cu-ATSM was inconsistent with tumor hypoxia and might be more representative of perfusion. Only at later times after Cu-ATSM administration (16–24 h postinjection), the ^{18}F -FMISO and ^{64}Cu -ATSM images corresponded. Authors did not dispute the potential utility of Cu-ATSM imaging as a tool in clinical management but for the first time, they pointed out that its uptake on hypoxic tumor was unclear (8). In the same way, a more recent study of McCall et al. tried to determine the pharmacokinetic behavior of ^{64}Cu -ATSM in combination with microscopic markers of hypoxia. The results of this study confirmed a rapid tumor uptake and retention of ^{64}Cu -ATSM (tumor-to-muscle ratio was 4:1 within 20 min after injection) with a strong positive spatial correlation to the highly perfused areas. At late time (18 h post injection), the tumor-to-muscle ratio was 12:1 and there was no spatial correlation with the perfused areas (21).

Furthermore, this time-dependent spatial distribution of ^{64}Cu -ATSM seemed to have retention variability in function of the tumor cell line. Briefly, a pre-clinical rat model was used and different tumor lines showed that ^{64}Cu -ATSM was a valid PET hypoxia marker (correlation of the autoradiographic distributions with hypoxia markers as EF5, pimonidazole, and CAIX) for adenocarcinoma and glioma tumor cell line but a hypoxia-independent uptake of ^{64}Cu -ATSM in fibrosarcoma was observed (22). Cell-dependent distribution and retention kinetics of Cu-ATSM are confirmed and underline the need for proper validation of animal models and PET acquisition protocols before exploration of any new clinical applications (23). This notion has recently been confirmed by Carlin et al., who showed that Cu-ATSM had the highest tumor accumulation and low renal clearance compared to fluorinated nitroimidazoles. However, the lack of correlation between Cu-ATSM distribution and immunohistochemistry hypoxia markers also casted some doubt on the hypoxia selectivity of Cu-ATSM (24). The suggested reason for the low correlation between Cu-ATSM uptake and hypoxic distribution, in some tumors, was the differing redox status of the tumor types.

Some of tumors might have a lower than-average redox potential with high concentrations of electron donors caused reduction and trapping of Cu-ATSM in both hypoxic and normoxic areas. Moreover, *in vivo*, in two different tumor types, Hueting et al. demonstrated that the distribution of radiocopper from Cu-ATSM in tumors essentially mirrors Cu-acetate suggesting that copper metabolism might also played a role in the mechanism of selectivity of Cu-ATSM (25). The mechanism of radiolabeled Cu-ATSM accumulation in hypoxic tumor area was currently under investigation but it was well-known that there was a high physiological accumulation of free ^{64}Cu in non-target organ and the liver was reported to be the principal dose-limiting organ (26). To reduce the liver absorbed dose, Yoshii et al. showed that the use of a copper chelator like penicillamine could reduce liver absorbed dose (increase of free copper renal clearance) but have no effect on the Cu-ATSM tumor accumulation (27).

In 2008, a clinical use of Cu-ATSM in cancer of the uterine cervix in 10 women permits to obtain high-quality images (high tumor-to-muscle ratio), which correlate with prognosis and patients outcome. Importantly, in this study, the uptake pattern was similar on the images obtained with two different imaging sessions 1–9 days apart, indicating that the microscopic distribution of chronic hypoxia did not change greatly over this interval (28).

Discussion/Conclusion

^{64}Cu -ATSM is a radiopharmaceutical developed for PET imaging and presented as a complex with high membrane permeability and low redox potential, ideal for hypoxia imaging. In theory, low redox potential helped to confer stability in normal tissue and led reduction by mitochondria with abnormally high electron concentrations in hypoxic cells.

During the *in vivo* biodistribution, ^{64}Cu -ATSM is known to present a high binding ratio to the serum proteins like albumin (approximately 95% for human, mouse, and rat) (29). The cellular uptake data of ^{64}Cu -ATSM suggested by various study show a combined passive diffusion and facilitated (protein-carrier-mediated) penetration mechanisms (10). In particular, organs like liver, the ^{64}Cu -ATSM complex is metabolized and free copper released follow its own metabolism with a high fixation on hepatobiliary tractus (30). This metabolic pathway could also occur in tumor cells and could explain the variable time-dependent spatial distribution in hypoxic tumors. From this physiological metabolism of copper, it appears than free copper present a negative impact on the PET image information of ^{64}Cu -ATSM. Nevertheless, this impact could be decreased by the co-administration of D-penicillamine, which will permit to accelerate the elimination of free copper without impact on the ^{64}Cu -ATSM tumor fixation (27).

^{64}Cu -ATSM has been examined in various *in vitro* and *in vivo* pre-clinical models and presented some variability for *in vivo* hypoxia mapping (mainly in term of cell line type and in term of acquisition time after injection). This heterogeneity in ^{64}Cu -ATSM uptake led to a complicated interpretation of tumor hypoxia mapping, and there is a need to determine what extent radiotracer distribution is important, defined by perfusion (early time) or by pO_2 level (late time).

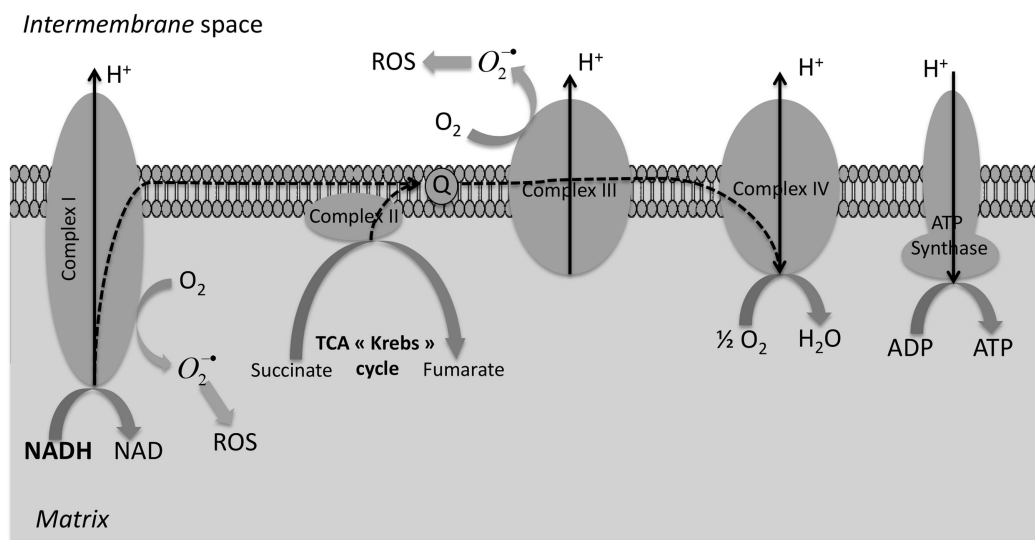


FIGURE 3 | Overproduction of reductive species (NADPH and NADH) in mitochondria during hypoxia. Under normoxia, NADH produced during the tricarboxylic acid (TCA) cycle are reduced in NAD^+ and the respiratory chain drove the electron (dash arrow) to dioxygen with a proton flux on the

intermembrane space whose flow back on the mitochondrial matrix by the ATP synthase produced ATP. During hypoxia, the respiratory chain is inhibited and we observe an accumulation of overreduced species (NADH and NADPH) and a diminution (in long-term) of ROS production.

In hypoxia biochemical pathway, the intracellular redox potential becoming progressively more reductive – this agreed with the observation that hypoxia induced a metabolic switch, which led to an increase (**Figure 3**) in the production of NADH and NADPH (the primary electron donors of the cell). This modification of the NADH/NAD^+ and $\text{NADPH}/\text{NADP}^+$ ratio in favor of reductive species (confirmed with the use of rotenone, a complex 1-inhibitor in mitochondria electron transport chain) seemed to be at the origin of the Cu-ATSM increased uptake in normoxic cells (15). Indeed, a disturbed electron flow in the electron transport chain, by inhibition of complex 1, caused reduction of Cu(II) to Cu(I) trapped in cells and fourfold higher reduction of Cu-ATSM was observed in normoxic cells treated with rotenone. Yoshii et al. deduced the supposed mechanism of Cu-ATSM retention in hypoxic cells: mitochondrial dysfunction chain (artificial or as result of hypoxia) caused an excess of electrons, and therefore, an over-reduced state in cells. Obata et al. also studied Cu-ATSM retention mechanism (18). They found some contribution of enzymes, in particular, NADH-cytochrome *b5* reductase and NADPH-cytochrome *p450* reductase. In addition, those enzymatic reductions were enhanced by induction of hypoxia. Ability in reduction was very sensitive and dependent of electron donors that are NADH or NADPH. They found that Cu(II) reduction depended on presence of NADH and NADPH in cells. More information on hypoxia, Cu-ATSM might appear to provide information on reductive enzyme expression and species in cells. Moreover, literature highlighted an increase of NADH concentration in hypoxic tissue (31). Finally, there was a strong link between hypoxia and redox potential in cells. Yoshii et al. also studied Cu-ATSM based on mitochondrial dysfunction models, including MELAS mitochondrial DNA mutation and cells depleted of mitochondrial DNA; their

hypothesis was based on mitochondrial dysfunction and over-reduced state in cells (15). In their study, Cu-ATSM accumulated in cells, which had a strong reducing potential, including normoxic cells, with very strong correlation with rate of NADH and NADPH. Authors suggested that Cu-ATSM could be an agent indicator of over-reduced intracellular state generated by increase of NADH and NADPH levels, including normoxic cells. Cu-ATSM seemed to be more than hypoxia agent, even if redox state and hypoxia were both related and dependent phenomena. This data would explain uptake variations according to cell types (8, 13, 16) and an explication of the low uptake of certain prostate tumor which overexpressed the FAS because this enzyme required a large amount of NADPH as cofactor for function. As previously described, impairment of the respiratory chain generated in a first time excessed electrons, which caused a quickly over-reduced intracellular state, which caused in first time a generation of ROS, increasing oxidative stress and damaging surrounding cells. This overproduction of ROS from mitochondria (32) leads to an oxidative stress in a tumor, which becomes hypoxic (33). In second time, this oxidative stress mediated the shift in oxidative phosphorylation to anaerobic glycolysis (down-regulation of mitochondria mediated by HIF, the major chronic mechanism of hypoxia adaptation in cells) to decrease ROS levels (34).

Finally, ^{64}Cu -ATSM seemed to be a marker of the over-reduced cell state and consequently an indirect marker of the hypoxia. In fact, during a severe and chronic hypoxia, the over-reduced cell state conducted to a down-regulation of the mitochondria oxidative phosphorylation and had for consequence a diminution of intracellular ROS. This affinity of Cu-ATSM for over-reduced cell was a complex phenomenon with various possibility of adaptive tumor cells response. To provide a direct answer to

radiation oncologists (35) requirement, more studies were needed to determine whether the Cu-ATSM uptake was linked to the low ROS level in cell. Moreover, the first clinical studies has shown a predictive response to traditional cancer therapies in patients with rectal (36), lung (37), and uterine cervix cancer (28, 38) where Cu-ATSM uptake was of worse prognosis.

References

- Brown JM, Wilson WR. Exploiting tumour hypoxia in cancer treatment. *Nat Rev Cancer* (2004) 4:437–47. doi:10.1038/nrc1367
- Thomlinson RH, Gray LH. The histological structure of some human lung cancers and the possible implications for radiotherapy. *Br J Cancer* (1955) 9:539–49. doi:10.1038/bjc.1955.55
- Chapman JD, Baer K, Lee J. Characteristics of the metabolism-induced binding of misonidazole to hypoxic mammalian cells. *Cancer Res* (1983) 43:1523–8.
- Hoffman JM, Rasey JS, Spence AM, Shaw DW, Krohn KA. Binding of the hypoxia tracer [3H]misonidazole in cerebral ischemia. *Stroke* (1987) 18:168–76. doi:10.1161/01.STR.18.1.168
- Fujibayashi Y, Taniuchi H, Yonekura Y, Ohtani H, Konishi J, Yokoyama A. Copper-62-ATSM: a new hypoxia imaging agent with high membrane permeability and low redox potential. *J Nucl Med* (1997) 38:1155–60.
- Dearling JL, Lewis JS, Mullen GED, Welch MJ, Blower PJ. Copper bis (thiosemicarbazone) complexes as hypoxia imaging agents: structure-activity relationships. *J Biol Inorg Chem* (2002) 7:249–59. doi:10.1007/s007750100291
- Maurer RI, Blower PJ, Dilworth JR, Reynolds CA, Zheng Y, Mullen GED. Studies on the mechanism of hypoxic selectivity in copper bis (thiosemicarbazone) radiopharmaceuticals. *J Med Chem* (2002) 45:1420–31. doi:10.1021/jm0104217
- Burgman P, O'Donoghue JA, Lewis JS, Welch MJ, Humm JL, Ling CC. Cell line-dependent differences in uptake and retention of the hypoxia-selective nuclear imaging agent Cu-ATSM. *Nucl Med Biol* (2005) 32:623–30. doi:10.1016/j.nucmedbio.2005.05.003
- Obata A, Yoshimi E, Waki A, Lewis JS, Oyama N, Welch MJ, et al. Retention mechanism of hypoxia selective nuclear imaging/radiotherapeutic agent Cu-diacetyl-bis(N4-methylthiosemicarbazone) (Cu-ATSM) in tumor cells. *Ann Nucl Med* (2001) 15:499–504. doi:10.1007/BF02988502
- Price KA, Crouch PJ, Volitakis I, Paterson BM, Lim S, Donnelly PS, et al. Mechanisms controlling the cellular accumulation of copper bis(thiosemicarbazone) complexes. *Inorg Chem* (2011) 50:9594–605. doi:10.1021/ic201334q
- Lewis JS, McCarthy DW, McCarthy TJ, Fujibayashi Y, Welch MJ. Evaluation of ⁶⁴Cu-ATSM in vitro and in vivo in a hypoxic tumor model. *J Nucl Med* (1999) 40:177–83.
- Dearling JL, Packard AB. Some thoughts on the mechanism of cellular trapping of Cu(II)-ATSM. *Nucl Med Biol* (2010) 37:237–43. doi:10.1016/j.nucmedbio.2009.11.004
- Liu J, Hajibeigi A, Ren G, Lin M, Siyambalapitiyage W, Liu Z, et al. Retention of the radiotracers ⁶⁴Cu-ATSM and ⁶⁴Cu-PTSM in human and murine tumors is influenced by MDR1 protein expression. *J Nucl Med* (2009) 50:1332–9. doi:10.2967/jnumed.109.061879
- Yoshii Y, Furukawa T, Kiyono Y, Watanabe R, Mori T, Yoshii H, et al. Internal radiotherapy with copper-64-diacetyl-bis (N4-methylthiosemicarbazone) reduces CD133+ highly tumorigenic cells and metastatic ability of mouse colon carcinoma. *Nucl Med Biol* (2011) 38:151–7. doi:10.1016/j.nucmedbio.2010.08.009
- Yoshii Y, Yoneda M, Ikawa M, Furukawa T, Kiyono Y, Mori T, et al. Radiolabeled Cu-ATSM as a novel indicator of overreduced intracellular state due to mitochondrial dysfunction: studies with mitochondrial DNA-less p0 cells and cybrids carrying MELAS mitochondrial DNA mutation. *Nucl Med Biol* (2012) 39:177–85. doi:10.1016/j.nucmedbio.2011.08.008
- Vavere AL, Lewis JS. Examining the relationship between Cu-ATSM hypoxia selectivity and fatty acid synthase expression in human prostate cancer cell lines. *Nucl Med Biol* (2008) 35:273–9. doi:10.1016/j.nucmedbio.2007.11.012
- Ko YH, Pedersen PL, Geschwind JF. Glucose catabolism in the rabbit VX2 tumor model for liver cancer: characterization and targeting hexokinase. *Cancer Lett* (2001) 173:83–91. doi:10.1016/S0304-3835(01)00667-X
- Obata A, Yoshimoto M, Kasamatsu S, Naiki H, Takamatsu S, Kashikura K, et al. Intra-tumoral distribution of ⁶⁴Cu-ATSM: a comparison study with FDG. *Nucl Med Biol* (2003) 30:529–34. doi:10.1016/S0969-8051(03)00047-7
- Dence CS, Ponde DE, Welch MJ, Lewis JS. Autoradiographic and small-animal PET comparisons between (18)F-FMISO, (18)F-FDG, (18)F-FLT and the hypoxic selective (64)Cu-ATSM in a rodent model of cancer. *Nucl Med Biol* (2008) 35:713–20. doi:10.1016/j.nucmedbio.2008.06.001
- O'Donoghue JA, Zanzonico P, Pugachev A, Wen B, Smith-Jones P, Cai S, et al. Assessment of regional tumor hypoxia using 18F-fluoromisonidazole and ⁶⁴Cu(II)-diacetyl-bis(N4-methylthiosemicarbazone) positron emission tomography: comparative study featuring microPET imaging, Po2 probe measurement, autoradiography, and fluorescent microscopy in the R3327-AT and FaDu rat tumor models. *Int J Radiat Oncol Biol Phys* (2005) 61:1493–502. doi:10.1016/j.ijrobp.2004.12.057
- McCall KC, Humm JL, Bartlett R, Reese M, Carlin S. Copper-64-diacetyl-bis(N4-methylthiosemicarbazone) pharmacokinetics in FaDu xenograft tumors and correlation with microscopic markers of hypoxia. *Int J Radiat Oncol Biol Phys* (2012) 84:e393–9. doi:10.1016/j.ijrobp.2012.05.005
- Yuan H, Schroeder T, Bowsher JE, Hedlund LW, Wong T, Dewhirst MW. Intertumoral differences in hypoxia selectivity of the PET imaging agent ⁶⁴Cu(II)-diacetyl-bis(N4-methylthiosemicarbazone). *J Nucl Med* (2006) 47:989–98.
- Valtorta S, Belloli S, Sanvito F, Masiello V, Di Grigoli G, Monterisi C, et al. Comparison of 18F-fluoroazomycin-arabinofuranoside and ⁶⁴Cu-diacetyl-bis(N4-methylthiosemicarbazone) in preclinical models of cancer. *J Nucl Med* (2013) 54:1106–12. doi:10.2967/jnumed.112.111120
- Carlin S, Zhang H, Reese M, Ramos NN, Chen Q, Ricketts S-A. A comparison of the imaging characteristics and microregional distribution of 4 hypoxia PET tracers. *J Nucl Med* (2014) 55:515–21. doi:10.2967/jnumed.113.126615
- Huetting R, Kersemans V, Cornelissen B, Tredwell M, Hussien K, Christlieb M, et al. A comparison of the behavior of (64)Cu-acetate and (64)Cu-ATSM in vitro and in vivo. *J Nucl Med* (2014) 55:128–34. doi:10.2967/jnumed.113.119917
- Laforest R, Dehdashti F, Lewis JS, Schwarz SW. Dosimetry of 60/61/62/⁶⁴Cu-ATSM: a hypoxia imaging agent for PET. *Eur J Nucl Med Mol Imaging* (2005) 32:764–70. doi:10.1007/s00259-004-1756-x
- Yoshii Y, Matsumoto H, Yoshimoto M, Furukawa T, Morokoshi Y, Sogawa C, et al. Controlled administration of penicillamine reduces radiation exposure in critical organs during ⁶⁴Cu-ATSM internal radiotherapy: a novel strategy for liver protection. *PLoS One* (2014) 9:e86996. doi:10.1371/journal.pone.0086996
- Lewis JS, Laforest R, Dehdashti F, Grigsby PW, Welch MJ, Siegel BA. An imaging comparison of ⁶⁴Cu-ATSM and ⁶⁰Cu-ATSM in cancer of the uterine cervix. *J Nucl Med* (2008) 49:1177–82. doi:10.2967/jnumed.108.051326
- Basken NE, Green MA. Cu(II) bis(thiosemicarbazone) radiopharmaceutical binding to serum albumin: further definition of species dependence and associated substituent effects. *Nucl Med Biol* (2009) 36:495–504. doi:10.1016/j.nucmedbio.2009.02.006
- Wang Y, Hodgkinson V, Zhu S, Weisman GA, Petris MJ. Advances in the understanding of mammalian copper transporters. *Adv Nutr* (2011) 2:129–37. doi:10.3945/an.110.000273
- Barlow CH, Harken AH, Chance B. Evaluation of cardiac ischemia by NADH fluorescence photography. *Ann Surg* (1977) 186:737–40. doi:10.1097/0000658-197712000-00013
- Indo HP, Davidson M, Yen H-C, Suenaga S, Tomita K, Nishii T, et al. Evidence of ROS generation by mitochondria in cells with impaired electron transport chain and mitochondrial DNA damage. *Mitochondrion* (2007) 7:106–18. doi:10.1016/j.mito.2006.11.026
- Dewhirst MW, Cao Y, Moeller B. Cycling hypoxia and free radicals regulate angiogenesis and radiotherapy response. *Nat Rev Cancer* (2008) 8:425–37. doi:10.1038/nrc2397

Acknowledgments

This work has been, in part, supported by a grant from the French National Agency for Research called «Investissements d'Avenir», Equipex Arronax-Plus ANR-11-EQPX-0004, and Labex IRON ANR-11-LABX-18-01.

34. Solaini G, Baracca A, Lenaz G, Sgarbi G. Hypoxia and mitochondrial oxidative metabolism. *Biochim Biophys Acta* (2010) **1797**:1171–7. doi:10.1016/j.bbabo.2010.02.011
35. Clausen MM, Hansen AE, Lundemann M, Hollensen C, Pommer T, Munck AF, et al. Dose painting based on tumor uptake of Cu-ATSM and FDG: a comparative study. *Radiat Oncol* (2014) **9**:228. doi:10.1186/s13014-014-0228-0
36. Dietz DW, Dehdashti F, Grigsby PW, Malyapa RS, Myerson RJ, Picus J, et al. Tumor hypoxia detected by positron emission tomography with ^{60}Cu -ATSM as a predictor of response and survival in patients undergoing neoadjuvant chemoradiotherapy for rectal carcinoma: a pilot study. *Dis Colon Rectum* (2008) **51**:1641–8. doi:10.1007/s10350-008-9420-3
37. Dehdashti F, Mintun MA, Lewis JS, Bradley J, Govindan R, Laforest R, et al. In vivo assessment of tumor hypoxia in lung cancer with ^{60}Cu -ATSM. *Eur J Nucl Med Mol Imaging* (2003) **30**:844–50. doi:10.1007/s00259-003-1130-4
38. Dehdashti F, Grigsby PW, Lewis JS, Laforest R, Siegel BA, Welch MJ. Assessing tumor hypoxia in cervical cancer by PET with ^{60}Cu -labeled diacetyl-bis(N4-methylthiosemicarbazone). *J Nucl Med* (2008) **49**:201–5. doi:10.2967/jnumed.107.048520

Conflict of Interest Statement: The authors declare that the research was conducted in the absence of any commercial or financial relationships that could be construed as a potential conflict of interest.

Copyright © 2015 Colombié, Gouard, Frindel, Vidal, Chérel, Kraeber-Bodéré, Rousseau and Bourgeois. This is an open-access article distributed under the terms of the Creative Commons Attribution License (CC BY). The use, distribution or reproduction in other forums is permitted, provided the original author(s) or licensor are credited and that the original publication in this journal is cited, in accordance with accepted academic practice. No use, distribution or reproduction is permitted which does not comply with these terms.

Imaging modalities to assess oxygen status in glioblastoma

Aurélien Corroyer-Dulmont^{1,2,3,4*}, Ararat Chakhoyan^{1,2,3,4}, Solène Collet^{1,2,3,4}, Lucile Durand^{1,2,3,4}, Eric T. MacKenzie^{1,2,3,4}, Edwige Petit^{1,2,3,4}, Myriam Bernaudin^{1,2,3,4}, Omar Touzani^{1,2,3,4} and Samuel Valable^{1,2,3,4*}

¹ CNRS, UMR 6301-Imagerie et stratégies thérapeutiques des pathologies cérébrales et tumorales (ISTCT), CERVOxy group, GIP Cyceron, Caen, France, ² CEA, Direction des Sciences du Vivant (DSV)/Institut d'Imagerie Biomédicale (I2BM), UMR 6301-Imagerie et stratégies thérapeutiques des pathologies cérébrales et tumorales (ISTCT), CERVOxy group, GIP Cyceron, Caen, France, ³ Université de Caen Normandie, UMR 6301-Imagerie et stratégies thérapeutiques des pathologies cérébrales et tumorales (ISTCT), CERVOxy group, GIP Cyceron, Caen, France, ⁴ Esplanade de la Paix, Normandie Université, Caen, France

OPEN ACCESS

Edited by:

Michel Chérel,
University of Nantes, France

Reviewed by:

Serge Goldman,
Université Libre de Bruxelles Hôpital
Érasme, Belgium
Amandine Pallardy,
Centre Hospitalier Universitaire de
Nantes, France

*Correspondence:

Aurélien Corroyer-Dulmont and
Samuel Valable,
UMR 6301-ISTCT, GIP Cyceron,
Bd H Becquerel, BP 5229,
Caen Cedex 14074, France
aurelien.dulmont@gmail.com;
valable@cyceron.fr

Specialty section:

This article was submitted to Nuclear
Medicine, a section of the journal
Frontiers in Medicine

Received: 11 June 2015

Accepted: 03 August 2015

Published: 19 August 2015

Citation:

Corroyer-Dulmont A, Chakhoyan A,
Collet S, Durand L, MacKenzie ET,
Petit E, Bernaudin M, Touzani O and
Valable S (2015) Imaging modalities to
assess oxygen status in glioblastoma.
Front. Med. 2:57.
doi: 10.3389/fmed.2015.00057

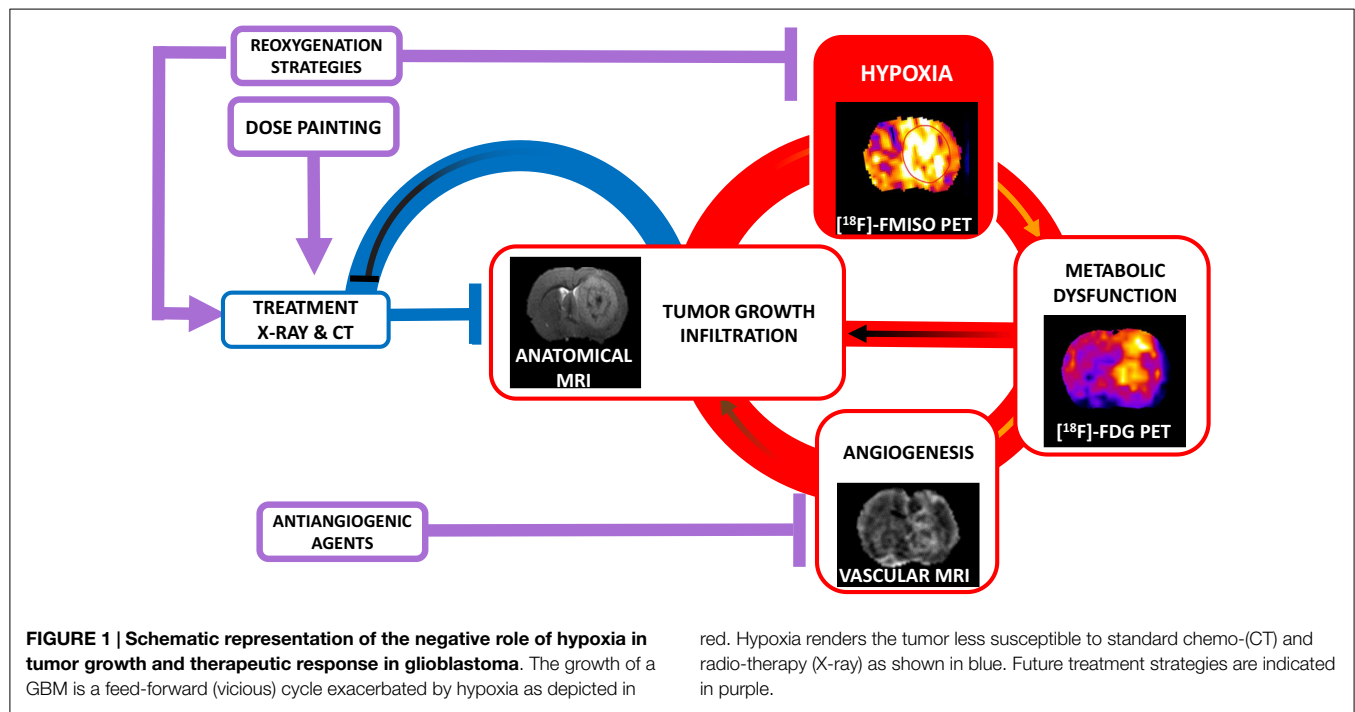
Hypoxia, the result of an inadequacy between a disorganized and functionally impaired vasculature and the metabolic demand of tumor cells, is a feature of glioblastoma. Hypoxia promotes the aggressiveness of these tumors and, equally, negatively correlates with a decrease in outcome. Tools to characterize oxygen status are essential for the therapeutic management of patients with glioblastoma (i) to refine prognosis, (ii) to adapt the treatment regimen, and (iii) to assess the therapeutic efficacy. While methods that are focal and invasive in nature are of limited use, non-invasive imaging technologies have been developed. Each of these technologies is characterized by its singular advantages and limitations in terms of oxygenation status in glioblastoma. The aim of this short review is, first, to focus on the interest to characterize hypoxia for a better therapeutic management of patients and, second, to discuss recent and pertinent approaches for the assessment of oxygenation/hypoxia and their direct implication for patient care.

Keywords: hypoxia, glioblastoma, MRI, PET, multimodal imaging

Hypoxia and Glioblastoma

As an aggressive solid tumor, glioblastoma (GBM) presents cardinal histological features of chaotic microvascular proliferation and necrotic foci. However, the neoangiogenesis is dysfunctional and normal tissue oxygen tension is not maintained (1). The resulting imbalance between oxygen consumption and supply is called hypoxia. An important spatial heterogeneity is observed in GBM with severely hypoxic zones and peripheral infiltration accompanied by a microvascular proliferation (2). GBM cells, in hypoxic conditions, express transcriptional factors, such as the hypoxia-inducible factor (HIF), which, by the induction of various gene expressions, is involved in tumor cell adaptation. Hypoxia plays a pivotal role in the spread of tumor cells and, hence, invasion (3). Hypoxia is also a key factor in the rapaciousness of human GBM and the characterization of hypoxia discriminates poor from long outcomes (4). Moreover, hypoxia greatly impacts therapeutic efficacy. For instance, it is known that the degree of oxygenation is critical for the efficacy of both radiation therapy and chemotherapy (5). All these aspects are summarized in **Figure 1**.

Abbreviations: BLI, bioluminescence imaging; EPR, electron paramagnetic resonance; GBM, glioblastoma; HB, hemoglobin; HIF, hypoxia-inducible factor; MRI, magnetic resonance imaging; NIRS, near infrared spectroscopy; PET, positron emission tomography; p_tO_2 , tissular oxygen pressure; SO_2 , oxygen saturation.



Hence, the assessment of tissue oxygen tension in GBM is crucial to personalize the treatment for each patient and to monitor its efficacy. Various methods, more or less invasive (Table 1), have been developed to assess the level of oxygenation at different compartments ranging from blood to cells.

Identification of Hypoxia at the Molecular Scale: Immunohistochemistry

Evaluation of hypoxia at the molecular scale can be performed by the detection of hypoxia-activated endogenous molecules, such as HIF α , and its targets, such as CAIX, Glut1, and VEGF. Another approach is to detect pimonidazole uptake in cells after systemic administration prior to biopsy. Immunohistochemistry has demonstrated its usefulness in the classification of GBM patients as a function of the level of hypoxia within the tumor and then predict recurrence and overall survival (4). The limitation to this technique is its invasive nature and the approach is restricted to a small biopsy, which may be not representative of the entire tumoral mass. Ideally and given the temporo-spatial heterogeneity of GBM, a method able to continuously and repeatedly assess hypoxia by three-dimensional imaging would be more than desirable.

Assessment of Local Tissue Oxygenation: Intracerebral Probes

The most direct assessment of tissue oxygenation is to measure the regional tissular oxygen pressure (p_tO_2) by probes implanted directly into the brain. The first probe developed was the Eppendorf polarographic p_tO_2 electrode, which relies on the measurement of the current generated at a cathode coated with thin gold

by ionization of oxygen at -700 mV. The needle is mounted on a stepping motor that sequentially advances and retracts the needle tip. This approach allows the creation of a histogram of p_tO_2 recorded from the tissue of interest. The temporal assessment of p_tO_2 is possible but the electrochemical reduction reduces the dissolved oxygen causing a continuous signal decrease with time. A second probe, more recently used, is the OxyLite™ probe (Oxford-Optronix). Light pulses carried by an optical fiber induce pulsatile fluorescence of a ruthenium luminophore incorporated into a silicone rubber polymer at the probe tip. The lifetime of the fluorescent pulses is inversely proportional to the oxygen tension in the tip. In a syngeneic model of rhabdomyosarcoma, the sensitivity of this method was exemplified by a real-time variation of tumor p_tO_2 during induced hypercapnia (6).

Despite the fact that oxygen sensitive probes allow a direct assessment of p_tO_2 , their major limitation is that they only allow a focal measurement of O_2 tensions. It is not possible to ascertain the exact location of the probe, e.g., in a necrotic or a peripheral area of the tumor. A second disadvantage is the invasiveness of these probes, which are unlikely to have clinical applications. Finally, there is also the fact that histography consumes oxygen.

Assessment of Hypoxia in Glioblastoma with Imaging

Several imaging methods have been developed to assess oxygen status in GBM patients but two main approaches are widely employed and based on MRI and PET technologies. These methods evaluate the level of oxygen in different physiological compartments: blood vessels (oxygen saturation, SO_2), tissue (p_tO_2), or cellular level and can thus render directly or indirectly indices of oxygenation.

TABLE 1 | Methodological approaches to evaluate oxygenation in glioblastoma: advantages and limitations.

	Advantages	Limitations
Immunohistochemistry	Routinely performed in neuropathology labs	Indirect assessment of p_tO_2 Invasive and localized
Probes	Direct and quantitative assessment of p_tO_2	Invasive and localized Low reproducibility Consumption of oxygen (for Eppendorf probes)
NIRS	Setup and application in clinical routine are easy No contrast agent injection	Indirect assessment of p_tO_2 Superficial and regional
qBOLD	Setup and application in clinical routine are easy Whole brain characterization Sensitive	Indirect assessment of p_tO_2 Specificity for hypoxia needs to be validated
[^{19}F]-MRI	Direct and quantitative assessment of p_tO_2	Needs contrast agent injection potentially toxic Needs ^{19}F coil (not easy for clinic application) Relatively low spatial resolution
EPR imaging	Direct and quantitative assessment of p_tO_2 Whole brain characterization	Localized (for EPR) Very low spatial resolution No studies in brain tumors
MOBILE	Whole brain characterization	Indirect and relative assessment of p_tO_2 No studies in brain tumors
Bioluminescence imaging	Indicator of cellular hypoxia	Needs genetically engineered tumor cells Not applicable for patients
^{15}O xygen	Whole brain characterization	Administration of a gaseous radioactive contrast agent No linear relation between oxygen consumption and cellular hypoxia
[^{62}Cu]/[^{64}Cu]-ATSM	Characterization of moderate hypoxia Whole brain characterization	Injection of a radioactive contrast agent Long half-life (12.7 h) Specificity for hypoxia is discussed
[^{18}F]-FMISO	Indicator of cellular hypoxia Particularly adapted to radiation therapy modulation Whole brain characterization	Injection of a radioactive contrast agent Relative long time before steady-state acquisition (2 h)
[^{18}F]-FAZA	Indicator of cellular hypoxia More rapid clearance than [^{18}F]-FMISO Whole brain characterization	Injection of a radioactive contrast agent Needs to be validated in a greater number of studies
[^{18}F]-HX4 and [^{18}F]-FETNIM	Indicator of cellular hypoxia Whole brain characterization	Injection of a radioactive contrast agent Not recommended for brain tumors
[^{18}F]-EF5	Indicator of cellular hypoxia Sensitivity near to immunohistochemistry Whole brain characterization	Injection of a radioactive contrast agent Synthesis of radiotracer remains difficult
[^{18}F]-RP-170	Reflect of cellular hypoxia Whole brain characterization	Injection of a radioactive contrast agent Needs to be validated in a greater number of studies

Estimation of Tumor Hypoxia in the Vascular Compartment: NIRS and BOLD-MRI

Near Infrared Spectroscopy

Near infrared spectroscopy (NIRS) is a simple, non-invasive but indirect method to characterize the level of oxygenation in blood. Hemoglobin (Hb) has an important photon absorption level in the near infrared range. The absorption spectrum is different if the hemoglobin is fully oxygenated or fully deoxygenated (deoxyHb). NIRS is able to characterize the concentration of the different forms of hemoglobin to reflect oxygen saturation (7). However, the NIRS characterization is superficial and is only reliable to a depth of 3–5 mm in the adult.

Blood Oxygen Level-Dependent MRI

Blood oxygen level-dependent MRI (BOLD-MRI) is a tomographic approach to detect changes in paramagnetic deoxyHb.

From the complex relationship between $T2^*$ and the Hb/deoxyHb ratio, a method to measure the SO_2 has been developed and termed as qBOLD-MRI where “q” stands for quantitative. The relationship between the $T2^*$ signal and SO_2 is multifactorial and depends on several parameters, such as cerebral blood volume (CBV), local hematocrit, $T2$ value, B_0 field, and oxygen saturation (8). With the quantification and integration of these parameters, a SO_2 map can be obtained. At a preclinical level, Christen and colleagues (8) have demonstrated the sensitivity of this method to detect changes not only in brain oxygenation during hypoxemia episodes but also in murine orthotopic models of GBM (9). Given that anatomical MRI is in use routinely, additional scan time to characterize tumor hypoxia by qBOLD-MRI could yield meaningful clinical data. The ready accessibility of MRI tempts one to use BOLD-MRI to assess hypoxia. However, BOLD-MRI, entirely focused on the vascular compartment (SO_2), corresponds to an indirect assessment of oxygenation in tissue. While the use of qBOLD-MRI corrects some pitfalls in the standard BOLD-MRI technique (10), the specificity of this approach for hypoxia still

requires validation. Indeed, SO_2 and $p_t\text{O}_2$ are non-linear and various parameters affect the sigmoid shape of the relationship between the two parameters. Nonetheless, the extrapolation of $p_t\text{O}_2$ from SO_2 is feasible under physiological circumstances, it is highly critical in a tumoral environment with several disturbed metabolic processes.

Imaging of Oxygenation in the Tissue Compartment: ^{19}F -MRI and EPRI

^{19}F -MRI

The relaxivity (R_1) of contrast agents saturated with ^{19}F fluorine (such as perfluorocarbons or hexafluorobenzene administered either intravenously or directly in the brain tissue) is directly proportional to $p_t\text{O}_2$. In a murine GBM model, Lemaire and colleagues (11) have shown the ability of ^{19}F -MRI to characterize the difference of tumor oxygenation between basal conditions ($p_t\text{O}_2 \approx 10$ mmHg) and during inhalation of 100% oxygen ($p_t\text{O}_2 \approx 170$ mmHg). Although ^{19}F -MRI is quantitative, this approach is limited by the potential toxicity of the tracer.

Electron Paramagnetic Resonance Imaging

Electron paramagnetic resonance (EPR) specifically responds only to atoms or molecules with unpaired electrons, including free radicals, free electrons, and some valence states of metal ions. The phenomenon that is observed with EPR is the transition (resonance absorption of energy) between the two energy states that can occur in an unpaired electron system placed within a magnetic field. This field separates the energy states associated with the two possible spin states of unpaired electrons. The presence of other unpaired electron species can affect the EPR spectrum. Molecular oxygen, with two unpaired electrons, can be detected either directly by EPR at ambient conditions due to fast relaxation of spins or detected indirectly from the oxygen-induced changes in the EPR spectrum of other paramagnetic probes in the system. From oxygen-induced EPR line bandwidth, one can quantify the oxygen concentration (12), in a preclinical study, have shown the ability and repeatability of electron paramagnetic resonance imaging (EPRI) to evaluate the different levels of oxygen in four brain tumor models. Furthermore, EPRI permits a spatial localization of $p_t\text{O}_2$ (13). However, because the signal is weak in EPRI, the slice thickness is important and the spatial resolution relatively low.

Assessment of Oxygenation at the Cellular Level: MOBILE and BLI

Mapping of Oxygen by Imaging Lipid relaxation Enhancement-MRI

Because oxygen is 11 times more soluble in lipids than in water, it has been proposed to measure T_1 relaxivity in lipids for the assessment of oxygen status (14). With GBM, this method holds promise given that the cerebral concentration of phospholipids is important in the brain. However, even if this method is sensitive to changes in $p_t\text{O}_2$ during gas inhalation, for example, studies in brain tumors have yet to be performed.

Bioluminescence Imaging

Bioluminescence imaging (BLI) is based on the detection of light emitted by cells expressing a luciferase gene under the control of a hypoxia-sensitive promoter containing hypoxia response elements (HRE) sequences, has been advanced to measure brain hypoxia. An engineered human GBM cell line expressing luciferase under the control of HRE was implanted orthotopically and well correlated with other hypoxic reporters (15). Nonetheless, BLI has a low-spatial resolution and the tumoral heterogeneity will be difficult to assess and no translation to man is feasible.

Assessment of Hypoxia with PET

^{15}O Oxygen

The first PET radiotracer, used to assess oxygen levels in brain, was the positron emitter ^{15}O oxygen which allowed several validated quantitative methods to map cerebral blood flow (CBF), CBV, oxygen extraction fraction (OEF), and the cerebral metabolic rate of oxygen (CMRO_2) using ^{15}O -labeled H_2O , CO , and O_2 (16). These methods are considered as the “gold standard” and are widely employed, among others, in the study of stroke.

However, these methods are not immediately translatable to oncology. Tumor metabolism is driven by the rate of glycolysis but without a corresponding increase in aerobic metabolism (the Warburg effect). In neoplasm, the inability of these techniques to reflect neither $p_t\text{O}_2$ nor true CMRO_2 has led to the development of various other PET tracers better adapted to this end. Two classes of radiotracers are employed: the $^{62}/^{64}\text{Cu}$ labeled-diacetyl-bis(N4-methylthiosemicarbazone) and ^{18}F -labeled nitroimidazoles analogs, discussed as follows.

Cu-Diacetyl-bis(N4-Methylthiosemicarbazone) (^{64}Cu) or ^{62}Cu -ATSM

$^{62}/^{64}\text{Cu}$ -ATSM has been promoted, not as an oxygen sensor, but as a hypoxia biomarker. Cu(II) -ATSM is reduced to an unstable Cu(I) -ATSM and then re-oxidized if oxygen is present but otherwise becomes trapped in hypoxic cells. This radiotracer has the capability to characterize moderate hypoxia with an enhanced uptake observed when $p_t\text{O}_2$ is <35 mmHg (17). The long half-life of ^{64}Cu -ATSM (12.7 h) is an advantage because production and transport would not only permit utilization in different clinical research centers but also a limitation in terms of radioprotection and the impossibility to repeat the measure more than once a week. With respect to neurooncology, Tateishi and colleagues (18) examined the interest of using ^{62}Cu -ATSM for glioma grading and correlated ^{62}Cu -ATSM uptake with HIF-1 α expression in glioma patients. However, several studies have suspected a non-specificity of this radiotracer in hypoxia with an absence of correlation between the spatial distribution of ^{64}Cu -ATSM uptake immunohistochemical characterization of hypoxia (19).

Fluorinated Nitroimidazole Compounds

Nitroimidazoles enter viable cells by passive diffusion where they undergo an active reduction. Under normoxic conditions, these molecules are re-oxidized and diffuse out of the cell. By contrast, in severe hypoxia, they eventually become irreversibly trapped

in the cell at a threshold $p_tO_2 < 10$ mmHg. Several nitroimidazole radiotracers are at various stages of preclinical and clinical development.

[¹⁸F]-Fluoromisonidazole ([¹⁸F]-FMISO)

Highly selective for hypoxia, [¹⁸F]-FMISO is the lead candidate to assess hypoxia with PET and is the most extensively studied radiotracer in clinical investigations. In high-grade glioma, where the p_tO_2 in the tumor is remarkably low (around 7 mmHg), [¹⁸F]-FMISO is increasingly used to estimate hypoxia (20). In our group, we have shown the ability of [¹⁸F]-FMISO to discriminate various states of hypoxia in different GBM models (21, 22). Others studies have shown that the uptake of [¹⁸F]-FMISO is inversely correlated to overall survival in GBM patients (23). The major limitation of this approach is the low sensitivity to moderate hypoxia (between 10 and 30 mmHg). The second limitation of this radiotracer is its relative long washout in non-hypoxic cells to obtain an optimal contrast (between 2 and 4 h after tracer injection).

Other Hydrophilic Tracers

[¹⁸F]-Fluoroazomycin-Arabinoside ([¹⁸F]-FAZA), [¹⁸F]-Flortanidazole ([¹⁸F]-HX4) and [¹⁸F]-Fluoroerythronitroimidazole ([¹⁸F]-FETNIM), 1-[2-[¹⁸F] Fluoro-1-(Hydroxymethyl)-Ethoxy]Methyl-2-Nitroimidazole ([¹⁸F]-RP-170)

These tracers ([¹⁸F]-Fluoroazomycin-arabinoside ([¹⁸F]-FAZA), [¹⁸F]-Flortanidazole ([¹⁸F]-HX4), and [¹⁸F]-fluoroerythronitroimidazole ([¹⁸F]-FETNIM), 1-[2-[¹⁸F] Fluoro-1-(hydroxymethyl)-ethoxy]methyl-2-nitroimidazole ([¹⁸F]-RP-170) because of their hydrophilic character, have a more rapid plasma half-life and rapid clearance from tissues than [¹⁸F]-FMISO. [¹⁸F]-FAZA has been used to determine hypoxia in models of gliomas and discriminated clusters of hypoxia and necrosis (24). [¹⁸F]-FAZA awaits clinical investigation for GBM patients. In glioma patients, [¹⁸F]-RP-170 was compared to p_tO_2 and HIF-1 α immunostaining and a selectivity of this tracer for hypoxia was observed (25). However, regarding their highly hydrophilic properties, these radiotracers are not recommended the study of brain tumors because their uptake will be largely influenced by BBB disruption (26).

2-(2-Nitro-1H-imidazol-1-yl)-N-(2,2,3,3,3-penta-fluoropropyl)-acetamide ([¹⁸F]-EF5)

In contradistinction to the hydrophilic tracers, a lipophilic radiotracer, [¹⁸F]-EF5, has been studied to detect hypoxia in human GBM. Initially, it was used for immunohistochemistry, [¹⁸F]-EF5 possesses a sensitivity near to that of immunohistochemistry but the synthesis seems problematic (27).

Interest of PET Tracers in the Management of GBM Patients

The conventional treatment of GBM is surgical resection when possible, followed by radiotherapy along with concomitant chemotherapy. Despite these treatment protocols, the median

survival fails to exceed 15 months. Imaging of hypoxia should ameliorate patient management in various ways (see **Figure 1**).

Optimization of Conventional Treatments

In the therapeutic management of glioma patients, it has been proposed to use imaging biomarkers of hypoxia to adapt the treatment according to hypoxic status (20). [¹⁸F]-FMISO seems particularly suited for the modulation of radiation dose in GBM because the range of p_tO_2 identified by [¹⁸F]-FMISO (from 0 to 10 mmHg) corresponds to the scale used to define the radiation dose adapted for hypoxic, radioresistant tumors (28). Hence, authors have advanced the use of the spatial information derived from [¹⁸F]-FMISO to compute the prescription for the radiation dose (29). The aim of dose escalation is (i) to increase the efficacy of treatment in hypoxic area, (ii) to compensate for the spatial heterogeneity, and (iii) to reduce the toxicity to healthy tissue. While a boost of radiotherapy in the most hypoxic areas appears attractive, this concept still requires validation.

Treatment Orientation

Glioblastoma is densely vascularized tumors and, therefore, targeted anti-angiogenic therapies, such as bevacizumab, (a humanized monoclonal antibody raised against VEGF), has been suggested, although recent phase III trials demonstrated disappointing results. An explanation for the failure could be that no patient selection was performed prior to the initiation of the treatment. PET-based imaging of hypoxia could be performed before treatment to stratify eligible patients for the anti-angiogenic strategy. After selection by markers of hypoxia, the use of radiosensitizers has also been proposed for head and neck cancers (EORTC trial 1219), an approach that could be applied to GBM patients. Our group has also demonstrated that hypoxia-inducible genes, such as erythropoietin, are involved in GBM growth and resistance to treatment (5). Grounded on hypoxia imaging, such proteins would represent novel and original targets for therapy.

Assessment of Treatment Effects

The interest in anti-VEGF therapies has been rekindled since the emergence of the concept of “normalization.” Anti-angiogenic treatments are now planned to transiently improve tumor vasculature, resulting in increased tumor perfusion and oxygenation. In a preclinical study in GBM, we have shown that sunitinib treatment decreases [¹⁸F]-FMISO uptake hypothetically due to vascular normalization (21). Similarly, Titz and colleagues (30) have proposed to program a model of responsivity to anti-angiogenic treatments from PET imaging of hypoxia in patients.

Conclusion

It is widely accepted that hypoxia is important not only in tumor growth but also in response to various therapeutic regimens. The characterization of oxygenation by non-invasive imaging remains a challenge for the management and adaptation of conventional treatments (radio- and chemotherapy) as well as to

follow the efficacy of treatment. Several attempts have been made to develop methods to measure and image tumor oxygen tensions *in vivo* without consuming oxygen and thus without exacerbating the degree of hypoxia. Various approaches have been proposed to evaluate brain oxygenation at different scales from vascular to molecular levels. In this review, we argue that, despite development of several other methods (summarized **Table 1**), PET imaging (especially with fluorinated nitroimidazole compounds) seems to be, until now, the most relevant tool to characterize hypoxia in GBM.

Author Contributions

Manuscript drafting or manuscript revision for important intellectual content: all authors. Manuscript final version approval:

all authors. Literature research: AC-D, AC, SC, EM, OT, and SV. Manuscript editing: AC-D, EM, and SV. Figure preparation: AC-D, AC, EM, and SV.

Acknowledgments

This study was funded by the Institut National Contre le Cancer (INCa), the Centre National de la Recherche Scientifique (CNRS), the French Ministère de l'Enseignement Supérieur et de la Recherche (MESR), the University of Caen- Normandie (UNICAEN), the Conseil Régional de Basse-Normandie, the European Union-Fonds Européen de Développement Régional (FEDER) "L'Europe s'engage en Basse-Normandie," the French National Agency for Research called "Investissements d'Avenir" no. ANR-11-LABEX-0018-01, ANR-11-BSV5-0004.

References

- Beppu T, Kamada K, Yoshida Y, Arai H, Ogasawara K, Ogawa A. Change of oxygen pressure in glioblastoma tissue under various conditions. *J Neurooncol* (2002) **58**:47–52. doi:10.1023/A:1015832726054
- Inda M-D-M, Bonavia R, Seoane J. Glioblastoma multiforme: a look inside its heterogeneous nature. *Cancers (Basel)* (2014) **6**:226–39. doi:10.3390/cancers6010226
- Vaupel P. Hypoxia and aggressive tumor phenotype: implications for therapy and prognosis. *Oncologist* (2008) **13**(Suppl 3):21–6. doi:10.1634/theoncologist.13-S3-21
- Evans S, Jenkins K, Chen H. The relationship among hypoxia, proliferation, and outcome in patients with de novo glioblastoma: a pilot study. *Transl Oncol* (2010) **3**:160–9. doi:10.1593/tlo.09265
- Pérès EA, Gérault AN, Valable S, Roussel S. Silencing erythropoietin receptor on glioma cells reinforces efficacy of temozolomide and X-rays through senescence and mitotic catastrophe. *Oncotarget* (2015) **6**:2101–19.
- Tran L-B-A, Bol A, Labar D, Jordan B, Magat J, Mignon L, et al. Hypoxia imaging with the nitroimidazole 18F-FAZA PET tracer: a comparison with OxyLite, EPR oximetry and 19F-MRI relaxometry. *Radiother Oncol* (2012) **105**:29–35. doi:10.1016/j.radonc.2012.04.011
- Mehagnoul-Schippier DJ, van der Kallen BFW, Colier WJNM, van der Sluijs MC, van Erning LJTO, Thijssen HOM, et al. Simultaneous measurements of cerebral oxygenation changes during brain activation by near-infrared spectroscopy and functional magnetic resonance imaging in healthy young and elderly subjects. *Hum Brain Mapp* (2002) **16**:14–23. doi:10.1002/hbm.10026
- Christen T, Lemasson B, Pannetier N, Farion R, Segebarth C, Rémy C, et al. Evaluation of a quantitative blood oxygenation level-dependent (qBOLD) approach to map local blood oxygen saturation. *NMR Biomed* (2011) **24**:393–403. doi:10.1002/nbm.1603
- Lemasson B, Christen T, Serduc R, Maisin C, Bouchet A, Le Duc G, et al. Evaluation of the relationship between MR estimates of blood oxygen saturation and hypoxia: effect of an antiangiogenic treatment on a gliosarcoma model. *Radiology* (2012) **265**:743–52. doi:10.1148/radiol.12112621
- Baudelet C, Gallez B. Current issues in the utility of blood oxygen level dependent BOLD MRI for the assessment of modulation in tumor oxygenation. *Curr. Med. Imaging Rev.* (2005) **1**:229–43. doi:10.2174/157340505774574754
- Lemaire L, Bastiat G, Franconi F, Lautram N, Duong Thi Dan T, et al. (2013). Perfluorocarbon-loaded lipid nanocapsules as oxygen sensors for tumor tissue pO₂ assessment. *Eur J Pharm Biopharm* **84**:479–86. doi:10.1016/j.ejpb.2013.01.003
- Khan N, Mupparaju S, Hou H, Williams BB, Swartz H. Repeated assessment of orthotopic glioma pO₂ by multi-site EPR oximetry: a technique with the potential to guide therapeutic optimization by repeated measurements of oxygen. *J Neurosci Methods* (2012) **204**:111–7. doi:10.1016/j.jneumeth.2011.10.026
- Matsumoto S, Saito K, Yasui H, Morris HD, Munasinghe JP, Lizak M, et al. EPR oxygen imaging and hyperpolarized ¹³C MRI of pyruvate metabolism as noninvasive biomarkers of tumor treatment response to a glycolysis inhibitor
- 3-bromopyruvate. *Magn Reson Med* (2013) **69**:1443–50. doi:10.1002/mrm.24355
- Jordan BF, Magat J, Colliez F, Ozel E, Fruytier AC, Marchand V, et al. Mapping of oxygen by imaging lipids relaxation enhancement: a potential sensitive endogenous MRI contrast to map variations in tissue oxygenation. *Magn Reson Med* (2013) **70**:732–44. doi:10.1002/mrm.24511
- Lo Dico A, Valtorta S, Martelli C, Belloli S, Gianelli U, Tosi D, et al. Validation of an engineered cell model for in vitro and in vivo HIF-1 α evaluation by different imaging modalities. *Mol Imaging Biol* (2014) **16**:210–23. doi:10.1007/s11307-013-0669-0
- Moustafa RR, Baron J-C. Clinical review: imaging in ischaemic stroke – implications for acute management. *Crit Care* (2007) **11**:227. doi:10.1186/cc5973
- Toma-Dasu I, Dasu A, Brahme A. Quantifying tumour hypoxia by PET imaging: a theoretical analysis. *Adv Exp Med Biol* (2009) **645**:267–72. doi:10.1007/978-0-387-85998-9
- Tateishi K, Tateishi U, Sato M, Yamanaka S, Kanno H, Murata H, et al. Application of 62Cu-diacetyl-bis (N4-methylthiosemicarbazone) PET imaging to predict highly malignant tumor grades and hypoxia-inducible factor-1 α expression in patients with glioma. *AJNR Am J Neuroradiol* (2013) **34**:92–9. doi:10.3174/ajnr.A3159
- Carlin S, Zhang H, Reese M, Ramos NN, Chen Q, Ricketts S-A. A comparison of the imaging characteristics and microregional distribution of 4 hypoxia PET tracers. *J Nucl Med* (2014) **55**:515–21. doi:10.2967/jnumed.113.126615
- Cher LM, Murone C, Lawrentschuk N, Ramdave S, Papenfuss A, Hannah A, et al. Correlation of hypoxic cell fraction and angiogenesis with glucose metabolic rate in PET, and immunohistochemical studies. *J Nucl Med* (2006) **47**:410–8.
- Valable S, Petit E, Roussel S, Marteau L, Toutain J, Divoux D, et al. Complementary information from magnetic resonance imaging and (18F)-fluoromisonidazole positron emission tomography in the assessment of the response to an antiangiogenic treatment in a rat brain tumor model. *Nucl Med Biol* (2011) **38**:781–93. doi:10.1016/j.nucmedbio.2011.01.010
- Corroyer-Dulmont A, Pérès EA, Petit E, Durand L, Marteau L, Toutain J, et al. Noninvasive assessment of hypoxia with 3-[18F]-fluoro-1-(2-nitro-1-imidazolyl)-2-propanol ([18F]-FMISO): a PET study in two experimental models of human glioma. *Biol Chem* (2013) **394**:529–39. doi:10.1515/hsz-2012-0318
- Swanson KR, Chakraborty G, Wang CH, Rockne R, Harpold HLP, Muzi M, et al. Complementary but distinct roles for MRI and 18F-fluoromisonidazole PET in the assessment of human glioblastomas. *J Nucl Med* (2009) **50**:36–44. doi:10.2967/jnumed.108.055467
- Belloli S, Brioschi A, Politi LS, Ronchetti F, Calderoni S, Raccagni I, et al. Characterization of biological features of a rat F98 GBM model: a PET-MRI study with [18F]FAZA and [18F]FDG. *Nucl Med Biol* (2013) **40**:831–40. doi:10.1016/j.nucmedbio.2013.05.004
- Beppu T, Terasaki K, Sasaki T, Fujiwara S, Matsuura H, Ogasawara K, et al. Standardized uptake value in high uptake area on positron emission tomography with 18F-FRP170 as a hypoxic cell tracer correlates with intratumoral oxygen pressure in glioblastoma. *Mol Imaging Biol* (2014) **16**:127–35. doi:10.1007/s11307-013-0670-7

26. Fleming IN, Manavaki R, Blower PJ, West C, Williams KJ, Harris AL, et al. Imaging tumour hypoxia with positron emission tomography. *Br J Cancer* (2015) **112**:238–50. doi:10.1038/bjc.2014.610
 27. Koch CJ, Scheuermann JS, Divgi C, Judy KD, Kachur AV, Freifelder R, et al. Biodistribution and dosimetry of 18F-EF5 in cancer patients with preliminary comparison of 18F-EF5 uptake versus EF5 binding in human glioblastoma. *Eur J Nucl Med Mol Imaging* (2010) **37**:2048–59. doi:10.1007/s00259-010-1517-y
 28. Spence AM, Muzi M, Swanson KR, O'Sullivan F, Rockhill JK, Rajendran JG, et al. Regional hypoxia in glioblastoma multiforme quantified with [18F]fluoromisonidazole positron emission tomography before radiotherapy: correlation with time to progression and survival. *Clin Cancer Res* (2008) **14**:2623–30. doi:10.1158/1078-0432.CCR-07-4995
 29. Toma-Dasu I, Uhrdin J, Antonovic L, Dasu A, Nuyts S, Dirix P, et al. Dose prescription and treatment planning based on FMISO-PET hypoxia. *Acta Oncol* (2012) **51**:222–30. doi:10.3109/0284186X.2011.599815
 30. Titz B, Kozak KR, Jeraj R. Computational modelling of anti-angiogenic therapies based on multiparametric molecular imaging data. *Phys Med Biol* (2012) **57**:6079–101. doi:10.1088/0031-9155/57/19/6079
- Conflict of Interest Statement:** The authors declare that the research was conducted in the absence of any commercial or financial relationships that could be construed as a potential conflict of interest.

Copyright © 2015 Corroyer-Dulmont, Chakhoyan, Collet, Durand, MacKenzie, Petit, Bernaudin, Touzani and Valable. This is an open-access article distributed under the terms of the Creative Commons Attribution License (CC BY). The use, distribution or reproduction in other forums is permitted, provided the original author(s) or licensor are credited and that the original publication in this journal is cited, in accordance with accepted academic practice. No use, distribution or reproduction is permitted which does not comply with these terms.



Development of biocompatible and functional polymeric nanoparticles for site-specific delivery of radionuclides

Nicolas Lepareur^{1,2*}, Loleh Leal E Costa^{1,3}, Maëva Bocqué^{1,3†}, Clément Blondelle^{1,3}, Clément Ruello^{1,3}, Marie Desjulets¹, Nicolas Noiret^{3,4} and Sandrine Cammas-Marion^{3,4}

¹Comprehensive Cancer Centre Eugene Marquis, Rennes, France, ²INSERM UMR-S 991, Rennes, France, ³Ecole Nationale Supérieure de Chimie de Rennes (ENSCR), Rennes, France, ⁴UMR 6226 CNRS, Institute of Chemical Sciences of Rennes, Rennes, France

OPEN ACCESS

Edited by:

Michel Chérel,
University of Nantes, France

Reviewed by:

Sandrine Huclier,
University of Nantes, France
Patrice Hildgen,
Université de Montréal, Canada

*Correspondence:

Nicolas Lepareur,
Centre Eugene Marquis, Avenue de
la Bataille Flandres-Dunkerque, CS
44229, Rennes Cedex 35042, France
n.lepareur@rennes.unicancer.fr

†Present address:

Maëva Bocqué,
CNRS UMR 5223, Laboratory of
Polymer Materials Engineering,
University Claude Bernard Lyon 1,
Lyon, France

Specialty section:

This article was submitted to Nuclear
Medicine, a section of the journal
Frontiers in Medicine

Received: 02 June 2015

Accepted: 21 August 2015

Published: 04 September 2015

Citation:

Lepareur N, Leal E Costa L,
Bocqué M, Blondelle C, Ruello C,
Desjulets M, Noiret N and Cammas-
Marion S (2015) Development of
biocompatible and functional
polymeric nanoparticles for
site-specific delivery of radionuclides.
Front. Med. 2:63.
doi: 10.3389/fmed.2015.00063

Introduction: Encapsulation of biologically active molecules into nanoparticles (NPs), for site-specific delivery, is a fast growing area. These NPs must be biocompatible, non-toxic, and able to release their load in a controlled way. We have developed a series of NPs based on (bio)degradable and biocompatible poly(malic acid) derivatives, poly(benzyl malate) (PMLABe), with its PEG-grafted stealth analog and target-specific biotin-PEG-*b*-PMLABe one. A lipophilic radiotracer has then been encapsulated into these NPs.

Methods: Monomers were synthesized from DL-aspartic acid. PEG₄₂-*b*-PMLABe₇₃ and Biot-PEG₆₆-*b*-PMLABe₇₃ block copolymers were obtained by anionic ring-opening polymerization of benzyl malolactonate in presence of α -methoxy- ω -carboxy-PEG₄₂ and α -biotin- ω -carboxy-PEG₆₆ as initiators. NPs were prepared by nanoprecipitation. Size, polydispersity, and zeta potential were measured by dynamic light scattering (DLS) and zetametry. ^{99m}Tc-SSS was prepared as previously described. Encapsulation efficacy was assessed by varying different parameters, such as encapsulation with preformed NPs or during their formation, influence of the solvent, and of the method to prepare the NPs. After decay, ^{99m}Tc-loaded NPs were also analyzed by DLS and zetametry. NPs' morphology was assessed by transmission electron microscopy.

Results: ^{99m}Tc-SSS was added during nanoprecipitation, using two different methods, to ensure good encapsulation. Radiolabeled NPs present increased diameters, with identical low polydispersity indexes and negative zeta potentials in comparison to non-radiolabeled NPs.

Conclusion: A radiotracer was successfully encapsulated, but some further optimization is still needed. The next step will be to modify these radiolabeled NPs with a hepatotrope peptide, and to replace ^{99m}Tc with ¹⁸⁸Re for therapy. Our team is also working on drugs' encapsulation and grafting of a fluorescent probe. Combining these modalities is of interest for combined chemo-/radiotherapy, bimodal imaging, and/or theranostic approach.

Keywords: functional nanoparticles, site-specific targeting, degradable poly(benzyl malate) derivatives, radionuclide encapsulation, technetium-99m

Introduction

Nanomedicine, the use of nanoparticles (NPs) in medicine, is an ever-growing research field as illustrated by the huge amount of scientific publications and the important number of formulations registered for clinical trials, especially for cancer therapies (1). Such a growing interest results from the urgent need for highly efficient anti-cancer drug delivery systems allowing an increased efficacy of the drugs together with a decrease of their non-specific distribution and toxicity (2–4). Indeed, despite better knowledge and understanding of cancer biology, significant improvements in cancer treatments are still needed, specifically to address a large amount of drugs at the site of action, to decrease their toxic side effects and to simplify the administration protocols. In this context, nanoparticulate systems (liposomes, micelles, polymer-based NPs, etc.) have attracted the interest of many researchers and numerous systems have been developed (1). However, the prepared NPs have to answer to very strict specifications: (i) they have to be non-toxic and biocompatible at any stage of their life, until their complete excretion from the body; (ii) they need to have stealth properties and reduced immunogenicity together with ability to carry large amount of drug and to deliver it at a specific site in a sustainable way. Even if undeniable progresses have been achieved in the design of the ideal drug carriers as evidenced by the Food and Drug Administration (FDA) approval obtained by some nanovectors and by the number of NPs in preclinical or clinical phases (1, 5, 6), several properties, such as biocompatibility, drug loading capacity and site-specificity of drug release, need to be further improved. Among the nanoplateforms designed to address these objectives, polymer-based NPs have attracted much interest mainly because of the versatile characteristics of polymers allowing adjustment of the physico-chemical and biological properties of the corresponding nanocarriers. Consequently, several families of polymers have been developed to formulate multifunctional drug carriers with properties adjusted to the considered application (2). However, when designing a polymer family, one must keep in mind that the resulting materials are prepared to be used *in vivo* and that they have to respect the very strict specifications defined above. Another property which can be of importance is the (bio)degradability of the polymers constituting the drug delivery systems, allowing their elimination thanks to the (bio) degradation of the copolymers constituting the NPs, thus avoiding NPs accumulation in the body. However, this means that the degradation process must lead to non-immunogenic, biocompatible, and/or (bio)assimilable low molecular weight molecules that can be eliminated from the body. In this context, several (bio)degradable polymers have been developed and formulated under various nanoplateforms with more or less success (7, 8).

Therefore, the design of (bio)degradable polymers, whose physico-chemical and biological properties can be adjusted either by copolymerization, chemical modifications, or both, is of great importance (9, 10). Poly(β -malic acid) (PMLA) is a very good candidate due to the presence of carboxylic acid pendant groups, which can be chemically modified to introduce molecules of interest, and ester cleavable bounds within the polymer backbone, allowing the degradation of the polymer main chain into biocompatible metabolites (11–13).

Recently, we have synthesized and characterized two amphiphilic derivatives of PMLA presenting stealth properties, the poly(ethylene glycol)-*b*-poly(benzyl malate) (PEG₄₂-*b*-PMLABe₇₃), and targeting properties, the biotin-PEG₆₆-*b*-PMLABe₇₃. These block copolymers are able to self-assemble in aqueous media, leading to well-defined NPs designed for site-specific sustainable drug release in the frame of hepatocellular carcinoma (HCC). We showed that an anti-cancer drug model, the Doxorubicin (Dox), can be encapsulated into both stealth and targeted NPs with quite high encapsulation efficiency (14, 15) and that both kind of empty NPs have no significant toxicity against normal and cancer cell lines even at high concentrations (14–16).

Among molecules of interest to be encapsulated, one can include radioisotopes, either for imaging (diagnostic) or therapy, or even both (theranostics). There is an abundant, and ever-growing literature on the subject (17–23). All types of NPs have been radiolabeled (24), from micelles (25), polymeric NPs (26), liposomes (27), nanocapsules (28), or dendrimers (29), to inorganic ones (30). Most of the applications have been in cancer imaging and/or therapy (17), but some applications in cardiovascular (20, 23) and inflammation/infection (31, 32) can be found. Radiolabeling NPs enables the following of the NPs *in vivo* (33), particularly as an image-guided system for targeted delivery (34, 35), or for the controlled delivery of a therapeutic radionuclide (36).

Due to its favorable physical and chemical properties, such as its 6-h half-life, its low energy gamma emission of 140 keV, and relatively low isotope cost, generator-produced technetium-99m (^{99m}Tc) has been the most used radionuclide in routine nuclear medicine and is still the subject of numerous investigations, in the search for new radiopharmaceuticals. Logically, attempts to label NPs with ^{99m}Tc have been done (26, 30, 37). ^{99m}Tc has also the advantage of being part of a matched pair with rhenium-186/188, two isotopes that could be used as therapeutic radionuclides. Rhenium-188 (¹⁸⁸Re), which is also conveniently generator-produced, like ^{99m}Tc, has great potential for radionuclide therapy (38, 39). Moreover, due to similar chemistries, it can be easily replaced with rhenium-188 ($E_{\beta\max} = 2.1$ MeV, $E_{\gamma} = 155$ keV (15%), $t_{1/2} = 17$ h) for therapy purposes (40–42).

Because of the growing interest in the site-specific and controlled delivery of radionuclides, we investigated the possibilities to entrap a lipophilic radiotracer, ^{99m}Tc-SSS, inside NPs based on PEG₄₂-*b*-PMLABe₇₃ or Biot-PEG₆₆-*b*-PMLABe₇₃. Several methods were used to encapsulate ^{99m}Tc-SSS with more or less success. The corresponding radiolabeled NPs were characterized in terms of encapsulation efficiency, diameters, polydispersities, zeta potentials, and morphology.

Materials and Methods

Materials

Nuclear magnetic resonance spectra (¹H NMR) were recorded at 400 MHz on a Bruker ARX400 instrument (Billerica, MA, USA). Data are reported as follows: chemical shift (multiplicity, number of hydrogen). The chemical shifts (δ) are reported as parts per million (ppm) referenced to the appropriate residual solvent peak. Abbreviations are as follows: *s* (singlet),

d (doublet), *t* (triplet), *q* (quartet), *dd* (doublet of doublet), *m* (multiplet).

Weight average molecular weight (*M_w*) and molecular weight distribution (*M_w/M_n* = *I_p*) values were determined by size exclusion chromatography (SEC) in THF at 40°C (flow rate = 1.0 mL·min⁻¹) on a GPC 2502 Viscotek apparatus (Malvern Instruments Ltd, Malvern, UK) equipped with a refractive index detector, a LT5000L mixed medium org 300 mm × 7.8 mm gel column and a GPC/SEC OmniSEC software. The polymer samples were dissolved in THF (2 mg·mL⁻¹). All elution curves were calibrated with poly(styrene) standards.

The dynamic light scattering (DLS) measurements were recorded on a Delsa™ Nano Beckman Coulter apparatus (Fullerton, CA, USA) at 25°C in water. The obtained correlation curve allows calculating the diffusion coefficient (*D*) using the CONTIN method. The hydrodynamic radius (*R_h*), and therefore the hydrodynamic diameter (*D_h*), is then calculated from this diffusion coefficient *D* using the Stokes–Einstein equation where *k* is the Boltzmann constant, *T* the temperature, and *η* the medium viscosity (fixed at 0.8878 cP): $D = kT/6\pi\eta R_h$.

The zeta potential was measured by zetametry using a Delsa™ Nano Beckman Coulter apparatus (Fullerton, CA, USA) at 25°C in water. Laser Doppler electrophoresis in a phase mode was conducted with sequential fast and slow field reversal applying a potential of ±150 V. The measured electrophoretic mobility (*μ*) was then converted to zeta potential using the Smoluchowski approximation.

Transmission electron microscopy (TEM) was realized using a Jeol 2100 LAB6 microscope (Peabody, MA, USA) equipped with a Gatan Orius 200D camera (Pleasanton, CA, USA). UV spectra were recorded on a Secomam apparatus (Alès, France) at 485 nm. Activity measurements were done in a CRC-127R well-counter (Capintec Inc., Ramsey NJ, USA).

Radiochemical purity (RCP) of the complex was determined using a Perkin-Elmer Cyclone Storage Phosphor Imager (Waltham, MA, USA), with the Packard Optiquant v05.00 software. All chemicals were used as received. Anhydrous THF was obtained by distillation over sodium/benzophenone under N₂ atmosphere.

Synthesis of the Monomers and Polymers

The monomer, benzyl malolactonate (MLABe), was synthesized from DL-aspartic acid according to the previously reported synthesis (43). PEG₄₂-*b*-PMLABe₇₃ and Biot-PEG₆₆-*b*-PMLABe₇₃ block copolymers were obtained by anionic ring opening polymerization of MLABe in presence of, respectively, α-methoxy ω-carboxy poly(ethylene glycol), PEG₄₂-CO₂H, and α-biotin ω-carboxy poly(ethylene glycol), Biot-PEG₆₆-CO₂H, as initiators following a protocol described elsewhere (14).

PEG₄₂-*b*-PMLABe₇₃

¹H NMR (400.1 MHz; (CD₃)₂CO), δ (ppm): 2.77–2.83 (*m*, 2nH, CO₂CH₂C₆H₅), 3.56–3.59 (*m*, 4mH (*m* = 42), CH₃O(CH₂CH₂O)₄₂), 4.97–5.06 (*m*, 2nH, CHCH₂CO₂), 5.39–5.44 (*m*, 1nH, CHCH₂CO₂), 7.19–7.27 (*m*, 5nH, CO₂CH₂C₆H₅). *M_{NMR}* = 15 860 g/mol for the PMLABe block. SEC (THF, polystyrene standards, 1 mL/min): *M_w* = 5 430 g/mol, *I_p* = 1.38.

Biot-PEG₆₆-*b*-PMLABe₇₃

¹H NMR (400.1 MHz; (CD₃)₂CO), δ (ppm): 2.83 (*s*, 2nH, CO₂CH₂C₆H₅), 3.56–3.59 (*m*, 4mH (*m* = 66), Biot(CH₂CH₂O)₆₂), 5.00–5.05 (*m*, 2nH, CHCH₂CO₂), 5.41–5.44 (*m*, 1nH, CHCH₂CO₂), 7.19–7.23 (*m*, 5nH, CO₂CH₂C₆H₅). *M_{NMR}* = 14 630 g/mol for the PMLABe block. SEC (THF, polystyrene standards, 1 mL/min): *M_w* = 5 510 g/mol, *I_p* = 1.45.

Preparation of the NPs

Nanoparticles were prepared by the nanoprecipitation technique described previously (14). Briefly, a solution of 5 mg of copolymer in acetone was rapidly added to 2 mL of water under vigorous stirring. After 10 min of stirring at room temperature, acetone was eliminated under vacuum.

A slightly modified nanoprecipitation procedure (Gel filtration method) was also used: 5 mg of block copolymer were dissolved in 100 μL of DMF or acetone and 50 μL of DMF or acetone, containing or not the [^{185/187}Re(PhCS₃)₂(PhCS₂)] (^{185/187}Re-SSS) prepared as previously described (40), were added. The DMF or acetone solution was rapidly added into 1 mL of water under vigorous stirring. This solution was stirred at room temperature for 1 h, passed through a gel filtration PD-10 Sephadex G-25 Medium column (GE Healthcare, Little Chalfont, UK) and eluted with 1.5 mL + 3.5 mL of water.

Characterization of the Nanoparticles

The size (average *D_h*, polydispersity (*Đ*) and zeta potential of the formulations were measured by respectively DLS and zetametry, without any dilution of the samples.

Nanoparticles were observed by TEM. NPs' suspensions in water were placed on a formvar–carbon film coated on a copper grid (300 mesh). After 6 min of deposition at room temperature, non-adherent NPs were eliminated and the sample was stained by phosphotungstic acid (0.1%) for 30 s. TEM imaging was performed under 80 kV accelerating voltage.

Synthesis of ^{99m}Tc-SSS Complex

^{99m}Tc-SSS complex preparation was adapted from previously described method (44). Briefly, kits containing sodium gluconate and tin (II) chloride were first prepared as described thereafter: 825 mg of sodium gluconate were dissolved in 9.9 mL of distilled water. This solution (0.9 mL) was placed into 10 flasks. In parallel, 8.25 mg of tin chloride (SnCl₂·2H₂O) were dissolved into 1.1 mL of 0.1N HCl solution. Then, 0.1 mL of this solution was added in each flask containing the gluconate solution. The flasks were lyophilized and crimped.

One milliliter of [^{99m}Tc]-pertechnetate (750–800 MBq), eluted from a ⁹⁹Mo/^{99m}Tc generator (ELU III, IBA Molecular, Gif-sur-Yvette, France) was added to a lyophilized kit containing sodium gluconate (75 mg) and SnCl₂·2H₂O (0.75 mg) prepared as described above. The mixture was shaken at room temperature for 15 min. Sodium dithiobenzoate (10 mg dissolved into 0.5 mL of 0.9% saline solution) was added, and the solution was heated at 100°C for 15 min. A thin layer chromatography (TLC) was realized in a mixture of hexane and dichloromethane 6/4 as eluent to assess RCP of the complex (*R_f* = 0.62).

Radiolabeling of the NPs

The ^{99m}Tc-SSS complex previously prepared was extracted with 1 mL of dichloromethane. The organic solvent was evaporated at 40°C. Two procedures were tested for radiolabeling of the NPs according to the ones tested for empty NPs and ^{185/187}Re-SSS loaded NPs.

Standard Nanoprecipitation

Acetone or ethanol (0.5 mL) was then added to the residue to solubilize the complex, and a solution of 5 mg of the selected block copolymers, into 0.5 mL of acetone, was added. The mixture was nanoprecipitated into 2 mL of 0.9% saline solution. After stirring, the organic solvent was eliminated by heating at 45°C, under slight vacuum, for 15 min. The flask was then centrifuged at 3,500 G for 20 min (Awel MF 20-R, Blain, France). The supernatant was discarded and the pellet containing the radiolabeled NPs was resuspended into 2 mL of physiological serum. The radioactivity of the flask before and after centrifugation and resuspension was measured and the encapsulation efficiency was calculated as the ratio of the resuspended pellet activity on total activity before centrifugation.

Gel Filtration

DMF or acetone (0.15 mL) was then added to the dried complex. Five milligrams of the selected block copolymer were dissolved into 100 µL of DMF or acetone and 50 µL of the solution containing the ^{99m}Tc-SSS complex were added. This organic solution was then rapidly added into 1 mL of water. The mixture was stirred at room temperature for 15 min, passed through a PD-10 Sephadex G-25 Medium column and eluted with 1.5 mL + 3.5 mL of water as described above. The radioactivity of the flask before and after passage on the column was measured and the encapsulation efficiency was calculated as the ratio of the collected fraction's activity on total activity before filtration.

After total decrease of the radioactivity, ^{99m}Tc-radiolabeled NPs were analyzed by DLS to determine their diameter, polydispersity index, and zeta potential. The radiolabeled NPs were also observed by TEM after complete radioactive decay following the procedure described just above. An energy dispersive X-ray spectrometry (EDS) analysis of the radiolabeled NPs was also realized during the TEM measurements.

Results and Discussion

We have been recently investigating the possibilities of radiolabeling PMLA derivatives-based NPs with the final goal of using such nanocarriers for the dual site-specific carrying of a radioelement (^{99m}Tc/¹⁸⁸Re-SSS) and an anti-cancer drug. To reach this objective, we studied the possibilities to use degradable stealth and/or targeted NPs, constituted by PMLA amphiphilic derivatives, for radionuclides' encapsulation.

In a first step, we synthesized two amphiphilic PMLA derivatives, PEG₄₂-*b*-PMLABe₇₃ and Biot-PEG₆₆-*b*-PMLABe₇₃, by anionic ring opening polymerization of the MLABe with, respectively, α-methoxy,ω-carboxylate PEG₄₂ and α-biotin,ω-carboxylate PEG₆₆ as initiator. MLABe was synthesized in four steps, starting from aspartic acid, following a well-described and

reproducible synthetic route (Figure 1) (14–16, 43). After purification by precipitation, allowing the elimination of unreacted initiator and low molecular weight oligomers, block copolymers were characterized by ¹H NMR (structure and molecular weight of the PMLABe block) and by SEC (average molecular weight and polymolecularity).

Polymers' characteristics are summarized in Table 1. For both block copolymers, the molecular weights of the PMLABe block were calculated from their ¹H NMR spectra on the basis of the integration of peaks corresponding to the PEG block, whose molecular weight is given by the supplier, and on the integration of peaks corresponding to the PMLABe block. Calculated molecular weights were very similar to theoretical ones chosen at 15,000 g/mol and fixed by the monomer/initiator ratio. On the other hand, the average molecular weights measured by SEC were lower than the block copolymers' global molecular weights, calculated from the PEG and PMLABe molecular weights, resulting from the fact that THF is not the best solvent for the block copolymers and that the measured molecular

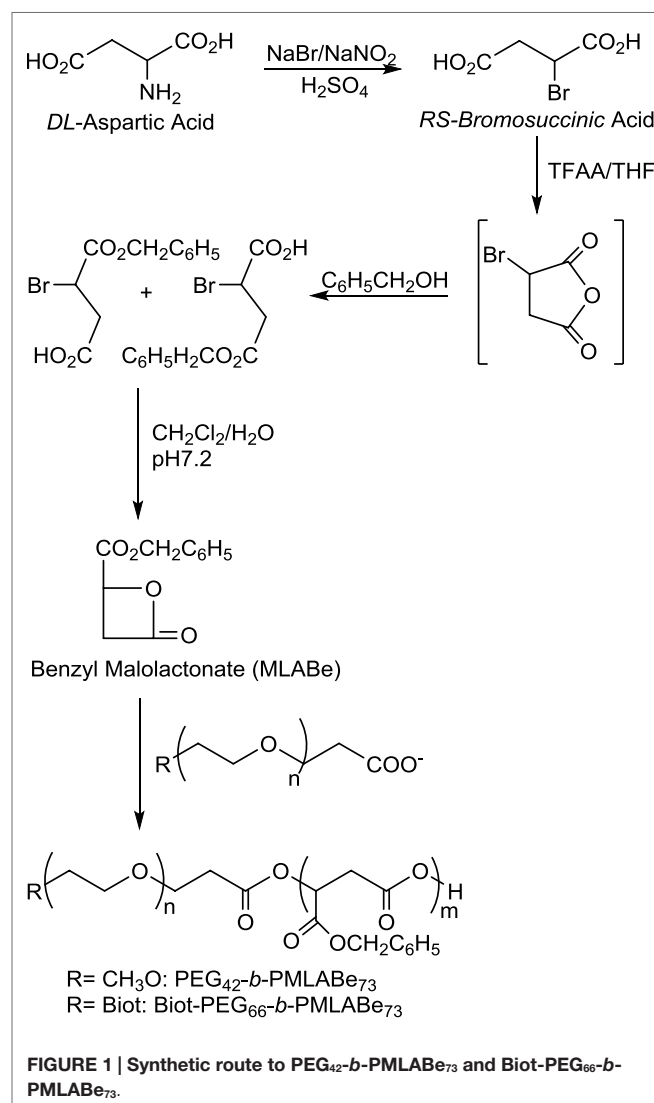


FIGURE 1 | Synthetic route to PEG₄₂-*b*-PMLABe₇₃ and Biot-PEG₆₆-*b*-PMLABe₇₃.

TABLE 1 | Characteristics of the synthesized block-copolymers.

Block copolymers	M _{PEG} ^a g/mol	M _{PMLABe} ^b g/mol	Mw ^c g/mol	Ip ^c
PEG ₄₂ - <i>b</i> -PMLABe ₇₃	2 015	15 860	5 430	1.38
Biot-PEG ₆₆ - <i>b</i> -PMLABe ₇₃	3 274	14 630	5 510	1.45

^aGiven by the supplier (PEG IrisBiotech).

^bDetermined by ¹H NMR using the relative intensity of protons of PEG and PMLABe blocks.

^cMeasured by size exclusion chromatography (SEC) in THF at 40°C with poly(styrene) standards (1 mL/min, RI detector).

weights are related to polystyrene standards having a different macromolecular structure than the one of PMLA derivatives. However, SEC analysis allows determining the molecular weight distribution (Ip = Mw/Mn) and verifying the obtaining of a block copolymer (only one peak). In our study, SEC chromatograms of both block-copolymers highlighted the presence of only one macromolecular species (only one peak) and a good control of the polymerization reaction, as shown by the quite low polymolecularity of the samples (Ip < 1.5) in light of these results, we were able to obtain well-defined block copolymers suitable to continue the study of NPs' preparation. However, we still have to further characterize the block copolymers, especially to determine their thermal properties (T_g, T_m) by differential scanning calorimetry (DSC), which gives an insight on the copolymer state (rubber or glassy state). Nevertheless, we can have a primary idea of the block copolymer's thermal properties since it should have both the thermal properties of each block, i.e., the ones of PEG (T_g = -20°C, T_m = 50°C) and the ones of PMLABe (T_g = 37°C).

Nanoparticles can be easily and reproducibly prepared from these amphiphilic block copolymers by the nanoprecipitation technique, consisting in a rapid addition of a water miscible solvent, in which the block copolymer was dissolved, to an aqueous solution under vigorous stirring at 20°C (14–16).

For the standard method, acetone was eliminated under vacuum, while for the gel filtration method, empty NPs and ^{185/187}Re-SSS loaded NPs were passed through a PD-10 Sephadex G-25 Medium column. The prepared NPs were analyzed by: (i) DLS, giving access to the average Dh and polydispersity (Đ), (ii) Zetametry, giving access to the surface charge of the NPs, and by (iii) TEM, allowing determining the NPs' morphology.

As shown by results gathered in **Table 2**, both the standard nanoprecipitation method with acetone and the gel filtration method (with DMF) allowed preparing both stealth and targeted NPs with Dh's varying between 65 and 99 nm with a quite small size distribution (Đ lower than 0.15), highlighting the formation of well-defined nano-objects in good agreement with the size of micelle-like NPs (45). On the other hand, the gel filtration method with acetone led to larger NPs with a higher dispersity (Đ around 0.2). However, the values stayed acceptable. The radiolabeling procedure was first tested with the non-radioactive ^{185/187}Re-SSS complex. The preparation of ^{185/187}Re-SSS loaded NPs by the standard nanoprecipitation method with acetone led to the formation of large aggregates with quite large size distribution (data not shown) and was not further used in this study. Therefore, we used the gel filtration method to load the ^{185/187}Re-SSS

TABLE 2 | Characteristics of empty and ^{185/187}Re-SSS loaded PMLABe derivatives-based NPs.

NPs	Hydrodynamic diameter (nm) ^a	Polydispersity index (Đ) ^a	Zeta potential (mV) ^b
PEG₄₂-<i>b</i>-PMLABe₇₃			
Standard nanoprecipitation method with acetone	80	0.06	-6
Gel filtration with acetone	113	0.17	-31
Gel filtration with DMF	99	0.11	-29
Biot-PEG₆₆-<i>b</i>-PMLABe₇₃			
Standard nanoprecipitation method with acetone	65	0.12	-7
Standard radiolabeling method with acetone	80	0.21	-
Gel filtration with acetone	87	0.20	-26
Gel filtration with DMF	68	0.15	-30
PEG₄₂-<i>b</i>-PMLABe₇₃[^{185/187}Re-SSS]			
Gel filtration with acetone	174	0.17	-37
Gel filtration with DMF	104	0.14	-32
Biot-PEG₆₆-<i>b</i>-PMLABe₇₃[^{185/187}Re-SSS]			
Gel filtration with acetone	135	0.18	-25
Gel filtration with DMF	99	0.15	-39

^aMeasured by dynamic light scattering (DLS).

^bMeasured by zetametry.

complex inside the NPs. As shown by results given in **Table 2**, gel filtration with DMF allowed obtaining quite well-defined NPs (low Đ) with a slightly increased Dh, probably as a result of the presence of the complex inside the NPs. On the contrary, with acetone, it led to larger NPs with higher polydispersity indexes. At this stage, we can conclude that gel filtration with DMF seems to lead to the best results in terms of size and size distribution. Stirring the solution for 15 min, instead of 1 h leads to not as good results (Dhs and Đ, respectively, 144 nm vs. 104 and 0.19 vs. 0.14 for ^{185/187}Re-SSS loaded PEG₄₂-*b*-PMLABe₇₃ in DMF), but it is better suited for the encapsulation of technetium-99m, due to radioactive decay considerations, and values are still satisfactory. The NPs prepared by the gel filtration methods (acetone and DMF) loaded or not with the ^{185/187}Re-SSS complex have zeta potentials around -30 mV highlighting a negative surface charge which can be associated with a good stability of the corresponding NPs. Such negative surface charges can be the result of a block copolymer chain conformation allowing the presence of carboxylate end groups of the PMLABe block at the surface of the NPs thus lowering the values of the zeta potential. However, further experiments (static light scattering, Cryo-TEM, etc.) are needed to determine the morphology of the NPs and if any change can be observed in function of the preparation procedure used to obtain the NPs.

In parallel, the selected radioactive complex [^{99m}Tc(PhCS₃)₂(PhCS₂)] (^{99m}Tc-SSS) has been prepared in two steps, starting from the generator-eluted pertechnetate ion, [^{99m}TcO₄]⁻, in 0.9% saline solution (**Figure 2**) (44). ^{99m}Tc-SSS complex was obtained with a RCP over 90%.

After those steps, we had to set up a simple and reproducible way of radiolabeling PEG₄₂-*b*-PMLABe₇₃ or Biot-PEG₆₆-*b*-PMLABe₇₃

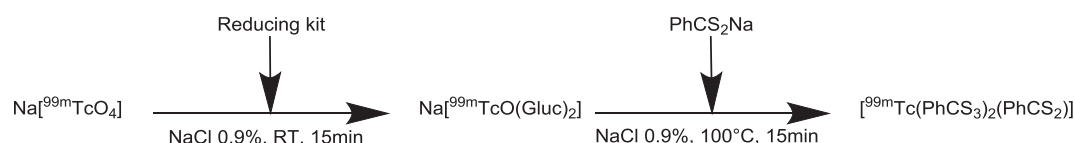


FIGURE 2 | Synthesis of the ^{99m}Tc-SSS radiocomplex.

TABLE 3 | Characteristics of radiolabeled PMLABe derivatives-based NPs.

NPs	Encapsulation efficiency (%) ^a	Hydrodynamic diameter (nm) ^b	Polydispersity index (Đ) ^b	Zeta potential (mV) ^b
PEG₄₂-<i>b</i>-PMLABe₇₃ [^{99m}Tc-SSS]				
Standard nanoprecipitation method with acetone	61	230	0.15	+0.2
Gel filtration with acetone	89	121	0.22	−37
Gel filtration with DMF	86	103	0.16	−38
Biot-PEG₆₆-<i>b</i>-PMLABe₇₃ [^{99m}Tc-SSS]				
Standard nanoprecipitation method with acetone	82	160	0.23	−4.3
Gel filtration with acetone	87	118	0.16	−16
Gel filtration with DMF	89	249	0.22	−25

^aDetermined by radioactivity measurement.

^bMeasured by DLS (Delsa Nano® Beckman Coulter).

based NPs. In a first attempt, we tried to encapsulate the ^{99m}Tc-SSS complex in already formed NPs, previously obtained by the nanoprecipitation technique as described above. However, we were not able to encapsulate the complex inside the preformed NPs because of their destabilization by the reducing agent which is present in the kits used for the complex formation. Consequently, it was necessary to extract the complex in dichloromethane in order to eliminate the kit constituents. Dichloromethane was then evaporated and the radiotracer retaken in a water-miscible organic solvent, then added to the acetone or DMF solution containing PEG₄₂-*b*-PMLABe₇₃ or Biot-PEG₆₆-*b*-PMLABe₇₃ block copolymers.

To determine the encapsulation efficiency, we have measured the NPs' radioactivity. For that, we have eliminated the non-encapsulated complex:

- either by centrifugation in the case of the standard nanoprecipitation using acetone: the supernatant was discarded and the pellet was again suspended in physiological serum. The total radioactivity of the flask before and after centrifugation and the radioactivity of the supernatant were measured. The encapsulation efficiency was given by the ratio between the radioactivity of the flask before centrifugation and the radioactivity of the flask after centrifugation and resuspension of NPs (Table 3). Some trials have been done with ethanol to solubilize ^{99m}Tc-SSS after dichloromethane evaporation, but this solvent is more difficult to evaporate than acetone, so the latter one was preferred.
- or by gel filtration through a PD-10 Sephadex G-25 Medium column. The total radioactivity of the flask before and after Sephadex filtration were measured and allowed to calculate the encapsulation efficiency (ratio between the radioactivity of the flask before and after filtration) (Table 3).

After the radioactivity decay, Dhs, polydispersity indexes, and zeta potentials of the complex-containing NPs were measured by DLS. As shown by results gathered in Table 3, ^{99m}Tc-SSS complex was successfully encapsulated in both PEG₄₂-*b*-PMLABe₇₃ and Biot-PEG₆₆-*b*-PMLABe₇₃ based NPs, using standard nanoprecipitation technique, with an encapsulation efficiency varying between 60 and 80%. Non-PEGylated PMLABe based NPs were also investigated to encapsulate ^{99m}Tc-SSS, but the resulting labeled NPs were not sufficiently stable in time to be studied after radioactivity decay. The radiolabeled NPs, obtained through the standard labeling method, present increased diameters with identical low polydispersity indexes, typically in the 0.15–0.23 range, and neutral zeta potentials in comparison to non-radiolabeled NPs (Table 3). Several reasons can explain the increase of the diameters measured by DLS: (i) a swelling of the inner-core by remaining acetone which is quite difficult to totally eliminate in the experimental conditions of the standard nanoprecipitation procedure used to prepare radiolabeled NPs, (ii) the presence of the radiotracer itself, or (iii) an aggregation of the NPs during the time necessary for radioactivity decay (3 days). Except for the simple PMLABe NPs, the NPs demonstrated good *in vitro* stability, with no size change over time (Table 4). Thus, the increase in size cannot be explained by the delay for the radioactivity to decay before measurements. The results obtained on empty NPs prepared using the same protocol than the one used for the preparation of radiolabeled NPs (standard radiolabeling method), and with NPs encapsulating non-radioactive complex based on “cold” ^{185/187}Re evidenced that the presence of the complex leads to an increase of the NPs' diameters without aggregation (Table 2). However, because the total elimination of acetone is quite difficult with the radioactive complex and centrifugation procedure is not satisfactory, with NPs still present in the supernatant, as evidenced by DLS measurements, thus

TABLE 4 | Over-time stability of PMLABe derivatives-based NPs (measured by DLS).

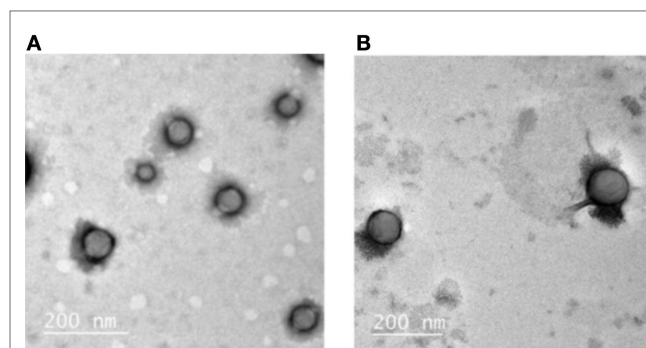
NPs	Hydrodynamic diameter (nm)	Polydispersity index (Đ)
PEG₄₂-b-PMLABe₇₃		
D0 (acetone)	113	0.17
D7 (acetone)	119	0.13
D0 (DMF)	99	0.11
D7 (DMF)	105	0.10
Biot-PEG₆₆-b-PMLABe₇₃		
D0 (acetone)	87	0.20
D7 (acetone)	87	0.19
D0 (DMF)	68	0.15
D7 (DMF)	88	0.15

probably minoring encapsulation yields, we tried to purify the radiolabeled NPs by dialysis. However, such method was time consuming, which is crippling with short half-life radionuclides, and led to no better results than centrifugation, so this method was not pursued.

We therefore used the gel filtration method to prepare radiolabeled NPs. Using this gel filtration procedure, we also observed larger Dh's with slightly higher polydispersity index values compared to empty NPs (Table 3). This increase in diameters is probably the result of the radiotracer encapsulation, because no significant differences were observed in diameter and polydispersity index values between the standard nanoprecipitation procedure and the gel filtration method (Table 2). However, the encapsulation efficiencies seem to be slightly higher when gel filtration method is used either with acetone or DMF, with encapsulation yields between 86 and 89%. Moreover, this procedure is faster and easier to set up than the standard nanoprecipitation method because no centrifugation is necessary, thus avoiding the difficulties to separate the supernatant and the pellet. As observed previously with empty NPs, this method led to NPs with negative zeta potentials despite the PEG chains. As already mentioned, further experiments will be done to understand the reasons for this observed phenomenon which is probably related to the chain conformation adopted by the block copolymer as mentioned above.

Both empty and radiolabeled NPs, after radioactivity decay, were analyzed by TEM in order to have an idea of their morphology (Figure 3).

Indeed, DLS allows only measuring Dh and size distribution without having access to NPs' morphology. As shown by Figure 3, both empty and radiolabeled NPs, prepared with the standard method, have a spherical shape with a diameter in good agreement with the Dh's measured by DLS: around 80 nm for empty NPs and 120 nm for radiolabeled NPs. Moreover, an EDS analysis of the radiolabeled NPs was also realized during the TEM measurements: this technique allows the determination of the elements present in the analyzed sample (46). EDS analysis evidenced the presence of sulfur inside the NPs, reflecting the presence of the ^{99m}Tc-SSS complex which contains sulfur atoms. On the contrary, EDS analysis realized on empty NPs did not highlight any presence of sulfur atoms. Therefore, it tends to

**FIGURE 3 | TEM images of (A) Empty Biot-PEG₆₆-b-PMLABe₇₃ based NPs and (B) Radiolabeled Biot-PEG₆₆-b-PMLABe₇₃ based NPs.**

prove that the ^{99m}Tc-SSS complex is effectively encapsulated inside the NPs constituting by PMLA derivatives. TEM experiments now need to be done on NPs prepared using the alternative gel filtration method to get more insight on the influence of the preparation method on NPs morphology.

Conclusion

Through this study, we highlighted that it is possible to obtain radiolabeled NPs based on PEGylated or biotinylated PEGylated degradable block copolymers with quite high encapsulation efficiency (up to 89%) in an easy and reproducible way. The radiolabeled NPs were characterized by Dh's ranging from 100 to 230 nm with quite low polydispersity indexes (under 0.2) and negative zeta potentials. The morphology of such NPs was shown to be spherical and the presence of sulfur, resulting from ^{99m}Tc-SSS complex, was detected inside the NPs.

We are now moving to ¹⁸⁸Re-SSS encapsulation and *in vitro* assays to confirm the potential of stealth and targeting NPs based on PMLABe derivatives as therapeutic nanovectors. Since our team has been working on DOX's encapsulation and the grafting of a fluorescent probe too, we likewise envision to combine these different approaches as potential theranostic tools of interest for combined chemo-/radiotherapy and/or bimodal imaging probes for instance.

Author Contributions

NL and SC-M designed and supervised the project, participated in the experiments and the analysis and interpretation of data, and wrote the manuscript. LC, MB, CB, CR, and MD made contribution in the design of the work, realized the experiments, and analyzed the results. NN designed and supervised the project and participated in the interpretation of data.

Acknowledgments

Vincent Dorcet and Thomas Vives are gratefully acknowledged for their help for, respectively, TEM and DLS measurements. This work was supported by Labex IRON (Grant no. ANR-11-LABX-0018).

References

- Wicki A, Witzigmann D, Balasubramanian V, Huwyler J. Nanomedicine in cancer therapy: challenges, opportunities, and clinical applications. *J Control Release* (2015) **200**:138–57. doi:10.1016/j.jconrel.2014.12.030
- Reddy LH, Couvreur P. Nanotechnology for therapy and imaging of liver diseases. *J Hepatol* (2011) **55**:1461–6. doi:10.1016/j.jhep.2011.05.039
- Elsaesser A, Howard CV. Toxicology of nanoparticles. *Adv Drug Deliv Rev* (2012) **64**:129–37. doi:10.1016/j.addr.2011.09.001
- Yan Y, Such GK, Johnston APR, Best JP, Caruso F. Engineering particles for therapeutic delivery: prospects and challenges. *ACS Nano* (2012) **6**:3663–9. doi:10.1021/nn3016162
- Malam Y, Loizidou M, Seifalian AM. Liposomes and nanoparticles: nano-sized vehicles for drug delivery in cancer. *Trends Pharmacol Sci* (2009) **30**:592–9. doi:10.1016/j.tips.2009.08.004
- Misra R, Acharya S, Sahoo SK. Cancer nanotechnology: application of nano-technology in cancer therapy. *Drug Discov Today* (2010) **15**:842–50. doi:10.1016/j.drudis.2010.08.006
- Chiellini F, Piras AM, Errico C, Chiellini E. Micro/nanostructured polymeric systems for biomedical and pharmaceutical applications. *Nanomedicine* (2008) **3**:367–93. doi:10.2217/17435889.3.3.367
- Kumari A, Yadav SK, Yadav SC. Biodegradable polymeric nanoparticles based drug delivery systems. *Colloids Surf B Biointerfaces* (2010) **75**:1–18. doi:10.1016/j.colsurfb.2009.09.001
- Piras AM, Chiellini F, Fiumi C, Bartoli C, Chiellini E, Fiorentino B, et al. New biocompatible nanoparticle delivery system for the release of fibrinolytic drugs. *Int J Pharm* (2008) **357**:260–71. doi:10.1016/j.ijpharm.2008.01.035
- Dessy A, Piras AM, Dinucci D, Chiellini F. 2-methoxy aniline grafted poly(maleic anhydride-alt-butyl vinyl ether) hemiester: a NEW biocompatible polymeric free radical scavenger. *Macromolecules* (2011) **44**:848–56. doi:10.1021/ma102309m
- Vert M, Lenz RW. Preparation and properties of poly-β-malic acid: a functional polyester of potential biomedical importance. *Polym Preprints* (1979) **20**:608–11.
- Cammas S, Béar MM, Moine L, Escalup R, Ponchel G, Kataoka K, et al. Polymers of malic acid and 3-alkylmalic acid as synthetical PHAs in the design of biocompatible hydrolyzable devices. *Int J Biol Macromol* (1999) **25**:273–82. doi:10.1016/S0141-8130(99)00042-2
- Cammas-Marion S, Guerin Ph design of malolactonic acid esters with a large spectrum of specified pendant groups in the engineering of biofunctional and hydrolyzable polyesters. *Macromol Symp* (2000) **153**:167–86. doi:10.1002/1521-3900(200003)153:1<167::AID-MASY167>3.0.CO;2-Q
- Huang ZW, Laurent V, Chetouani G, Ljubimova JY, Holler E, Benvegnu T, et al. New functional degradable and bio-compatible nanoparticles based on poly(malic acid) derivatives for site-specific anticancer drug delivery. *Int J Pharm* (2012) **423**:84–92. doi:10.1016/j.ijpharm.2011.04.035
- Loyer P, Bedhouche W, Huang ZW, Cammas-Marion S. Degradable and biocompatible nanoparticles decorated with cyclic RGD peptide for efficient drug delivery to hepatoma cells *in vitro*. *Int J Pharm* (2013) **454**:727–37. doi:10.1016/j.ijpharm.2013.05.060
- Cammas-Marion S, Loyer P. Natural and synthetic poly(malic acid)-based derivatives: a family of versatile biopolymers for the design of drug nanocarriers. *J Drug Target* (2014) **22**:556–75. doi:10.3109/1061186X.2014.936871
- Ting G, Chang CH, Wang HE. Cancer nanotargeted radiopharmaceuticals for tumor imaging and therapy. *Anticancer Res* (2009) **29**:4107–18.
- Muthu MS, Wilson B. Multifunctional radionanomedicine: a novel nano-platform for cancer imaging and therapy. *Nanomedicine* (2010) **5**:169–71. doi:10.2217/nnm.09.107
- Huang WY, Davis JJ. Multimodality and nanoparticles in medical imaging. *Dalton Trans* (2011) **40**:6087–103. doi:10.1039/c0dt01656j
- De Barros ALB, Tsourkas A, Saboury B, Cardoso VN, Alavi A. Emerging role of radiolabeled nanoparticles as an effective diagnostic technique. *EJNMMI Res* (2012) **2**:39–53. doi:10.1186/2191-219X-2-39
- Lee DH, Koo H, Sun IC, Ryu JH, Kim K, Kwon IC. Multifunctional nanoparticles for multimodal imaging and theragnosis. *Chem Soc Rev* (2012) **41**:2656–72. doi:10.1039/C2CS15261D
- Vanpouille-Box C, Hindré F. Nanovectorized radiotherapy: a new strategy to induce anti-tumor immunity. *Front Oncol* (2012) **2**:136. doi:10.3389/fonc.2012.00136
- Guo Y, Aweda T, Black KCL, Liu Y. Chemistry and theranostic applications of radiolabeled nanoparticles for cardiovascular, oncological, and pulmonary research. *Curr Top Med Chem* (2013) **13**:470–8. doi:10.2174/15680266113131040007
- Mitra A, Nan A, Line BR, Ghandehari H. Nanocarriers for nuclear imaging and radiotherapy of cancer. *Curr Pharm Des* (2006) **12**:4729–49. doi:10.2174/138161206779026317
- Peng CL, Shih YH, Lee PC, Mon-Hsian Hsieh T, Luo TY, Shieh MJ. Multimodal image-guided photothermal therapy mediated by ¹⁸⁸Re-labeled micelles containing a cyanine-type photosensitizer. *ACS Nano* (2011) **5**:5594–607. doi:10.1021/nn201100m
- Polyák A, Hajdu I, Bodnár M, Trencsényi G, Pöstényi Z, Haász V, et al. ^{99m}Tc-labelled nanosystem as tumour imaging agent for SPECT and SPECT/CT modalities. *Int J Pharm* (2013) **449**:10–7. doi:10.1016/j.ijpharm.2013.03.049
- Phillips WT, Bao A, Sou K, Li S, Goins B. Radiolabeled liposomes as drug delivery nanotheranostics. In: Li C, Tian M, editors. *Drug Delivery Applications of Noninvasive Imaging: Validation from Biodistribution to Sites of Action*. Hoboken, NJ: John Wiley & Sons, Inc (2013). p. 252–67.
- Allard E, Hindre F, Passirani C, Lemaire L, Lepareur N, Noiret N, et al. ¹⁸⁸Re-loaded lipid nanocapsules as a promising radiopharmaceutical carrier for internal radiotherapy of malignant gliomas. *Eur J Nucl Med Mol Imaging* (2008) **35**:1838–46. doi:10.1007/s00259-008-0735-z
- Kovacs L, Tassano M, Cabrera M, Fernandez M, Porcal W, Anjos RM, et al. Labeling polyamidoamine (PAMAM) dendrimers with technetium-99m via hydrazinonicotinamide (HYNIC). *Curr Radiopharm* (2014) **7**:115–22. doi:10.2174/1874471007666140825121615
- Torres Martin de Rosales R, Tavaré R, Glaria A, Varma G, Protti A, Blower PJ. ^{99m}Tc-bisphosphonate-iron oxide nanoparticle conjugates for dual-modality biomedical imaging. *Bioconjug Chem* (2011) **22**:455–65. doi:10.1021/bc100483k
- Dams ETM, Oyen WJG, Boerman OC, Storm G, Laverman P, Kok PJM, et al. ^{99m}Tc-PEG liposomes for the scintigraphic detection of infection and inflammation: clinical evaluation. *J Nucl Med* (2000) **41**:622–30.
- Pereira MA, Mosqueira VCF, Carmo VA, Ferrari CS, Reis ECO, Ramaldes GA, et al. Biodistribution study and identification of inflammatory sites using nanocapsules labeled with ^{99m}Tc-HMPAO. *Nucl Med Commun* (2009) **30**:749–55. doi:10.1097/MNM.0b013e32832f2b59
- Torres Miranda Sa L, de Souza Albernaz M, Ferreira de Carvalho Patricio B, Villela Falcão Junior M, Feliciano Coelho B, Bordim A, et al. Biodistribution of nanoparticles: initial considerations. *J Pharm Biomed Anal* (2012) **70**:602–4. doi:10.1016/j.jpba.2012.06.008
- Iyer AK, He J, Amiji MM. Image-guided nanosystems for targeted delivery in cancer therapy. *Curr Med Chem* (2012) **19**:3230–40. doi:10.2174/092986712800784685
- Snehalatha M, Kolachina V, Saha RN, Babbar AK, Sharma N, Sharma RK. Enhanced tumor uptake, biodistribution and pharmacokinetics of etoposide loaded nanoparticles in Dalton's lymphoma tumor bearing mice. *J Pharm Bioallied Sci* (2013) **5**:290–7. doi:10.4103/0975-7406.120081
- Vanpouille-Box C, Lacoeuille F, Belloche C, Lepareur N, Lemaire L, Le Jeune JJ, et al. Tumor eradication in rat glioma and bypass of immunosuppressive barriers using internal radiation with ¹⁸⁸Re-lipid nanocapsules. *Biomaterials* (2011) **32**:6781–90. doi:10.1016/j.biomaterials.2011.05.067
- Douglas SJ, Davis SS. Radiolabelling of poly(butyl 2-cyanoacrylate) nanoparticles with a technetium-99m-dextran complex. *J Labelled Comp Radiopharm* (1986) **23**:495–504. doi:10.1002/jlcr.2580230506
- Lambert B, de Klerk JMH. Clinical applications of ¹⁸⁸Re-labelled radiopharmaceuticals for radionuclide therapy. *Nucl Med Commun* (2006) **27**:223–9. doi:10.1097/00006231-200603000-00004

39. Pillai MRA, Dash A, Knapp FF Jr. Rhenium-188: availability from the ¹⁸⁸W/¹⁸⁸Re generator and status of current applications. *Curr Radiopharm* (2012) 5:228–43. doi:10.2174/1874471011205030228
40. Lepareur N, Mévellec F, Noiret N, Refosco F, Tisato F, Porchia M, et al. Syntheses and reactivity of « sulphur rich » Re(III) and Tc(III) complexes containing trithioperoxybenzoate, dithiobenzoate and dithiocarbamate ligands. *Dalton Trans* (2005) 17:2866–75. doi:10.1039/b503938j
41. Heeg MJ, Jurisson SS. The role of inorganic chemistry in the development of radiometal agents for cancer therapy. *Acc Chem Res* (1999) 32:1053–60. doi:10.1021/ar980002c
42. Ballot S, Noiret N, Hindré F, Denizot B, Garin E, Rajerison H, et al. ^{99m}Tc/¹⁸⁸Re-labelled lipid nanocapsules as promising radiotracers for imaging and therapy: formulation and biodistribution. *Eur J Nucl Med Mol Imaging* (2006) 33:602–7. doi:10.1007/s00259-005-0007-0
43. Cammas S, Renard I, Langlois V, Guérin Ph Poly(β-malic acid): obtaining of high molecular weights by improvement of the synthesis route. *Polymer* (1996) 37(18):4215–20. doi:10.1016/0032-3861(96)00204-2
44. Garin E, Noiret N, Malbert CH, Lepareur N, Roucoux A, Dazord L, et al. Development of ^{99m}Tc labelled Lipiodol: biodistribution following injection into the hepatic artery of the healthy pig. *Nucl Med Commun* (2004) 25:291–8. doi:10.1097/00006231-200403000-00013
45. Yokoyama M, Kwon GS, Okano T, Sakurai Y, Seto T, Kataoka K. Preparation of micelle-forming polymer-drug conjugates. *Bioconjugate Chem* (1992) 3:295–301. doi:10.1021/bc00016a007
46. Keil K, Fitzgerald R, Heinrich KF. Celebrating 40 years of energy dispersive X-ray spectrometry in electron probe microanalysis: a historic and nostalgic look back into the beginnings. *Microsc Microanal* (2009) 15:476–83. doi:10.1017/S1431927609990377

Conflict of Interest Statement: The authors declare that the research was conducted in the absence of any commercial or financial relationships that could be construed as a potential conflict of interest.

Copyright © 2015 Lepareur, Leal E Costa, Bocqué, Blondelle, Ruello, Desjulets, Noiret and Cammas-Marion. This is an open-access article distributed under the terms of the Creative Commons Attribution License (CC BY). The use, distribution or reproduction in other forums is permitted, provided the original author(s) or licensor are credited and that the original publication in this journal is cited, in accordance with accepted academic practice. No use, distribution or reproduction is permitted which does not comply with these terms.



Alpha particles induce autophagy in multiple myeloma cells

Jean-Baptiste Gorin^{1,2,3}, Sébastien Gouard^{1,2,3}, Jérémie Ménager^{1,2,3}, Alfred Morgenstern⁴, Frank Bruchertseifer⁴, Alain Faivre-Chauvet^{1,2,3,5}, Yannick Guilloux^{1,2,3}, Michel Chérel^{1,2,3,6}, François Davodeau^{1,2,3} and Joëlle Gaschet^{1,2,3*}

¹ CRCNA – UMR 892 INSERM, Nantes, France, ² 6299 CNRS, Nantes, France, ³ Université de Nantes, Nantes, France, ⁴ Institute for Transuranium Elements, Karlsruhe, Germany, ⁵ Nuclear Medicine Department, CHU Nantes, Nantes, France, ⁶ Institut de Cancérologie de l'Ouest, Saint-Herblain, France

OPEN ACCESS

Edited by:

Anil Kumar Mishra,
Institute of Nuclear Medicine, India

Reviewed by:

Puja Panwar Hazari,
Institute of Nuclear Medicine and
Allied Sciences, India
Maria Mathew D'Souza,
Institute of Nuclear Medicine and
Allied Sciences, India
Baljinder Singh,
Postgraduate Institute of Medical
Education and Research, India

*Correspondence:

Joëlle Marcelle Gaschet
joelle.gaschet@univ-nantes.fr

Specialty section:

This article was submitted to Nuclear
Medicine, a section of the journal
Frontiers in Medicine

Received: 30 July 2015

Accepted: 02 October 2015

Published: 19 October 2015

Citation:

Gorin J-B, Gouard S, Ménager J,
Morgenstern A, Bruchertseifer F,
Faivre-Chauvet A, Guilloux Y,
Chérel M, Davodeau F and Gaschet J
(2015) Alpha particles induce
autophagy in multiple myeloma cells.
Front. Med. 2:74.
doi: 10.3389/fmed.2015.00074

Objectives: Radiation emitted by the radionuclides in radioimmunotherapy (RIT) approaches induce direct killing of the targeted cells as well as indirect killing through the bystander effect. Our research group is dedicated to the development of α -RIT, i.e., RIT using α -particles especially for the treatment of multiple myeloma (MM). γ -irradiation and β -irradiation have been shown to trigger apoptosis in tumor cells. Cell death mode induced by ^{213}Bi α -irradiation appears more controversial. We therefore decided to investigate the effects of ^{213}Bi on MM cell radiobiology, notably cell death mechanisms as well as tumor cell immunogenicity after irradiation.

Methods: Murine 5T33 and human LP-1 MM cell lines were used to study the effects of such α -particles. We first examined the effects of ^{213}Bi on proliferation rate, double-strand DNA breaks, cell cycle, and cell death. Then, we investigated autophagy after ^{213}Bi irradiation. Finally, a coculture of dendritic cells (DCs) with irradiated tumor cells or their culture media was performed to test whether it would induce DC activation.

Results: We showed that ^{213}Bi induces DNA double-strand breaks, cell cycle arrest, and autophagy in both cell lines, but we detected only slight levels of early apoptosis within the 120 h following irradiation in 5T33 and LP-1. Inhibition of autophagy prevented ^{213}Bi -induced inhibition of proliferation in LP-1 suggesting that this mechanism is involved in cell death after irradiation. We then assessed the immunogenicity of irradiated cells and found that irradiated LP-1 can activate DC through the secretion of soluble factor(s); however, no increase in membrane or extracellular expression of danger-associated molecular patterns was observed after irradiation.

Conclusion: This study demonstrates that ^{213}Bi induces mainly necrosis in MM cells, low levels of apoptosis, and autophagy that might be involved in tumor cell death.

Keywords: bismuth-213, multiple myeloma, radiobiology, autophagy, immunogenicity, ionizing radiation

INTRODUCTION

Ionizing radiation (IR) is widely used in the treatment of cancer. External beam radiation therapy (EBRT) using X- or γ -rays is a primary treatment for a wide range of localized cancer, brachytherapy is commonly used as an effective treatment for cervical, prostate, breast, and skin cancer, and radioimmunotherapy (RIT) using β -emitters has proved its efficacy for the treatment of refractory non-Hodgkin lymphoma (1, 2).

New trials are now assessing the efficacy of α -particle emitters in non-targeted or targeted therapies against hematological or solid cancers (3). Indeed, the physical and biological characteristics of those radioisotopes make them attractive candidates for the treatment of disseminated or residual cancers. α -particles exhibit a high linear energy transfer (LET) (~ 100 keV/ μ m) with a short range of 50–90 μ m into the tissues combined with a high energy of 5–9 MeV. In addition, energy deposition along their path follows a Bragg peak, resulting in an increased LET at the end of the track and therefore an increased cytotoxicity. Like other high LET particles, α -emitters induce complex clusters of DNA damages including DNA double-strand breaks (DSBs) which lead to a cell cycle arrest that is more marked than with γ -rays (4). Cell nucleus traversal with one to three α -particles is sufficient to cause tumor cell death when 1000–5000 β -emitters would be required (5). Furthermore, radiobiological effects associated with α -radionuclides are largely independent of dose rate, oxygenation, and cell proliferation (6). A few studies have investigated the cell death mechanisms *in vitro* and *ex vivo* after α -irradiation and led to contrasting results. Some groups showed that cells undergo apoptosis following exposure to ^{213}Bi (7–9) while others observed cell death independent of apoptosis (10–12), therefore reinforcing the need for further investigation of such mechanisms.

Diverse α -emitters have been used in the clinic so far, displaying short half-lives, like ^{213}Bi , ^{211}At , and ^{212}Pb as well as long-lived like ^{223}Ra and ^{225}Ac (3). Our group has done several *in vitro* and preclinical studies on multiple myeloma (MM) (12–16) using ^{213}Bi produced by $^{225}\text{Ac}/^{213}\text{Bi}$ radionuclide generators. Therefore, we thought to further investigate the impact of this α -emitter on the radiobiology of MM cells, especially cell death mechanisms.

Moreover, experiments using EBRT have shown that in addition to direct tumor cell killing, IR can generate specific immune responses directed against tumor cells. Besides creating a local inflammatory context, it has been demonstrated that irradiation can induce immunogenic cell death (ICD) of cancer cells along with the release of danger-associated molecular patterns (DAMPs) (17, 18). Inflammation, ICD, and DAMPs promote the recruitment of immune cells to the tumor site, such as dendritic cells (DCs), which can internalize dying tumor cells. Then cross-presentation of tumor antigens by activated DCs primes antitumor T-cell response (19). Recently, we and others have shown that α -particle emitters ^{213}Bi or ^{224}Ra can induce similar ICD of tumor cells (20–22) in combination with Hsp70 and HMGB-1 release, leading to efficient T-cell-dependent antitumor response (20, 21).

The aim of this study was to investigate the radiobiological effects, in particular cell death mechanisms, of ^{213}Bi on MM

cells and to assess if irradiation of these tumor cells can lead to immune cell activation. Murine 5T33 and human LP-1 MM cell lines were used; we showed that ^{213}Bi induces inhibition of proliferation, DSBs, cell cycle arrest, and autophagy in both cell lines. Inhibition of autophagy prevented ^{213}Bi -induced inhibition of proliferation in LP-1, suggesting that autophagy is one of the tumor cell death mechanisms after α -irradiation. We then evaluated the immunogenicity of irradiated cells and found that irradiated LP-1 can activate DCs through the secretion of soluble factor(s).

MATERIALS AND METHODS

Cell Culture, ^{213}Bi -Irradiation, and Pharmacological Treatment

5T33 (provided by Dr. Radl, TNO Institute, Leiden, Netherlands) and LP-1 cells (DSMZ: ACC 41) were maintained in RPMI 1640 (Gibco) supplemented with 10% FCS, 2 mM glutamine (Gibco), 100 U/mL penicillin, and 100 μ g/mL streptomycin (Gibco) at 37°C and 5% CO_2 .

At least 2 h prior to irradiation, the cells were plated at 8×10^5 cells/mL in fresh culture medium. A solution containing ^{213}Bi diluted in culture medium was then added to the cells. Thus, a final concentration of 4×10^5 cells/mL was obtained in the presence of the desired activity of ^{213}Bi .

For autophagy inhibition, cells were treated with 1.25 mM 3-methyladenine (3-MA) (Sigma).

Preparation of ^{213}Bi -BSA

Cyclohexyl diethylene triamine penta-acetic acid (CHX-A"-DTPA; Macrocylics) was conjugated to BSA (Sigma) and controlled by indium labeling. For labeling with ^{213}Bi , conjugated BSA was incubated with ^{213}Bi eluted from a $^{225}\text{Ac}/^{213}\text{Bi}$ generator (Institute for Transuranium Elements, Karlsruhe, Germany) for 10 min at 37°C in 0.4 M ammonium acetate (pH, 5.3). The resulting ^{213}Bi -BSA conjugate was purified from unbound ^{213}Bi by size exclusion chromatography using a PD-10 column (GE Healthcare).

^3H -Thymidine Incorporation Assay

Approximately 16 h after ^{213}Bi -irradiation, cells were plated in quadruplicates at 4×10^5 cells/mL in 100 μ L in 96-well flat-bottom microtiter plates and incubated at 37°C. Forty-two hours after irradiation, 10 μ L of ^3H -thymidine (925 kBq/mL; Perkin Elmer) was added to each well and incubated at 37°C. Six hours later (i.e., 48 h after irradiation), cells were harvested (Harvester 96–Tomtec) on glass fiber Filtermat A (Perkin Elmer). Radioactive emission was amplified with Betaplate Scint (Perkin Elmer) and read using 1450 Microbeta Plus counter (Wallac). Results are expressed as quadruplicate mean \pm SD.

Colony-Forming Assay

Sixteen hours after irradiation, cells were plated in 96-well U-bottom microtiter plates at densities of 30, 10, 1, and 0.3 cells per well and cultured 2–3 weeks at 37°C, 5% CO_2 . Growth frequency was then calculated using Poisson distribution.

γ H2AX Staining

5T33 and LP-1 cells were fixed with 2% PFA (EMS, Washington, PA, USA) and permeabilized with methanol in PBS–0.5% BSA. γ H2AX staining was performed with PE- γ H2AX antibody (BD Pharmingen) for 1 h at 4°C. After two washes with PBS–0.5% BSA and once with PBS, analysis of at least 10,000 events was performed using a BD FACScalibur flow cytometer and FlowJo software.

Cell Cycle Analysis

Cells were harvested, centrifuged, and resuspended in 200 μ L PBS. LP-1 and 5T33 were fixed by adding 1 mL of cold ethanol or methanol, respectively, for at least 10 min at 4°C. Cells were then stained with propidium iodide as described previously (13) and at least 10,000 events were analyzed using a BD FACScalibur flow cytometer and FlowJo software.

Annexin V and 7-AAD Staining

Staining was performed according to manufacturer's instructions (BD Annexin V-PE Apoptosis detection kit). Briefly, 10^5 cells were stained with 5 μ L Annexin V-PE and/or 7-AAD for 15 min at room temperature in the dark. At least 10,000 events were analyzed using BD FACScalibur flow cytometer and FlowJo software.

Western Blotting

Cells were lysed in 1% Triton X-100 lysis buffer containing protease inhibitors (5 μ g/mL aprotinin, 5 μ g/mL leupeptin, and 4 mM Pefablock®) for 15 min on ice. Cell debris were pelleted at $11,000 \times g$ for 20 min at 4°C, and protein concentrations were determined by BCA reagent (Interchim). Proteins were separated by SDS-PAGE in a 15% acrylamide gel and transferred onto PVDF membranes. Blots were incubated 1 h in blocking buffer (TBS, 0.1% Tween 20, and 5% milk) before incubation for 2 h with primary antibodies either rabbit anti-LC3B antibody (1 μ g/mL; Sigma) that recognizes both LC3B-I and LC3B-II forms or goat anti-actin (C-11, 50 ng/mL; Santa Cruz, CA, USA). Blots were then incubated 1 h with the appropriate HRP-conjugated secondary antibody and processed to detect electrochemiluminescence (Roche). The signal was acquired with the Fusion FX7 camera and its intensity determined using Bio-1D software (Vilber Lourmat).

Transmission Electron Microscopy

Non-irradiated and ^{213}Bi -irradiated 5T33 and LP-1 cells were fixed in cacodylate buffered 4% glutaraldehyde for 15 min at 4°C, washed, and post-fixed in cacodylate buffered 2% osmium tetroxide for 20 min at 4°C. Samples were dehydrated in successive dilutions of ethanol and embedded overnight in Epon at 37°C and for two other days at 55°C. Sections (80 nm thick) were cut with an Ultracut E ultramicrotome (Reichert-Jung), mounted on copper grids, stained with uranyl acetate, and observed on a JEOL 1010 TEM.

DCs Production

Human DCs were obtained by differentiation of human monocytes. Monocytes were purified from PBMCs by counterflow centrifugal elutriation and cultured 5 days in RPMI supplemented

with 2% human albumin, 2 mM glutamine, 100 U/mL penicillin, 100 μ g/mL streptomycin, GM-CSF 1000 IU/mL (CellGro), and IL-4 200 IU/mL (BruCells). Mouse DCs were obtained by differentiation of bone marrow from C57Bl/6 thigh bone as described previously (20).

Coculture Assays

For DC coculture assay with tumor cells, five million ^{213}Bi -treated tumor cells (LP-1 or 5T33) or non-irradiated tumor cells were centrifuged 48 h after irradiation. Tumor cell pellets were resuspended in 1 mL fresh medium and added to one million DCs (human or mouse) in a total volume of 2 mL and plated in six-well dishes. Twenty-four hours after coculture at 37°C, DC maturation was analyzed by immunofluorescence phenotyping.

For DC coculture assay with tumor cell supernatant, 48 h after irradiation, 1 mL of tumor cell supernatant, obtained after centrifugation of five million irradiated or non-irradiated tumor cells (LP-1 or 5T33), was added to one million DCs (human or mouse) in a total volume of 2 mL and plated in 12-well plates.

Immunofluorescence Analysis

Cells were washed once in 0.1% BSA–PBS and then stained for 1 h at 4°C with primary antibody. When secondary antibody was needed, cells were washed three times in 0.1% BSA–PBS before incubation with secondary antibody. After staining, cells were washed twice in 0.1% BSA–PBS and once in PBS before acquisition in flow cytometer. The following antibodies and their respective control isotypes were used in this study: PE anti-human CD80 (L307.4; BD), APC anti-human CD83 (HB15e; BD), APC anti-human CD86 (2331 FUN-1; BD), and PE anti-HLA-DR (G46.6; BD). All immunofluorescence analyses were performed using a FACScalibur flow cytometer (BD Pharmingen) and analyzed with FlowJo software.

RESULTS

^{213}Bi Irradiation Hampers Cell Proliferation

5T33 cells and LP-1 cells were irradiated with increasing activities of ^{213}Bi and their proliferation rate was assessed 48 h later by ^3H -thymidine incorporation assay. Results show a dose-dependent inhibition of ^3H -thymidine incorporation attesting of a diminution of DNA synthesis and as a result a diminution of their proliferation ability (Figure 1). ^{213}Bi activities sufficient to cause at least 80% inhibition of proliferation for each cell line were then used for the rest of the study, respectively, 370 kBq/mL for 5T33 and 425 kBq/mL for LP-1. Such activities ensure a strong biological effect but remain low enough that the cells are not sterilized by irradiation.

Inhibition of Proliferation is Correlated with Tumor Cell Death

In order to determine to what extent the inhibition of proliferation had an impact on tumor cell survival, we performed colony-forming assays. This approach consists in seeding irradiated and non-irradiated cells in clonal conditions to measure the impact

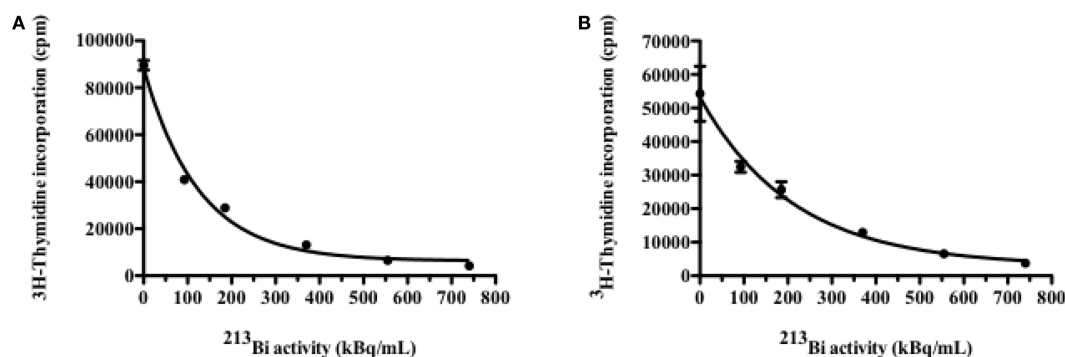


FIGURE 1 | Inhibition of cell proliferation by ^{213}Bi irradiation. Proliferation of irradiated 5T33 (A) and LP-1 (B) cells assessed 48 h after irradiation by incorporation of ^3H -thymidine. Data are expressed as quadruplicate mean \pm SD and are representative of two independent experiments.

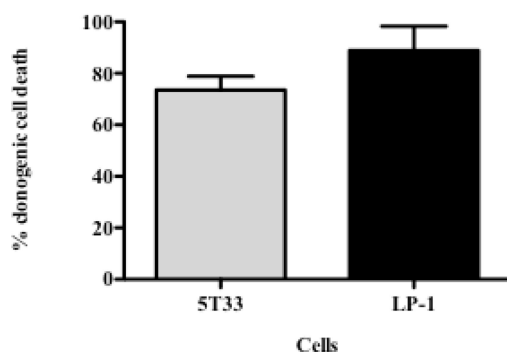


FIGURE 2 | Clonogenic death of 5T33 and LP-1 cells after ^{213}Bi irradiation. Cell death of ^{213}Bi -irradiated 5T33 (370 kBq/mL) and LP-1 (425 kBq/mL) was calculated as defined in Table 1. Data represent mean \pm SD of three independent experiments.

TABLE 1 | Colony-forming assay of 5T33 and LP-1 cells after ^{213}Bi irradiation.

Cells	Condition	Growth efficiency (%)	Survival (%)	Death (%)
5T33	Control	22.4 \pm 6.0	100	0
	370 kBq/mL	5.8 \pm 1.8	26.5 \pm 4.6	73.5 \pm 4.6
LP-1	Control	40.2 \pm 31.6	100	0
	425 kBq/mL	6.4 \pm 6.7	11.2 \pm 7.1	88.8 \pm 7.1

Colony-forming assays were performed 16 h after irradiation with non-irradiated or ^{213}Bi -irradiated 5T33 (370 kBq/mL) and LP-1 (425 kBq/mL) cells to determine growth using Poisson distribution. Data represent mean \pm SD of three independent experiments.

of ^{213}Bi irradiation on cell growth efficiency. We observed that clonogenic cell death after irradiation reached $73.5 \pm 4.6\%$ for 5T33 cells treated at 370 kBq/mL and $88.8 \pm 7\%$ for LP-1 treated at 425 kBq/mL (Figure 2; Table 1). This confirmed that blockade of 5T33 and LP-1 cell proliferation is indeed correlated to the same extent to tumor cell death induced on the long term after ^{213}Bi treatment.

^{213}Bi Induces DNA DSBs in MM Cells

Induction of DSBs in 5T33 and LP-1 cells was investigated after ^{213}Bi irradiation at 370 kBq/mL or 425 kBq/mL, respectively (Figure 3). Irradiation appeared homogenous since for both cell lines, the entire cell population exhibited γH2AX staining (Figure 3). For both cell lines also, DSBs were detectable already 15 min after treatment and their amount increased following the same kinetic over time to reach a maximum at 2 h. Then, phosphorylation of H2AX histone decreased, as observed 3 h after irradiation.

^{213}Bi Blocks Cell Cycle

Cell cycle arrest can arise from DNA damages; therefore, the effect of ^{213}Bi on 5T33 and LP-1 cell cycle at different time points following irradiation was then investigated (Figure 4). Accumulation in the G2/M phase occurred quite rapidly after irradiation in both cell lines. In 5T33 cells (Figure 4A), cell cycle blockade was seen as soon as 6 h after irradiation with 370 kBq/mL of ^{213}Bi and reached a maximum at 24 h with around 45% of the cells in the G2 phase. In LP-1 cells (Figure 4B), cell cycle blockade was slower, being noticeable 24 h after treatment with 425 kBq/mL and reaching a maximum at 36 h with almost 63% of the cells blocked in the G2 phase. These results demonstrate that α -particles cause a blockade at the G2/M checkpoint with a kinetic that varies depending on the cell line.

^{213}Bi Induces Necrosis in MM Cells

Since 5T33 and LP-1 cells experience serious DSBs, are blocked in G2 phase, and stop proliferating after ^{213}Bi irradiation, experiments were conducted to determine the mechanisms that would eventually lead to cell death. Annexin V/7AAD staining was performed on the two MM cell lines at different time points after irradiation to investigate early apoptosis [Annexin V (+) cells] as well as late apoptosis and necrosis [Annexin V (+) 7AAD (+) cells] (Figure 5). Non-irradiated MM cells were studied in parallel. Early apoptosis was barely detectable in any of the cell lines and was not observed immediately after irradiation but to a small extent at later time point, after 36 h for 5T33 and 96 h for

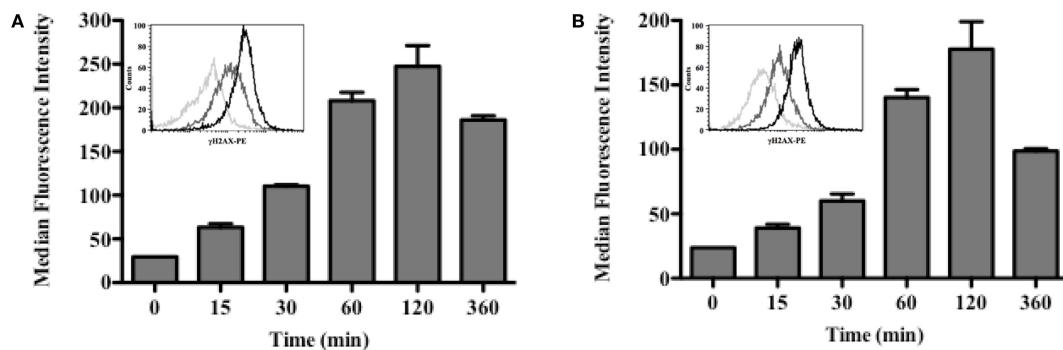


FIGURE 3 | DSBs are induced shortly after irradiation with ^{213}Bi . 5T33 (A) and LP-1 (B) cells were irradiated at 370 and 425 kBq/mL, respectively. DSBs were analyzed at different time points after irradiation by flow cytometry using an anti- γH2AX mAb. Flow cytometry histograms illustrate homogeneous γH2AX staining for both cell lines: 0 min (light gray), 30 min (dark gray), and 120 min (black). Bar graphs represent median \pm SD of two independent experiments.

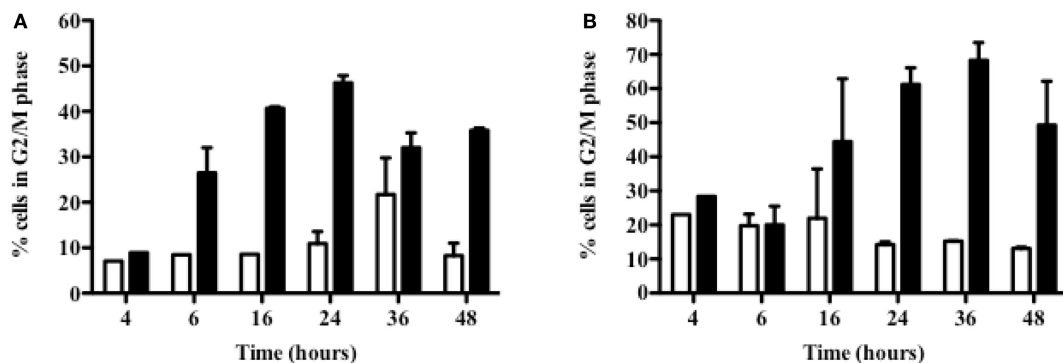


FIGURE 4 | Accumulation in G2 phase of ^{213}Bi -irradiated 5T33 and LP-1 cells. 5T33 (A) and LP-1 (B) cells were irradiated at 370 and 425 kBq/mL, respectively. Then cell cycle analysis was performed at different time points after ^{213}Bi irradiation of the cells (black bars) and compared to control non-irradiated cells (white bars). Data represent mean \pm SD of two independent experiments.

LP-1. These data suggest that cell death occurs mainly through necrosis. This was confirmed by active caspase-3 detection and DNA fragmentation analysis that also showed small levels of early apoptosis (data not shown). In 5T33 cells, necrosis appeared at 36 h and reached a maximum at 96 h after irradiation at 370 kBq/mL of ^{213}Bi . In LP-1, necrosis seems to arise later and is strikingly increased at 96 h after irradiation at 425 kBq/mL. Non-irradiated 5T33 control cells kept dividing actively over the time of the experiment and despite splitting exhibited important cell death as observed after 96 h of culture.

^{213}Bi Induces Autophagy in MM Cells

Autophagy can be induced in cells as a response to a variety of stress factors, including IR-induced oxidative stress, and is characterized by an increased number of autophagosomes that exhibit a lipid bilayer membrane. At the molecular level, when autophagy is activated, the LC3-B protein is converted from the cytosolic LC3B-I form to the LC3B-II form recruited on the autophagosome membrane. Common methods to assess autophagy are Western blot of the LC3-B protein, TEM, and use of autophagy inhibitors.

Western blot assays on irradiated and non-irradiated MM cell lysates were analyzed by standardization of LC3B-II form to actin as mentioned by Mizushima and Yoshimori (23) and showed a strong induction of LC3B-I form conversion to the LC3B-II form after ^{213}Bi irradiation (Figure 6). Accumulation of the LC3B-II form of the LC3B protein was observed in 5T33 cells at 24 h, further increased at 36 h, and remained stable until 72 h after irradiation at 370 kBq/mL. In LP-1 cells, after a transient and early accumulation at 16 h, LC3B-II form decreased before raising again at 48 h and remained stable at 96 h after treatment with 425 kBq/mL of ^{213}Bi . For both cell lines, non-irradiated cells did not exhibit major changes in LC3B-II form accumulation over the time of experiments (Figure 6). Moreover, the presence of autophagosomes in ^{213}Bi -treated 5T33 and LP-1 cells was confirmed by TEM analysis (Figure 7). Altogether, these results demonstrate that α -particles induce autophagy in MM cells.

Autophagy has been described both as a cell survival and cell death mechanism depending on the stimuli, context, and/or cell lines studied. To assess the role of autophagy in our cell lines after irradiation with ^{213}Bi , both proliferation and colony-forming assays

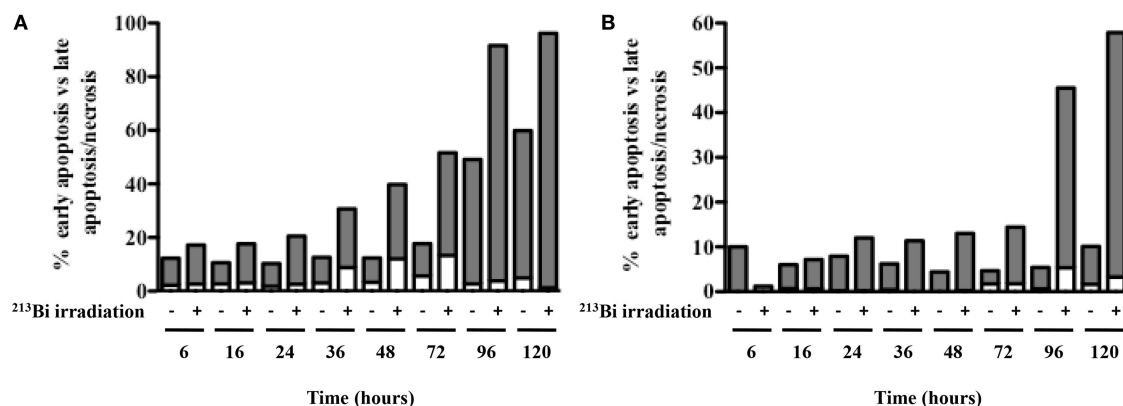


FIGURE 5 | Apoptosis and necrosis in MM cells after ^{213}Bi irradiation. Early apoptosis (white bars) and late apoptosis/necrosis (gray bars) were assessed at different time points after irradiation of 5T33 cells (A) at 370 kBq/mL and LP-1 cells (B) at 425 kBq/mL. Data are representative of two independent experiments.

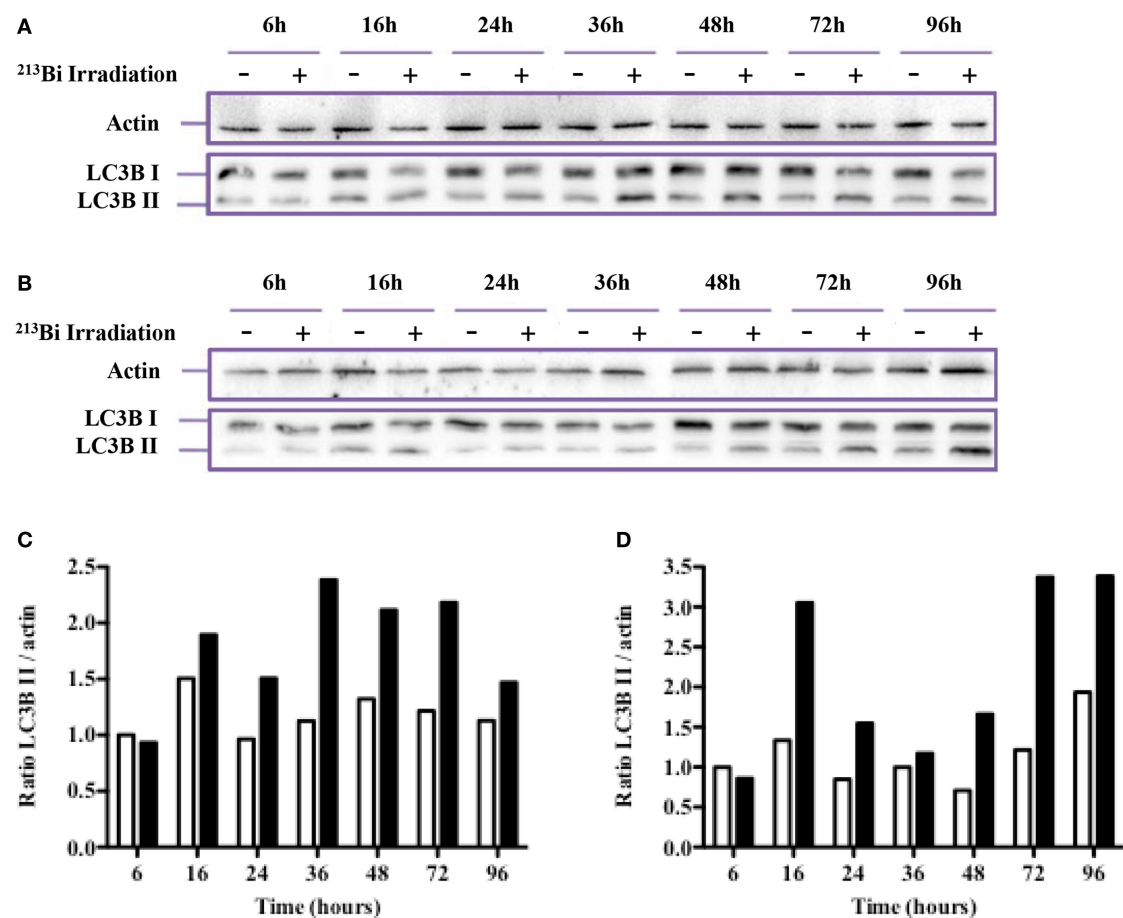


FIGURE 6 | ^{213}Bi irradiation induces autophagy in 5T33 and LP-1 cells. To analyze autophagy, Western blot analysis of LC3B I conversion to the LC3B II form was performed at different time points after irradiation in 5T33 cells (A) at 370 kBq/mL and LP-1 cells (B) at 425 kBq/mL. Densitometry analysis of the blots was performed to determine the LC3B II to actin ratios in control non-irradiated (white bars) and irradiated (black bars) 5T33 (C) and LP-1 (D) cells. Data are representative of three independent experiments.

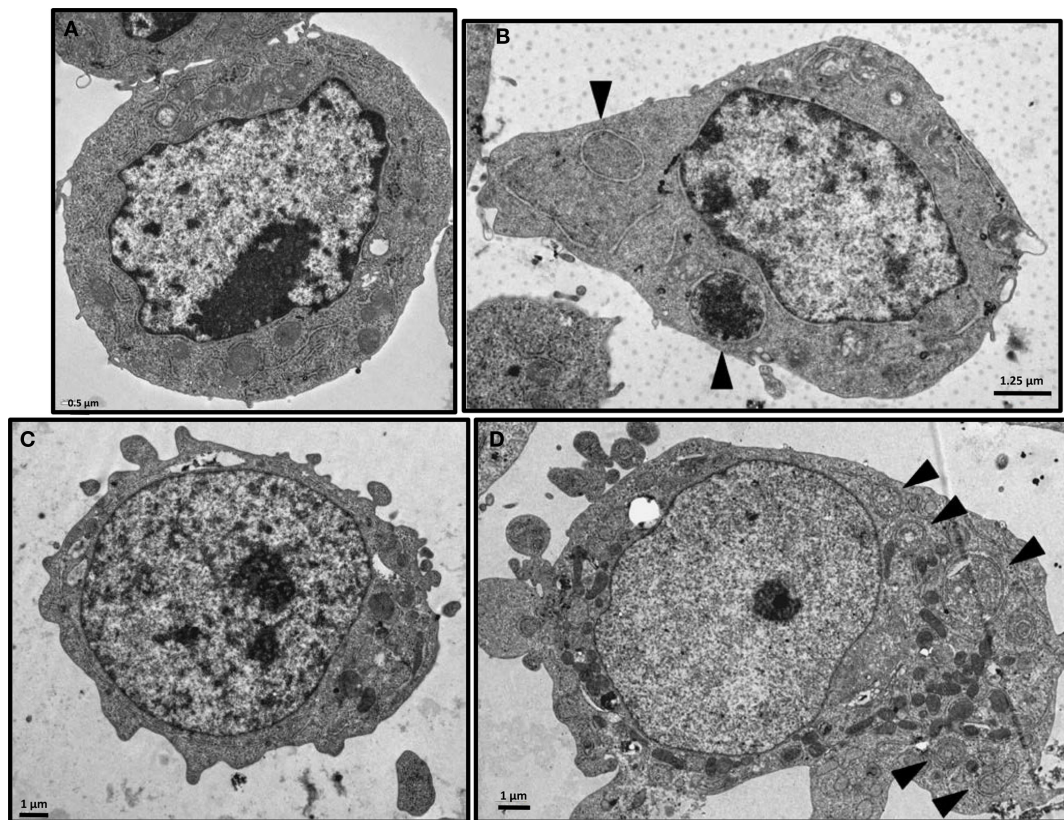


FIGURE 7 | Electron microscopy of ^{213}Bi -treated cells. Analysis was performed on 5T33 cells: untreated (A) or 48 h after irradiation with 370 kBq/mL ^{213}Bi (B) and on LP-1 cells: untreated (C) or 72 h after irradiation with 425 kBq/mL ^{213}Bi (D). Autophagic vacuoles presenting lipid bilayer membrane are indicated by arrows.

were conducted in the presence of an autophagy inhibitor – 3-methyladenine (3-MA) – which inhibits more specifically class III phosphoinositide 3-kinase activity known to be essential for autophagy induction. In 5T33, at 1.25 mM of 3-MA, the proliferation rate after ^{213}Bi treatment with or without inhibition of autophagy was quite similar (data not shown). However, for LP-1 cells, when autophagy was blocked by 3-MA, the proliferation rate after irradiation was affected. As shown in **Figure 8A**, the amount of 3-MA used in that experiment had no major effect on proliferation of non-irradiated LP-1 cells. As shown previously, treatment of LP-1 cells at 425 kBq/mL with ^{213}Bi induced around 90% decrease in proliferation rate. Then, when LP-1 cells were irradiated with ^{213}Bi in the presence of 3-MA, the cells appeared protected from irradiation and kept proliferating at least for 72 h. These results raise the hypothesis that autophagy is involved, at least in part, as a cell death mechanism after treatment with ^{213}Bi . Nevertheless, when clonogenic colony assays were performed on ^{213}Bi -irradiated LP-1 in the presence of 3-MA, cell death occurred to the same extent with or without autophagic inhibition (**Figure 8B**).

^{213}Bi -Treated Tumor Cells Activate Dendritic Cells

Besides its direct killing of tumor cells, IR has been shown to induce indirect killing via the immune system. To assess the immunogenicity of alpha-irradiated tumor cells, ^{213}Bi -treated

LP-1 (425 kBq/mL) or their culture media have been cultured with human DCs. After 1 day of coculture, the DC expression of activation markers (CD80, CD83, CD86, and HLA-DR) was determined by flow cytometry. The culture media of irradiated LP-1 yielded a strong activation of DCs (**Figure 9**). However, such activation was not observed when DCs were cocultured directly with the irradiated cells alone (without their culture media) (**Figure 9**). Coculture with irradiated tumor cells plus their culture media did not result in further DC activation (data not shown). These data suggest that the factor(s) capable of activating DCs are secreted in the culture media after irradiation with ^{213}Bi . Experiments performed with irradiated 5T33 cells and irradiated 5T33 cell supernatants showed quite similar results on murine DC activation.

To identify the potential factor(s), dosage of common DAMPs was performed on culture media of irradiated 5T33 and LP-1 at 370 kBq/mL or 425 kBq/mL, respectively. No difference in release of HMGB1, Hsp70, or TNF α was observed after irradiation with ^{213}Bi (data not shown). The membrane expression of Hsp70, Hsp90, and calreticulin was also tested by flow cytometry; again, no difference was seen after α -irradiation (data not shown).

DISCUSSION

In this study, we showed that ^{213}Bi irradiation of MM cells induced DSBs followed by a cell cycle arrest in G2/M phase and an increased

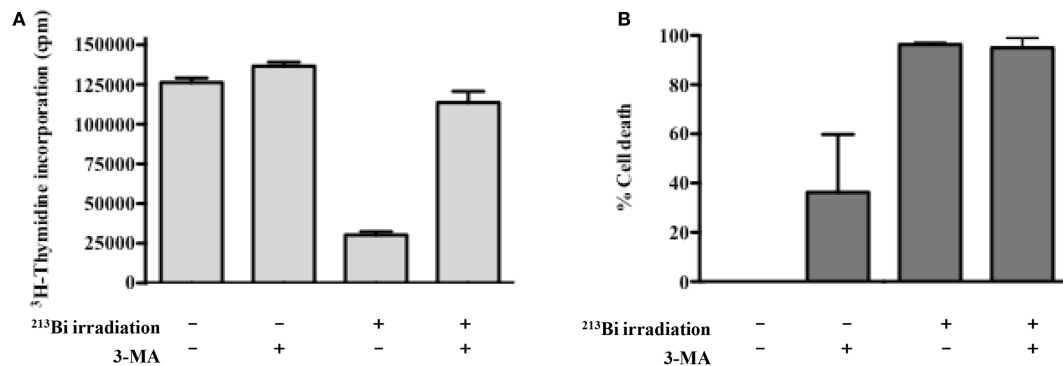


FIGURE 8 | Inhibition of autophagy restores proliferation of LP-1 cells but do not impact clonogenic cell death. (A) Proliferation of irradiated or control LP-1 cells with or without autophagic inhibitor was assessed 72 h after irradiation by incorporation of ^3H -thymidine. **(B)** Clonogenic cell death of untreated LP-1 or after ^{213}Bi irradiation with or without autophagic inhibitor. Data represent mean \pm SEM of two independent experiments.

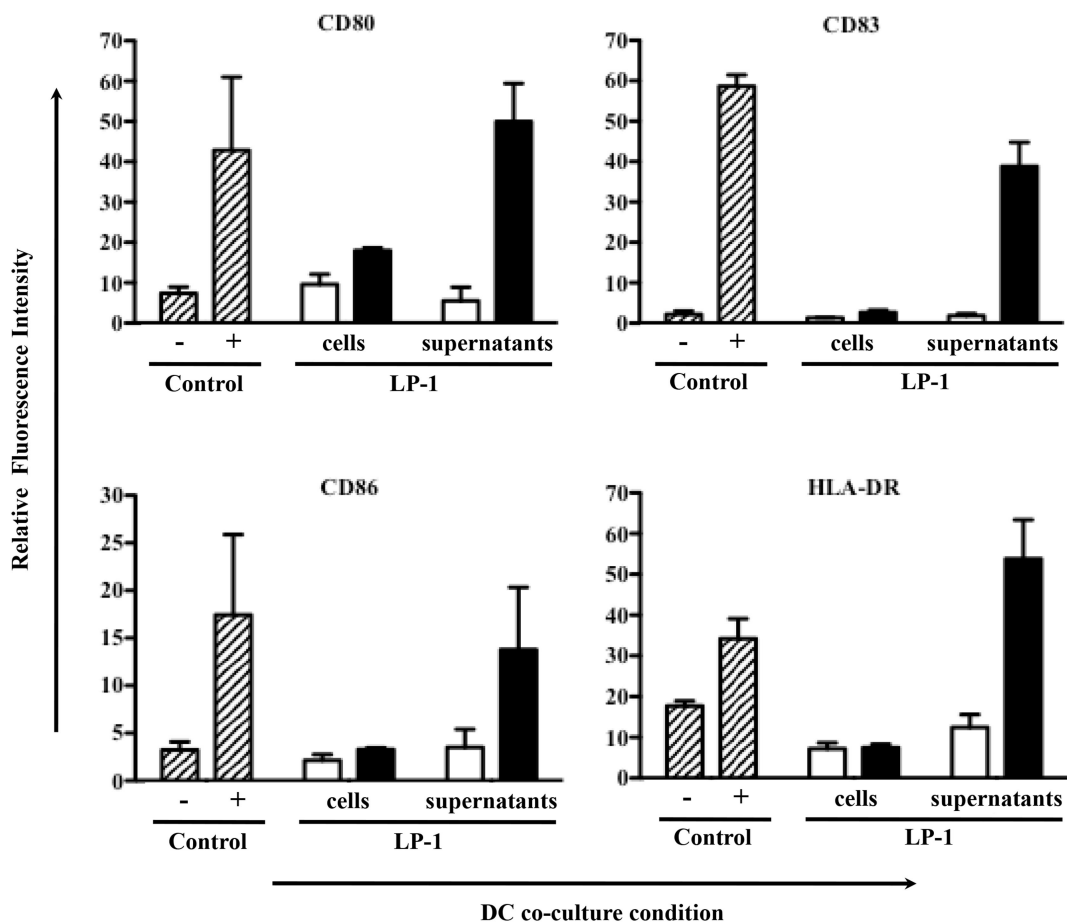


FIGURE 9 | Effect of ^{213}Bi irradiation on immune cells. DC cell activation markers were analyzed 24 h after coculture with ^{213}Bi -treated (black bars) LP-1 cells or LP-1 supernatants as well as untreated (white bars) LP-1 cells or LP-1 supernatants. Control DCs (dashed bars) cocultured alone were used as negative control (-), whereas DCs cocultured with LPS and $\text{TNF}\alpha$ were used as positive control (+). Data represent means of ratio of fluorescence intensity \pm SEM of two independent experiments.

amount of LC3B-II protein, indicating a raise in autophagy. Mechanisms leading to the death of irradiated cells seem to implicate apoptosis, necrosis, and could also involve autophagy.

We used ^{213}Bi -BSA, a non-specific vector in order to perform a homogeneous irradiation of the cells. Irradiation was indeed homogenous as demonstrated by the γH2AX flow cytometry

histograms, since 100% of cells exhibited DSBs with a maximum reached around 2 h after α -irradiation (**Figure 3**). Following induction of DSBs by ^{213}Bi treatment, we observed a cell cycle blockade in the MM cells. IR is known to induce cell cycle arrest in G1 and G2 phase (24). However, cell cycle blockade in G1 is controlled by p53 and is therefore scarce in tumor cells. It has been shown that α -emitters could also induce a G1 arrest in cells that present a functional p53 (25, 26). The fact that neither LP-1 nor 5T33 cells exhibit such blockade in G1 phase indicates that p53 is deficient in these cell lines. *TP53* gene is actually mutated in LP-1 cells and is also hypermethylated compared to normal plasma cells (27). On the other hand, to our knowledge, no study has shown so far that p53 could be mutated or inactivated in the 5T33 cells. Cell cycle arrest in G2/M phase is common in tumor cell lines and has been shown previously by our team and by others on MM cells (9, 13) and on different types of cancer cell lines (4, 11). This G2/M arrest sensitizes the cells to a second irradiation cycle. Even though they are less dependent than X-rays or γ -radiation, α -particle emitters are not completely insensitive to cell cycle distribution. Indeed, it has been demonstrated that α -irradiation of tumor cells was potentiated when cells were pre-treated with chemotherapies that lead to a blockade in G2 phase (12, 28). These data suggest that combining such chemotherapies with α -RIT or repeated injection of α -RIT could enhance RIT treatment.

When we studied the cell death mechanisms resulting from ^{213}Bi irradiation, regardless of the detection method used, we observed only low levels of apoptosis, around 9% and 5% in 5T33 and LP-1, respectively (**Figure 5**). p53 status in LP-1 and 5T33 cell lines cannot be accounted for this result since both cell lines exhibited very high apoptosis during the same time frame when subjected to UV-B radiation (data not shown). A few studies have shown that tumor cells undergo apoptosis following ^{213}Bi irradiation (7–9). These studies used different irradiation protocols, diverse methods to assess cell death, and various tumor cells, which might explain the discrepancy in the results. In particular, Teiluf et al. (9) assessed apoptosis in human MM cells treated *in vitro* with ^{213}Bi -anti-CD38 mAb using Western blot analysis which makes difficult to estimate the percent of cells actually undergoing apoptosis. They observed caspase-3 activation and PARP cleavage 48–96 h after irradiation, which correlates with the time frame where we detected some apoptosis in 5T33 and LP-1 cells (**Figure 5**). Based on their results, we could hypothesize that those cells despite irradiation bypass the G2/M checkpoint to enter mitosis before undergoing apoptosis. This will have to be further studied.

Ionizing radiation induces different cell death mechanisms, including apoptosis, necrosis, necroptosis, mitotic catastrophe, senescence, and autophagic cell death (29–31). We followed cell death over 5 days after ^{213}Bi treatment and we observed in between 55 and 95% mortality (**Figure 5**) while on the long term, clonogenic cell death reached 73.5–88.8% depending on the MM cell line (**Table 1**). Therefore, other cell death mechanisms might be involved later after irradiation, such as mitotic catastrophe that can occur after several cell divisions or cell senescence that would prevent colony formation. Alternatively, preliminary data in our group showed that expression of DRAM, a gene implicated

in autophagy, was increased in T cells after irradiation with ^{211}At and ^{213}Bi (unpublished data). Therefore, we performed Western blot analyses of LC3B-II form, which is correlated with the presence of autophagosomes at different time points after irradiation with ^{213}Bi . Our results show an increase of LC3B-II form after irradiation, and the presence of autophagosomes characterized by a lipidic bilayer membrane was confirmed through TEM. Altogether, these data suggest that α -emitters induce autophagy in MM cells. EBRT is known to induce autophagy (32), and few studies have shown that irradiation with high LET neutrons can also induce such mechanism (33, 34), but to our knowledge, no study so far had investigated the impact of α -particle emitters on autophagy.

The implication of autophagy in cell death has been questioned, being considered either as a programmed cell death mechanism (35, 36) or as a stress response mechanism which can eventually lead to cell death (37, 38). In our study, we observed that the use of autophagy inhibitor 3-MA resulted in protecting LP-1 against ^{213}Bi -induced proliferation inhibition, suggesting that autophagy is involved in tumor sensitization to irradiation and cell death induction. Moreover, it has been already shown that excess autophagy could lead to MM cell death (39, 40). We also observed that when clonogenic colony assays were performed on ^{213}Bi -irradiated LP-1 in the presence of 3-MA, cell death occurred to the same extent than without autophagic inhibition. This suggests that autophagy is involved in cell death after ^{213}Bi irradiation, but when this mechanism is blocked, other cell death pathways are activated, for example, necrosis. However, to reinforce our data, we will have to further depict the exact mechanism of autophagy after ^{213}Bi irradiation, by confirming that 3-MA indeed acts on the amount of autophagosomes, by using other inhibitors like bafilomycin A1 that inhibits the final phase of autophagy, the autophagosome degradation, or siRNA directed against protein involved in the autophagic process, and by studying more MM cell lines. It would also be interesting to investigate how cell death occurs when autophagy is inhibited with 3-MA. In this study, we did not observe any effect of 3-MA on the 5T33 cells after irradiation. We used nevertheless the same inhibitor concentration in both MM cell lines (1.25 nM) even though they do not have the same proliferation rate. Indeed 5T33 cells cycle faster than LP-1 cells with a doubling time around 14 versus 28 h, respectively. This cell cycle difference between the two cell lines was also noticeable in proliferation assays where mean ^3H -thymidine incorporation was around 90,000 cpm for 5T33 at 0 kBq/mL versus around 54,000 cpm for LP-1 (**Figure 1**) as well as in cell cycle assays where G2/M arrest occurred already at 6 h after irradiation in 5T33 and at 24 h in LP-1 (**Figure 4**). Therefore, it would be important to repeat the experiments with increasing amounts of 3-MA to ensure that we use the optimal concentration in 5T33 cells.

The role of autophagy in cancer has also been a subject of debate. Some studies have shown that autophagy contributes to tumor cell radioresistance (41, 42) while others have demonstrated that autophagy participates in tumor cell radiosensitization (43, 44). However, a recent study has shown that if autophagy inhibition radiosensitizes tumor cells *in vitro*, it does

reduce *in vivo* radioresponse highlighting the importance of the autophagic process in immunogenic signaling, especially through the release of ATP (45). Activation of autophagy is mandatory for ATP secretion in the extracellular medium (46) and leads to ICD (47). Extracellular ATP is a very potent chemoattractant for immune cells to ICD sites (48) and promotes DCs differentiation (49), inflammasome activation, and further proinflammatory IL-1 β cytokine secretion (50). In this study, we observed that ^{213}Bi -treated MM cells, especially LP-1 cell line, released a soluble factor capable of activating DCs, suggesting that the tumor cells underwent ICD after α -irradiation. We recently demonstrated that ^{213}Bi was indeed able of inducing ICD in MC-38 cells resulting in Hsp70 and HMGB1 secretion in the extracellular medium and promoting a specific antitumor immune response (20, 21). However, when we looked at potential DAMPs in ^{213}Bi -treated MM cell supernatants, we could not detect any significant release of HMGB1, Hsp70, or TNF α or membrane expression of Hsp70, Hsp90, or calreticulin on irradiated tumor cells. Interestingly, no DC activation was seen when irradiated culture media were subjected to freeze-thaw cycle. This loss of biological activity suggests that the activation factor is unstable but does not provide insights on its molecular nature. Therefore, it would be important to screen other proinflammatory cytokines. Alternatively, based on current literature, it would be interesting to dose ATP or ROS.

In summary, this radiobiology study shows that ^{213}Bi induces DSBs in MM cells, followed by cell proliferation arrest related to cell cycle blockade in G2 phase, finally leading to cell death. We only observed low levels of apoptosis, and necrosis seems to be the major cell death mode induced in MM cells after treatment with ^{213}Bi . In addition, ^{213}Bi irradiation induces autophagy in MM cells, which could be involved in initial

proliferation arrest and cell death. Finally, this study opens new prospects on α -particle action since induction of autophagy in MM tumor cells could be an advantageous feature to activate immune cells.

AUTHOR CONTRIBUTIONS

J-BG, FD, and JG contributed to conception and design. J-BG, SG, JM, AM, FB, AF-C, YG, MC, and JG contributed to development of methodology. J-BG, SG, JM, AM, FB, AF-C, YG, and JG contributed to acquisition of data. J-BG, SG, JM, AM, FB, AF-C, YG, MC, FD, and JG contributed to analysis and interpretation of data. J-BG, SG, JM, AM, FB, AF-C, YG, MC, FD, and JG contributed to writing and review of the manuscript. MC, FD, and JG contributed to study supervision.

ACKNOWLEDGMENTS

We would like to thank Paul Pilet, SC3M Platform, for his help with TEM. We thank the Development and clinical transfer platform (CICBT0503, Nantes) as well as the Cytocell and Radioactivity platforms (SFR François Bonamy, IRS-UN, University of Nantes). We would also like to thank Marie-Hélène Gaugler for critical reading of the manuscript.

FUNDING

This work was supported by grants from La Ligue Contre le Cancer and the Pays de la Loire Council “Nucléaire pour la Santé” (Nucsan). J-BG and JM are supported by MESR grants from the French Ministry of Research and Higher Education. AM and FB are supported by the European Commission.

REFERENCES

- Kaminski MS, Estes J, Zasady KR, Francis IR, Ross CW, Tuck M, et al. Radioimmunotherapy with iodine (131)I tositumomab for relapsed or refractory B-cell non-Hodgkin lymphoma: updated results and long-term follow-up of the University of Michigan experience. *Blood* (2000) **96**:1259–66.
- Witzig TE, Gordon LI, Cabanillas F, Czuczman MS, Emmanouilides C, Joyce R, et al. Randomized controlled trial of yttrium-90-labeled ibritumomab tiuxetan radioimmunotherapy versus rituximab immunotherapy for patients with relapsed or refractory low-grade, follicular, or transformed B-cell non-Hodgkin's lymphoma. *J Clin Oncol* (2002) **20**:2453–63. doi:10.1200/JCO.2002.11.076
- de Kruijff RM, Wolterbeek HT, Denkova AG. A critical review of alpha radionuclide therapy – how to deal with recoiling daughters? *Pharmaceuticals (Basel)* (2015) **8**:321–36. doi:10.3390/ph8020321
- Yong KJ, Milenic DE, Baidoo KE, Brechbiel MW. (212)Pb-radioimmunotherapy induces G(2) cell-cycle arrest and delays DNA damage repair in tumor xenografts in a model for disseminated intraperitoneal disease. *Mol Cancer Ther* (2012) **11**:639–48. doi:10.1158/1535-7163.MCT-11-0671
- Kitson SL, Cuccurullo V, Moody TS, Mansi L. Radionuclide antibody-conjugates, a targeted therapy towards cancer. *Curr Radiopharm* (2013) **6**:57–71. doi:10.2174/1874471011306020001
- Sgouros G, Roeske JC, McDevitt MR, Palm S, Allen BJ, Fisher DR, et al. MIRD Pamphlet No. 22 (abridged): radiobiology and dosimetry of alpha-particle emitters for targeted radionuclide therapy. *J Nucl Med* (2010) **51**:311–28. doi:10.2967/jnumed.108.058651
- Friesen C, Glatting G, Koop B, Schwarz K, Morgenstern A, Apostolidis C, et al. Breaking chemoresistance and radioresistance with [213Bi]anti-CD45 antibodies in leukemia cells. *Cancer Res* (2007) **67**:1950–8. doi:10.1158/0008-5472.CAN-06-3569
- Friesen C, Roscher M, Hormann I, Leib O, Marx S, Moreno J, et al. Anti-CD33-antibodies labelled with the alpha-emitter Bismuth-213 kill CD33-positive acute myeloid leukaemia cells specifically by activation of caspases and break radio- and chemoresistance by inhibition of the anti-apoptotic proteins X-linked inhibitor of apoptosis protein and B-cell lymphoma-extra large. *Eur J Cancer* (2013) **49**:2542–54. doi:10.1016/j.ejca.2013.04.008
- Teiluf K, Seidl C, Bleichert B, Gaertner FC, Gilbertz K-P, Fernandez V, et al. α -Radioimmunotherapy with 213Bi-anti-CD38 immunoconjugates is effective in a mouse model of human multiple myeloma. *Oncotarget* (2015) **6**:4692–703. doi:10.18632/oncotarget.2986
- Seidl C, Schröck H, Seidenschwang S, Beck R, Schmid E, Abend M, et al. Cell death triggered by alpha-emitting 213Bi-immunoconjugates in HSC45-M2 gastric cancer cells is different from apoptotic cell death. *Eur J Nucl Med Mol Imaging* (2005) **32**:274–85. doi:10.1007/s00259-004-1653-3
- Seidl C, Port M, Gilbertz K-P, Morgenstern A, Bruchertseifer F, Schwaiger M, et al. 213Bi-induced death of HSC45-M2 gastric cancer cells is characterized by G2 arrest and up-regulation of genes known to prevent apoptosis but induce necrosis and mitotic catastrophe. *Mol Cancer Ther* (2007) **6**:2346–59. doi:10.1158/1535-7163.MCT-07-0132
- Supiot S, Gouard S, Charrier J, Apostolidis C, Chatal J-F, Barbet J, et al. Mechanisms of cell sensitization to alpha radioimmunotherapy by doxorubicin or paclitaxel in multiple myeloma cell lines. *Clin Cancer Res* (2005) **11**:7047s–52s. doi:10.1158/1078-0432.CCR-1004-0021
- Supiot S, Faivre-Chauvet A, Couturier O, Heymann MF, Robillard N, Kraeber-Bodéré F, et al. Comparison of the biologic effects of MA5 and B-B4

- monoclonal antibody labeled with iodine-131 and bismuth-213 on multiple myeloma. *Cancer* (2002) **94**:1202–9. doi:10.1002/cncr.10286
14. Chérel M, Gouard S, Gaschet J, Sai-Maurel C, Bruchertseifer F, Morgenstern A, et al. 213Bi radioimmunotherapy with an anti-mCD138 monoclonal antibody in a murine model of multiple myeloma. *J Nucl Med* (2013) **54**:1597–604. doi:10.2967/jnumed.112.111997
 15. Gouard S, Pallardy A, Gaschet J, Faivre-Chauvet A, Bruchertseifer F, Morgenstern A, et al. Comparative analysis of multiple myeloma treatment by CD138 antigen targeting with bismuth-213 and Melphalan chemotherapy. *Nucl Med Biol* (2014) **41**(Suppl):e30–5. doi:10.1016/j.nucmedbio.2014.02.008
 16. Ménager J, Gorin J-B, Maurel C, Drujont L, Gouard S, Louvet C, et al. Combining α -radioimmunotherapy and adoptive T cell therapy to potentiate tumor destruction. *PLoS One* (2015) **10**:e0130249. doi:10.1371/journal.pone.0130249
 17. Apetoh L, Ghiringhelli F, Tesniere A, Obeid M, Ortiz C, Criollo A, et al. Toll-like receptor 4-dependent contribution of the immune system to anticancer chemotherapy and radiotherapy. *Nat Med* (2007) **13**:1050–9. doi:10.1038/nm1622
 18. Golden EB, Frances D, Pellicciotti I, Demaria S, Barcellos-Hoff MH, Formenti SC. Radiation fosters dose-dependent and chemotherapy-induced immunogenic cell death. *Oncoimmunology* (2014) **3**:e28518. doi:10.4161/onci.28518
 19. Formenti SC, Demaria S. Combining radiotherapy and cancer immunotherapy: a paradigm shift. *J Natl Cancer Inst* (2013) **105**:256–65. doi:10.1093/jnci/djs629
 20. Gorin J-B, Ménager J, Gouard S, Maurel C, Guilloux Y, Faivre-Chauvet A, et al. Antitumor immunity induced after α irradiation. *Neoplasia* (2014) **16**:319–28. doi:10.1016/j.neo.2014.04.002
 21. Gorin J-B, Guilloux Y, Morgenstern A, Chérel M, Davodeau F, Gaschet J. Using α radiation to boost cancer immunity? *Oncoimmunology* (2014) **3**:e954925. doi:10.4161/21624011.2014.954925
 22. Keisari Y, Hochman I, Confino H, Korenstein R, Kelson I. Activation of local and systemic anti-tumor immune responses by ablation of solid tumors with intratumoral electrochemical or alpha radiation treatments. *Cancer Immunol Immunother* (2014) **63**:1–9. doi:10.1007/s00262-013-1462-2
 23. Mizushima N, Yoshimori T. How to interpret LC3 immunoblotting. *Autophagy* (2007) **3**:542–5. doi:10.4161/auto.4600
 24. Bernhard EJ, Maity A, Muschel RJ, McKenna WG. Effects of ionizing radiation on cell cycle progression. A review. *Radiat Environ Biophys* (1995) **34**:79–83. doi:10.1007/BF01275210
 25. Gadbois DM, Crissman HA, Nastasi A, Habbersett R, Wang SK, Chen D, et al. Alterations in the progression of cells through the cell cycle after exposure to alpha particles or gamma rays. *Radiat Res* (1996) **146**:414–24. doi:10.2307/3579303
 26. Azzam EI, de Toledo SM, Waker AJ, Little JB. High and low fluences of alpha-particles induce a G1 checkpoint in human diploid fibroblasts. *Cancer Res* (2000) **60**:2623–31.
 27. Hurt EM, Thomas SB, Peng B, Farrar WL. Reversal of p53 epigenetic silencing in multiple myeloma permits apoptosis by a p53 activator. *Cancer Biol Ther* (2006) **5**:1154–60. doi:10.4161/cbt.5.9.3001
 28. Vallon M, Seidl C, Blechert B, Li Z, Gilbertz K-P, Baumgart A, et al. Enhanced efficacy of combined 213Bi-DTPA-F3 and paclitaxel therapy of peritoneal carcinomatosis is mediated by enhanced induction of apoptosis and G2/M phase arrest. *Eur J Nucl Med Mol Imaging* (2012) **39**:1886–97. doi:10.1007/s00259-012-2203-z
 29. Eriksson D, Stigbrand T. Radiation-induced cell death mechanisms. *Tumour Biol* (2010) **31**:363–72. doi:10.1007/s13277-010-0042-8
 30. Lauber K, Ernst A, Orth M, Herrmann M, Belka C. Dying cell clearance and its impact on the outcome of tumor radiotherapy. *Front Oncol* (2012) **2**:116. doi:10.3389/fonc.2012.00116
 31. Mirzayans R, Andrais B, Scott A, Wang YW, Murray D. Ionizing radiation-induced responses in human cells with differing TP53 status. *Int J Mol Sci* (2013) **14**:22409–35. doi:10.3390/ijms141122409
 32. Palumbo S, Comincini S. Autophagy and ionizing radiation in tumors: the “survive or not survive” dilemma. *J Cell Physiol* (2013) **228**:1–8. doi:10.1002/jcp.24118
 33. Altmeyer A, Ignat M, Denis J-M, Messaddeq N, Gueulette J, Mutter D, et al. Cell death after high-LET irradiation in orthotopic human hepatocellular carcinoma in vivo. *In vivo* (2011) **25**:1–9.
 34. Jin X, Liu Y, Ye F, Liu X, Furusawa Y, Wu Q, et al. Role of autophagy in high linear energy transfer radiation-induced cytotoxicity to tumor cells. *Cancer Sci* (2014) **105**:770–8. doi:10.1111/cas.12422
 35. Gozuacik D, Kimchi A. Autophagy as a cell death and tumor suppressor mechanism. *Oncogene* (2004) **23**:2891–906. doi:10.1038/sj.onc.1207521
 36. Tsujimoto Y, Shimizu S. Another way to die: autophagic programmed cell death. *Cell Death Differ* (2005) **12**(Suppl 2):1528–34. doi:10.1038/sj.cdd.4401777
 37. Kroemer G, Galluzzi L, Vandenabeele P, Abrams J, Alnemri ES, Baehrecke EH, et al. Classification of cell death: recommendations of the Nomenclature Committee on Cell Death 2009. *Cell Death Differ* (2009) **16**:3–11. doi:10.1038/cdd.2008.150
 38. Galluzzi L, Vitale I, Abrams JM, Alnemri ES, Baehrecke EH, Blagosklonny MV, et al. Molecular definitions of cell death subroutines: recommendations of the Nomenclature Committee on Cell Death 2012. *Cell Death Differ* (2012) **19**:107–20. doi:10.1038/cdd.2011.96
 39. Hoang B, Benavides A, Shi Y, Frost P, Lichtenstein A. Effect of autophagy on multiple myeloma cell viability. *Mol Cancer Ther* (2009) **8**:1974–84. doi:10.1158/1535-7163.MCT-08-1177
 40. Michallet A-S, Mondiere P, Taillardet M, Leverrier Y, Genestier L, Defrance T. Compromising the unfolded protein response induces autophagy-mediated cell death in multiple myeloma cells. *PLoS One* (2011) **6**:e25820. doi:10.1371/journal.pone.0025820
 41. Lomonaco SL, Finniss S, Xiang C, DeCarvalho A, Umansky F, Kalkanis SN, et al. The induction of autophagy by gamma-radiation contributes to the radioresistance of glioma stem cells. *Int J Cancer* (2009) **125**:717–22. doi:10.1002/ijc.24402
 42. Chaachouay H, Ohneseit P, Toulany M, Kehlbach R, Multhoff G, Rodemann HP. Autophagy contributes to resistance of tumor cells to ionizing radiation. *Radiother Oncol* (2011) **99**:287–92. doi:10.1016/j.radonc.2011.06.002
 43. Kim KW, Moretti L, Mitchell LR, Jung DK, Lu B. Combined Bcl-2/mamman target of rapamycin inhibition leads to enhanced radiosensitization via induction of apoptosis and autophagy in non-small cell lung tumor xenograft model. *Clin Cancer Res* (2009) **15**:6096–105. doi:10.1158/1078-0432.CCR-09-0589
 44. Chang S-H, Minaei-Tehrani A, Shin J-Y, Park S, Kim J-E, Yu K-N, et al. Beclin1-induced autophagy abrogates radioresistance of lung cancer cells by suppressing osteopontin. *J Radiat Res* (2012) **53**:422–32. doi:10.1269/jrr.11148
 45. Ko A, Kanehisa A, Martins I, Senovilla L, Chargari C, Dugue D, et al. Autophagy inhibition radiosensitizes in vitro, yet reduces radioresponses in vivo due to deficient immunogenic signalling. *Cell Death Differ* (2013) **21**:92–9. doi:10.1038/cdd.2013.124
 46. Michaud M, Martins I, Sukkurwala AQ, Adjemian S, Ma Y, Pellegatti P, et al. Autophagy-dependent anticancer immune responses induced by chemotherapeutic agents in mice. *Science* (2011) **334**:1573–7. doi:10.1126/science.1208347
 47. Kepp O, Senovilla L, Vitale I, Vacchelli E, Adjemian S, Agostinis P, et al. Consensus guidelines for the detection of immunogenic cell death. *Oncoimmunology* (2014) **3**:e955691. doi:10.4161/21624011.2014.955691
 48. Elliott MR, Chekeni FB, Trampont PC, Lazarowski ER, Kadl A, Walk SF, et al. Nucleotides released by apoptotic cells act as a find-me signal to promote phagocytic clearance. *Nature* (2009) **461**:282–6. doi:10.1038/nature08296
 49. Ma Y, Adjemian S, Mattarollo SR, Yamazaki T, Aymeric L, Yang H, et al. Anticancer chemotherapy-induced intratumoral recruitment and differentiation of antigen-presenting cells. *Immunity* (2013) **38**:729–41. doi:10.1016/j.immuni.2013.03.003
 50. Ghiringhelli F, Apetoh L, Tesniere A, Aymeric L, Ma Y, Ortiz C, et al. Activation of the NLRP3 inflammasome in dendritic cells induces IL-1 β -dependent adaptive immunity against tumors. *Nat Med* (2009) **15**:1170–8. doi:10.1038/nm.2028

Conflict of Interest Statement: The authors declare that the research was conducted in the absence of any commercial or financial relationships that could be construed as a potential conflict of interest.

Copyright © 2015 Gorin, Gouard, Ménager, Morgenstern, Bruchertseifer, Faivre-Chauvet, Guilloux, Chérel, Davodeau and Gaschet. This is an open-access article distributed under the terms of the Creative Commons Attribution License (CC BY). The use, distribution or reproduction in other forums is permitted, provided the original author(s) or licensor are credited and that the original publication in this journal is cited, in accordance with accepted academic practice. No use, distribution or reproduction is permitted which does not comply with these terms.



Improvement of the Targeting of Radiolabeled and Functionalized Liposomes with a Two-Step System Using a Bispecific Monoclonal Antibody (Anti-CEA × Anti-DTPA-In)

Aurore Rauscher^{1,2}, Mathieu Frindel^{1,3}, Holisoa Rajerison¹, Sébastien Gouard¹, Catherine Maurel¹, Jacques Barbet^{1,4}, Alain Faivre-Chauvet^{1,3} and Marie Mougín-Degraef^{1,3*}

¹ Centre de Recherche en Cancérologie Nantes-Angers (CRCNA), 6299 CNRS, UMR 892 – INSERM, Université de Nantes, Nantes, France, ² Nuclear Medicine Department, Institut de Cancérologie de l'Ouest, Saint Herblain, France, ³ Nuclear Medicine Department, University Hospital Nantes, Nantes, France, ⁴ GIP Arronax, Saint Herblain, France

OPEN ACCESS

Edited by:

Helmut Robert Maecke,
University Hospital Freiburg, Germany

Reviewed by:

Roger Schibli,
Paul Scherrer Institute, Switzerland
Robert James Mairs,
University of Glasgow, UK

*Correspondence:

Marie Mougín-Degraef
marie.degraef@univ-nantes.fr

Specialty section:

This article was submitted to
Nuclear Medicine,
a section of the
journal *Frontiers in Medicine*

Received: 09 July 2015

Accepted: 06 November 2015

Published: 25 November 2015

Citation:

Rauscher A, Frindel M, Rajerison H,
Gouard S, Maurel C, Barbet J,
Faivre-Chauvet A and
Mougín-Degraef M (2015)
Improvement of the Targeting of
Radiolabeled and Functionalized
Liposomes with a Two-Step System
Using a Bispecific Monoclonal
Antibody (Anti-CEA × Anti-DTPA-In).
Front. Med. 2:83.
doi: 10.3389/fmed.2015.00083

This study proposes liposomes as a new tool for pretargeted radioimmunotherapy (RIT) in solid tumors. Tumor pretargeting is obtained by using a bispecific monoclonal antibody [BsmAb, anti-CEA × anti-DTPA-indium complex (DTPA-In)] and pegylated radioactive liposomes containing a lipid-hapten conjugate (DSPE-PEG-DTPA-In). In this work, the immunospecificity of tumor targeting is demonstrated both *in vitro* by fluorescence microscopy and *in vivo* by biodistribution studies.

Methods: Carcinoembryonic antigen (CEA)-expressing cells (LS174T) were used either in cell culture or as xenografts in nude mice. Doubly fluorescent liposomes or doubly radiolabeled liposomes were, respectively, used for *in vitro* and *in vivo* studies. In each case, a tracer of the lipid bilayer [rhodamine or indium-111 (¹¹¹In)] and a tracer of the aqueous phase [fluorescein or iodine-125 (¹²⁵I)] were present. The targeting of liposomes was assessed with BsmAb for active targeting or without for passive targeting.

Results: Data obtained with the lipid bilayer tracer showed a fluorescent signal on cell membranes two to three times higher for active than for passive targeting. This immunospecificity was confirmed *in vivo* with tumor uptake of $7.5 \pm 2.4\%$ ID/g (percentage of injected dose per gram of tissue) for active targeting versus $4.5 \pm 0.45\%$ ID/g for passive targeting ($p = 0.03$). Regarding the aqueous phase tracer, results are slightly more contrasted. *In vitro*, the fluorescent tracer seems to be released in the extracellular matrix, which can be correlated with the *in vivo* data. Indeed, the tumor uptake of ¹²⁵I is lower than that of ¹¹¹In: $5.1 \pm 2.5\%$ ID/g for active targeting and $2.7 \pm 0.6\%$ ID/g for passive targeting, but resulted in more favorable tumor/organs ratios.

Conclusion: This work demonstrated the tumor targeting immunospecificity of DSPE-PEG-DTPA-In liposomes by two different methods. This original and new approach suggests the potential of immunospecific targeting liposomes for the RIT of solid tumors.

Keywords: pegylated liposomes, radioimmunotherapy, bispecific antibody, pretargeting, solid tumors

INTRODUCTION

The main purpose of radioimmunotherapy (RIT) is to kill cancer cells by immunospecific targeting radionuclides to specific antigens expressed at their surface. It has been demonstrated to be effective for the treatment of hematologic malignancies using directly radiolabeled antibodies targeting differentiation antigens, particularly in the treatment of malignant B cell lymphomas (1, 2). But despite promising results, RIT is not as successful against solid malignancies, which are usually more radioresistant and less accessible to radiolabeled antibodies (3). Higher absorbed doses are necessary but administered activity is limited by normal organ toxicities (4).

In order to optimize the RIT of solid tumors, multi-step techniques, referred to as pretargeting, have been developed to improve target-to-normal tissues ratios and increase administered activities while limiting healthy organ exposure. One of the pretargeting approaches is the affinity enhancement system (AES), which is based on bispecific monoclonal antibodies (BsmAb) and radiolabeled bivalent haptens (5). This approach has been extensively tested in the clinic and has shown an increase of overall survival of patients with progressive metastatic Medullary Thyroid Carcinoma, which provided the first evidence of survival improvement by RIT in solid tumors (6, 7). Nevertheless, the radiolabeled small molecular bivalent haptens are limited for RIT by the amount of activity they can carry in practice (8). Up to now, the specific activity of developed haptens labeled with available radionuclides does not exceed 100–150 MBq/nmol and even less for radionuclides with a long half-life, which limits the activity delivered to tumor cells. In this context, liposomes, which up to now have been especially developed for drug targeting, can represent a new and original method of radiotherapy of cancers. The development of imaging applications with radioactive liposomes is widely described (9, 10), but their advantages for carrying therapeutic radionuclides for cancer therapy could be further exploited.

This study aims at using immunospecific radiolabeled liposomes for RIT of solid tumors because they offer the possibility to carry high radionuclide activities, by radiolabeling their membrane, the inner aqueous phase or both. The potentially high number of radioactive atoms carried by each liposome should increase the dose delivered to the tumor and the avidity effect expected from the multiplicity of the liposome – target cell connections should increase activity accretion in tumors, as with the AES that uses bivalent haptens to achieve cooperative binding to target cells. Finally, this liposome targeting approach will allow us to obtain an intermediate system between the direct targeting of radiolabeled mAb, which expose normal tissues, especially the red bone marrow, to excessive radiations and cause hematologic toxicities, and pretargeting which improves the tumor to background activity ratios but with a limitation in the activity that haptens can deliver to tumor cells.

In this paper, we aim to target tumors, by a two-step approach, using functionalized liposomes and a BsmAb (hMN14 × 734) that recognizes on one arm the carcinoembryonic antigen (CEA) and on the other the DTPA–indium complex (DTPA–In). We used PEGylated liposomes that have been shown to be capable of

very long circulation after intravenous injection with the hapten (DTPA–In) coupled at the end of the PEG chains (**Figure 1**). Surface plasmon resonance (SPR) was used previously to characterize specific interactions between antibodies and functionalized liposomes in order to select the best formulation in terms of hapten presentation and density of PEG chains (11). The chosen formulation optimizes the antibody-hapten recognition by orienting the haptens away from the PEG structure (apparent dissociation constant $K_D = 6.3 \times 10^{-9} \text{M}$), while keeping a long half-life *in vivo* ($T_{1/2} = 12.5 \text{ h}$). The functionalized liposomes present a large number of hapten molecules at their surface (around 400), favorable pharmacokinetic parameters, and the possibility to be radiolabeled at high specific activities. For that, an original method to label preformed liposomes was previously developed, that could be extended to radionuclides of interest for therapy (iodine-131 or astatine-211). This technique is based on the use of radioiodinated Bolton-Hunter reagent (BH) and liposomes containing high concentration of arginine in order to radiolabel the inner aqueous core with ^{125}I (12). The liposome membrane was also radiolabeled with ^{111}In , using a chelating lipid inserted in the bilayer (DSPE–PEG–DTPA). The DTPA–Indium complex formed is the hapten specifically recognized by the 734 arm of the hMN14 × 734 bispecific antibody.

Then, specific tumor targeting experiments were performed *in vitro*, by fluorescence microscopy, on CEA-expressing cells (LS734T), and *in vivo* in nude mice xenografted with human colorectal adenocarcinoma cells (LS734T) to demonstrate the immunospecificity of pretargeting using functionalized liposomes and a bispecific antibody. Doubly fluorescent liposomes or doubly radiolabeled liposomes were, respectively, used for *in vitro* and *in vivo* studies. The double radiolabeling, with a tracer of the lipid bilayer (rhodamine or ^{111}In) and a tracer of the aqueous phase

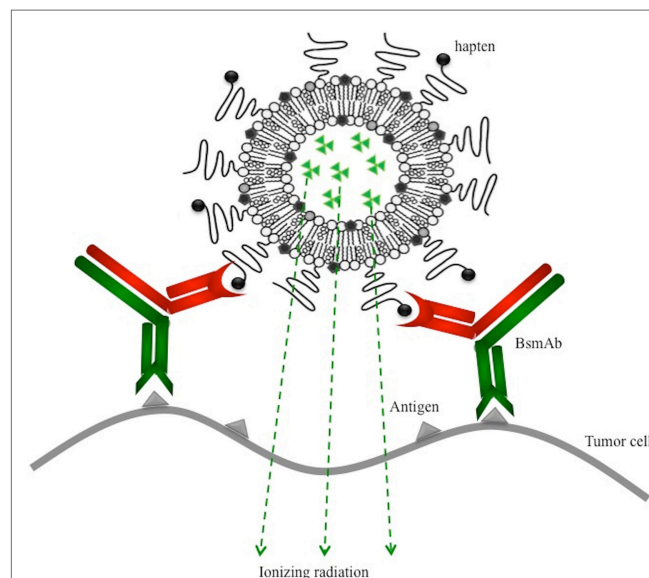


FIGURE 1 | Pretargeting of radiolabeled and functionalized liposomes using a bispecific monoclonal antibody (BsmAb) and a lipid-hapten conjugate.

(fluorescein or ^{125}I), was very useful to monitor the liposome integrity during the experiments and to know the behavior of the liposome contents.

MATERIALS AND METHODS

Reagents

N-succinimidyl-3-(4-hydroxyphenyl)-propionate (BH) was purchased from Pierce Chemical Co. (Rockford, IL, USA). Arginine, chloramine T, fluorescein isothiocyanate (FITC), 1,2-distearoyl-glycero-3-phosphocholine (DSPC), and cholesterol (Chol) were from Sigma-Aldrich (Steinheim, Germany).

1,2-Distearoyl-sn-glycerol-3-phosphoethanolamine-*N*-[Methoxy(Poly-ethylene glycol)-2000], M.W: 2805.54 (DSPE-PEG2000) and 1,2-dioleoyl-sn-glycerol-3-phosphoethanolamine-*N*-(lissamine rhodamine B sulfonyl) M.W: 1301.7 (DPPE-rhodamine) were purchased from Avanti Polar Lipids (Alabaster, AL, USA). DSPE-PEG2000-DTPA was synthesized by Ecole Nationale Supérieure de Chimie de Rennes (France).

Vesicle extruder and filter supports were purchased from Avanti Polar Lipids, Inc. Polycarbonate membranes for vesicle extrusion (100 nm pore size, Nucleopore) were from Whatman. All phospholipids were dissolved in 9:1 chloroform/methanol mixture (HPLC grade, Carlo Erba, and Fisher Scientific).

The anti-CEA/anti-DTPA-In (hMN14 \times 734) BsmAb was kindly provided by IBC Pharmaceuticals, Inc. (Morris Plains, NJ, USA).

Stable indium chloride (^{115}In) was purchased from Sigma-Aldrich and radioactive indium-111 chloride (^{111}In) was purchased from Covidien (Petten, The Netherlands). ^{125}I -iodide sodium was purchased from Perkin-Elmer (Wellesley, MA, USA).

Liposome Preparation and Characterization

DSPC/Chol/DSPE-PEG2000/DSPE-PEG2000-DTPA (64.5:30.5:3.5:1.5 molar ratio) or DSPC/Chol/DSPE-PEG2000/DSPE-PEG2000-DTPA/DPPE-Rhodamine (64:30.5:3.5:1.5:0.5 molar ratio) liposomes were prepared according to the lipid film hydration method described by Bangham (13).

Briefly, a total of 20 μmol of lipids (according to the molar ratios) was dissolved in chloroform/methanol (9:1 v/v) in a round bottom flask. A thin dry lipid film was obtained by solvent evaporation using a rotary evaporator (Rotavapor®, Buchi). Hydration of the lipid film was performed by addition of 1 ml aqueous phase. The flask was vortexed vigorously and maintained above the transition temperature of lipids during 2 h in a rotary evaporator without vacuum at 74°C (gel-crystal transition temperature of DSPE). The final concentration of the liposome suspension was 20 μmol of lipids/ml.

The aqueous phase was composed of 80 mM HEPES buffer pH 8 containing 80 mM arginine for radioactive liposomes and arginine 80 mM/HEPES 80 mM/FITC 20 mM for the fluorescent liposomes.

To obtain small and homogeneous vesicles, the liposome suspension was extruded through Nucleopore polycarbonate filters using a manual thermostat-heated extrusion device (Avanti®

Polar Lipids, Alabaster, AL, USA). The suspension was filtered 20 times through filters with a pore size of 100 nm, at 74°C.

The size and the polydispersity of the vesicles were determined by granulometry by dynamic laser light-scattering measurements using a Malvern High Performance Particle Sizer (HPPS-ET, Instrument SA, UK). Measurements were performed in triplicate after dilution of the suspension in filtered buffer.

Before liposome labeling, untrapped arginine was removed by FPLC (fast protein liquid chromatography) using a size-exclusion Superdex® 200 column (Amersham pharmacia biotech, Orsay, France) eluted in 150 mmol/l, pH 5.6 phosphate buffer.

Radiolabeling Procedure

The aqueous phase radiolabeling was obtained by encapsulation of ^{125}I using an active-loading method in which radioiodinated BH reagent reacts with pre-encapsulated arginine after crossing the lipid bilayer (12). The resulting positively charged conjugate (^{125}I -BH-arginine) is then trapped inside the liposomes. In order to check the integrity of liposomes *in vivo*, they were also radiolabeled on the surface with ^{111}In by complexation with DTPA coupled to phospholipids (14). Moreover, the DTPA-In complex constitutes also the hapten specifically recognized by the antibody 734.

Bolton-Hunter reagent was first radiolabeled with ^{125}I by the chloramine T method and purified by solvent extraction (12). The organic solvent was then evaporated using a dry nitrogen stream.

Then, the double radiolabeling was obtained in one-step on preformed liposomes. Arginine-containing liposomes were added to the dry ^{125}I -BH reagent (90 nmol of reagent for 1 μmol total lipids). Then, citrate buffer (100 mM, pH 5.0) was added, in order to obtain a final citrate concentration of 10 mM and a pH range of 5–6 required for ^{111}In membrane radiolabeling. A mixture of a known amount of $^{115}\text{InCl}_3$ with a trace activity of $^{111}\text{InCl}_3$ (in HCl 0.06N) was added. Membrane radiolabeling was performed with a ratio of one indium ($^{115}\text{In} + ^{111}\text{In}$) molar equivalent per mole of available DTPA. The activity of ^{111}In was used to determine the radiolabeling efficiency and the molar amount of ^{115}In bound to DTPA that reflects the number of haptens expressed at the liposome surface. The liposomes were then incubated for 30 min at 37°C with ^{125}I -BH and ^{111}In . At the end of incubation, a solution of EDTA was added to chelate free indium (10 EDTA molar equivalent per mole of indium) before purification by size-exclusion chromatography using a PD10 column (Sephadex G25, Bio-Rad). The labeling efficiencies were determined after purification by counting the different elution fractions for the two isotopes, with a γ -counter (Wallac 1480-Wizard®3, Perkin-Elmer, Paris, France).

Fluorescent Liposomes

To investigate the integrity of the DSPC/Chol/DSPE-PEG2000/DSPE-PEG2000-DTPA/DPPE-Rhodamine liposomes, the lipid bilayer of the fluorescent liposomes was labeled with Rhodamine and the aqueous phase with Fluorescein (Rho-labeled Fluo-Arg-loaded liposomes). Fluorescein was used in the form of isothiocyanate (FITC),

coupled beforehand with arginine to form fluorescein–arginine (Fluo–Arg) conjugate, and encapsulated in a passive way during the preparation of liposomes, to a concentration of approximately 20 mM.

To be in the same conditions as with the radioactive liposomes and in order to form the DTPA–In hapten, functionalized liposomes were then saturated with non-radioactive ^{115}In . This saturation was performed in acetate buffer 10 mM pH 5, by addition of indium chloride (HCl 0.06N) with 10 molar equivalents of ^{115}In per mole of DTPA.

Fluorescence Microscopy

Cell Lines

The cell line was the same for *in vitro* and *in vivo* experiments. These human colorectal adenocarcinoma cells (LS174T) were acquired from American Type Culture Collection (USA) and expressed strongly the CEA antigen on their surface. They were cultured in medium suggested by RPMI 1640 (Gibco®) supplemented with glutamine 2 mM (Invitrogen, France) and 10% (*v/v*) fetal bovine serum (FBS) (Laboratory PAA, France). Cells were grown in tissue culture flasks to confluence at 37°C in humidified atmosphere with a partial pressure of CO_2 of 5%.

Fluorescence microscopy studies were performed in time-lapse to monitor the kinetics of interaction between cells and liposomes. LS174T cells (100,000/well) were washed once before to replace the culture medium by 300 μl of a diluted solution of BsmAb (10 $\mu\text{g}/\text{ml}$ for specific targeting or 0 μg as control). After 1 h of incubation, cells were washed three times by 300 μl of culture medium. Rho-labeled Fluo–Arg-loaded functionalized liposomes were diluted (25 nmol/ml of lipids in RPMI) and 300 μl were incubated with cells, which represents approximately 750,000 liposomes per cell. Acquisitions were performed in time-lapse after 15 min of incubation between liposome suspension and cells, during 6 h. To compare active (specific targeting with BsmAb) and passive targeting (without BsmAb), the fraction of liposomes bound to cells was quantified by measuring the fluorescence intensity of rhodamine.

Detection by Fluorescence Microscopy

Imaging of interactions between functionalized liposomes and cells was performed using a Nikon A1 Rsi confocal microscope (objectives Plan Apo $\times 60/1.4$ and Plan Apo $\times 20/0.75$). The microscope is adapted to the confocal imaging of fixed or living cells (control of the temperature or of the rate of CO_2).

Fluorescence signals of fluoresceine and rhodamine were recorded after excitation by an argon laser and by a diode laser (respectively 488 and 561 nm exciter bandpass filters). The emitted fluorescence was respectively collected at 525 and 595 nm (emitter bandpass filters). The images were acquired in a matrix size of 512×512 pixels and analyzed by the Fiji software and the NIS element (Nikon) software.

Biodistribution Studies

Animal experiments were carried out in compliance with French regulation and approved by the Ethics Committee for animal

experimentation – Région Pays de la Loire France (approval number: B44.565) according to the protocol CEEA.2012.171. NMRI-nu (*nu/nu*) mice were purchased from Janvier® (Le Genest Saint Isle, France). Mice were housed under standard conditions (standard diet and water *ad libitum*) and maintained in post-entry quarantine for 2 weeks before experiments.

Tumor targeting was performed in mice with CEA-expressing subcutaneous tumor xenografts. Isolated human colorectal adenocarcinoma LS174T cells (2.5×10^6) in 100 μl of sterile physiologic serum were injected into the right flank of NMRI-nu (*nu/nu*) mice. Biodistribution studies were performed at 10–15 days post-graft according to tumor growth (4–8 mm diameter tumors). Liposomes and antibodies were injected by intravenous bolus injection via the tail vein.

For the active targeting protocol, unlabeled anti-CEA/anti-DTPA–In BsmAb (130 μg in 100 μl PBS, which corresponds to 1.3 nmol) was injected first. Then, selected liposome formulations were injected 24 h after the BsmAb. Mice received 100 μl of doubly radiolabeled liposomes containing 0.037–0.185 MBq (1–5 μCi) with 500 nmol of total lipids/mouse (100 nmol of functionalized liposomes that corresponds to 0.5 nmol of hapten and 400 nmol of non-functionalized liposomes co-injected to saturate the reticulo-endothelial system) (15). Control experiments were performed to determine the passive targeting of liposomes, without injection of the BsmAb, under the same conditions.

Groups of four to five mice were used for each time point of biodistribution study: 3, 24, and 48 h post-injection. At each time point, blood samples were collected just before sacrifice and then tumor and normal organs were dissected. All samples were weighed and counted in a gamma counter calibrated for the two isotopes. Standards of the injected material were made in duplicate and used to calculate the total injected dose and to correct for decay of the radioisotopes. The total radioactivity in the blood was determined by assuming that the total volume of blood was 7% of the mice body weight (16). The results are expressed as a percentage of the total administered liposome dose accumulated per gram of tissues or remained in the blood (% DI/gram) \pm SD.

The data from the biodistribution studies were compared using the non-parametric Wilcoxon's test, due to the small numbers of animals, using $p = 0.05$.

RESULTS

Liposomes Preparation and Characterization

After filtration of the liposomes with the extruder, the mean size obtained for the different formulations was 105.5 ± 6.4 nm (polydispersity index < 0.1).

The double radiolabeling of the liposomes, by ^{125}I –BH encapsulation in the aqueous phase and by ^{111}In chelation on DSPE–PEG–DTPA at the surface, was performed by 30 min incubation at 37°C. Around 60% of encapsulation was obtained and the surface radiolabeling efficiency was above 77%. The number of DTPA–In on the liposome surface was estimated using a known amount of ^{115}In and a tracer proportion of ^{111}In to be around 5 nmol/ μmol of lipids.

Fluorescence Microscopy

The kinetics of binding of the liposomes to the cells were assessed by time-lapse fluorescence microscopy (**Figure 2**). From the beginning of the acquisition and during 6 h, we observed an intense binding of rhodamine to cell membranes while no fluorescence was observed inside the cells. The membrane-associated fluorescence was very intense and stable over time, but leakage of Fluo-Arg contained in the liposomes occurred when they interacted with the cell surface. Very quickly, a diffuse green fluorescence was observed in the extracellular area.

To demonstrate the immunospecificity of functionalized liposome targeting to LS174T cells, acquisitions were performed by comparing the rhodamine signal bound to the membranes, with or without preincubation of cells with the bispecific antibody. In order to remove liposomes unbound to the cells, three washes were carried out by replacing the culture medium after 3 h of incubation with the liposomes. Signal obtained with rhodamine is represented in **Figure 3**, respectively for active targeting with antibody and passive targeting without antibody. These images represent the amount of fluorescence signal of five consecutive focal planes acquired along the Z axis and spaced with 2 μm .

Then, we selected two fields (zoom 1 and zoom 2) in which cells were counted in order to evaluate the fluorescence signal according to the number of cells. The intensity of the signal was thresholded by the Otsu algorithm (**Table 1**). For zoom 1, the mean fluorescence signal was 103 pixels per cell for active targeting and 29 pixels per cell for passive targeting, a bonding of Rho-labeled liposomes 3.6 times higher for active targeting. For zoom 2, where the difference of fluorescence was the lowest visually between passive and active targeting, the mean signal was 66 and 31 pixels per cell, respectively, for the active and passive targeting, with a ratio of 2.1 for active targeting.

Biodistribution Experiments

The best formulation of functionalized liposomes was defined in preliminary studies in terms of affinity to the BsmAb, tested by SPR, and in terms of pharmacokinetic parameters *in vivo* (11, 14). The chosen formulation (DSPC/Chol/DSPE-PEG2000/DSPE-PEG2000-DTPA) showed the best affinity with 6.3 nM and favorable pharmacokinetic parameters ($T_{1/2\beta} \cong 12.5$ h). This formulation with DTPA at the end of the PEG chains orientates

the hapten away from the PEG structure, in order to avoid steric hindrance.

In vivo biodistribution in tumor-xenografted nude mice is represented in **Table 2**. The activities in blood and in major organs are presented at 3, 24, and 48 h. The blood activities are quite comparable for the two radioisotopes that confirm the integrity of the circulating liposomes *in vivo*. Uptake in major organs was higher at 24 h with a higher accumulation in liver, spleen, and kidneys, as widely described in the literature. Moreover, indium-labeled phospholipids remained in liver and spleen, which reflects the accumulation of radiolabeled phospholipids in catabolizing organs, whereas the radioiodinated BH-arginine is quickly eliminated from blood after liposome destruction. For example, the uptakes in liver, spleen and kidneys are respectively 16.5 ± 2.4 , 34.3 ± 3.5 , $8.8 \pm 1.7\%$ ID/g with ^{111}In and 4.1 ± 1.1 , 9.1 ± 3.7 , $2.1 \pm 0.8\%$ ID/g with ^{125}I .

Comparison of organ uptake for passive and active targeting is presented in **Figure 4**, for the two tracers. Results are presented at 24 h, when tumor uptake is highest. Biodistribution in healthy tissues was comparable for active and passive targeting, and no significant difference was shown for liver, spleen, kidneys and blood between passive and active targeting ($p > 0.05$).

Concerning tumor uptake, results showed a relatively important passive targeting of the liposomes, in particular for the tracer of the lipid bilayer, with $4.4 \pm 0.4\%$ ID/g of tumor with ^{111}In , and $2.7 \pm 0.6\%$ ID/g with ^{125}I . In spite of this high passive targeting, results demonstrated significant specific targeting, after BsmAb injection, with $7.5 \pm 2.4\%$ ID/g of tumor with ^{111}In , and $5.1 \pm 2.5\%$ ID/g with ^{125}I ($p = 0.03$), demonstrating the immunospecificity of the two-step targeting using functionalized liposomes and BsmAb.

On the other hand, it seemed interesting to take into account all the results of the biodistribution, by calculating the areas under the curve (AUC), which integrated the activities at 3, 24, and 48 h (**Table 3**). The values of AUC were calculated by the trapeze method from the mean activities for each time point. If we compare the results obtained with ^{111}In (surface labeling) and ^{125}I (internal labeling), we can notice that for the healthy organs, the AUC is two to four times higher for the membrane labeling than for the internal phase labeling. Tumor/organs ratios are 0.4,

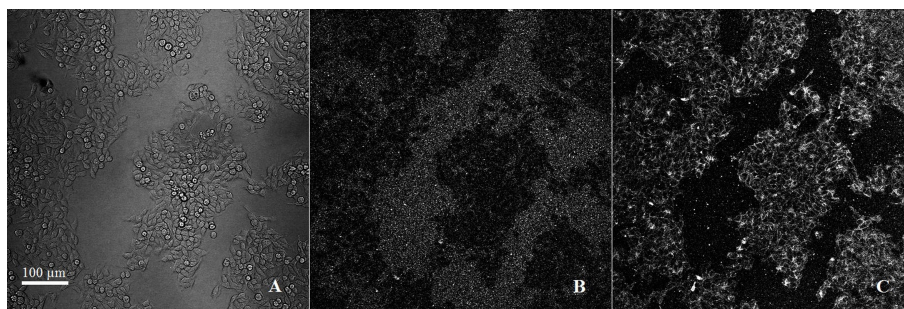


FIGURE 2 | Observation in time-lapse confocal microscopy (zoom $\times 20/640 \mu\text{m} \times 640 \mu\text{m}$): active targeting of doubly fluorescent functionalized liposomes on LS174T cells. (A) cells in brightfield, (B) FITC signal (ex/em 488/525 nm), (C) rhodamine signal (ex/em 561/595 nm). Scale bar: 100 μm .

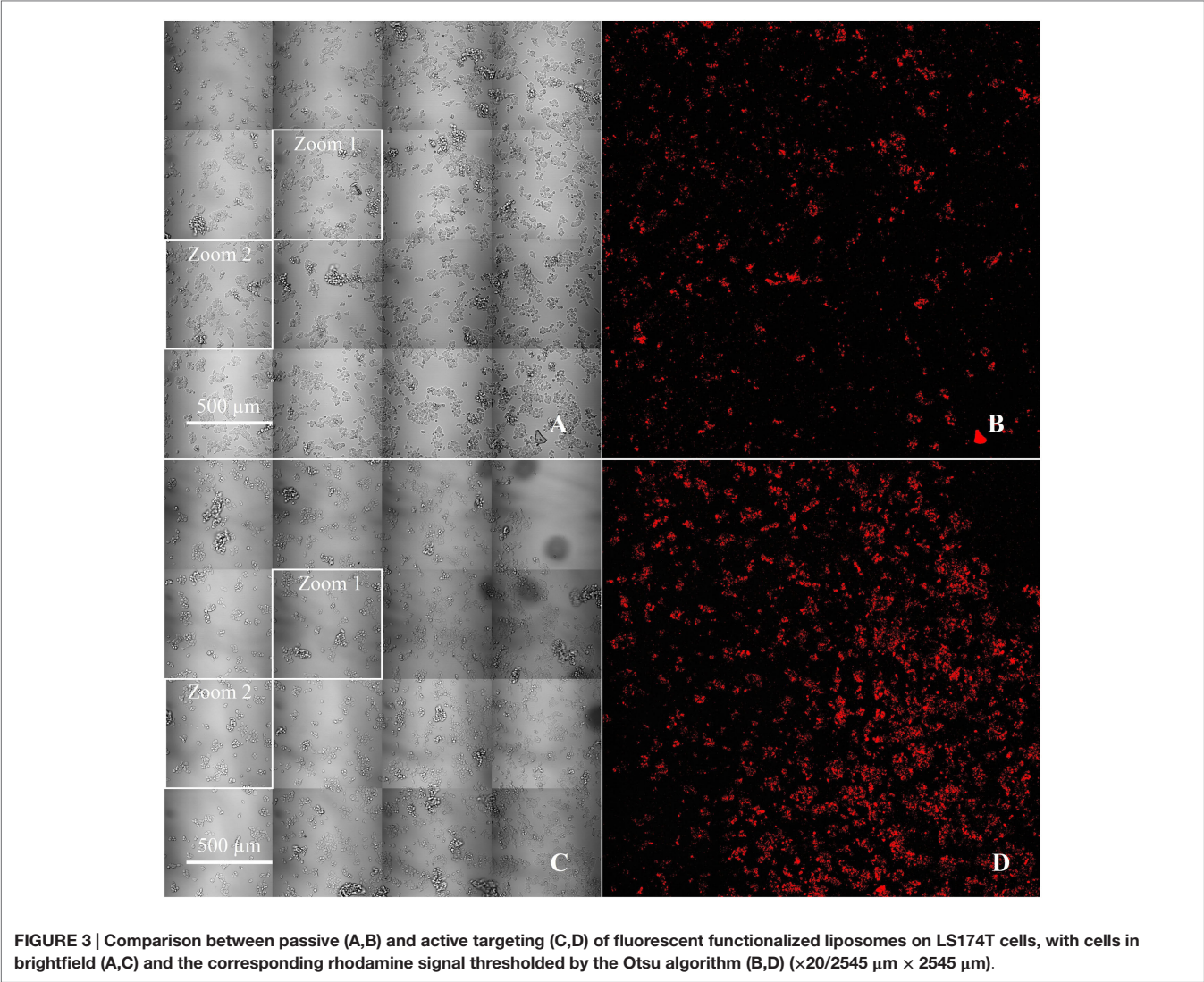


TABLE 1 | Data obtained *in vitro* with rhodamine (lipid bilayer tracer) after quantification of the fluorescent signal on the LS174T cells membrane compared to the number of the cells for active targeting or passive targeting of fluorescent and functionalized liposomes.

Targeting	16 fields		Zoom 1		Zoom 2		
	Fluorescence (pixels)	Cells	Fluorescence (pixels)	Pixels per cells	Cells	Fluorescence (pixels)	Pixels per cells
Passive targeting	107,498	622	17,929	29	583	17,929	31
Active targeting	331,454	424	43,881	103	343	22,646	66
Ratio	3:1	–	–	3:6	–	–	2:1

Zoom 1 and Zoom 2 correspond to the selected areas on **Figure 3**.

0.2, and 0.7 in ¹¹¹In and 0.9, 0.4, and 1.6 in ¹²⁵I, respectively, for liver, spleen, and kidneys. These ratios are more favorable for the internal labeling with values from 1.5 to 2 times superior to the ratios obtained for the membrane labeling.

DISCUSSION

The originality of this study was to design a two-step targeting system with liposomes, similar to that used in AES, for the RIT

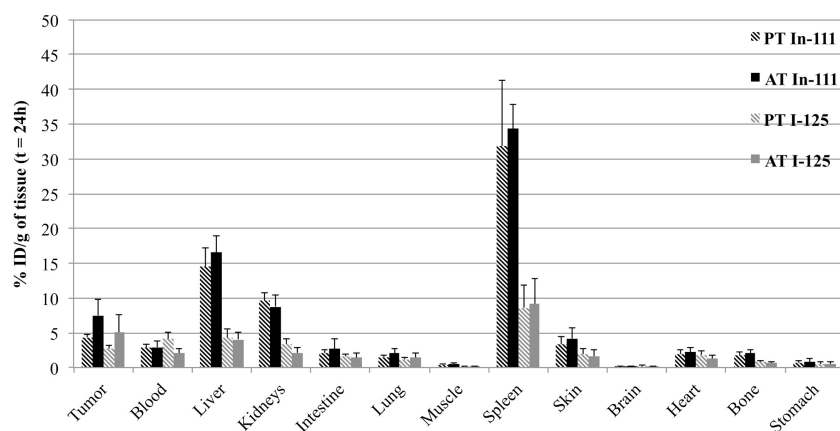
of solid tumors. Once the radiolabeling technique was finalized and the best formulation was selected by SPR (11), we were able to test these liposomes on a cellular model, using CEA-expressing LS174T cells, in order to characterize the specific interactions between liposomes and target cells.

In vitro, liposomes were surface-labeled with rhodamine and contained entrapped Fluo-Arg. Indeed, it seemed important in this work to monitor liposome integrity using a tracer of the membrane and a tracer encapsulated in the aqueous phase (17).

TABLE 2 | Biodistribution of functionalized DSPC/Chol/DSPE-PEG₂₀₀₀/DSPE-PEG₂₀₀₀-DTPA-In (64.5:30.5:3.5:1.5) liposomes injected in LS174T-xenografted nude mice (0.5 nmol of hapten/mouse and 1–5 μ Ci for each radionuclide: ¹¹¹In and ¹²⁵I) 24 h after bispecific antibody (130 μ g hMN14 \times 734).

% ID/g	¹¹¹ In			¹²⁵ I		
	3 h (n = 4)	24 h (n = 4)	48 h (n = 4)	3 h (n = 4)	24 h (n = 4)	48 h (n = 4)
Tumor	3.6 \pm 0.2	7.5 \pm 2.4	5.6 \pm 1.1	2.5 \pm 1.0	5.1 \pm 2.5	1.2 \pm 0.3
Blood	20.3 \pm 2.5	2.9 \pm 1.0	0.5 \pm 0.2	18.0 \pm 3.5	2.1 \pm 0.6	0.3 \pm 0.1
Liver	11.4 \pm 1.1	16.5 \pm 2.4	15.3 \pm 2.0	6.7 \pm 1.3	4.1 \pm 1.0	0.5 \pm 0.1
Kidneys	6.9 \pm 1.0	8.8 \pm 1.7	7.6 \pm 2.4	3.5 \pm 0.7	2.1 \pm 0.8	1.1 \pm 0.3
Intestine	2.8 \pm 1.0	2.7 \pm 1.5	3.0 \pm 0.6	2.0 \pm 0.6	1.4 \pm 0.7	0.5 \pm 0.2
Lung	7.0 \pm 1.1	2.0 \pm 0.7	1.3 \pm 0.3	5.1 \pm 1.4	1.4 \pm 0.6	0.25 \pm 0.08
Muscle	0.6 \pm 0.1	0.5 \pm 0.1	0.42 \pm 0.09	0.35 \pm 0.07	0.16 \pm 0.05	0.04 \pm 0.01
Spleen	21.2 \pm 1.9	34.3 \pm 3.5	29.4 \pm 2.4	8.7 \pm 0.3	9.1 \pm 3.7	4.3 \pm 2.2
Skin	1.8 \pm 0.4	4.2 \pm 1.6	4.1 \pm 0.5	1.0 \pm 0.3	1.6 \pm 0.9	0.6 \pm 0.1
Brain	1.1 \pm 0.4	0.16 \pm 0.04	0.08 \pm 0.01	0.8 \pm 0.3	0.12 \pm 0.04	0.014 \pm 0.003
Heart	4.8 \pm 2.2	2.2 \pm 0.7	2.0 \pm 0.4	4.8 \pm 1.8	1.3 \pm 0.4	0.6 \pm 0.2
Bone	3.4 \pm 0.7	2.0 \pm 0.6	1.6 \pm 0.2	2.3 \pm 0.5	0.6 \pm 0.3	0.13 \pm 0.04
Stomach	0.8 \pm 0.1	0.8 \pm 0.5	0.6 \pm 0.4	0.66 \pm 0.09	0.5 \pm 0.3	0.18 \pm 0.09

The data are expressed as the percentage of total administered dose per gram of tissue (% ID/g, mean \pm SD).

**FIGURE 4 | Biodistribution of doubly radiolabeled liposomes (¹¹¹In in black and ¹²⁵I in gray) at 24 h in LS174T-xenografted nude mice for passive targeting or active targeting.** Mice were injected i.v. with functionalized liposomes (0.5 nmol of hapten/mouse and 1–5 μ Ci for each radionuclide) without BsmAb injection (PT for Passive Targeting) or 24 h after BsmAb injection (AT for Active Targeting). The data are expressed as the percentage of total administered dose per gram of tissue (% ID/g, mean SD).

To observe the kinetics of interaction of the liposomes with the cells, time-lapse fluorescence microscopy was used. The incubation of LS174T cells with Rho-labeled Fluo-Arg-loaded functionalized liposomes did not result in a co-localization of the fluorescent tracers. An intense fixation of the rhodamine on cell membranes was observed during 6 h, while the Fluo-Arg was totally released (diffuse green fluorescence in the extracellular medium). This leakage was attributed to the interaction of the cell surface proteins with the liposome bilayer, and depends on the liposome formulation, in particular when the Chol lipid proportion increased from 30 to 40 moles% of lipids (18).

In this work, despite a supplementation of the medium by 10% of FBS, non-specific binding was observed after incubating the cells and liposomes, without BsmAb (passive targeting). Nevertheless, the rhodamine fluorescence signal associated to the liposomes was higher in the case of active targeting compared to passive targeting with a ratio of 3:1 obtained by signal quantification.

TABLE 3 | Areas under the curve (AUC) and tumor/organs ratios (T/O) calculated for the main organs (% ID/g) after biodistribution (3, 24, and 48 h) of functionalized liposomes administered i.v. 24 h after BsmAb injection in LS174T-xenografted nude mice.

	¹¹¹ In		¹²⁵ I	
	AUC	T/O	AUC	T/O
Tumor	278	1.0	158	1.0
Blood	437	0.6	329	0.5
Liver	692	0.4	178	0.9
Kidneys	371	0.7	103	1.6
Spleen	1379	0.2	361	0.4

In second part, the ability of functionalized and pegylated liposomes to target CEA-expressing tumors, was tested in xenografted nude mice, with the two-step targeting system using the hMN14 \times 734 BsmAb. The double radiolabeling proved of real

interest to compare the behavior of the radioactivity encapsulated in the aqueous phase and that carried by radiolabeled phospholipids in the lipid bilayer.

Blood levels of the two tracers remained the same at different times after injection, thus demonstrating the stability of the liposomes in the circulation. By contrast, phospholipids radiolabeled with residualizing ^{111}In accumulate in catabolizing organs, with a prominent uptake in liver and spleen, whereas encapsulated- ^{125}I -BH-arginine was quickly eliminated in urine after liposome destruction (14). The maximum tumor uptake was observed at 24 h. At this time, tumor/organ ratios were superior to 1 for ^{125}I , except for the spleen. For liver, spleen and kidneys, ratios were, respectively, 1.24, 0.56, and 2.42 for ^{125}I and 0.45, 0.22, and 0.85 for ^{111}In .

In spite of relatively high tumor uptake with passive targeting, results demonstrated significant specific targeting, after BsmAb injection, with $7.5 \pm 2.4\%$ ID/g of tumor with ^{111}In , and $5.1 \pm 2.5\%$ ID/g with ^{125}I . The lower tumor uptake obtained with ^{125}I confirms *in vitro* results. A release of the content was effectively observed by fluorescence microscopy, as the liposomes interacted with the cellular target. Pegylation of the liposomes provides a long half-life, which allows them to reach the tumor, but after interaction with the target cells, the encapsulated-tracer (^{125}I -BH-arginine or Fluo-Arg) is released in part. However, encapsulating the radioactivity in the aqueous phase favors a more rapid elimination of the hydrophilic radiolabeled compound and reduces the healthy organs irradiation.

If specific targeting of functionalized liposomes has been documented extensively *in vitro* (17, 19, 20), most of the *in vivo* targeting experiments described in the literature do not show significant differences between passive and active targeting. For example, Petersen et al. described a tumor targeting with a somatostatin analog (TATE)-functionalized liposomes. Results obtained for specific targeting were $5.2 \pm 0.5\%$ ID/g versus $5.5 \pm 0.3\%$ ID/g with non-specific control liposomes (21). Similarly, no difference in tumor accumulation was obtained using folate-functionalized liposomes to target different tumors which overexpressed folate receptors (22). In this particular case, it was shown that despite the enhanced affinity of specific liposomes to tumor cells, tumor uptake was not improved because of a rapid elimination of the functionalized liposomes by the liver. By using immunoliposomes, carrying monoclonal

antibodies or their fragments, specific targeting does not improve tumor accumulation, essentially resulting from the well known enhanced permeability and retention (EPR) effect (23), but nevertheless authors conclude that immunoliposomes can increase interaction with the cells, and notably by internalization (24). On the other hand, no significant difference was demonstrated between passive targeting and active targeting, when the target antigen is internalizing, either with immunoliposomes or with pretargeting (25). The pretargeting system used in our study is based on the recognition of CEA antigen, widely known to be very slowly internalized and not to promote the endocytosis of liposomes (26, 27). In this system, a specific tumor targeting, *in vitro* and *in vivo*, was thus demonstrated with the pretargeted functionalized liposomes.

CONCLUSION

Specific targeting of liposomes is difficult to demonstrate *in vivo* because they accumulate in tumors passively through the EPR effect. Nevertheless, this study shows the interest of a two-step targeting, using functionalized liposomes and BsmAb, of a non-internalizing antigen. Indeed, the specific targeting observed *in vitro*, on CEA-expressing cells, is confirmed *in vivo* by a significant increase of tumor uptake *in vivo*, which was not previously described in the literature. The immunospecificity of targeting is indeed often offset by the EPR effect and by the rapid elimination of the immunoliposomes or by the internalization of the antibody used in the pretargeting system. In this work, the pretargeting approach allowed us to use stable unlabeled BsmAb and liposomes tailored for optimal *in vivo* behavior and suitable for extemporaneous radiolabeling. This original and new approach suggests a potential for immunospecific liposome pretargeting for RIT.

ACKNOWLEDGMENTS

The authors thank D. M. Goldenberg (Immunomedics, Inc. Morris Plains, NJ, USA) for providing the hMN14 \times 734 bispecific antibody and the Picell platform (SFR Santé F. Bonamy, France) for the confocal microscopy images. This work has been supported in part by a grant from the French National Agency for Research called "Investissements d'Avenir," Labex IRON n ANR-11-LABX-0018-01.

REFERENCES

- Witzig TE, Gordon LI, Cabanillas F, Czuczman MS, Emmanouilides C, Joyce R, et al. Randomized controlled trial of yttrium-90-labeled ibritumomab tiuxetan radioimmunotherapy versus rituximab immunotherapy for patients with relapsed or refractory low-grade, follicular, or transformed B-cell non-Hodgkin's lymphoma. *J Clin Oncol* (2002) 20(10):2453–63. doi:10.1200/JCO.2002.11.076
- Illidge T, Morschhauser F. Radioimmunotherapy in follicular lymphoma. *Best Pract Res Clin Haematol* (2011) 24(2):279–93. doi:10.1016/j.beha.2011.03.005
- Sharkey RM, Goldenberg DM. Cancer radioimmunotherapy. *Immunotherapy* (2011) 3(3):349–70. doi:10.2217/imt.10.114
- DeNardo SJ, Denardo GL. Targeted radionuclide therapy for solid tumors: an overview. *Int J Radiat Oncol Biol Phys* (2006) 66:89–95. doi:10.1016/j.ijrobp.2006.03.066
- Barbet J, Kraeber-Bodéré F, Vuillez JF, Gautherot E, Rouvier E, Chatal JF. Pretargeting with the affinity enhancement system for radioimmunotherapy. *Cancer Biother Radiopharm* (1999) 14(3):153–66. doi:10.1089/cbr.1999.14.153
- Kraeber-Bodéré F, Salaun PY, Ansquer C, Dru D, Mirallié E, Faivre-Chauvet A, et al. Pretargeted radioimmunotherapy (pRAIT) in medullary thyroid cancer (MTC). *Tumor Biol* (2012) 33(3):601–6. doi:10.1007/s13277-012-0359-6
- Kraeber-Bodere F, Rousseau C, Bodet-Milin C, Ferrer L, Faivre-Chauvet A, Campion L, et al. Targeting, toxicity, and efficacy of 2-step, pretargeted radioimmunotherapy using a chimeric bispecific antibody and ^{131}I -labeled bivalent hapten in a phase I optimization clinical trial. *J Nucl Med* (2006) 47(2):247–55.
- Goodwin DA, Meares CF. Advances in pretargeting biotechnology. *Biotechnol Adv* (2001) 19(6):435–50. doi:10.1016/S0734-9750(01)00065-9
- Phillips WT, Goins B, Bao A. Radioactive liposomes. *Nanomed Nanobiotechnol* (2009) 1(1):69–83. doi:10.1002/wnan.3

10. Ting G, Chang CH, Wang HE, Lee TW. Nanotargeted radionuclides for cancer nuclear imaging and internal radiotherapy. *J Biomed Biotechnol* (2010) **2010**: 1–17. doi:10.1155/2010/953537
11. Rauscher A, Frindel M, Maurel C, Maillasson M, Le Saëc P, Rajerison H, et al. Influence of pegylation and hapten location at the surface of radiolabelled liposomes on tumour immunotargeting using bispecific antibody. *Nucl Med Biol* (2014) **41**:e66. doi:10.1016/j.nucmedbio.2013.12.012
12. Mougin-Degraef M, Jestin E, Bruel D, Remaud-Le Saëc P, Morandeau L, Faivre-Chauvet A, et al. High-activity radio-iodine labeling of conventional and stealth liposomes. *J Liposome Res* (2006) **16**(1):91–102. doi:10.1080/08982100500528941
13. Bangham AD, Standish MM, Watkins JC. Diffusion of univalent ions across the lamellae of swollen phospholipids. *J Mol Biol* (1965) **13**(1):238–252. doi:10.1016/S0022-2836(65)80093-6
14. Mougin-Degraef M, Bourdeau C, Jestin E, Saï-Maurel C, Bourgeois M, Le Saëc P, et al. Doubly radiolabeled liposomes for pretargeted radioimmunotherapy. *Int J Pharm* (2007) **344**(1–2):110–117. doi:10.1016/j.ijpharm.2007.05.024
15. Oja CD, Semple SC, Chonn A, Cullis PR. Influence of dose on liposomes clearance: critical role of blood proteins. *Biochim Biophys Acta* (1996) **1281**:31–7. doi:10.1016/0005-2736(96)00003-X
16. Wu MS, Robbins JC, Bugianesi RL, Ponpipom MM, Shen TY. Modified in vivo behavior of liposomes containing synthetic glycolipids. *Biochim Biophys Acta* (1981) **674**(1):19–29. doi:10.1016/0304-4165(81)90342-1
17. Torchilin V. Fluorescence microscopy to follow the targeting of liposomes and micelles to cells and their intracellular fate. *Adv Drug Deliv Rev* (2005) **57**(1):95–109. doi:10.1016/j.addr.2004.06.002
18. Düzgünes N, Nir S. Mechanisms and kinetics of liposome-cell interactions. *Adv Drug Deliv Rev* (1999) **40**:3–18. doi:10.1016/S0169-409X(99)00037-X
19. Castelli DD, Terreno E, Cabella C, Chaabane L, Lanzardo S, Tei L, et al. Evidence for in vivo macrophage mediated tumor uptake of paramagnetic/fluorescent liposomes. *NMR Biomed* (2009) **22**(10):1084–92. doi:10.1002/nbm.1416
20. Rangger C, Helbok A, Sosabowski J, Kremser C, Koehler G, Prassl R, et al. Tumor targeting and imaging with dual-peptide conjugated multifunctional liposomal nanoparticles. *Int J Nanomedicine* (2013) **8**:4659–71. doi:10.2147/IJN.S51927
21. Petersen AL, Binderup T, Jølcck RI, Rasmussen P, Henriksen JR, Pfeifer AK, et al. Positron emission tomography evaluation of somatostatin receptor targeted ⁶⁴Cu-TATE-liposomes in a human neuroendocrine carcinoma mouse model. *J Control Release* (2012) **160**(2):254–63. doi:10.1016/j.jconrel.2011.12.038
22. Gabizon A, Horowitz AT, Goren D, Tzemach D, Shmeeda H, Zalipsky S. In vivo fate of folate-targeted polyethylene-glycol liposomes in tumor-bearing mice. *Clin Cancer Res* (2003) **9**(17):6551–9.
23. Maeda H, Bharate GY, Daruwalla J. Polymeric drugs for efficient tumor-targeted drug delivery based on EPR-effect. *Eur J Pharm Biopharm* (2009) **71**(3):409–19. doi:10.1016/j.ejpb.2008.11.010
24. Kirpotin DB, Drummond DC, Shao Y, Shalaby MR, Hong K, Nielsen UB, et al. Antibody targeting of long-circulating lipidic nanoparticles does not increase tumor localization but does increase internalization in animal models. *Cancer Res* (2006) **13**:6732–40.
25. Lehtinen J, Raki M, Bergström KA, Uutela P, Lehtinen K, Hiltunen A, et al. Pre-targeting and direct immunotargeting of liposomal drug carriers to ovarian carcinoma. *PLoS One* (2012) **7**(7):e41410. doi:10.1371/journal.pone.0041410
26. Bryan JN, Jia F, Mohsin H, Sivaguru G, Miller WH, Anderson CJ, et al. Comparative uptakes and biodistributions of internalizing vs. non-internalizing copper-64 radioimmunoconjugates in cell and animal models of colon cancer. *Nucl Med Biol* (2005) **32**(8):851–8. doi:10.1016/j.nucmedbio.2005.05.006
27. Boudousq V, Bobyk L, Busson M, Garambois V, Jarlier M, Charalambatou P, et al. Comparison between internalizing anti-HER2 mAbs and non-internalizing anti-CEA mAbs in alpha-radioimmunotherapy of small volume peritoneal carcinomatosis using ²¹²Pb. *PLoS One* (2013) **8**(7):e69613. doi:10.1371/journal.pone.0069613

Conflict of Interest Statement: The authors declare that the research was conducted in the absence of any commercial or financial relationships that could be construed as a potential conflict of interest.

Copyright © 2015 Rauscher, Frindel, Rajerison, Gouard, Maurel, Barbet, Faivre-Chauvet and Mougin-Degraef. This is an open-access article distributed under the terms of the Creative Commons Attribution License (CC BY). The use, distribution or reproduction in other forums is permitted, provided the original author(s) or licensor are credited and that the original publication in this journal is cited, in accordance with accepted academic practice. No use, distribution or reproduction is permitted which does not comply with these terms.



Therapeutic Efficacy of Alpha-RIT Using a ^{213}Bi -Anti-hCD138 Antibody in a Mouse Model of Ovarian Peritoneal Carcinomatosis

Aurélien Derrien^{1,2,3,4}, Sébastien Gouard^{1,2,3}, Catherine Maurel^{1,2,3}, Marie-Hélène Gaugler^{1,2,3}, Frank Bruchertseifer⁵, Alfred Morgenstern⁵, Alain Faivre-Chauvet^{1,2,3,6}, Jean-Marc Classe^{1,2,3,7} and Michel Chérel^{1,2,3,8*}

¹ Centre Régional de Recherche en Cancérologie Nantes/Angers (CRCNA) UMR892 INSERM, Nantes, France, ² 6299 CNRS, Nantes, France, ³ Université de Nantes, Nantes, France, ⁴ Service de Gynécologie-Obstétrique, CHU de Poitiers, Poitiers, France, ⁵ Institute for Transuranium Elements, European Commission Joint Research Centre, Karlsruhe, Germany, ⁶ Service de Médecine Nucléaire, CHU de Nantes, Nantes, France, ⁷ Service de Chirurgie Oncologique, Institut de Cancérologie de l'Ouest, Saint-Herblain, France, ⁸ Service de Médecine Nucléaire, Institut de Cancérologie de l'Ouest, Saint-Herblain, France

OPEN ACCESS

Edited by:

Jean-Pierre Pouget,
INSERM, France

Reviewed by:

Tom A. Bäck,
University of Gothenburg, Sweden
Damien Huglo,
Centre Hospitalier Régional
Universitaire de Lille, France

*Correspondence:

Michel Chérel
michel.cherel@univ-nantes.fr

Specialty section:

This article was submitted to Nuclear
Medicine,
a section of the journal
Frontiers in Medicine

Received: 14 September 2015

Accepted: 30 November 2015

Published: 21 December 2015

Citation:

Derrien A, Gouard S, Maurel C,
Gaugler M-H, Bruchertseifer F,
Morgenstern A, Faivre-Chauvet A,
Classe J-M and Chérel M (2015)
Therapeutic Efficacy of Alpha-RIT
Using a ^{213}Bi -Anti-hCD138 Antibody
in a Mouse Model of Ovarian
Peritoneal Carcinomatosis.
Front. Med. 2:88.
doi: 10.3389/fmed.2015.00088

Purpose: Ovarian peritoneal carcinomatosis is a pathology for which effective cures are currently lacking. New research protocols seek to eradicate residual micrometastases following cytoreductive surgery by using hyperthermic intraperitoneal chemotherapy (HIPEC) or radioimmunotherapy (RIT). This study aims to first develop alpha-RIT using an anti-CD138 mAb radiolabeled with an alpha-emitter, bismuth-213 (^{213}Bi -B-B4) and HIPEC in a nude mouse model and second to compare and combine these techniques.

Material and methods: A murine model of postoperative ovarian peritoneal carcinomatosis was established. A pilot group of six mice received an intraperitoneal injection of luciferase-tagged SHIN-3 cells and bioluminescence was measured every day. Cytoreductive surgery was performed at day 14 ($n = 4$) and 29 ($n = 2$). Because the residual bioluminescence signal measured after surgery was equivalent to that obtained 3 days after the graft, HIPEC or alpha-RIT treatments were applied 3 days after the graft. Ten mice were treated by HIPEC with cisplatin (37.5 mg/mL), 11 with 7.4 MBq of ^{213}Bi -B-B4, seven with 11.1 MBq of ^{213}Bi -B-B4, and 10 mice were treated with the combined therapy (HIPEC + 7.4 MBq of ^{213}Bi -B-B4). Eleven mice received no treatment. Bioluminescence imaging and survival were assessed.

Results: Alpha-RIT 7.4 MBq and 11.1 MBq significantly improved survival ($p = 0.0303$ and $p = 0.0070$, respectively), whereas HIPEC and HIPEC + alpha-RIT treatments did not significantly ameliorate survival as compared to the control group.

Conclusion: Survival was significantly increased by alpha-RIT treatment in mice with peritoneal carcinomatosis of ovarian origin; however, HIPEC alone or in combination with alpha-RIT had no significant effect.

Keywords: radioimmunotherapy, alpha-particles, HIPEC, ovarian peritoneal carcinomatosis, CD138

INTRODUCTION

Epithelial ovarian carcinoma (EOC) is the leading cause of mortality linked to gynecological cancer in France with 3357 deaths in 2006 (1). The first line of treatment is based on a combination of maximal cytoreductive surgery and adjuvant chemotherapy with platinum salt and taxanes (2). Seventy-five percent of patients will experience cancer recurrence, and in the absence of complete remission in the initial period, the disease will become incurable (3). After initial treatment, the prognosis is closely correlated with residual tumor volume (4, 5). As EOC is mainly confined to the peritoneal cavity in the form of peritoneal carcinomatosis, several techniques including hyperthermic intraperitoneal chemotherapy (HIPEC) or radioimmunotherapy (RIT) are used to target the postoperative intraperitoneal residue.

HIPEC involves applying high concentrations of chemotherapy at cytotoxic temperatures to the intraperitoneal cavity during the perioperative cytoreductive period (6). A recent French phase III and IV multicenter retrospective cohort study of 566 patients treated with HIPEC found mortality and morbidity levels of 0.8 and 31.3%, respectively, for advanced and recurrent ovarian cancer (7). In addition, another multicenter retrospective study estimated that overall 4-year survival rates for patients treated with HIPEC was 75.6% compared to 19.4% for the control group (8), and recently a retrospective observational multi-institutional study was conducted showing that HIPEC results in encouraging survival rates for patients treated for a first relapse of ovarian cancer (9).

RIT is based on a radiopharmaceutical product composed of a specific tumor cell vector and a radioisotope. The radiopharmaceutical binds to an antigen which is overexpressed by the tumor cells and thus ensures selective irradiation. In this context, CD138 or Syndecan 1, a transmembrane receptor belonging to the heparan sulfate group overexpressed in ovarian tumors compared to healthy ovarian tissue, regardless of their status of chemoresistance or hormonal sensitivity (10, 11), could be a good target candidate. RIT is preferentially used on disseminated tumors or small-sized nodules as is the case with peritoneal carcinomatosis. A recent review by Tomblyn et al. summarized over 24 studies of RIT treatment of ovarian cancer in both preclinical and clinical studies (phases I–III) (12). The beta-particle emitters (iodine-131, rhenium-186, lutetium-177, and yttrium-90) were prioritized up until a phase III randomized study by Verheijen et al. in 2006 (13) which failed to establish an improvement in terms of survival only reduction of intraperitoneal relapses. One of the explanations lay in the choice of the radioelement (14). The development of alpha-particle emitters has enabled new studies, notably those using antibodies or antibody fragments ($F(ab')_2$) labeled with astatine-211, with the results showing good efficacy on tumor cell lysis with higher mean doses of radiotherapy absorbed (22 Gy) (15).

This study aims to target the residual pathology of ovarian peritoneal carcinomatosis by means of a monoclonal humanized anti-CD138 antibody radiolabeled with an alpha-particle emitter (bismuth-213) and to compare and combine this treatment with HIPEC.

MATERIALS AND METHODS

Cell Line

The SHIN-3 cell line was established from a 56-year-old Japanese woman diagnosed with serous cystadenocarcinoma of the ovary and was provided by the Medical University of Nara, Japan (16). A cDNA sequence coding for Luciferase was obtained from the pGL3 vector (Promega). The fragment was subcloned into the retroviral vector pMX (17) and retroviral transduction of SHIN-3 cells was performed by standard molecular methods. SHIN-3-Luc+ cells were grown in RPMI 1640 medium (Sigma-Aldrich) supplemented with 10% heat-inactivated fetal calf serum (PAA), 2 mM glutamine (Invitrogen), 100 U/mL penicillin (Invitrogen), and 100 µg/mL streptomycin (Invitrogen) at 37°C, 5% CO₂, and 100% humidity. The doubling time of SHIN-3-Luc+ cells was 29 h.

Cellular Expression of CD138 and CEA by Flow Cytometry

To measure cellular expression of CD138 and CEA on SHIN-3-Luc+ cells, 200,000 cells were incubated for 1 h at 4°C with anti-CD138 (B-B4, Diaclone), anti-CEA (T84.66) antibodies or with isotype control mouse IgG1 (BD Biosciences) at 10 µg/mL, followed by a secondary phycoerythrin conjugated anti-rat antibody (Jackson Immuno Research) for 1 h. Analysis was carried out using a FACSAArray flow cytometer (Becton Dickinson). Data analysis was conducted using Flowjo software.

Ovarian Peritoneal Carcinomatosis Mouse Model

NMRI-nu (nu/nu) mice were purchased from Janvier and housed under conventional conditions at the UTE animal facility (SFR François Bonamy, IRS-UN, University of Nantes, license number: B-44-278). Experiments were approved by the local veterinary committee (License number: CEEA.2013.2).

Mice were 7–10 weeks old at the time of experiments and were grafted using intraperitoneal injection with 5×10^6 SHIN-3-Luc+ cells in 0.3 mL of phosphate buffer saline.

Monitoring of Ovarian Peritoneal Carcinomatosis by Bioluminescence

One hundred microliters of luciferin solution (12 mg/mL) was injected intraperitoneally 5 min before the acquisition of images (17). The mice were then anesthetized in an airtight container containing 3.5% of isoflurane (Abbott Laboratories) and isoflurane was maintained using a nose cone delivery system when passing under the “photon Imager” camera (Biospace Lab). Images were taken for each mouse for 1 min on both sides (in prone and supine positions). All images were analyzed (software M3viewer 2.2, Biospace Lab) while determining a specific region of interest (ROI) encompassing the entire surface of the mouse (except tail). For each mouse, each time point was the sum of the photon counts obtained in both prone and supine positions.

Cytoreductive Surgery and Postoperative Residual Volume Determination

Cytoreductive surgery was performed 14 days ($n = 4$) and 29 days ($n = 2$) after injection of 5×10^6 SHIN-3-Luc+ cells. Mice were anesthetized following intraperitoneal injection of 100 μ L/10 g anesthetic solution (consisting of 1 mL ketamine at 100 mg/mL, Panpharma; 0.5 mL xylazine at 20 mg/mL, Bayer; and 8.5 mL PBS). A midline laparotomy was performed. Thorough exploration of the abdominal cavity was carried out using magnifiers for the 13 standard regions defined by Sugarbaker (6) and adapted to rodents by Klaver et al. (18). For the present study, descriptions of tumor damage by Peritoneal Carcinomatosis Index (PCI) scores are summarized in **Figure 1**. Scores from 0 to 3 were defined for each region (0): no macroscopic tumor; (1): lesion from 1 to 2 mm, 1 to 2 sites; (2): lesion from 2 to 4 mm, 1 to 2 sites; and (3): lesion over 4 mm or more than 10 sites. The total PCI score was calculated as the sum of the score for each region and could thus range from 0 to 39. All observed nodules were resected using an electric scalpel blade. At the end of the procedure, the quality of the exeresis was described and classified using a “completeness of cytoreduction” (CC) score adapted from Sugarbaker (6) and Klaver et al. (18): CC0: absence of macroscopic residue, CC1: tumoral residue below 2.5 mm, and CC2: tumoral residue above 2.5 mm. The lining was sutured along two planes. Postoperative analgesia was provided by i.p. injection of 0.20 μ L buprenorphine at 0.3 mg/mL (Axience), repeated after 12 h, followed by oral administration of anti-inflammatory drugs (Ibuprofen, 7.5 mg/kg, Wyeth).

Bioluminescent imaging was carried out after cytoreductive surgery while the animals were still under anesthesia to evaluate the correlation between postoperative residual tumor volume and bioluminescence signal.

Determination of the Optimal Time of Treatment After Engraftment

Eleven mice were grafted with 5×10^6 SHIN-3-Luc+ cells (control mice). Bioluminescence imaging was performed 1, 2, 3, 7, 11, 14,

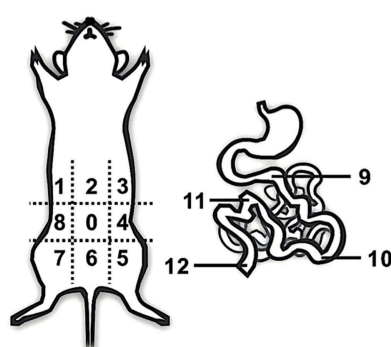
18, and 21 days after engraftment. To determine the time after engraftment mimicking the postoperative residual tumor volume, i.e., time of HIPEC/alpha-RIT treatment, bioluminescence signals were compared to those obtained from the four and two mice which had cytoreductive surgery 14 and 29 days after engraftment, respectively.

HIPEC

Mice were anesthetized in an induction chamber and maintained using a mask (isoflurane 1.5%). Mice were placed on a heat pad and a 1–2-cm midline incision was made. The instillation tube and a multiperforated suction appliance were inserted inside the abdomen and cisplatin was administered (Generic Merck, 37.5 mg/mL or 75 mg/m²). The Erlenmeyer flask containing the cisplatin was placed in a water bath heated to 49°C, and administration was achieved using a peristaltic pump (3 mL/min). The temperature of the intraperitoneal solution was 39°C as previously described by Muller et al. (19) and was regularly checked using a thermal probe. The tubes were often repositioned in the abdominal cavity and the abdomen was regularly massaged. After 60 min, the lining was sutured along two planes using Vicryl® 4-0. The animal recovered consciousness under a heat lamp and postoperative analgesia was provided as previously described.

B-B4 Radiolabeling with Bismuth-213 and In vivo Alpha-RIT

B-B4 was conjugated with the chelating agent CHX-A"-DTPA (Macrocyclics) according to the protocol described by Supiot et al. (20). The bismuth-213 was eluted from the actinium-225/bismuth-213 generator using a solution composed of 500 μ L of 0.2 M NaI and 500 μ L of 0.2 N HCl (21). One hundred micrograms of antibody, along with 195 μ L of 4 M NaOAc buffer solution and 75 μ L of 20% ascorbic acid were added. After 10 min at 37°C, the antibody was purified of free bismuth-213 on a PD-10 desalting column (GE Healthcare) in 0.3 mL PBS fractions. The fractions with highest activity were combined and the total activity was assessed using a NaI detector (X-ray test). Next, ²¹³Bi-B-B4 was filtered through a 0.2 μ m filter (Whatman, Anotop 10) before being injected i.p.



		Score	Tumor size
0	Central abdomen		
1	Right upper quadrant		
2	Epigastric region	0	no macroscopic lesion
3	Left upper quadrant		
4	Left middle quadrant	1	Lesion from 1 to 2 mm, 1 to 2 sites
5	Left lower quadrant		
6	Pubic region		
7	Right lower quadrant	2	Lesion from 2 to 4 mm, 1 to 2 sites
8	Right middle quadrant		
9	Proximal jejunum		
10	Distal jejunum	3	lesion over 4 mm or more than 10 sites
11	Proximal ileum		
12	Distal ileum		

FIGURE 1 | Peritoneal carcinomatosis index (PCI) in mice. Exploration of the 13 standard regions of the abdominal cavity was carried out using magnifiers according to the descriptions of tumor damage by PCI scoring adapted from those of Klaver et al. (18) and Sugarbaker (6).

(from 350 to 430 μ L). The specific activity after filtration was 0.48 ± 0.07 MBq/ μ g of mAb.

Three days after engraftment, for alpha-RIT, 7.4 MBq or 11.1 MBq of ^{213}Bi -B-B4 were injected and for the HIPEC + alpha-RIT group, 7.4 MBq of ^{213}Bi -B-B4 were injected immediately after HIPEC surgery, either during or after recovery.

Animal Monitoring

Every week, the mice were weighed, clinically assessed and bioluminescence imaging was carried out. The animals were sacrificed if they met the ethical conditions of euthanasia; signs of abnormal behavior (difficulty moving and feeding), excessive weight loss, major ascites. Next, an autopsy was performed on all mice. For each animal the tumor volume was assessed and assigned a PCI score. The endpoint of the study was set at 90 days. Blood samples were collected into tubes containing 5% EDTA. Platelets, white, and red blood cells were counted by a quantitative automated hematology analyzer (Melet-Schloesing).

Statistical Analysis

Statistical analysis was conducted via GraphPad Prism software (GraphPad Software Inc., San Diego CA). Analysis of the different groups of treated mice at the end of the study was conducted using a two-way repeated measures variance analysis (two-way ANOVA). Corrections for the multiple groups were carried out using Bonferroni tests. Comparison of postoperative average signals of bioluminescence was obtained using a Student's *t*-test with 4 degrees of freedom. Finally, survival was examined by means of a Kaplan–Meier survival curve and log-rank test analysis.

RESULTS

Expression of CD138 and CEA by SHIN-3-Luc+ Cells

The expression of CD138 by SHIN-3-Luc+ cells was compared to that of CEA which has previously been used as a RIT target (22). The data relating to flow cytometry analysis of SHIN-3-Luc+ cells (**Figure 2**) show that CD138 expression was 10 times higher than that of CEA (MFI of 26,825 and 2,530, respectively).

Ovarian Peritoneal Carcinomatosis Model

Female nude mice were injected with 5×10^6 SHIN-3-Luc+ cells. The first ascitic fluid was apparent on day 27 after grafting. The distribution of nodules was very heterogeneous and disseminated as shown in **Figures 3A,B**, closely mimicking human ovarian peritoneal carcinomatosis. A similar heterogeneity and dissemination were observed from the bioluminescence signal acquisition (**Figure 3C**).

Determining the Correspondence Between Postoperative Residual Tumor Volume and Bioluminescence Signal

Currently, therapies such as HIPEC or RIT are considered as adjuvant therapies applied immediately before or after cytoreductive

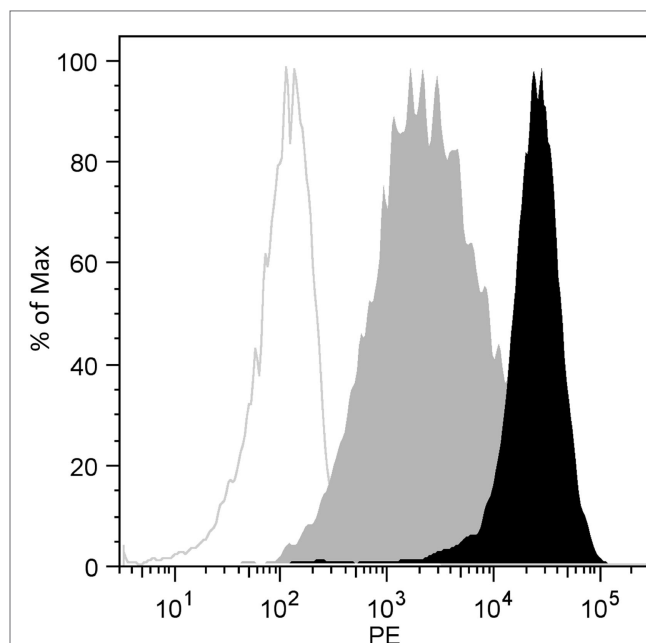


FIGURE 2 | CD138 and CEA expression by flow cytometry. The SHIN-3-Luc+ cells were incubated in the presence of a saturating dose of anti-CD138 (IgG1 mouse, B-B4, black), anti-CEA (IgG1 mouse, T84.66; gray), or an isotype control antibody (IgG1 mouse, gray line). One representative experiment (out of 3 independent experiments) is shown.

surgery. In order to treat animals in a comparable manner while avoiding cytoreductive surgery, the postoperative residual tumor volume was assessed by bioluminescence imaging on 6 mice grafted with 5×10^6 SHIN-3-Luc+ cells. Four mice with a total PCI score ranging from 2 to 5 (2, 3, 3, and 5) had cytoreductive surgery on day 14. After the procedure, the CC was between 0 and 1 (0, 0, 1, and 1). Two other mice with a total PCI score of 6 and 11, respectively, had cytoreductive surgery on day 29. Both mice had a CC score of 1 after the surgery.

Bioluminescence signals obtained postoperatively from these mice operated 14 and 29 days after engraftment were, respectively, $4.9 \times 10^5 \pm 3.3 \times 10^5$ counts ($n = 4$) and $3.7 \times 10^5 \pm 1.7 \times 10^5$ counts ($n = 2$). The comparison of these two means using a Student's *t*-test with 4 degrees of freedom did not show any significant difference ($p < 0.005$). Hence, a postoperative bioluminescence signal was established at 4.3×10^5 counts accumulated per mouse corresponding to postoperative residual tumor volume (i.e., CC between 0 and 1).

Determining by Bioluminescence the Day After Engraftment Mimicking Postoperative Residual Tumor Volume

Bioluminescence was measured for 11 mice from 1 to 21 days after engraftment. **Figure 4** shows the progression of the disease expressed as the evolution of the bioluminescence signals according to the day after the engraftment. Postoperative bioluminescence signals of 4.9×10^5 counts, 3.7×10^5 counts and 4.3×10^5 counts reported on the y-axis of **Figure 4** (see insert), correspond

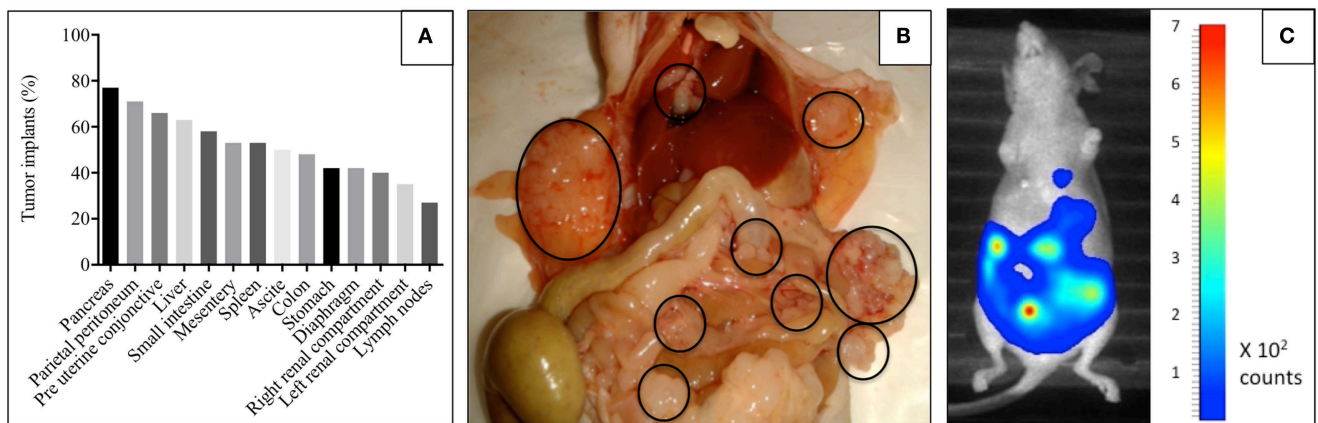


FIGURE 3 | SHIN-3-Luc+ ovarian peritoneal carcinomatosis model in nude mice. (A) Shows the frequency in the localization of intra-abdominal tumoral damage in nude mice after grafting with 5×10^6 SHIN-3-Luc+ cells. These evaluations were carried out on all mice during cytoreductive surgery or following death. **(B)** Is a photograph illustrating the distribution of tumoral lesions in the abdominal cavity in a nude mouse with a graft of 5×10^6 SHIN-3-Luc+ cells after sacrifice. Circles highlight visible tumor lesions. **(C)** Is a photograph illustrating the bioluminescence signal measured with the photon imager.

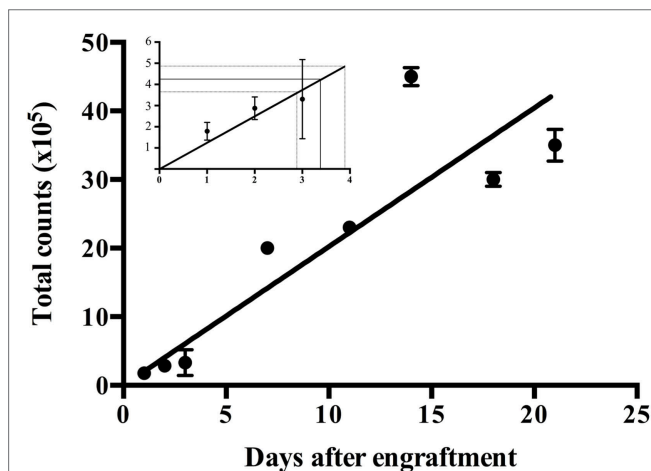


FIGURE 4 | Progression of the bioluminescence signal according to the day after engraftment. Bioluminescence signals were measured for 11 mice up until 21 days after engraftment. The insert focuses on the first 4 days after engraftment. The day after engraftment mimicking the postoperative residual tumor volume, i.e., the disease status after cytoreductive surgery, was determined by reporting the postoperative bioluminescence signals on the y-axis to against the corresponding day on the x-axis.

on the x-axis to an interval of one day, just before day 3 and day 4, after engraftment. Day 3 was defined as the day after engraftment mimicking the postoperative residual tumor volume, i.e., the disease status after cytoreductive surgery.

To verify the tumor status 3 days after engraftment, five mice grafted with 5×10^6 SHIN-3-Luc+ cells were sacrificed after bioluminescence imaging 3 days later ($3.9 \times 10^5 \pm 1.6 \times 10^5$ counts). As shown in **Table 1**, the total PCI score for each mouse was 3, 3, 1, 2, and 1. All tumor lesions were less than 2 mm as the PCI score for each region was never >1 . Thus, the tumor status of each mouse at day 3 was equivalent to a CC score <1 .

Treatment of Residual Tumor Volume

In two independent experiments, 49 mice were randomly assigned to the different treatment groups which were initiated on day 3 after the graft. A first experiment included control ($n = 6$), HIPEC only ($n = 5$), alpha-RIT 7.4 MBq ($n = 6$), and HIPEC + alpha-RIT 7.4 MBq ($n = 5$) groups. The second experiment included control ($n = 5$), HIPEC only ($n = 5$), alpha-RIT 7.4 MBq ($n = 5$), alpha-RIT 11.1 MBq ($n = 7$), and HIPEC + alpha-RIT 7.4 MBq ($n = 5$) groups. During HIPEC, the intraperitoneal temperatures of both the HIPEC and the HIPEC + alpha-RIT groups remained at a stable average temperature of 39°C. Two intraoperative deaths were observed.

Clinical Results

The mice receiving HIPEC treatment alone had a weight loss of 2 g at day 4 after the treatment, equal to that of the alpha-RIT groups, while those from the HIPEC + alpha-RIT group experienced a weight loss of 4 g (**Figure 5**). At day 7, the mice treated with alpha-RIT recovered their initial weights. On the contrary, the weights of HIPEC and HIPEC + alpha-RIT mice were never restored (**Figure 5**).

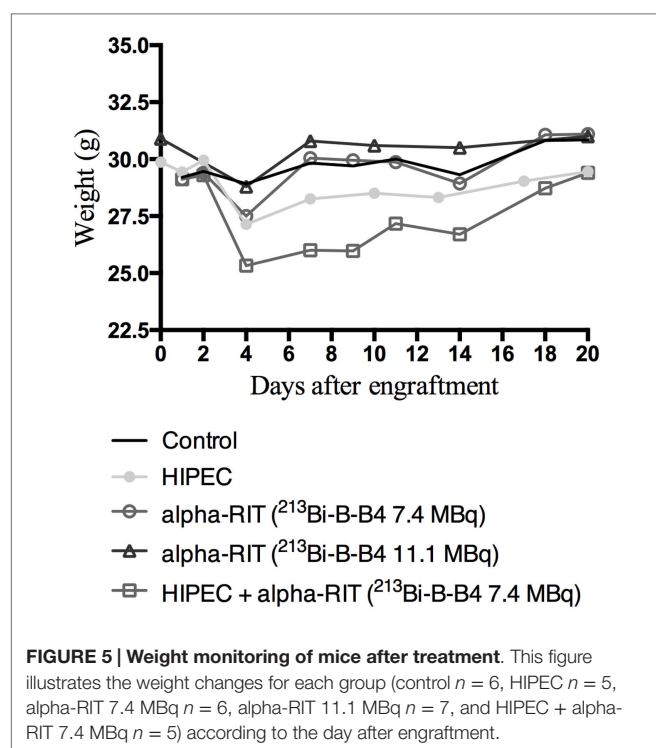
Bioluminescence Results and PCI-Scoring

Figure 6 shows changes in the bioluminescence signal for each mouse in relation to the treatment received. These results show that the bioluminescence signal was much weaker for the groups having received alpha-RIT. Only the curves relating to HIPEC come close to matching those of the mice receiving no treatment.

At sacrifice, the abdominal cavity of the mice was explored to establish the PCI score. The average PCI score was compared to the average maximal bioluminescence signal, with results showing a correlation of the two parameters. Indeed, for the control group an average PCI of 32.4 was found for a maximal average bioluminescence signal of 2.7×10^7 photon counts. For the HIPEC group only a PCI average of 26.6 with an average

TABLE 1 | PCI scoring 3 days after engraftment in the 13 standard regions ($n = 5$).

	Region number													Total PCI
	0	1	2	3	4	5	6	7	8	9	10	11	12	
Mouse 1	0	0	0	1	0	0	1	0	1	0	0	0	0	3
Mouse 2	0	0	0	0	0	0	0	1	1	0	0	0	1	3
Mouse 3	0	0	1	0	0	0	0	0	0	0	0	0	0	1
Mouse 4	0	0	0	1	0	0	0	1	0	0	0	0	0	2
Mouse 5	0	0	0	1	0	0	0	0	0	0	0	0	0	1



maximal bioluminescence signal of 2.2×10^7 counts, for the combined HIPEC + alpha-RIT group a PCI average of 28.5 for an average maximal bioluminescence signal of 1.2×10^7 counts, and for the alpha-RIT group at 7.4 MBq an average PCI of 10.6 with a maximal average bioluminescence signal of 0.45×10^7 counts.

Toxicity

In terms of blood toxicity, **Figure 7** shows a transient but nonetheless insignificant reduction in platelets and white blood cells for all treatments. For HIPEC alone, a substantial reduction in red blood cells was highlighted 51 days after treatment with no hemorrhage being observed.

Survival

The survival curves are shown in **Figure 8**. The first deaths occurred intraoperatively for the mice from the HIPEC + alpha-RIT group and the HIPEC group (two deaths on the day of the procedure). Similarly, the two groups receiving HIPEC experienced the most premature deaths (two on day 8 after the graft

and one on day 13 after the graft), without evident causes being established via autopsies. Median survival was 68 days for the control group, 75.5 days for the combined HIPEC + alpha-RIT group and 37.5 days for the HIPEC group. Median survival rates for the groups having received RIT alone cannot be calculated, given that over 50% of the mice were still alive at the end of the experiment. Indeed, at 90 days, seven mice out of 11 (63.6%) were still alive in the group receiving alpha-RIT 7.4 MBq and five out of seven (71.4%) in the group with alpha-RIT 11.1 MBq. In this last group, one mouse was sacrificed due to major weight loss and the necropsy could only establish two small millimeter-sized tumoral nodules. As compared to the control group curve, HIPEC and HIPEC + alpha-RIT curves were not significantly different whereas alpha-RIT 7.4 MBq and alpha-RIT 11.1 MBq were significantly different ($p = 0.0303$ and $p = 0.0070$, respectively).

DISCUSSION

The present preclinical study is the first to compare and combine HIPEC and alpha-RIT for the treatment of ovarian peritoneal carcinomatosis in a model mimicking postoperative residual tumor illness. Alpha-RIT, combining anti-CD138, and bismuth-213 showed a substantial increase in overall survival in correlation with low bioluminescence signals. However, HIPEC did not show significant improvements in terms of survival but did show a reduction in median survival and disease progression measured by bioluminescence, similar to the control group. Finally, a combination of both therapies did not show significant improvements in overall survival. With an uncertain prognosis (3) and based on residual tumor volume after surgery (4, 5), the development of innovative therapies in EOC is required for reliable and reproducible preclinical models. Our model based on SHIN-3 cells offers the advantage of rapidly establishing peritoneal carcinoma disease (**Figure 3**) that is identical to that found in advanced ovarian cancer.

Cytoreductive surgery plays a key role in the treatment of EOC, and disease prognosis depends on the degree of its success (5). The possibility of applying this surgery to preclinical models on animals has been demonstrated, notably with rats for colon cancer (18, 23) but also with mice (24). Nevertheless, the teams studying therapies targeting postoperative residual tumor volume seek to amend surgery, and administer their therapies at an early stage of the graft, often day 1 or day 2, under the assumption that the tumor volume must be the same at day 1 and day 2 (24), without taking into account the viability of the graft at

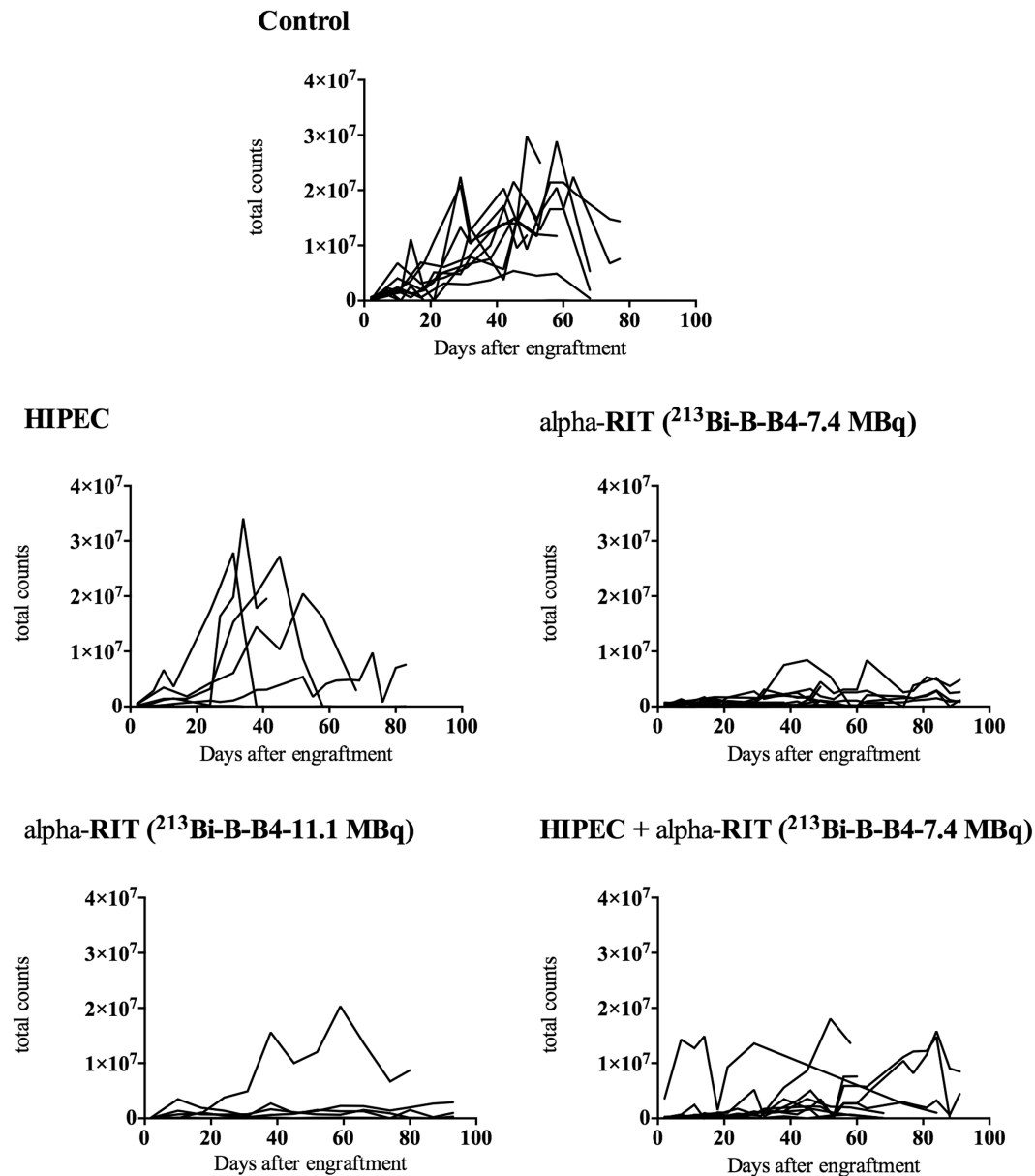
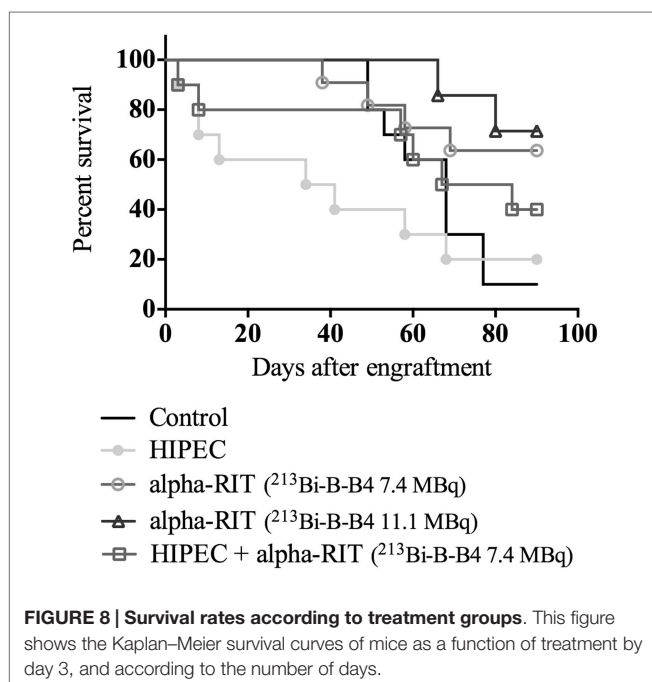
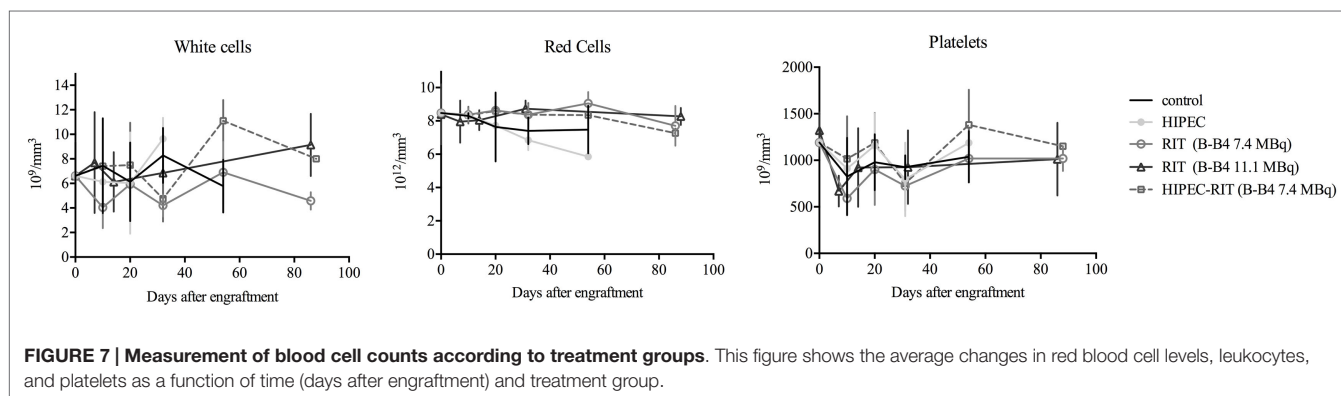


FIGURE 6 | Changes in bioluminescence signal in relation to treatment received. This figure shows changes in bioluminescence signal for each group treated (control $n = 11$, HIPEC $n = 7$, alpha-RIT 7.4 MBq $n = 11$, alpha-RIT 11.1 MBq $n = 7$, and HIPEC + alpha-RIT 7.4 MBq $n = 10$) as a function of time (days after engraftment). For each mouse and each time point, the sum of the bioluminescence signal obtained in both the prone and the supine positions is represented.

this early stage. Our cytoreductive surgery model performed on 6 mice has enabled us to determine the correspondence between the bioluminescence signal obtained immediately after surgery and the one obtained after engraftment. We therefore decided to treat the animals on day 3 in order to be as close as possible to the postoperative state of the tumor. Finally, cytoreductive surgery was performed in the context of PCI scoring between 2 and 11, corresponding to advanced phases of disease, with the results of cytoreduction (CC 0–1) similar to those obtained in the clinic (7).

RIT has been used for EOC treatment since the 1980s (25) with constant clinical inefficiency of RIT using beta particles (13). However, the efficacy of alpha particle vectorization has been demonstrated in preclinical ovarian cancer models (15), subsequently leading to a phase I clinical trial (26). In our study, we used bismuth-213 as an alpha-particle emitter. Although the half-life of bismuth-213 (45 min) seems theoretically more advantageous than that of astatine-211 (7.2 h) with the aim of restricting intraperitoneal cavity activity, a study by Gustafsson has shown similar effects between two alpha particle emitters



(27). The activities of bismuth-213 used in our study (7.4 and 11.1 MBq) did not result in acute blood toxicity and are consistent with a study by Song et al. (28) which showed, for an antibody injected by i.p., a MTD of 35 MBq for a nude mouse of 30g. In the same manner, HIPEC, developed to improve the benefits of intraperitoneal chemotherapy while amending inflammatory procedures, may be worthwhile as a direct application of intra-operative RIT on difficult or partial areas of resection so as to target residual disease.

CD138 or syndecan-1 belongs to the heparan sulfate proteoglycan family and is often targeted during RIT treatments. Two studies have examined the expression of CD138 in ovarian cancer: the first (10) revealed the presence of CD138 in benign tumors and the borderline of the ovary, and in adenocarcinomas (present in epithelial and stromal cells), while not being expressed by healthy ovarian tissue. The second study showed higher CD138 expression in all cancer types compared to healthy ovarian tissue, without any correlation in terms of chemoresistance or exposure

to estrogens (11). Therefore, we considered CD138 as a potential innovative target antigen for the treatment of ovarian cancer by RIT, in the same way as other emerging targets such as Her2 (29) or VEGF (30). This choice was strengthened by the results that we obtained in this study on CD138 expression and RIT. CD138-targeted alpha-RIT results in a marked difference in terms of bioluminescence signals (Figure 6). Furthermore, as shown in Figure 8, we observed a significant increase in survival (63.6 and 71.4%, respectively) at 90 days for the alpha-RIT 7.4 MBq ($p = 0.0303$) and alpha-RIT 11.1 MBq ($p = 0.0070$) groups compared with 10% for the untreated mice. In addition, the mice treated with alpha-RIT experienced lower weight loss than the other groups, and a markedly lower tumor volume at necropsy (PCI average of 10.6).

The HIPEC technique used in this study was designed to reproduce as faithfully as possible the technique used on humans with EOC, consisting of a semiopen procedure with cisplatin perfusion at 3 mL/min (24). In France, cisplatin is the most frequent chemotherapeutic product used in ovarian HIPEC (7). Doses $>80 \text{ mg/m}^2$ result in renal failure (31). In this study, the concentration of cisplatin was 75 mg/m^2 or 2 mg/kg . The upper intraperitoneal temperature limit tolerated was 40°C , as bowel lesions can occur in rodents at higher temperatures (32). In a preliminary study, we demonstrated that using temperatures above 40°C on SHIN-3 cells required an increase in the concentration of cisplatin in order to obtain a similar cytotoxic effect (19).

In the present study, the group receiving HIPEC alone did not show any differences in terms of bioluminescence signal (Figure 6) or overall survival (Figure 8) compared to the control group. Median survival of these animals is even lower than that of the control group: 34 versus 68 days. There is a paucity of mouse studies evaluating cisplatin-based HIPEC in EOC. A study on the impact of the addition of sodium arsenite and variations in temperature in cisplatin HIPEC did not include survival as an assessment criterion and all the animals were euthanized from day 1 (24). In preclinical studies on colon cancer, HIPEC is associated with intense toxicity and a general worsening state, including lethargy, substantial weight loss, and bacterial translocations (33). However, we did not observe intense toxicity in our group of animals treated with HIPEC. Indeed, on average, initial weight loss of 2 g was observed, which was equivalent to the alpha-RIT-treated group, and below that of the combined

HIPEC + alpha-RIT-treated group. Similarly, blood sample analysis did not indicate greater toxicity in this group. In 2010, Klaver et al. compared the survival of cancer bearing rats treated by cytoreductive surgery alone or combined cytoreductive surgery and HIPEC, with greater survival for animals treated by HIPEC surgery (18). Next we combined HIPEC and alpha-RIT for the first time in an animal model. The alpha-RIT injection was carried out immediately after HIPEC, and only one mouse had to be reinjected with alpha-RIT due to leakage of the radiolabeled vector. While the bioluminescence curve appeared different to the control group (Figure 6), no significant difference was noted in terms of survival (Figure 8). Examination of the survival curve of the HIPEC + alpha-RIT group, showed early deaths potentially due to the toxicity of the combined treatments. This hypothesis is supported by the higher initial weight loss in this group (4 g), but did not correlate with toxicity as measured by blood sample analysis (Figure 7). Second, this group displayed fewer deaths and mice appeared similar to those of the groups treated with alpha-RIT. Currently, no study has associated these two treatments. Only one Dutch team has compared them in two separate studies. The first used rats with peritoneal carcinoma of colorectal origin treated by HIPEC or alpha-RIT after cytoreductive surgery was focused on animal survival (34). A second study, using the same model, focused on the impact of these treatments on abdominal healing after surgery (35). In the first study, concerning survival (34), the results are in favor of alpha-RIT, with a non-significant increase in survival for the HIPEC group compared to the control group.

CONCLUSION

The present study indicates the potential therapeutic effect of alpha-RIT in EOC. It demonstrates that the use of postoperative

alpha-RIT in a context mimicking the residual tumor after cytoreductive surgery dramatically increased survival rates of mice with peritoneal carcinomatosis of ovarian origin. Under the same conditions, HIPEC treatment alone or combined HIPEC + alpha-RIT did not offer significant improvements to survival rates. We believe alpha-RIT provides a potentially interesting alternative adjuvant treatment along with cytoreductive surgery in the treatment of ovarian cancer. Furthermore, our study has extended the scope of available target antigens for RIT, showing that CD138 can be used effectively to target peritoneal carcinoma cells.

AUTHOR CONTRIBUTIONS

Conceived and designed the experiments: AD, SG, and MC. Performed the experiments: AD, SG, CM, J-MC, and MC. Analyzed the data: AD, SG, J-MC, and MC. Wrote the paper: AD, SG, M-HG, and MC.

ACKNOWLEDGMENTS

We would like to thank Sandrine Minault and Sylvia Lambot (CRCNA) for their technical help as well as the UTE and Radioactivity facilities (SFR François Bonamy, IRS-UN, University of Nantes).

FUNDING

This work has been supported in part by grants from the French National Agency for Research, called “Investissements d’Avenir” IRON Labex no. ANR-11-LABX-0018-01 and ArronaxPlus Equipex no. ANR-11-EQPX-0004.

REFERENCES

- Guerin S, Doyon F, Hill C. [The frequency of cancer in France in 2006, mortality trends since 1950, incidence trends since 1980 and analysis of the discrepancies between these trends]. *Bull Cancer* (2009) **96**:51–7. doi:10.1684/bdc.2008.0795
- Leitao MM Jr, Kardos S, Barakat RR, Chi DS. Tertiary cytoreduction in patients with recurrent ovarian carcinoma. *Gynecol Oncol* (2004) **95**:181–8. doi:10.1016/j.ygyno.2004.07.033
- Dowdy SC, Constantinou CL, Hartmann LC, Keeney GL, Suman VJ, Hillman DW, et al. Long-term follow-up of women with ovarian cancer after positive second-look laparotomy. *Gynecol Oncol* (2003) **91**:563–8. doi:10.1016/j.ygyno.2003.08.036
- Bristow RE, Tomacruz RS, Armstrong DK, Trimble EL, Montz FJ. Survival effect of maximal cytoreductive surgery for advanced ovarian carcinoma during the platinum era: a meta-analysis. *J Clin Oncol* (2002) **20**:1248–59. doi:10.1200/JCO.20.5.1248
- Eisenkop SM, Spirtos NM, Friedman RL, Lin WC, Pisani AL, Peticucci S. Relative influences of tumor volume before surgery and the cytoreductive outcome on survival for patients with advanced ovarian cancer: a prospective study. *Gynecol Oncol* (2003) **90**:390–6. doi:10.1016/S0090-8258(03)00278-6
- Sugarbaker PH. Intraperitoneal chemotherapy and cytoreductive surgery for the prevention and treatment of peritoneal carcinomatosis and sarcomatosis. *Semin Surg Oncol* (1998) **14**:254–61. doi:10.1002/(SICI)1098-2388(199804/05)14:3<254::AID-SSU10>3.0.CO;2-U
- Bakrin N, Bereder JM, Decullier E, Classe JM, Msika S, Lorimier G, et al. Peritoneal carcinomatosis treated with cytoreductive surgery and hyperthermic intraperitoneal chemotherapy (HIPEC) for advanced ovarian carcinoma: a French multicentre retrospective cohort study of 566 patients. *Eur J Surg Oncol* (2013) **39**:1435–43. doi:10.1016/j.ejso.2013.09.030
- Le Brun JF, Campion L, Berton-Rigaud D, Lorimier G, Marchal F, Ferron G, et al. Survival benefit of hyperthermic intraperitoneal chemotherapy for recurrent ovarian cancer: a multi-institutional case control study. *Ann Surg Oncol* (2014) **21**:3621–7. doi:10.1245/s10434-014-3693-7
- Classe JM, Glehen O, Decullier E, Bereder JM, Msika S, Lorimier G, et al. Cytoreductive surgery and hyperthermic intraperitoneal chemotherapy for first relapse of ovarian cancer. *Anticancer Res* (2015) **35**:4997–5005.
- Davies EJ, Blackhall FH, Shanks JH, David G, McGown AT, Swindell R, et al. Distribution and clinical significance of heparan sulfate proteoglycans in ovarian cancer. *Clin Cancer Res* (2004) **10**:5178–86. doi:10.1158/1078-0432.CCR-03-0103
- Helpman L, Katz BZ, Safra T, Schreiber L, Levine Z, Nemzer S, et al. Systematic antigenic profiling of hematopoietic antigens on ovarian carcinoma cells identifies membrane proteins for targeted therapy development. *Am J Obstet Gynecol* (2009) **201**(196):e1–7. doi:10.1016/j.ajog.2009.05.013
- Tomblyn MB, Katin MJ, Wallner PE. The new golden era for radioimmunotherapy: not just for lymphomas anymore. *Cancer Control* (2013) **20**:60–71.
- Verheijen RH, Massuger LF, Benigno BB, Epenetos AA, Lopes A, Soper JT, et al. Phase III trial of intraperitoneal therapy with yttrium-90-labeled HMFG1 murine monoclonal antibody in patients with epithelial ovarian cancer after a surgically defined complete remission. *J Clin Oncol* (2006) **24**:571–8. doi:10.1200/JCO.2005.02.5973
- Meredith RF, Buchsbaum DJ, Alvarez RD, Lobuglio AF. Brief overview of preclinical and clinical studies in the development of intraperitoneal radioimmunotherapy for ovarian cancer. *Clin Cancer Res* (2007) **13**:5643s–5s. doi:10.1158/1078-0432.CCR-07-0985

15. Elgqvist J, Andersson H, Back T, Claesson I, Hultborn R, Jensen H, et al. Alpha-radioimmunotherapy of intraperitoneally growing OVCAR-3 tumors of variable dimensions: outcome related to measured tumor size and mean absorbed dose. *J Nucl Med* (2006) 47:1342–50.
16. Imai S, Kiyozuka Y, Maeda H, Noda T, Hosick HL. Establishment and characterization of a human ovarian serous cystadenocarcinoma cell line that produces the tumor markers CA-125 and tissue polypeptide antigen. *Oncology* (1990) 47:177–84. doi:10.1159/000226813
17. Berger F, Paulmurugan R, Bhaumik S, Gambhir SS. Uptake kinetics and biodistribution of ¹⁴C-D-luciferin – a radiolabeled substrate for the firefly luciferase catalyzed bioluminescence reaction: impact on bioluminescence based reporter gene imaging. *Eur J Nucl Med Mol Imaging* (2008) 35:2275–85. doi:10.1007/s00259-008-0870-6
18. Klaver YL, Hendriks T, Lomme RM, Rutten HJ, Bleichrodt RP, De Hingh IH. Intraoperative hyperthermic intraperitoneal chemotherapy after cytoreductive surgery for peritoneal carcinomatosis in an experimental model. *Br J Surg* (2010) 97:1874–80. doi:10.1002/bjs.7249
19. Muller M, Cherel M, Dupre PF, Gouard S, Collet M, Classe JM. Cytotoxic effect of hyperthermia and chemotherapy with platinum salt on ovarian cancer cells: results of an in vitro study. *Eur Surg Res* (2011) 46:139–47. doi:10.1159/000324395
20. Supiot S, Faivre-Chauvet A, Couturier O, Heymann MF, Robillard N, Kraeber-Bodere F, et al. Comparison of the biologic effects of MA5 and B-B4 monoclonal antibody labeled with iodine-131 and bismuth-213 on multiple myeloma. *Cancer* (2002) 94:1202–9. doi:10.1002/cncr.10286
21. Brechbiel MW. Targeted alpha-therapy: past, present, future? *Dalton Trans* (2007) 43:4918–28. doi:10.1039/b704726f
22. Juweid M, Swayne LC, Sharkey RM, Dunn R, Rubin AD, Herskovic T, et al. Prospects of radioimmunotherapy in epithelial ovarian cancer: results with iodine-131-labeled murine and humanized MN-14 anti-carcinoembryonic antigen monoclonal antibodies. *Gynecol Oncol* (1997) 67:259–71. doi:10.1006/gyno.1997.4870
23. Aarts F, Hendriks T, Boerman OC, Koppe MJ, Oyen WJ, Bleichrodt RP. A comparison between radioimmunotherapy and hyperthermic intraperitoneal chemotherapy for the treatment of peritoneal carcinomatosis of colonic origin in rats. *Ann Surg Oncol* (2007) 14:3274–82. doi:10.1245/s10434-007-9509-2
24. Muenyi CS, States VA, Masters JH, Fan TW, Helm CW, States JC. Sodium arsenite and hyperthermia modulate cisplatin-DNA damage responses and enhance platinum accumulation in murine metastatic ovarian cancer xenograft after hyperthermic intraperitoneal chemotherapy (HIPEC). *J Ovarian Res* (2011) 4:9. doi:10.1186/1757-2215-4-9
25. Hunter RE, Doherty P, Griffin TW, Gionet M, Hnatowich DJ, Bianco JA, et al. Use of indium-111-labeled OC-125 monoclonal antibody in the detection of ovarian cancer. *Gynecol Oncol* (1987) 27:325–39. doi:10.1016/0090-8258(87)90254-X
26. Andersson H, Cederkrantz E, Back T, Divgi C, Elgqvist J, Himmelman J, et al. Intraperitoneal alpha-particle radioimmunotherapy of ovarian cancer patients: pharmacokinetics and dosimetry of (211)At-MX35 F(ab')₂ – a phase I study. *J Nucl Med* (2009) 50:1153–60. doi:10.2967/jnumed.109.062604
27. Gustafsson AM, Back T, Elgqvist J, Jacobsson L, Hultborn R, Albertsson P, et al. Comparison of therapeutic efficacy and biodistribution of ²¹³Bi- and ²¹¹At-labeled monoclonal antibody MX35 in an ovarian cancer model. *Nucl Med Biol* (2012) 39:15–22. doi:10.1016/j.nucmedbio.2011.07.003
28. Song EY, Qu CF, Rizvi SM, Raja C, Beretov J, Morgenstern A, et al. Bismuth-213 radioimmunotherapy with C595 anti-MUC1 monoclonal antibody in an ovarian cancer ascites model. *Cancer Biol Ther* (2008) 7:76–80. doi:10.4161/cbt.7.1.5132
29. Milenic DE, Wong KJ, Baidoo KE, Nayak TK, Regino CA, Garmestani K, et al. Targeting HER2: a report on the in vitro and in vivo pre-clinical data supporting trastuzumab as a radioimmunoconjugate for clinical trials. *MAbs* (2010) 2:550–64. doi:10.4161/mabs.2.5.13054
30. Ashrafi SA, Hosseinimehr SJ, Varmira K, Abedi SM. Radioimmunotherapy with 131I-bevacizumab as a specific molecule for cells with overexpression of the vascular endothelial growth factor. *Cancer Biother Radiopharm* (2012) 27:420–5. doi:10.1089/cbr.2012.1224
31. Leopold KA, Oleson JR, Clarke-Pearson D, Soper J, Berchuck A, Samulski TV, et al. Intraperitoneal cisplatin and regional hyperthermia for ovarian carcinoma. *Int J Radiat Oncol Biol Phys* (1993) 27:1245–51. doi:10.1016/0360-3016(93)90550-F
32. Lehmann K, Rickenbacher A, Jang J, Oberkofler CE, Vonlanthen R, Von Boehmer L, et al. New insight into hyperthermic intraperitoneal chemotherapy: induction of oxidative stress dramatically enhanced tumor killing in vitro and in vivo models. *Ann Surg* (2012) 5:730–7. doi:10.1097/SLA.0b013e3182737517
33. Pelz JO, Doerfer J, Hohenberger W, Meyer T. A new survival model for hyperthermic intraperitoneal chemotherapy (HIPEC) in tumor-bearing rats in the treatment of peritoneal carcinomatosis. *BMC Cancer* (2005) 5:56. doi:10.1186/1471-2407-5-56
34. Aarts F, Koppe MJ, Hendriks T, Van Eerd JE, Oyen WJ, Boerman OC, et al. Timing of adjuvant radioimmunotherapy after cytoreductive surgery in experimental peritoneal carcinomatosis of colorectal origin. *Ann Surg Oncol* (2007) 14:533–40. doi:10.1245/s10434-006-9247-x
35. Aarts F, Bleichrodt RP, De Man B, Lomme R, Boerman OC, Hendriks T. The effects of adjuvant experimental radioimmunotherapy and hyperthermic intraperitoneal chemotherapy on intestinal and abdominal healing after cytoreductive surgery for peritoneal carcinomatosis in the rat. *Ann Surg Oncol* (2008) 15:3299–307. doi:10.1245/s10434-008-0070-4

Conflict of Interest Statement: The authors declare that the research was conducted in the absence of any commercial or financial relationships that could be construed as a potential conflict of interest.

Copyright © 2015 Derrien, Gouard, Maurel, Gaugler, Bruchertseifer, Morgenstern, Faivre-Chauvet, Classe and Chérel. This is an open-access article distributed under the terms of the Creative Commons Attribution License (CC BY). The use, distribution or reproduction in other forums is permitted, provided the original author(s) or licensor are credited and that the original publication in this journal is cited, in accordance with accepted academic practice. No use, distribution or reproduction is permitted which does not comply with these terms.



Single-dose anti-CD138 radioimmunotherapy: bismuth-213 is more efficient than lutetium-177 for treatment of multiple myeloma in a preclinical model

OPEN ACCESS

Edited by:

Denis Guilloteau,
Université de Tours and CHRU Tours,
France

Reviewed by:

Roger Schibli,
Paul Scherrer Institute, Switzerland
Damien Huglo,
University of Lille, France
Elisabet Esteve Manasanch,
University of Texas, USA

*Correspondence:

Nolwenn Fichou
nolwenn.fichou@univ-nantes.fr

[†]These authors contributed equally
to this work

[‡]These authors share senior
co-authorship

Specialty section:

This article was submitted to Nuclear
Medicine, a section of the
journal *Frontiers in Medicine*

Received: 30 July 2015

Accepted: 19 October 2015

Published: 04 November 2015

Citation:

Fichou N, Gouard S, Maurel C,
Barbet J, Ferrer L, Morgenstern A,
Bruchertseifer F, Faivre-Chauvet A,
Bigot-Corbel E, Davodeau F,
Gaschet J and Chérel M (2015)
Single-dose anti-CD138
radioimmunotherapy: bismuth-213 is
more efficient than lutetium-177 for
treatment of multiple myeloma in a
preclinical model.
Front. Med. 2:76.
doi: 10.3389/fmed.2015.00076

Nolwenn Fichou^{1,2,3*†}, Sébastien Gouard^{1,2,3†}, Catherine Maurel^{1,2,3}, Jacques Barbet^{1,2,3},
Ludovic Ferrer^{1,2,3,4}, Alfred Morgenstern⁵, Frank Bruchertseifer⁵, Alain Faivre-Chauvet^{1,2,3,6},
Edith Bigot-Corbel^{1,2,3}, François Davodeau^{1,2,3}, Joëlle Gaschet^{1,2,3‡} and Michel Chérel^{1,2,3,4‡}

¹ Centre Régional de Recherche en Cancérologie Nantes/Angers (CRCNA) – UMR 892 INSERM, Université de Nantes,
Nantes, France, ² CNRS 6299, Université de Nantes, Nantes, France, ³ Université de Nantes, Nantes, France, ⁴ Institut de
Cancérologie de l'Ouest, Saint-Herblain, France, ⁵ Institute for Transuranium Elements, Karlsruhe, Germany, ⁶ Nuclear
Medicine Department, CHU Nantes, Nantes, France

Objectives: Radioimmunotherapy (RIT) has emerged as a potential treatment option for multiple myeloma (MM). In humans, a dosimetry study recently showed the relevance of RIT using an antibody targeting the CD138 antigen. The therapeutic efficacy of RIT using an anti-CD138 antibody coupled to ²¹³Bi, an α -emitter, was also demonstrated in a preclinical MM model. Since then, RIT with β -emitters has shown efficacy in treating hematologic cancer. In this paper, we investigate the therapeutic efficacy of RIT in the 5T33 murine MM model using a new anti-CD138 monoclonal antibody labeled either with ²¹³Bi for α -RIT or ¹⁷⁷Lu for β -RIT.

Methods: A new monoclonal anti-CD138 antibody, 9E7.4, was generated by immunizing a rat with a murine CD138-derived peptide. Antibody specificity was validated by flow cytometry, biodistribution, and α -RIT studies. Then, a β -RIT dose-escalation assay with the ¹⁷⁷Lu-radiolabeled 9E7.4 mAb was performed in KalwRij C57/BL6 mice 10 days after i.v. engraftment with 5T33 MM cells. Animal survival and toxicological parameters were assessed to define the optimal activity.

Results: α -RIT performed with 3.7 MBq of ²¹³Bi-labeled 9E7.4 anti-CD138 mAb increased median survival to 80 days compared to 37 days for the untreated control and effected cure in 45% of animals. β -RIT performed with 18.5 MBq of ¹⁷⁷Lu-labeled 9E7.4 mAb was well tolerated and significantly increased mouse survival (54 vs. 37 days in the control group); however, no mice were cured with this treatment.

Conclusion: This study revealed the advantages of α -RIT in the treatment of MM in a preclinical model where β -RIT shows almost no efficacy.

Keywords: lutetium-177, bismuth-213, multiple myeloma, CD138, radioimmunotherapy

INTRODUCTION

Multiple myeloma (MM) represents 1% of all cases of cancer and 10% of hematological malignancies (1). The physiopathology of MM consists of an uncontrolled proliferation of a monoclonal plasma cell in the bone marrow, resulting in the abnormal secretion of a monoclonal immunoglobulin, known as paraprotein, which can be detected in patients' serum or urine. Common features of MM include organ damage due to plasma cell proliferation – also known as CRAB (hypercalcemia, renal failure, anemia, and bone diseases) – at least one focal lesion, and a ratio of involved:uninvolved circulating light chain higher than 100 (2, 3). Depending on the patient's age, standard clinical care comprises high-dose therapy, which may be combined with autologous stem cell transplantation (4). Although new drugs such as bortezomib and lenalidomide, and new indications, such as for thalidomide, have significantly improved the overall survival rate for patients, MM remains an incurable disease. Therefore, treatments must be constantly improved and new drugs or new strategies continuously assessed.

In the past two decades, radioimmunotherapy (RIT) has emerged as a novel strategy in the anti-cancer arsenal. This therapeutic approach consists in specifically targeting tumor cells using an antibody coupled with a radionuclide. The radionuclide can then kill tumor cells by direct cytotoxicity as well as through a bystander effect (5–9). Among the radionuclides which have been tested in clinical trials, there are a few β^- emitters, such as ^{131}I , ^{90}Y , ^{177}Lu , and a number of α -emitters such as ^{213}Bi , ^{211}At , or ^{225}Ra (10–15). The efficacy of RIT depends on the choice of radionuclide, which is determined by the vector and the nature of the cancer (16). Indeed, the characteristics of α - and β -ionizing radiation differ, with α -particles having a much higher linear energy transfer than β^- emitters. Their range of penetration into tissues also differs: 50–100 μm for α -particles vs. 2–10 mm for β^- particles. Based on these characteristics, α -particles appear better suited to treating disseminated cancer or micrometastases. The proof of concept of α -RIT in humans was provided by a clinical trial using an anti-CD33 mAb coupled to ^{213}Bi as a treatment for myeloid leukemia (17). In this study, which was conducted in patients with large tumor burdens, no significant extramedullary toxicity was observed, nor was any complete response elicited supporting the hypothesis that α -RIT is more appropriate for treating small tumor volumes, residual disease, and micrometastases. Several clinical trials using β -RIT have also shown promising results with hematologic diseases, such as non-Hodgkin's lymphomas (NHL) (18, 19) and with solid tumors, such as metastatic prostate cancer (20, 21). ^{177}Lu appears to be an excellent candidate for RIT because of its short range of action (2 mm in tissues). This range is similar to that of ^{131}I (2.9 mm), but shorter than that of ^{90}Y (11 mm). This characteristic may reduce non-specific radiation damage to surrounding healthy tissues. In addition, its low γ -emission (208 keV) is an advantage in terms of radioprotection.

Our group has recently proven RIT to be effective in treating MM in humans (22) and α -RIT to be effective in an immunocompetent preclinical MM model (23). Both studies were performed with antibodies targeting the CD138 antigen, which is expressed by more than 95% of MM cells (24). CD138, or syndecan-1, is a

member of the syndecan family of heparan sulfate proteoglycans; it is expressed by epithelial cells, precursor B cells, and normal plasma cells. It is also expressed at high levels in MM tumors (24–26) and is a key regulator in the disease (27). Finally, high levels of CD138 in patient serum are associated with poor prognosis in MM disease progression (28–30).

Based on our study in MM patients with ^{131}I -CD138 mAb (22), and the promising results obtained in treatment of NHL patients with β -RIT using an anti-CD20 mAb labeled with ^{90}Y and ^{177}Lu (18, 19), we decided to investigate the therapeutic efficacy of β -RIT in a preclinical model of MM using an anti-CD138 mAb coupled to ^{177}Lu . We first generated and validated a new murine anti-CD138 antibody (9E7.4 mAb) and confirmed that it could effectively treat MM tumors using α -RIT. Then, we studied the tissue distribution of ^{177}Lu -9E7.4 mAb and went on to perform dose-escalation and toxicity studies. Finally, we administered ^{177}Lu -9E7.4 at different times during disease progression.

MATERIALS AND METHODS

Reagents, Cell Lines, and Mice

The bifunctional chelators S-2-(4-Isothiocyanatobenzyl)-1,4,7,10-tetraazacyclododecane tetraacetic acid (p-SCN-Bn-DOTA) and 2-(4-isothiocyanato-benzyl)-cyclohexyl-diethylethylamine-penta-acetic (SCN-CHX-A"-DTPA) were purchased from Macrocyclics (USA). $^{177}\text{LuCl}_3$ was purchased from Perkin Elmer (France) in 0.05 N HCl and $^{225}\text{Ac}/^{213}\text{Bi}$ generator was obtained from the Institute for Transuranium Elements (Karlsruhe, Germany). All buffers were prepared in H_2O milliQ (0.2 μm ; 3 ppb; 18 M Ω) and Trace SELECT chemicals, when available. Rat IgG2a, κ anti-mouse CD138 antibody (clone 281-2) (ref.553712) was purchased from BD Pharmingen (France).

The 5T33 murine MM cell line was kindly provided by Dr. Harvey Turner (Department of Nuclear Medicine, Fremantle Hospital, Western Australia) with permission from Dr. J. Radl (TNO Institute, Leiden, The Netherlands) (31, 32). The SP2/o-Ag14 myeloma cell line (ATCC® CRL-1581™) and the CTLL-2 T lymphocyte cell line (ATCC® TIB-214™) were purchased from ATCC. All cell lines were cultured in RPMI 1640 medium (Life Technologies, France) containing 2 mM L-glutamine, 100 U/mL penicillin/100 $\mu\text{g}/\text{mL}$ streptomycin and 10% heat-inactivated fetal calf serum (Life Technologies, France). Cells were incubated at 37°C, 5% CO_2 in a humidity-saturated incubator.

Female C57BL/KalwRij mice were purchased from Harlan CPB and housed under conventional conditions at the UTE animal facility (SFR François Bonamy, IRS-UN, University of Nantes, license number: B-44-278). Experiments were approved by the local veterinary committee (License No. CEEA.2013.2). Mice were 8–12 weeks old at the time of experiments.

Anti-CD138 9E7.4 mAb Production and Characterization

The 9E7.4 mAb was produced by immunization of a rat with a 40-amino-acid peptide (GeneCust, Luxembourg) derived from the murine CD138 protein (aa 90–130) (GenBank: CAA80254.1). The isotype of 9E7.4 immunoglobulin was determined using a

Rat Isotyping Kit (RMT1, AbD serotec, UK) according to the manufacturer's instructions.

The specificity and affinity of 9E7.4 mAb for CD138 were determined by flow cytometry (FACS Calibur™, BD Biosciences). Staining was detected indirectly with a secondary antibody, anti-rat IgG/PE (Jackson-ImmunoResearch Laboratories).

Anti-CD138 mAb Conjugation

A reaction solution containing a 20M excess of p-SCN-Bn-DOTA or SCN-CHX-A"-DTPA over the 9E7.4 mAb in 0.3M carbonate buffer pH 8.7 was incubated overnight (16 h) at room temperature (RT). Free chelator was eliminated and the conjugation buffer was exchanged for 0.25M NH₄OAc, pH 7 (DOTA-9E7.4 mAb) or for PBS (CHX-A"-DTPA-9E7.4 mAb) by several centrifugal filtration steps using a 30-kDa cutoff Centricon concentrator (Amicon, Millipore). Integrity of the immunoconjugate was verified by size-exclusion HPLC. The conjugated 9E7.4 mAb was filtered through a 0.2-μm filter before storage at 4°C. The number of chelators per antibody was estimated at between 1 and 4 for p-SCN-Bn-DOTA and 2 for SCN-CHX-A"-DTPA by an ¹¹¹In dilution assay (23) and/or mass spectrometry.

Anti-CD138 mAb Radiolabeling

¹⁷⁷Lu-chloride (370 MBq) was added to a solution containing DOTA-9E7.4 mAb, prepared in 0.25M NH₄OAc pH 7 and 0.05M ascorbic acid buffer pH 5.5, and was adjusted to pH 5.5 with 0.5M NH₄OAc. The reaction mixture was incubated at 42 ± 1°C for 3 h. Complexation was then stopped by adding a 10M excess of EDTA and mixing for 15 min at RT. Labeling of anti-CD138 9E7.4 mAb with ²¹³Bi was performed as described in Chérel et al. (23). Radiiodination of anti-CD138 antibodies was performed as described in Fraker and Speck (33). All radiolabeled immunoconjugates were purified by gel filtration on a Sephadex G-25 PD-10 desalting column (GE Healthcare Life Science, France) and eluted in 0.9% NaCl. The radiochemical purity was verified by instant thin layer chromatography (ITLC-SG) as described in Koppe et al. (34), using citrate buffer (0.1M pH 4.5) as the mobile phase. For all experiments, purities of the ¹⁷⁷Lu and ²¹³Bi immunoconjugates were >98%, and purity of the ¹²⁵I immunoconjugate was >95%. The immunoreactive fraction of the radiolabeled conjugates was determined using CD138-peptide-coated magnetic beads. In all cases, the immunoreactive fraction was estimated at ≥80%.

Biodistribution

To determine the biodistribution of anti-mouse CD138 mAb, 3 μg of ¹²⁵I immunoconjugate were administered intravenously (i.v.) to tumor-free C57BL/KalwRij (*n* = 3 in each group). Mice were sacrificed 5 min, 4, and 24 h later. To study the tissue distribution of ¹⁷⁷Lu-9E7.4 mAb, 3 μg were i.v. injected into tumor-free C57BL/KalwRij (*n* = 3 in each group). Mice were sacrificed 5 min, 2, 8, 24, 48, 96, or 168 h later. For all experiments, tissues were collected and radioactivity was counted using a γ-counter (Wizard 1480, PerkinElmer, France). To account for physical decay of radioactivity, a triplicate standard dose was counted alongside the samples, and results were expressed as a percentage of injected dose per gram of tissue.

Dose-Escalation and Therapeutic Studies

Mice were engrafted with 1 × 10⁶ 5T33 MM cells. α-RIT was then performed on day 10 and β-RIT on day 10, 15, or 20. Animal survival was monitored over time. Mice were sacrificed when paralysis was detected and/or their weight dropped by 20%. In some cases, tumor masses were detected. For α-RIT, a single dose of 3.7 MBq ²¹³Bi-9E7.4 mAb (*n* = 20) was injected i.v., in line with the previously described protocol (23). For β-RIT, a dose-escalation study was performed with i.v. injection of 3.7 (*n* = 14), 7.4 (*n* = 5), 11.1 (*n* = 5), 14.8 (*n* = 5), 18.5 (*n* = 15), 27.75 (*n* = 11), or 37 MBq (*n* = 7) ¹⁷⁷Lu-9E7.4 mAb at a specific activity of 1480 ± 74 MBq/mg of antibody.

Toxicity Study

To assess hematologic toxicity, blood was collected from the retro-orbital sinus for leukocyte, erythrocyte, and thrombocyte counting on an automated hematology analyzer (Melet-Schloesing Laboratories, France). Plasma was isolated from blood samples, pooled, and then used to monitor bone marrow, liver, and kidney toxicity based on the following biomarkers: Flt3-L – measured at different time points using DuoSet ELISA kits (DY427, R&D System, France), according to the supplier's instructions – ASAT, ALAT, urea, and creatinin – concentrations of these markers were monitored using a Roche Cobas Analyzer (Roche, Meylan, France) with the appropriate reagents (Roche, Meylan, France).

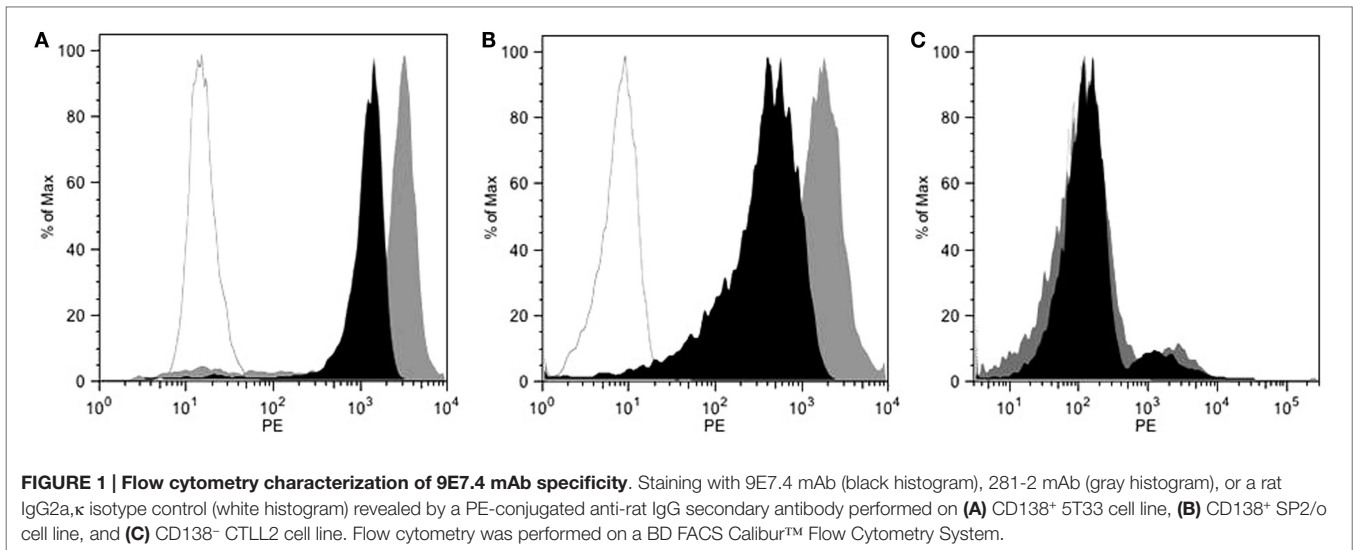
Statistical Analyses

Data are presented as mean ± SEM. Statistical significance was determined using the Mann-Whitney test. Animal survival data were analyzed using Kaplan-Meier survival curves combined with the log-rank test. All statistical analyses were performed using GraphPad Prism® software (GraphPad Software).

RESULTS

Characterization and Validation of the 9E7.4 Antibody

The 9E7.4 mAb was produced by immunizing a rat with a 40-aa peptide derived from the extracellular domain of murine CD138. The isotype of this antibody was determined to be IgG2a,κ, and its binding specificity was initially validated by ELISA using the 40-aa peptide (data not shown). This specificity was confirmed by flow cytometry on different cell lines and compared to that of 281-2 mAb, a commercial anti-mouse CD138 mAb, which we had previously used (23) (Figure 1). The two anti-CD138 mAbs could bind to CD138-expressing MM cell lines 5T33 and SP2/o, whereas no binding to the negative control cell line was observed in either case. An *in vitro* competition assay indicated that these two anti-CD138 mAbs bind to different epitopes on CD138 (data not shown). The binding affinity for mAbs 281-2 and 9E7.4 on 5T33 MM cells was comparable: 1 × 10⁻¹⁰ and 2.3 × 10⁻¹⁰M, respectively (data not shown). However, maximal binding of the 281-2 mAb was at least twofold more intense than 9E7.4 mAb binding (Figure 1). This difference in maximal binding led us to investigate the *in vivo* behavior of the 9E7.4 anti-CD138 mAb based on its tissue

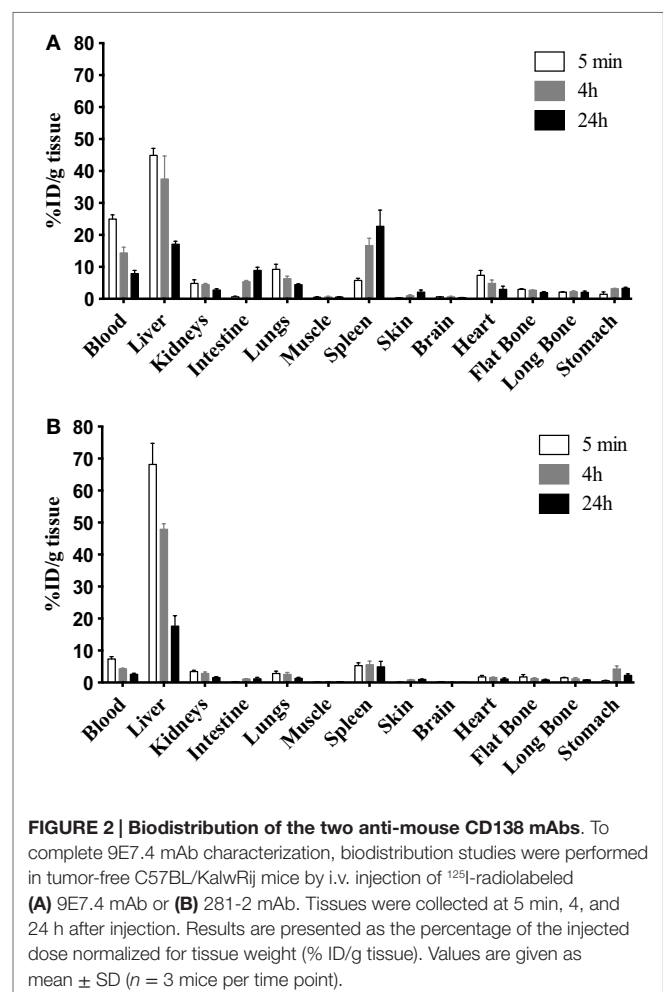


distribution. The two mAbs were ^{125}I -radioiodinated before injection into tumor-free C57BL/KalwRij mice, animals were sacrificed at 5 min, 4, and 24 h and the percentage injected dose per gram of tissue (% ID/g tissue) was calculated (Figure 2). These results showed the 9E7.4 mAb and the 281-2 mAb to distribute differently in blood, liver, and spleen. Five minutes after administration, $25 \pm 1.3\%$ ID/g tissue for 9E7.4 mAb was detected in the blood compared to $7.4 \pm 0.8\%$ ID/g tissue for 281-2 mAb. ^{125}I -281-2 mAb was taken up at a higher level in the liver compared to the ^{125}I -9E7.4 mAb, which could explain this difference. Liver uptake might be in part related to CD138 expression by mouse hepatocytes as the liver is a hematopoietic organ in mouse (35, 36). Differences were also noted for spleen uptake, with 9E7.4 mAb uptake increasing over time, whereas 281-2 mAb uptake remained stable. This difference may be related to the lower liver uptake, and the higher level of circulating 9E7.4 mAb molecules. Consequently, more molecules could reach the spleen and bind to the CD138⁺ plasma cells present in this secondary lymphoid organ (37). Beyond blood, liver, and spleen, the overall tissue distribution was quite comparable for the two mAbs, with a low uptake in other healthy organs.

To further endorse the specificity and relevance of the 9E7.4 mAb, α -RIT using ^{213}Bi was performed and the results compared with those from our previous study using the 281-2 mAb (23). Applying the same protocol as described in Chérel et al. (23), 1×10^6 5T33 MM cells were engrafted in mice, and α -RIT was performed by injecting 3.7 MBq of ^{213}Bi -radiolabeled 9E7.4 mAb 10 days later. Survival results are presented in Figure 3 and show that α -RIT significantly increased median survival (80 days) compared to the control group (37 days). Moreover, no mice survived in the control group, whereas 45% of the mice treated by α -RIT were still alive 110 days after tumor engraftment. All these data validated the use of 9E7.4 mAb in therapy.

Biodistribution of ^{177}Lu -9E7.4 mAb

The tissue distribution of 9E7.4 mAb labeled with ^{177}Lu was also studied in tumor-free C57BL/KalwRij. Results are presented at different time points after injection in Figure 4. Five minutes after



injection, $27.9 \pm 1.4\%$ ID/g tissue of antibody was detected in blood. As with ^{125}I -9E7.4 mAb, a relatively high liver uptake was observed ($45.9 \pm 6.9\%$ ID/g tissue). This level of uptake was due to specific binding, as confirmed by comparison with a ^{177}Lu -isotype

control (data not shown). Uptake of ^{177}Lu -9E7.4 mAb was also high in the spleen ($27.6 \pm 8.2\%$ ID/g tissue between 2 and 48 h) and in the intestines ($18.8 \pm 9.1\%$ ID/g tissue at 24 and 48 h) (Figure 4). Finally, accumulation of the ^{177}Lu -9E7.4 mAb in other healthy organs was similar to what has been described with other radioimmunoconjugates (38).

Dose-Escalation Study with ^{177}Lu -9E7.4 mAb

Next, we tested the efficacy of β -RIT using the ^{177}Lu -radiolabeled 9E7.4 mAb in the 5T33 MM mouse model. As above, mice were engrafted with 1×10^6 5T33 MM cells 10 days before injecting seven different activities of ^{177}Lu -9E7.4 mAb ranging from 3.7 to 37 MBq (Figure 5A). No statistical difference in median survival compared to the control group (37 days) was observed in any group receiving an activity below 18.5 MBq, indicating that below 18.5 MBq, β -RIT had no therapeutic efficacy (Figure 5B). By contrast, survival was significantly increased compared to the control group in mice injected with 18.5 MBq, reaching 54 days. Nevertheless, even

with this level of activity, no long-term survival was observed. Interestingly, the group which received 27.75 MBq exhibited a median survival of 48 days, which, although slightly higher than the control group (37 days), is lower than that obtained with 18.5 MBq. Once again, none of the mice survived. This effect was even more dramatic in the 37 MBq group, where median survival was reduced to 22 days – considerably less than the control group. In this group, no sign of paralysis was detected, but all mice had to be sacrificed due to excessive weight loss (Figure S1 in Supplementary Material) suggestive of toxicity rather than MM disease.

Together, these results indicate that 18.5 MBq of ^{177}Lu -9E7.4 mAb provides optimal activity in this murine MM model, increasing median survival. However, this activity is not sufficient to cure MM.

Toxicity Study

To determine whether the limited efficacy of β -RIT was due to toxicity, we first assessed hematologic toxicity. To do this, leukocyte, erythrocyte, and thrombocyte counts were monitored in the blood at different time points after initiating treatment (Figure 6). Results were normalized against the initial cell counts – before engraftment – and are expressed as percentages. Eleven days after β -RIT with 3.7 MBq, the leukocyte count was reduced by 24.5%; levels returned to normal at day 32 after initiation of the treatment (Figure 6A). With the 18.5 and 27.75 MBq activities, a dramatic nadir was reached with a decrease in leukocyte count of 75.5 and 81.1%, respectively (Figure 6A). A return to normal levels was only achieved with the 18.5 MBq activity 40 days after treatment, while in the 27.75 MBq group, leukocyte counts remained extremely low until the end of the study. Figure 6B shows that no major variations in erythrocyte counts were noted at any activity. By contrast, thrombocytes were also reduced by 26.3% for the 18.5 MBq group and 48.1% for the 27.75 MBq group (Figure 6C). These reductions occurred later than the drop in leukocyte counts at day 22 after β -RIT. Together, these results indicate that of the cell populations examined (1), leukocytes appear to be the most sensitive to ^{177}Lu ; (2) thrombocytes are also sensitive but to a lesser extent; (3) β -ionizing radiation from ^{177}Lu does not directly affect erythrocytes. The hematologic toxicity observed at 18.5 and

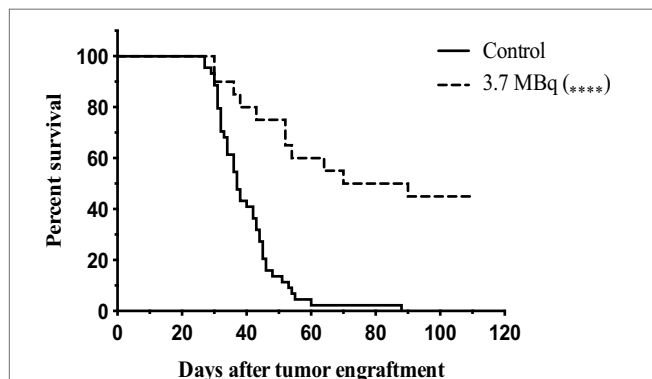


FIGURE 3 | Survival curves after α -RIT with ^{213}Bi -9E7.4 mAb. At day 0, all mice were engrafted with 1×10^6 of 5T33 cells by i.v. injection. α -RIT was performed on day 10 by i.v. administration of 3.7 MBq ^{213}Bi -9E7.4 mAb (dotted line; $n = 20$). The control group (solid line; $n = 44$) received NaCl. p values were determined using the log-rank test and found to be highly significant, **** $p < 0.0001$ (3.7 MBq vs. control).

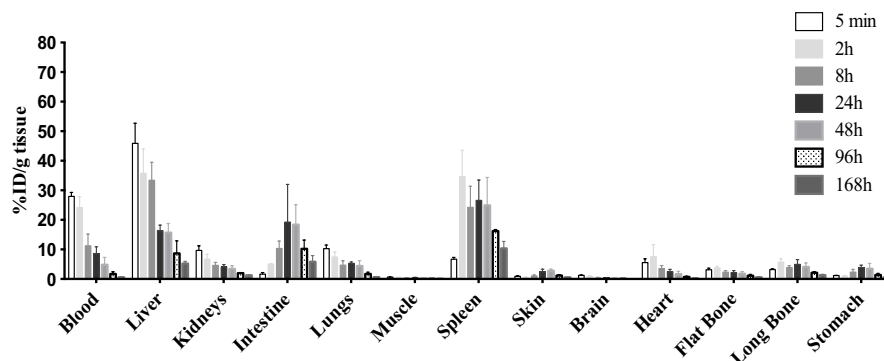


FIGURE 4 | Biodistribution of ^{177}Lu -9E7.4 mAb. The 9E7.4 mAb radiolabeled with ^{177}Lu was injected i.v. into tumor-free C57BL/KalwRij mice ($n = 3$). Tissues were collected 5 min, 2, 8, 24, 48, 96, and 168 h after injection. Results are presented as the percentage of the injected dose normalized for tissue weight (% ID/g tissue).

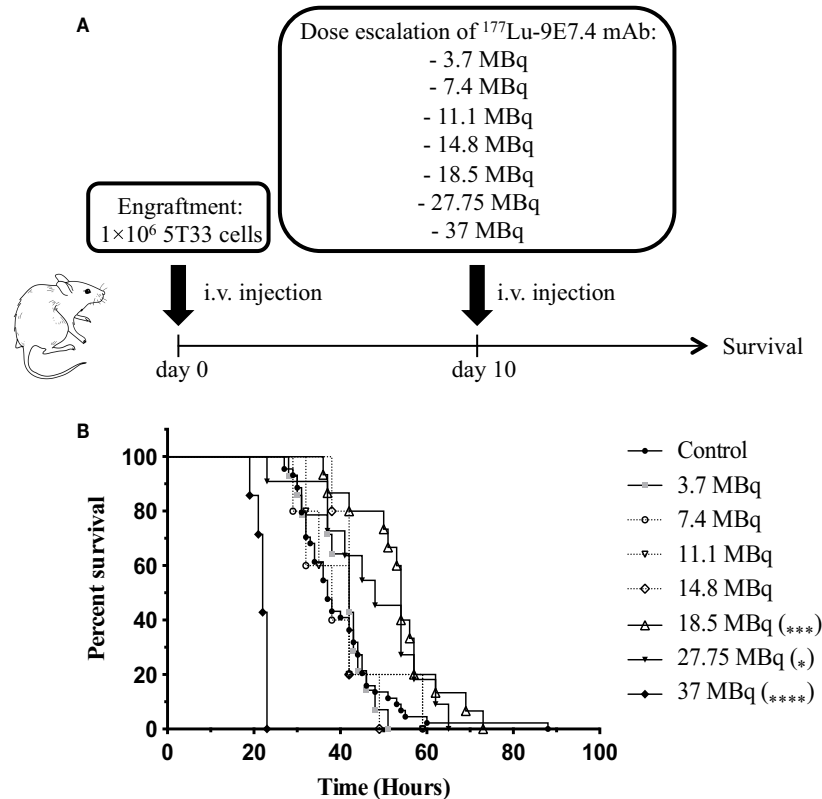


FIGURE 5 | β -RIT dose-escalation in mice developing MM. (A) Mice were engrafted with 1×10^6 5T33 cells on day 0. On day 10, “treated” mice received various activities of ^{177}Lu -9E7.4 mAb i.v.; “control” mice ($n = 44$) received NaCl. **(B)** Kaplan–Meier survival curves after β -RIT with 3.7 ($n = 14$), 7.4 ($n = 5$), 11.1 ($n = 5$), 14.8 ($n = 5$), 18.5 ($n = 15$), 27.75 ($n = 11$), and 37 MBq ($n = 7$) of ^{177}Lu -9E7.4 mAb. **** $p < 0.0001$ (37 MBq vs. control), *** $p = 0.0007$ (18.5 MBq vs. control), and * $p = 0.0367$ (27.75 MBq vs. control), differences between treated and control groups were not statistically significant for other doses. p Values were determined by the log-rank test.

27.75 MBq appears significant but reversible, or almost reversible, and might not be a major contributing factor to the mortality observed in these groups of animals.

We next studied non-hematologic toxicity in the bone marrow by monitoring the Flt3-L concentration in plasma (39) at different time points after β -RIT (Figure 6D). In control mice, the Flt3-L concentration was around 250 pg/mL at all time points, and a similar level was recorded for mice treated with 3.7 MBq. At day 8 after β -RIT, the Flt3-L concentration increased to 500 pg/mL in mice injected with 18.5 and 27.75 MBq of ^{177}Lu -9E7.4 mAb. Levels returned to normal in both groups on around day 32 and 29, respectively, suggesting that myeloid toxicity was mild and reversible. Mice receiving a dose of 37 MBq exhibited a dramatic increase in Flt3-L level, reaching a mean of 1250 pg/mL, indicative of major myeloid toxicity that might account for the rapid mortality observed in that group.

We also assessed liver toxicity by monitoring level of ASAT and ALAT concentrations in plasma and kidney toxicity by measuring uremia and creatinemia. All markers were measured in the plasma at different time points after β -RIT (Figure 7). Figure 7A shows that, as in the control group, mice treated with 3.7, 18.5, and 27.75 MBq showed no variation in ASAT concentrations. In

the 37 MBq group, a dramatic rise (≈ 700 UI/L) was noted 11 days after initiating the treatment. Similar results were observed for ALAT concentration (≈ 250 UI/L) and uremia (a 2.5-fold increase) (Figures 7B,C). Even though we noticed a certain variability in creatinemia over time in all the groups (Figure 7D), we observed a striking 2.5-fold increase in the 37 MBq group. Altogether, these results demonstrate that 37 MBq of ^{177}Lu -9E7.4 mAb induces major liver and kidney toxicities.

β -RIT with More Advanced Myeloma Disease

At the optimal activity of ^{177}Lu -9E7.4 mAb, no cure and no major toxicity were observed in our study. We, therefore, hypothesized that β -RIT might be more efficient in the treatment of more advanced MM disease. Indeed, due to its physical properties, it has been shown that ^{177}Lu is better adapted to the treatment of small solid tumors and metastases (11). We, thus, decided to test β -RIT at day 15 or 20 after tumor engraftment. Survival rates are shown in Figure 8. These data confirmed that survival was improved for mice treated at day 10 (44 days) compared to the control group (31 days). However, median survival for mice

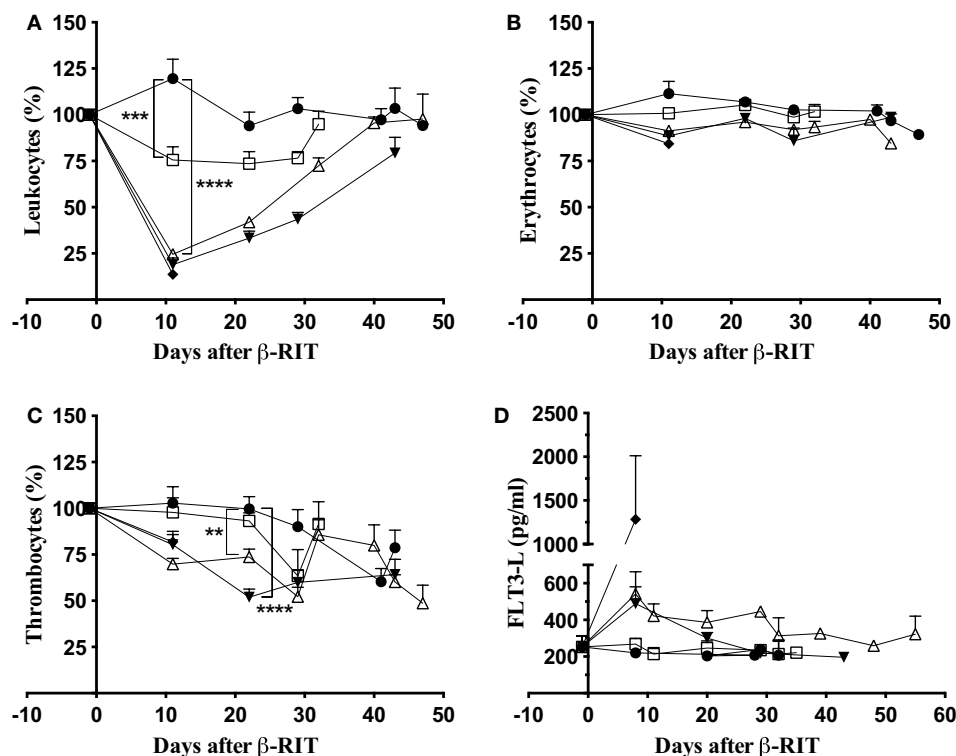


FIGURE 6 | Hematologic and bone marrow toxicity after β -RIT. Mice, engrafted with 1×10^6 5T33 cells, were treated with various ^{177}Lu -9E7.4 mAb activities at day 10: 3.7 MBq (\square), 18.5 MBq (Δ), 27.75 MBq (∇), 37 MBq (\blacklozenge), and control (\bullet). (A) Leukocyte, (B) erythrocyte, and (C) thrombocyte counts were monitored using an automated hematology analyzer. Data represent three independent experiments with $n = 8$ (37 MBq), 11 (27.75 MBq), 14 (3.7 MBq), 15 (18.5 MBq), and 20 (control). Results are presented as mean \pm SEM. ** $p = 0.039$, *** $p = 0.0003$, **** $p < 0.0001$, and p values were determined using the Mann-Whitney test. (D) FLT3-L concentration in plasma was determined by ELISA. Data represent the mean \pm SD for three independent experiments on pooled plasma.

treated at day 15 or 20 after tumor engraftment did not improve further – 38 and 40.5 days, respectively. In addition, once again, no cure was recorded whatever the day of treatment, and none of the mice survived long term in any group. In summary, these results demonstrate that β -RIT is not an efficient treatment even for more advanced MM disease.

DISCUSSION

The literature describes promising results with RIT as a treatment for disseminated cancer or micrometastases. Most of the studies have been done in hematologic cancer and micrometastases [for review, see Ref. (11)]. MM is a malignant hemopathy mainly located in the bone marrow, and RIT has already been shown to be effective in treating human MM through targeting of CD138 (22). Our group has also demonstrated that α -RIT using the 281-2 anti-CD138 mAb is efficient in the treatment of MM in an immunocompetent mouse model (23). All these results suggested that β -RIT, targeting CD138 antigen on tumor cells, could also be a promising approach in this disease.

In this study, we developed a new anti-mouse CD138 mAb, 9E7.4, directed against a CD138-specific 40-aa peptide. Generation of proprietary hybridomas is an essential part of producing bispecific antibodies to reap the full benefit of these

promising theranostic tools in nuclear medicine (40). The affinity of the 9E7.4 mAb for the CD138 antigen was similar to that of the 281-2 mAb, in the range of 10^{-10}M . However, maximal binding of 9E7.4 mAb on CD138-expressing cells was at least twofold lower than maximal binding of 281-2 mAb (Figure 1). This difference might be due to the fact that they do not recognize the same epitope (data not shown), and how the two antibodies were generated. The 9E7.4 mAb was obtained using CD138-peptide immunization, while 281-2 was generated using CD138-expressing cells. Thus, the glycosylation status of the CD138 in the immunization could have been different, and this could influence binding of these antibodies (supported by our unpublished data).

With this new 9E7.4 anti-mouse CD138 mAb, we confirmed our previous results demonstrating that in the 5T33 immunocompetent MM mouse model, a single dose of α -RIT significantly raises median survival (80 vs. 37 days for control, untreated mice) and results in long-term survival for 45% of animals. In contrast, we showed that single-dose β -RIT performed in the same conditions was not sufficient to cure mice developing MM.

This lack of efficacy cannot be ascribed to the new anti-CD138 mAb since α -RIT was effective and tissue distributions of ^{125}I -radioiodinated 281-2 and 9E7.4 mAbs were very similar. The only differences observed were a lower uptake in the liver and a higher uptake in the spleen with both ^{125}I and ^{177}Lu -radiolabeled

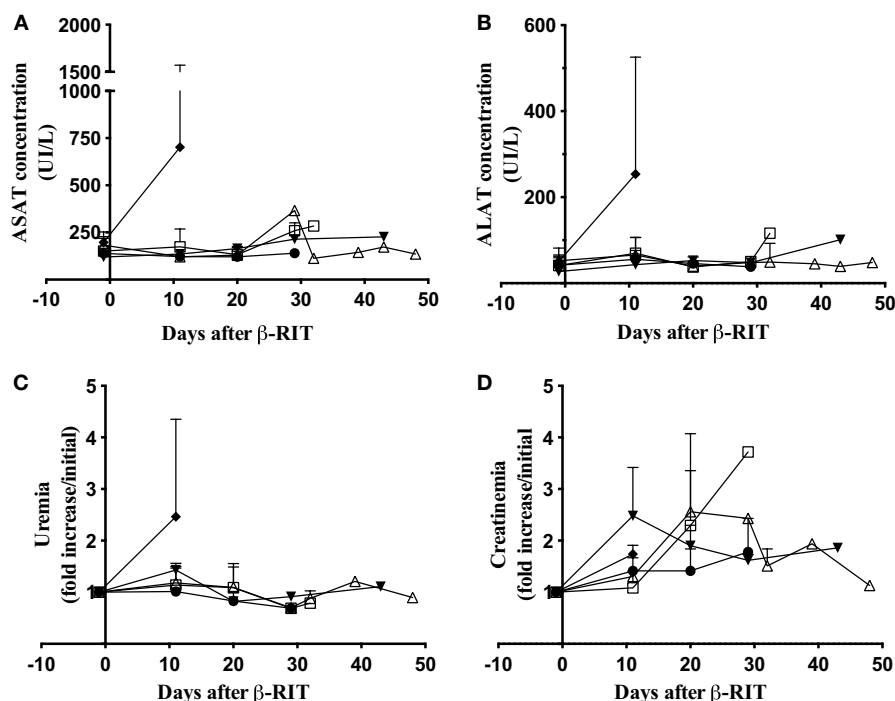


FIGURE 7 | Hepatic and kidney toxicity after β -RIT. (A) ASAT, (B) ALAT, (C) urea, and (D) Creatinin concentrations were measured in pooled plasma from mice in the control group (●) or after β -RIT at 3.7 MBq (□), 18.5 MBq (△), 27.75 MBq (▼), or 37 MBq (◆). Results are expressed as mean \pm SD. Data represent pooled plasma from three independent experiments.

9E7.4 mAb compared to 281-2 mAb. These differences might be explained as mentioned above and will have to be further investigated. However, the difference in liver uptake could be correlated to the lower binding level of 9E7.4 mAb to CD138 compared to 281-2 mAb. Whatever the explanation, our results with ^{177}Lu -9E7.4 mAb suggest that the therapeutic effect of β -RIT is not enough to offset its toxicity. Thus, accumulation of ^{177}Lu -9E7.4 mAb appears to be deleterious in the bone marrow and liver. Many other studies performed with β -emitters have reported dose-limiting toxicity due to hematologic and bone marrow toxicities (19, 20, 41, 42). Here, we observed severe toxicity at 37 MBq at the hematologic, myeloid, hepatic, and kidney levels. Indeed, this activity was lethal and all the mice in this group had to be euthanized soon after RIT due to weight loss without any sign of disease progression (data not shown). A dramatic increase in Flt3-L in plasma confirmed that this treatment induced severe myeloid toxicity, as well as liver and kidney toxicity – as evidenced by ALAT, ASAT, urea, and creatinin plasma concentrations. At 27.75 MBq, overall toxicity was less pronounced, but hematologic toxicity remained significant with a dramatic but almost reversible nadir for leukocytes. In the group of mice treated with 18.5 MBq of ^{177}Lu -9E7.4 mAb, the leukocyte count returned to normal more rapidly. Leukocytes are more sensitive than thrombocytes and erythrocytes because the main target of ionizing radiation is DNA, not present in either of the latter. Moreover, the absence of nucleus and their short life span (7–10 days), suggests that the drop in thrombocyte levels

is probably due to destruction of their precursors in the bone marrow. This hypothesis is supported by the increase in plasma Flt3-L noted for these two groups. Based on the uremia, there was no apparent kidney toxicity in these two groups, although creatinemia indicated a certain level of toxicity at 27.75 MBq. However, this experiment was only performed once and will have to be confirmed. Finally, at these activity levels, no hepatic toxicity was observed, even though it is important to note that in the 27.75 MBq group, one mouse had to be sacrificed soon after treatment as it exhibited the same signs of toxicity as animals in the 37 MBq group. All these results combine to indicate that the potential efficacy of the treatment at 27.75 MBq is counterbalanced by its toxicity. This suggests that 18.5 MBq is not only the maximum tolerated dose, but also that this is the only activity, administered as a single dose, allowing a certain efficacy of the treatment. However, in the group which received 18.5 MBq, despite the lower toxicity and statistical improvement in median survival compared to the control group, no cure was effected. Mice in this group were euthanized because of paralysis and an increase in plasma paraprotein, with one exception (data not shown). Therefore, even if the treatment was associated with some toxicity, animals mainly died due to tumor burden.

^{177}Lu emits β -ionizing radiation in a range of 2 mm within tissues, and the literature indicates that these β -particles are more efficient in hematologic cancers with a high-tumor burden (41). In our hands, 10 days after 5T33 MM engraftment, tumor development was weak, as previously shown using Luciferase-transfected

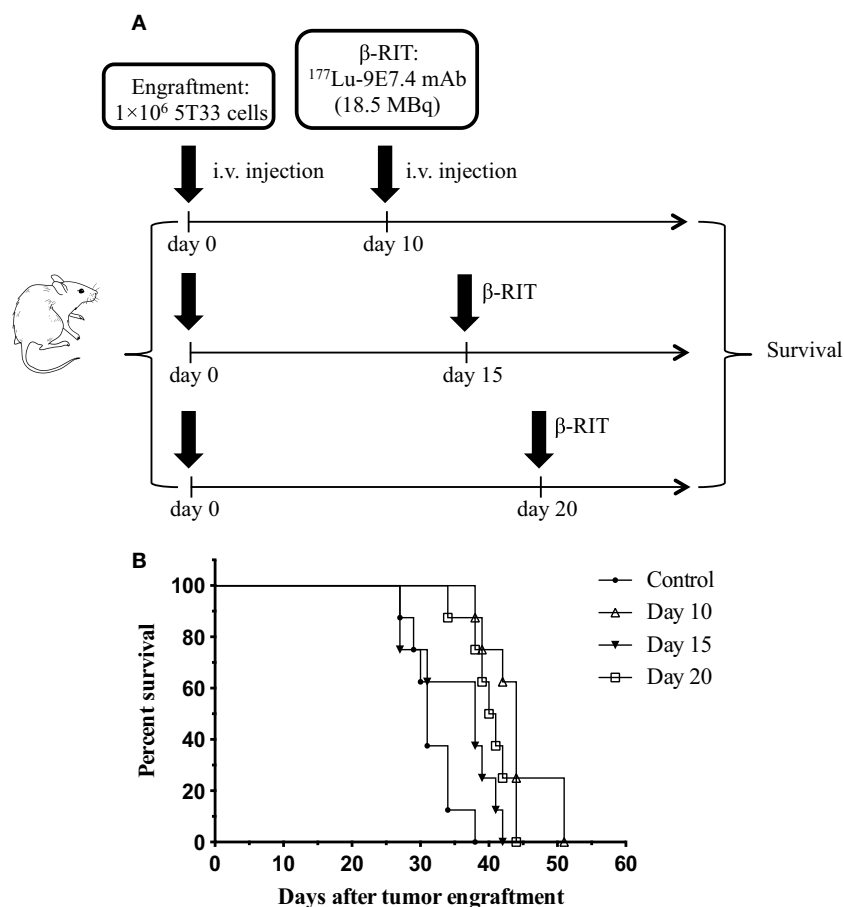


FIGURE 8 | Survival rates after treatment with β -RIT at different stages of MM development. (A) At day 0, mice were engrafted with 1×10^6 5T33 cells. β -RIT (i.v. administration of 18.5 MBq ^{177}Lu -9E7.4 mAb) was performed either at day 10, 15, or 20 after tumor engraftment; $n = 8$ mice per group. **(B)** Kaplan-Meier survival curves. The log-rank test indicated $p = 0.0001$ (day 10 vs. control) and $p = 0.0004$ (day 20 vs. control).

5T33 (23). Therefore, we thought that tumor burden at day 15 or 20 after tumor engraftment might be more appropriate for β -RIT treatment. However, even when β -RIT was performed on a more developed disease, no improvement in median survival was noted, and no cures were effected.

The difference between α -RIT and β -RIT in our MM model could be due to a difference in the radiosensitivity of 5T33 MM cells. Our group has already demonstrated that ^{213}Bi -281-2 mAb killed the human MM cell line U266 more efficiently than ^{131}I -281-2 mAb (26). Therefore, we will need to compare the sensitivity of 5T33 MM cells to α (^{213}Bi) vs. β (^{177}Lu) ionizing radiation at the cellular level.

Finally, although our study does not demonstrate any advantage of using β -RIT to treat MM, some therapeutic efficacy was observed with ^{131}I -B-B4 mAb in a previous dosimetric study (22). In the previous study, two of the four patients treated exhibited either a stabilization of the paraprotein level for 1 year, or a break in its progression. In addition, the patient for whom paraprotein levels stabilized also reported an analgesic effect, with a decrease in disease-related bone pain, which made it possible for them to

return to work. In these circumstances, we believe that β -RIT could improve therapeutic efficacy in this preclinical MM model, perhaps by using a fractionated dose strategy. Indeed, with a fractionation approach, the total activity administered can be higher than that delivered with a single dose, allowing improved efficacy compared to a single-dose regimen while reducing toxicity (43). Dose fractionation has already shown its efficacy, notably in treatment of NHL (44–46) and also for metastatic prostate cancer (47). Finally, Orozco et al. (48) demonstrated that β -RIT was less efficient when performed with ^{177}Lu than with ^{90}Y in an acute myeloid leukemia syngeneic mouse model. These authors hypothesized that the lower dose-rate and longer half-life of ^{177}Lu could be responsible for the effect observed and suggested that dose fractionation is better adapted to the physical properties of this radionuclide. Therefore, further studies with the ^{177}Lu -9E7.4 mAb in the immunocompetent MM mouse model will focus on assessing fractionated β -RIT treatment. In conclusion, this preclinical study indicates that, with a single dose, α -RIT is more efficient than β -RIT in treating MM in this mouse model.

AUTHOR CONTRIBUTIONS

Conception and design: NF, SG, CM, JB, LF, AM, FB, AF-C, JG, and MC. Method development: NF, SG, CM, JB, LF, AM, FB, AF-C, EB-C, FD, JG, and MC. Data acquisition: NF, SG, CM, EB-C, JG, and MC. Data analysis and interpretation: NF, SG, CM, JB, LF, AM, FB, AF-C, EB-C, FD, JG, and MC. Writing, review, and/or revision of the manuscript: NF, SG, JB, LF, AM, FB, AF-C, EB-C, FD, JG, and MC. Study supervision: JB, JG, and MC.

ACKNOWLEDGMENTS

We would like to thank Sandrine Minault and Sylvia Lambot (CRCNA) for their technical help, as well as the UTE, Cytocell, P2R (Protéines Recombinantes-Biogenouest) and Radioactivity facilities (SFR François Bonamy, IRS-UN, University of Nantes). We would also like to thank Patricia Remaud-Le Saëc (CRCNA) for her advice on ^{177}Lu radiolabeling and Marie-Hélène Gaugler

for critical reading of the manuscript, as well as Maighread Gallagher-Gambarelli for advice on English language usage.

FUNDING

This work was made possible thanks to the support of the Labex IGO project (no. ANR-11-LABX-0016-01), the Labex IRON project (no. ANR-11-LABX-0018-01), and the ArronaxPlus Equipex (no. ANR-11-EQPX-0004) funded by the French Government “Investissements d’Avenir” program, managed by the French National Research Agency (ANR). NF is supported by a grant from the Labex IGO project (no. ANR-11-LABX-0016-01). AM and FB are supported by the European Commission.

SUPPLEMENTARY MATERIAL

The Supplementary Material for this article can be found online at <http://journal.frontiersin.org/article/10.3389/fmed.2015.00076>

REFERENCES

- Dispenzieri A, Kyle RA. Multiple myeloma: clinical features and indications for therapy. *Best Pract Res Clin Haematol* (2005) **18**:553–68. doi:10.1016/j.beha.2005.01.008
- Rajkumar SV, Dimopoulos MA, Palumbo A, Blade J, Merlini G, Mateos MV, et al. International myeloma working group updated criteria for the diagnosis of multiple myeloma. *Lancet Oncol* (2014) **15**(12):e538–48. doi:10.1016/S1470-2045(14)70442-5.Epub
- Palumbo A, Attal M, Roussel M. Shifts in the therapeutic paradigm for patients newly diagnosed with multiple myeloma: maintenance therapy and overall survival. *Clin Cancer Res* (2011) **17**:1253–63. doi:10.1158/1078-0432.CCR-10-1925
- Moreau P, Attal M, Facon T. Frontline therapy of multiple myeloma. *Blood* (2015) **125**:3076–84. doi:10.1182/blood-2014-09-568915
- Mukherjee D, Coates PJ, Lorimore SA, Wright EG. Responses to ionizing radiation mediated by inflammatory mechanisms. *J Pathol* (2014) **232**:289–99. doi:10.1002/path.4299
- Vacchelli E, Vitale I, Tartour E, Eggermont A, Sautès-Fridman C, Galon J, et al. Trial watch: anticancer radioimmunotherapy. *Oncoimmunology* (2013) **2**:e25595. doi:10.4161/onci.25595
- Rödel F, Frey B, Multhoff G, Gaip U. Contribution of the immune system to bystander and non-targeted effects of ionizing radiation. *Cancer Lett* (2015) **356**:105–13. doi:10.1016/j.canlet.2013.09.015
- Gorin J-B, Ménager J, Gouard S, Maurel C, Guilloux Y, Faivre-Chauvet A, et al. Antitumor immunity induced after α irradiation. *Neoplasia* (2014) **16**:319–28. doi:10.1016/j.neo.2014.04.002
- McBride WH, Chiang C-S, Olson JL, Wang C-C, Hong J-H, Pajonk F, et al. A sense of danger from radiation. *Radiat Res* (2004) **162**:1–19. doi:10.1667/RR3196
- Witzig TE, Gordon LL, Cabanillas F, Czuczman MS, Emmanouilides C, Joyce R, et al. Randomized controlled trial of yttrium-90-labeled ibritumomab tiuxetan radioimmunotherapy versus rituximab immunotherapy for patients with relapsed or refractory low-grade, follicular, or transformed B-cell non-Hodgkin’s lymphoma. *J Clin Oncol* (2002) **20**:2453–63. doi:10.1200/JCO.2002.11.076
- Barbet J, Bardiès M, Bourgeois M, Chatal J-F, Chérel M, Davodeau F, et al. Radiolabeled antibodies for cancer imaging and therapy. *Methods Mol Biol* (2012) **907**:681–97. doi:10.1007/978-1-61779-974-7_38
- Parker C, Nilsson S, Heinrich D, Helle SI, O’Sullivan JM, Fossà SD, et al. Alpha emitter radium-223 and survival in metastatic prostate cancer. *N Engl J Med* (2013) **369**:213–23. doi:10.1056/NEJMoa1213755
- Cheetham PJ, Petrylak DP. Alpha particles as radiopharmaceuticals in the treatment of bone metastases: mechanism of action of radium-223 chloride (Alpharadin) and radiation protection. *Oncol (Williston Park)* (2012) **26**(330–337):341.
- Andersson H, Cederkrantz E, Bäck T, Divgi C, Elgqvist J, Himmelman J, et al. Intraperitoneal alpha-particle radioimmunotherapy of ovarian cancer patients: pharmacokinetics and dosimetry of (211)At-MX35 F(ab’)2 – a phase I study. *J Nucl Med* (2009) **50**:1153–60. doi:10.2967/jnumed.109.062604
- Couturier O, Supiot S, Degraef-Mouglin M, Faivre-Chauvet A, Carlier T, Chatal J-F, et al. Cancer radioimmunotherapy with alpha-emitting nuclides. *Eur J Nucl Med Mol Imaging* (2005) **32**:601–14. doi:10.1007/s00259-005-1803-2
- Kraeber-Bodéré F, Bodet-Milin C, Rousseau C, Eugène T, Pallardy A, Frampas E, et al. Radioimmunoconjugates for the treatment of cancer. *Semin Oncol* (2014) **41**:613–22. doi:10.1053/j.seminoncol.2014.07.004
- Jurcic JG, Larson SM, Sgouros G, McDevitt MR, Finn RD, Divgi CR, et al. Targeted alpha particle immunotherapy for myeloid leukemia. *Blood* (2002) **100**:1233–9.
- Morschhauser F, Radford J, Van Hoof A, Vitolo U, Soubeyran P, Tilly H, et al. Phase III trial of consolidation therapy with yttrium-90-ibritumomab tiuxetan compared with no additional therapy after first remission in advanced follicular lymphoma. *J Clin Oncol* (2008) **26**:5156–64. doi:10.1200/JCO.2008.17.2015
- Forrer F, Oechsli-Oberholzer C, Campana B, Herrmann R, Maecke HR, Mueller-Brand J, et al. Radioimmunotherapy with ^{177}Lu -DOTA-rituximab: final results of a phase I/II study in 31 patients with relapsing follicular, mantle cell, and other indolent B-cell lymphomas. *J Nucl Med* (2013) **54**:1045–52. doi:10.2967/jnumed.112.115170
- Bander NH, Milowsky MI, Nanus DM, Kostakoglu L, Vallabhajosula S, Goldsmith SJ. Phase I trial of ^{177}Lu -labeled J591, a monoclonal antibody to prostate-specific membrane antigen, in patients with androgen-independent prostate cancer. *J Clin Oncol* (2005) **23**:4591–601. doi:10.1200/JCO.2005.05.160
- Tagawa ST, Milowsky MI, Morris M, Vallabhajosula S, Christos P, Akhtar NH, et al. Phase II study of lutetium-177-labeled anti-prostate-specific membrane antigen monoclonal antibody J591 for metastatic castration-resistant prostate cancer. *Clin Cancer Res* (2013) **19**:5182–91. doi:10.1158/1078-0432.CCR-13-0231
- Rousseau C, Ferrer L, Supiot S, Bardiès M, Davodeau F, Faivre-Chauvet A, et al. Dosimetry results suggest feasibility of radioimmunotherapy using anti-CD138 (B-B4) antibody in multiple myeloma patients. *Tumour Biol* (2012) **33**:679–88. doi:10.1007/s13277-012-0362-y
- Chérel M, Gouard S, Gaschet J, Sai-Maurel C, Bruchertseifer F, Morgenstern A, et al. ^{213}Bi radioimmunotherapy with an anti-mCD138 monoclonal antibody in a murine model of multiple myeloma. *J Nucl Med* (2013) **54**:1597–604. doi:10.2967/jnumed.112.111997
- Bayer-Garner IB, Sanderson RD, Dhodapkar MV, Owens RB, Wilson CS. Syndecan-1 (CD138) immunoreactivity in bone marrow biopsies of multiple

- myeloma: shed syndecan-1 accumulates in fibrotic regions. *Mod Pathol* (2001) **14**:1052–8. doi:10.1038/modpathol.3880435
25. Wijdenes J, Vooijs WC, Clément C, Post J, Morard F, Vita N, et al. A plasmacyte selective monoclonal antibody (B-B4) recognizes syndecan-1. *Br J Haematol* (1996) **94**:318–23. doi:10.1046/j.1365-2141.1996.d01-1811.x
 26. Supiot S, Faivre-Chauvet A, Couturier O, Heymann MF, Robillard N, Kraeber-Bodéré F, et al. Comparison of the biologic effects of MA5 and B-B4 monoclonal antibody labeled with iodine-131 and bismuth-213 on multiple myeloma. *Cancer* (2002) **94**:1202–9. doi:10.1002/cncr.10286
 27. Sanderson RD, Yang Y. Syndecan-1: a dynamic regulator of the myeloma microenvironment. *Clin Exp Metastasis* (2008) **25**:149–59. doi:10.1007/s10585-007-9125-3
 28. Seidel C, Sundan A, Hjorth M, Turesson I, Dahl IM, Abildgaard N, et al. Serum syndecan-1: a new independent prognostic marker in multiple myeloma. *Blood* (2000) **95**:388–92.
 29. Lovell R, Dunn JA, Begum G, Barth NJ, Plant T, Moss PA, et al. Soluble syndecan-1 level at diagnosis is an independent prognostic factor in multiple myeloma and the extent of fall from diagnosis to plateau predicts for overall survival. *Br J Haematol* (2005) **130**:542–8. doi:10.1111/j.1365-2141.2005.05647.x
 30. Kim JM, Lee JA, Cho IS, Ihm CH. Soluble syndecan-1 at diagnosis and during follow up of multiple myeloma: a single institution study. *Korean J Hematol* (2010) **45**:115–9. doi:10.5045/kjh.2010.45.2.115
 31. Radl J, Croese JW, Zurcher C, Van den Enden-Vieeen MH, de Leeuw AM. Animal model of human disease. Multiple myeloma. *Am J Pathol* (1988) **132**:593–7.
 32. Garrett IR, Dallas S, Radl J, Mundy GR. A murine model of human myeloma bone disease. *Bone* (1997) **20**:515–20. doi:10.1016/S8756-3282(97)00056-2
 33. Fraker PJ, Speck JC. Protein and cell membrane iodinations with a sparingly soluble chloroamide, 1,3,4,6-tetrachloro-3a,6a-diphenylglycoluril. *Biochem Biophys Res Commun* (1978) **80**:849–57. doi:10.1016/0006-291X(78)91322-0
 34. Koppe MJ, Bleichrodt RP, Soede AC, Verhofstad AA, Goldenberg DM, Oyen WJG, et al. Biodistribution and therapeutic efficacy of (125/131)I-, (186)Re-, (88/90)Y-, or (177)Lu-labeled monoclonal antibody MN-14 to carcinoembryonic antigen in mice with small peritoneal metastases of colorectal origin. *J Nucl Med* (2004) **45**:1224–32.
 35. Shi Q, Jiang J, Luo G. Syndecan-1 serves as the major receptor for attachment of hepatitis C virus to the surfaces of hepatocytes. *J Virol* (2013) **87**:6866–75. doi:10.1128/JVI.03475-12
 36. Vanderkerken K, De Raeve H, Goes E, Van Meirvenne S, Radl J, Van Riet I, et al. Organ involvement and phenotypic adhesion profile of 5T2 and 5T33 myeloma cells in the C57BL/KaLwRij mouse. *Br J Cancer* (1997) **76**:451–60. doi:10.1038/bjc.1997.409
 37. Tung JW, Mrazek MD, Yang Y, Herzenberg LA, Herzenberg LA. Phenotypically distinct B cell development pathways map to the three B cell lineages in the mouse. *Proc Natl Acad Sci U S A* (2006) **103**:6293–8. doi:10.1073/pnas.0511305103
 38. Vera DRB, Eigner S, Henke KE, Lebeda O, Melichar F, Beran M. Preparation and preclinical evaluation of 177Lu-nimotuzumab targeting epidermal growth factor receptor overexpressing tumors. *Nucl Med Biol* (2012) **39**:3–13. doi:10.1016/j.nucmedbio.2011.07.001
 39. Prat M, Demarquay C, Frick J, Thierry D, Gorin N-C, Bertho JM. Radiation-induced increase in plasma Flt3 ligand concentration in mice: evidence for the implication of several cell types. *Radiat Res* (2005) **163**:408–17. doi:10.1667/RR3340
 40. Frampas E, Rousseau C, Bodet-Milin C, Barbet J, Chatal JF, Kraeber-Bodéré F. Improvement of radioimmunotherapy using pretargeting. *Front Oncol* (2013) **3**:159. doi:10.3389/fonc.2013.00159
 41. Mulligan T, Carrasquillo JA, Chung Y, Milenic DE, Schlom J, Feuerstein I, et al. Phase I study of intravenous Lu-labeled CC49 murine monoclonal antibody in patients with advanced adenocarcinoma. *Clin Cancer Res* (1995) **1**:1447–54.
 42. Stillebroer AB, Zegers CML, Boerman OC, Oosterwijk E, Mulders PFA, O'Donoghue JA, et al. Dosimetric analysis of 177Lu-cG250 radioimmunotherapy in renal cell carcinoma patients: correlation with myelotoxicity and pretherapeutic absorbed dose predictions based on 111In-cG250 imaging. *J Nucl Med* (2012) **53**:82–9. doi:10.2967/jnumed.111.094896
 43. DeNardo GL, Schlom J, Buchsbaum DJ, Meredith RF, O'Donoghue JA, Sgouros G, et al. Rationales, evidence, and design considerations for fractionated radioimmunotherapy. *Cancer* (2002) **94**:1332–48. doi:10.1002/cncr.10304
 44. DeNardo GL, DeNardo SJ, Lamborn KR, Goldstein DS, Levy NB, Lewis JP, et al. Low-dose, fractionated radioimmunotherapy for B-cell malignancies using 131I-Lym-1 antibody. *Cancer Biother Radiopharm* (1998) **13**:239–54. doi:10.1089/cbr.1998.13.239
 45. Illidge TM, Mayes S, Pettengell R, Bates AT, Bayne M, Radford JA, et al. Fractionated ⁹⁰Y-ibritumomab tiuxetan radioimmunotherapy as an initial therapy of follicular lymphoma: an international phase II study in patients requiring treatment according to GELF/BNLI criteria. *J Clin Oncol* (2014) **32**:212–8. doi:10.1200/JCO.2013.50.3110
 46. Morschhauser F, Kraeber-Bodéré F, Wegener WA, Harousseau J-L, Petillon M-O, Huglo D, et al. High rates of durable responses with anti-CD22 fractionated radioimmunotherapy: results of a multicenter, phase I/II study in non-Hodgkin's lymphoma. *J Clin Oncol* (2010) **28**:3709–16. doi:10.1200/JCO.2009.27.7863
 47. Tagawa S, Vallabhaajosula S, Osborn J, Goldsmith S, Petrillo K, Tyrell L, et al. Phase I trial of fractionated-dose 177Lu-radiolabeled anti-prostate-specific membrane antigen (PSMA) monoclonal antibody J591 (177Lu-J591) in patients (pts) with metastatic castration-resistant prostate cancer (met CPC). *J Clin Oncol* (2010) **28**(15suppl):abstr4667.
 48. Orozco JJ, Balkin ER, Gooley TA, Kenoyer A, Hamlin DK, Wilbur DS, et al. Anti-CD45 radioimmunotherapy with 90Y but not 177Lu is effective treatment in a syngeneic murine leukemia model. *PLoS One* (2014) **9**:e113601. doi:10.1371/journal.pone.0113601

Conflict of Interest Statement: The authors declare that the research was conducted in the absence of any commercial or financial relationships that could be construed as a potential conflict of interest.

Copyright © 2015 Fichou, Gouard, Maurel, Barbet, Ferrer, Morgenstern, Bruchertseifer, Faivre-Chauvet, Bigot-Corbel, Davodeau, Gaschet and Chérel. This is an open-access article distributed under the terms of the Creative Commons Attribution License (CC BY). The use, distribution or reproduction in other forums is permitted, provided the original author(s) or licensor are credited and that the original publication in this journal is cited, in accordance with accepted academic practice. No use, distribution or reproduction is permitted which does not comply with these terms.



Pharmacokinetics and Dosimetry Studies for Optimization of Pretargeted Radioimmunotherapy in CEA-Expressing Advanced Lung Cancer Patients

Caroline Bodet-Milin^{1,2*}, Ludovic Ferrer^{2,3,4}, Aurore Rauscher^{2,3}, Damien Masson⁵, Latifa Rbah-Vidal⁶, Alain Faivre-Chauvet^{1,2}, Evelyne Cerato¹, Caroline Rousseau^{2,3}, José Hureau⁶, Olivier Couturier⁷, Pierre-Yves Salaün⁸, David M. Goldenberg^{9,10}, Robert M. Sharkey¹⁰, Françoise Kraeber-Bodéré^{1,2,3} and Jacques Barbet^{2,11}

¹ Department of Nuclear Medicine, University Hospital Nantes, Nantes, France, ² CNRS UMR 6299, Centre Régional de Recherche en Cancérologie Nantes/Angers (CRCNA), INSERM U892, Nantes, France, ³ Department of Nuclear Medicine, ICO Cancer Centre, Saint-Herblain, France, ⁴ Physics Unit, ICO Cancer Centre, Saint-Herblain, France, ⁵ Department of Biochemistry, University Hospital Nantes, Nantes, France, ⁶ Department of Pneumology, University Hospital Angers, Angers, France, ⁷ Department of Nuclear Medicine, University Hospital Angers, Angers, France, ⁸ Department of Nuclear Medicine, University Hospital Brest, Brest, France, ⁹ IBC Pharmaceuticals, Inc., Morris Plains, NJ, USA, ¹⁰ Immunomedics, Inc., Morris Plains, NJ, USA, ¹¹ GIP Arronax, Saint-Herblain, France

OPEN ACCESS

Edited by:

Jean-Pierre Pouget,
INSERM, France

Reviewed by:

Thierry Stora,
CERN, Switzerland
Michael Lassmann,
University of Würzburg, Germany

*Correspondence:

Caroline Bodet-Milin
cbodetmilin@gmail.com

Specialty section:

This article was submitted to
Nuclear Medicine,
a section of the journal
Frontiers in Medicine

Received: 16 July 2015

Accepted: 09 November 2015

Published: 27 November 2015

Citation:

Bodet-Milin C, Ferrer L, Rauscher A, Masson D, Rbah-Vidal L, Faivre-Chauvet A, Cerato E, Rousseau C, Hureau J, Couturier O, Salaün P-Y, Goldenberg DM, Sharkey RM, Kraeber-Bodéré F and Barbet J (2015) Pharmacokinetics and Dosimetry Studies for Optimization of Pretargeted Radioimmunotherapy in CEA-Expressing Advanced Lung Cancer Patients. *Front. Med.* 2:84. doi: 10.3389/fmed.2015.00084

Objectives: A phase I pretargeted radioimmunotherapy trial (EudractCT 200800603096) was designed in patients with metastatic lung cancer expressing carcinoembryonic antigen (CEA) to optimize bispecific antibody and labeled peptide doses, as well as the delay between their injections.

Methods: Three cohorts of three patients received the anti-CEA × anti-histamine-succinyl-glycine (HSG)-humanized trivalent bispecific antibody (TF2) and the IMP288 bivalent HSG peptide. Patients underwent a pretherapeutic imaging session S1 (44 or 88 nmol/m² of TF2 followed by 4.4 nmol/m², 185 MBq, of ¹¹¹In-labeled IMP288) and, 1–2 weeks later, a therapy session S2 (240 or 480 nmol/m² of TF2 followed by 24 nmol/m², 1.1 GBq/m², of ¹⁷⁷Lu-labeled IMP288). The pretargeting delay was 24 or 48 h. The dose schedule was defined based on preclinical TF2 pharmacokinetic (PK) studies, on our previous clinical data using the previous anti-CEA-pretargeting system, and on clinical results observed in the first patients injected using the same system in Netherlands.

Results: TF2 PK was represented by a two-compartment model in which the central compartment volume (V_c) was linearly dependent on the patient's surface area. PK was remarkably similar, with a clearance of 0.33 ± 0.03 L/h/m². ¹¹¹In- and ¹⁷⁷Lu-IMP288 PK was also well represented by a two-compartment model. IMP288 PK was faster (clearance 1.4–3.3 L/h). The V_c was proportional to body surface area, and IMP288 clearance depended on the molar ratio of injected IMP288 to circulating TF2 at the time of IMP288 injection. Modeling of image quantification confirmed the dependence of IMP288 kinetics on circulating TF2, but tumor activity PK was variable. Organ-absorbed doses were not significantly different in the three cohorts, but the tumor dose was significantly higher with the higher molar doses of TF2 (*p* < 0.002). S1 imaging predicted absorbed doses calculated in S2.

Conclusion: The best dosing parameters corresponded to the shorter pretargeting delay and to the highest TF2 molar doses. S1 imaging session accurately predicted PK as well as absorbed doses of S2, thus potentially allowing for patient selection and dose optimization.

Trial Registration: ClinicalTrials.gov NCT01221675 (EudractCT 200800603096).

Keywords: lung cancer, radioimmunotherapy, pretargeting, pharmacokinetics, scintigraphy, SPECT, SPECT/CT, dosimetry

INTRODUCTION

Radioimmunotherapy (RAIT) is a molecular targeted therapy whereby irradiation from radionuclides is delivered to target tumors using monoclonal antibodies (mAb) directed to tumor antigens. RIT delivers a heterogeneous low dose-rate irradiation with an efficacy demonstrated in hematological malignancies sensitive to radiation therapy (1). In solid tumors, more resistant to radiation and less accessible to large molecules, such as mAb, clinical efficacy remains limited and fractionated injections, combination of RAIT with chemotherapy, as well as pretargeting approaches, are being studied to improve antitumor efficacy (2).

Pretargeted RAIT (pRAIT) was originally designed to improve the therapeutic index (tumor-to-normal tissue ratios) and to deliver increased absorbed doses to tumors, as compared to directly radiolabeled antibodies or antibody fragments (3, 4). pRAIT may be achieved in several different ways. Here, a bispecific mAb (BsmAb) is administered, followed a few days later by a radiolabeled bivalent hapten. With this technology, the radioactive bivalent hapten binds avidly to the BsmAb attached to the cell surface, whereas the nontargeted radioactive hapten clears from the circulation through the kidneys. RAIT using directly radiolabeled anti-carcinoembryonic antigen (CEA) mAb has shown promising clinical results in metastatic medullary thyroid carcinoma (MTC) and metastatic colon cancer (5, 6), but pretargeting of CEA-expressing tumors has demonstrated a more favorable therapeutic index and antitumor efficacy in preclinical MTC and colorectal cancer (CRC) models (7, 8) and clinical feasibility in MTC and small-cell lung cancer (SCLC) (9, 10). Two phase I clinical trials assessing

anti-CEA \times anti-diethylene-triamine-pentaacetic acid (DTPA)-indium BsmAb (murine F6 \times 734 and chimeric hMN14 \times 734 BsmAb) with ^{131}I -labeled di-DTPA-indium hapten showed encouraging therapeutic results in patients with progressive metastatic MTC, with a significantly improved overall survival for intermediate- and high-risk patients (11). However, murine and chimeric BsmAb (human/mouse) used in these studies induced in a high rate of immunization and 26% human antihuman antibody (HAHA) or human antimouse antibody (HAMA) detection, as reported by Salaün et al. (12).

New generation humanized, recombinant, trivalent BsmAb (anti-CEA TF2) and histamine-succinyl-glycine (HSG) peptides have thus been developed (13). TF2, composed of a humanized anti-HSG Fab fragment derived from the 679 anti-HSG mAb and two humanized anti-CEA Fab fragments derived from the hMN14 mAb (labetuzumab; Immunomedics, Inc.) by the dock-and-lock procedure, should reduce immunogenicity and facilitate repeated injections (14, 15). Moreover, the HSG peptide, IMP288, allows facile and stable labeling with different radiometals, such as ^{177}Lu and ^{90}Y , having favorable physical features that could improve pRAIT efficacy. However, Schoffelen et al. (16) have shown that doses and pretargeting delays must be entirely revisited with the dock-and-lock BsmAb because of the very different pharmacokinetic (PK) properties of these new agents, as compared to the chemically coupled Fab fragments used previously (17).

A phase I/II clinical trial was designed to optimize and assess, in CEA-expressing lung cancer patients, the new generation pretargeting reagents, i.e., the anti-CEA \times anti-HSG TF2 BsmAb, and the radiolabeled IMP288 HSG peptide. The clinical protocol includes two parts: the first part aims at optimizing BsmAb and peptide molar doses and administration schedules for pRAIT in three cohorts of three patients, using detailed PK and dosimetry analyses, and the second part aims at determining the maximum tolerated dose of pRAIT using escalated peptide activities and the parameters optimized in the first study part. In the two parts of the study, the IMP288 peptide is radiolabeled with indium-111 for pretherapeutic imaging and lutetium-177 for therapy. Here, we report the results of the optimization part of the study, performed in three cohorts of patients receiving different doses of BsmAb and peptide, the ratio of BsmAb and peptide molar doses being kept constant between the imaging and therapy sessions, as suggested by Schoffelen et al. (16). A population PK approach was used to model the serum kinetics of the BsmAb and of the radiolabeled hapten for the two sessions. Whole body (WB) planar scintigraphy and single photon emission computed tomography (SPECT)

Abbreviations: ALT, alanine transaminase; AST, aspartate transaminase; BSA, body surface area; BsmAb, bispecific monoclonal antibody(ies); CEA, carcinoembryonic antigen; Cl, clearance; CRC, colorectal cancer; CT, computed tomography; DOTA, 1,4,7,10-tetraazacyclododecane-1,4,7,10-tetraacetic acid; DTPA, diethylene-triamine-pentaacetic acid; EGFR, epidermal growth factor receptor; FDG-PET, positron emission computed tomography using ^{18}F -fluorodeoxy-glucose; HAHA, human antihuman antibody; HAMA, human antimouse antibody; HSG, histamine-succinyl-glycine; mAb, monoclonal antibody(ies); MR, molar ratio of injected hapten to the amount of TF2 present in the patients' serum; MTC, medullary thyroid carcinoma; NSCLC, non-small-cell lung cancer; PET, positron emission computed tomography; PK, pharmacokinetic(s); pRAIT, pretargeted radioimmunotherapy; RAIT, radioimmunotherapy; SCLC, small-cell lung cancer; SD, standard deviation; SPECT, single photon emission computed tomography; TF2, anti-CEA \times anti-HSG bispecific monoclonal antibody; Vc, central compartment volume; WB, whole body.

allowed the description of the biodistribution of the radiolabeled peptide and quantitative imaging analyses. Dosimetry assessment was performed together with population PK analysis of the time–activity curves.

MATERIALS AND METHODS

Patients

The target population was male or female 18 years of age with histological diagnosis of CEA-positive lung cancer including

- small-cell lung cancer who are in partial response or who failed after at least two lines of standard radiation and/or chemotherapy;
- non-small-cell lung cancer (NSCLC) without activating mutation of epidermal growth factor receptor (EGFR) gene and who failed after at least one line of chemotherapy.

Only patients with CEA serum level ≥ 10 ng/mL or CEA expression by tissues staining, with at least one known tumor site detected by computed tomography (CT) and positron emission CT using ^{18}F -fluoro-deoxy-glucose (FDG-PET), were eligible for the study. All patients had an Eastern Cooperative Oncology Group performance ≤ 2 or Karnofsky performance status $\geq 60\%$ and a minimum life expectancy of 3 months. For entry into the study, patients were required to be at least 4 weeks beyond any major surgery, external radiotherapy, chemotherapy, immunotherapy, or angiogenesis inhibitor therapy. The patients were required to have normal levels of transaminases (AST and ALT $\leq 2.5 \times$ the upper limit of normal), total bilirubin level ≤ 30 mmol/L, creatinine ($\leq 2.5 \times$ the upper limit of normal), neutrophils $\geq 1,500/\text{mL}$, and platelets $\geq 100,000/\text{mL}$. Pregnant or breast-feeding women were excluded, as were premenopausal women not willing to practice adequate birth control methods during the study and for 3 months afterward. Patients with another known type of intercurrent cancer, uncontrolled diabetes, or a psychiatric disorder were also excluded.

All patients gave informed written consent in accordance with institutional guidelines, including the Declaration of Helsinki. The trial was approved by the responsible ethics committee and registered at ClinicalTrial.gov NCT01221675 (EudractCT 200800603096).

Investigational Products and Labeling

The trivalent TF2-humanized mAb and the IMP288 peptide, which bears two HSG groups (hapten) recognized by the 679 mAb

and one 1,4,7,10-tetraazacyclododecane-1,4,7,10-tetraacetic acid (DOTA) moiety (13, 18), were prepared suitable for human use by Immunomedics, Inc. (Morris Plains, NJ, USA). IMP288 (146 $\mu\text{g/mL}$ in acetate buffer) was labeled with 185 MBq of ^{111}In (Mallinckrodt Medical B.V., Petten, Netherlands) for the imaging sessions. IMP288 (24 mol/ m^2) was labeled with 1.1 GBq/ m^2 of ^{177}Lu (IDB Radiopharmacy B.V., Baarle-Nassau, Netherlands) for the therapy sessions. The radiochemical purity, determined using high performance liquid chromatography (Eckert Ziegler, Germany) using a C18 column (ACE 15 cm \times 3 mm, France) and a gradient of trifluoroacetic acid (0.1% in water) and acetonitrile was greater than 90% ($94.5 \pm 2.2\%$) for ^{111}In -IMP288 and greater than 99.0% ($99.5 \pm 0.4\%$) for ^{177}Lu -IMP288. TF2 was diluted in 250 mL 0.9% NaCl and administered by i.v. infusion over a period of 30–60 min. ^{111}In - or ^{177}Lu -IMP288 was diluted in 50 mL of 0.9% NaCl in water and administered by i.v. infusion over a period of 30 min. Median-specific activities were 24 MBq/nmol (range 16–30) for ^{111}In -IMP288 and 47 (range 45–53) for ^{177}Lu -IMP288.

Study Design and Treatment

Three different pretargeting conditions were examined in three cohorts of three patients (Table 1). All patients underwent a pretherapy imaging session (S1) using TF2 and ^{111}In -labeled IMP288 injections before a therapy session (S2). In the first cohort (C1), patients received 7 mg/ m^2 (44 nmol/ m^2) of TF2 followed 48 h later by 4.4 nmol/ m^2 of IMP288 labeled with 185 MBq of ^{111}In in S1 and 37.5 mg/ m^2 (240 nmol/ m^2) of TF2 followed 48 h later by 24 nmol/ m^2 of IMP288 labeled with 1.1 GBq/ m^2 of ^{177}Lu in S2. Only patients with successful tumor targeting in S1 were eligible to participate in S2. In the second cohort (C2), TF2 doses were increased from 7 (44 nmol/ m^2) to 14 mg/ m^2 (88 nmol/ m^2) in S1 and from 37.5 (240 nmol/ m^2) to 75 mg/ m^2 (480 nmol/ m^2) in S2, whereas IMP doses, ^{111}In and ^{177}Lu activities, and the pretargeting delay remained identical that in C1. In the third cohort (C3), patients received the same TF2 and IMP doses and the same ^{111}In and ^{177}Lu activities than in C2 but with a lower pretargeting interval (24H instead of 48H). For each cohort of patients, TF2 and IMP288 were administered using the same pretargeting interval and the same TF2/IMP288 molar ratio in S1 and S2.

Six French centers were allowed to include and treat patients in this multicentric study: Nantes University Hospital Nuclear Medicine Department, Nantes ICO Cancer Centre Nuclear Medicine Department, Brest University Hospital Nuclear Medicine Department, Angers University Hospital

TABLE 1 | Dosing scheme.

	S1: pretherapy imaging session			S2: therapy session		
	TF2 dose	Delay (h)	^{111}In -IMP288	TF2 dose	Delay (h)	^{177}Lu -IMP288
Cohort I	7 mg/ m^2 44 nmol/ m^2	48	185 MBq 4.4 nmol/ m^2	37.5 mg/ m^2 240 nmol/ m^2	48	1.1 GBq/ m^2 24 nmol/ m^2
Cohort II	14 mg/ m^2 88 nmol/ m^2	48	185 MBq 4.4 nmol/ m^2	75 mg/ m^2 480 nmol/ m^2	48	1.1 GBq/ m^2 24 nmol/ m^2
Cohort III	14 mg/ m^2 88 nmol/ m^2	24	185 MBq 4.4 nmol/ m^2	75 mg/ m^2 480 nmol/ m^2	24	1.1 GBq/ m^2 24 nmol/ m^2

Nuclear Medicine Department, Clermont-Ferrand University Hospital Nuclear Medicine department, and Grenoble University Hospital Nuclear Medicine Department.

Safety was assessed during infusions by monitoring vital signs, physical examination, and adverse events. Patients were premedicated with antihistamine (xyzall®) and corticosteroid (intravenous dexamethasone) before each TF2 and peptide infusion.

NCI Common Toxicity Criteria Version 3.0 were used to evaluate toxicity. Total WBC and lymphocytes were monitored and reported every week until 8 weeks post-¹⁷⁷Lu-IMP288 injection or until platelet (>100 g/L without transfusion), hemoglobin (>10 g/dl without transfusion), and leukocyte (>2 g/L) recovery. Assessment of hematological toxicity was only based on hemoglobin level (Hgb), absolute neutrophil counts, and platelet counts. Biochemical tests including serum creatinine, creatinine clearance, AST, ALT, total bilirubin, alkaline phosphatase, calcium, phosphorus, uric acid, sodium, potassium, and serum electrophoresis were performed 4 weeks, 8 weeks, and then every 3 months after pRAIT.

Assessment of response was based on physical examination, CEA serum level, CT and FDG-PET performed 4 weeks after pRAIT, at 3 months, and then every 3 months until progression. Responses were scored according to the Response Evaluation Criteria in Solid Tumors (RECIST 1.0) (19).

Human antihuman antibody was determined within 2 days of the second TF2 infusion, then 4 weeks, 8 weeks, and 3 months after the last TF2 infusion using an ELISA method. The detection limit for positive HAHA was 50 ng/mL.

Pharmacokinetics

Blood samples were collected in separator tubes for serum collection at the following times after TF2 injection and after administration of ¹¹¹In-IMP288 or ¹⁷⁷Lu-IMP288: before the beginning of the infusion, 5 min before the end of the infusion, then 5 min, 1 h, 2–4 h, 24 h, and then at four other times over 7 days. Blood samples were collected for all patients during S1 and S2. Serum samples (at least 1 mL) were prepared from blood samples and stored frozen. TF2 concentrations were determined using an ELISA (Immunomedics), as described previously (18). The indium-111 or lutetium-177 activity in each serum sample was determined by counting 0.1–0.2 mL of serum in a calibrated gamma counter. Counting was performed immediately after the end of each blood collection series and corrected for radioactive decay.

Modeling of the serum concentration PK was performed using a two-compartment model for the bispecific antibody (TF2) and two or three compartment models for the radiolabeled hapten (IMP288), using a population PK software package,

developed in the laboratory and validated against Monolix (20). Patients' body surface areas (BSAs) were used as covariables. In the hapten PK analyses, several covariables were tested to represent the effect of TF2 on the kinetics of IMP288. Finally, the molar ratio of injected hapten to the amount of TF2 present in the patients' serum (MR), calculated as the concentration of TF2 extrapolated to the time of hapten injection multiplied by the central compartment volume (Vc) obtained in the TF2 PK analysis, was the covariable used to take the effect of TF2 on IMP288 PK into account. Since the addition of a third compartment did not improve data fitting, two-compartment models were used. Parameters for the two-compartment model of serum kinetics for both TF2 and IMP288 were the transfer rates ($k_{2,1}$ and $k_{1,2}$), the elimination rate (k_{el}), and the Vc per BSA unit (volume/m²). The Vc was a dependent parameter ($Vc = \text{volume} / m^2 \times \text{patient BSA}$). For the serum IMP288 PK, clearance was calculated as $A_s \times MR^{BS}$, MR being the ratio of the number of moles of injected IMP288 to the number of moles of TF2 present in the circulation at the time of IMP288 injection, A_s and B_s being two adjustable parameters, and k_{el} was calculated as clearance/Vc.

For the WB IMP288 kinetics, the activity calculated from WB images was modeled as the sum of the central and distribution compartments with adjustable transfer rates ($k_{2,1}$ and $k_{1,2}$) and two additional adjustable parameters, A_{WB} and B_{WB} , used to calculate the elimination rate: $k_{el} = A_{WB} \times MR^{B_{WB}}$.

For the PK analysis of tissue distribution from image quantification, the WB kinetics was used as an input function, and the IMP288 distribution in tissues of interest was modeled using a tissue-specific distribution compartment and a fraction of the activity in the central compartment. The on and off rate constants, k_{on} and k_{off} , and the fraction of activity (fraction) were adjustable parameters.

TABLE 3 | Characteristics of patients.

Median age	65 (53–80)
Male/female	7/2
Histological type	6 SCLC/3 NSCLC
Karnofsky index	
90–100	5
70–80	2
60–70	2
Median CEA plasma level (min–max)	79 ng/mL (10–388)
Prior treatment	
Chemotherapy	100%
Radiotherapy	67%
Surgery	33%
Tyrosine kinase inhibitors	11%
Site of disease	
Lung	78%
Mediastinum	78%
Liver	56%
Pancreas	22%
Adrenal	33%
Infradiaphragmatic nodes	33%
Bone	11%
Muscle	11%
Brain	11%
Median delay from initial diagnosis (min–max)	25 months (10–64)

TABLE 2 | ¹¹¹In and ¹⁷⁷Lu system sensitivities for both types of gamma cameras in all centers.

System sensitivity (counts/MBq s)		
Crystal thickness	¹¹¹ In	¹⁷⁷ Lu
3/8"	170 ± 2	15 ± 2
5/8"	230 ± 2	18 ± 2

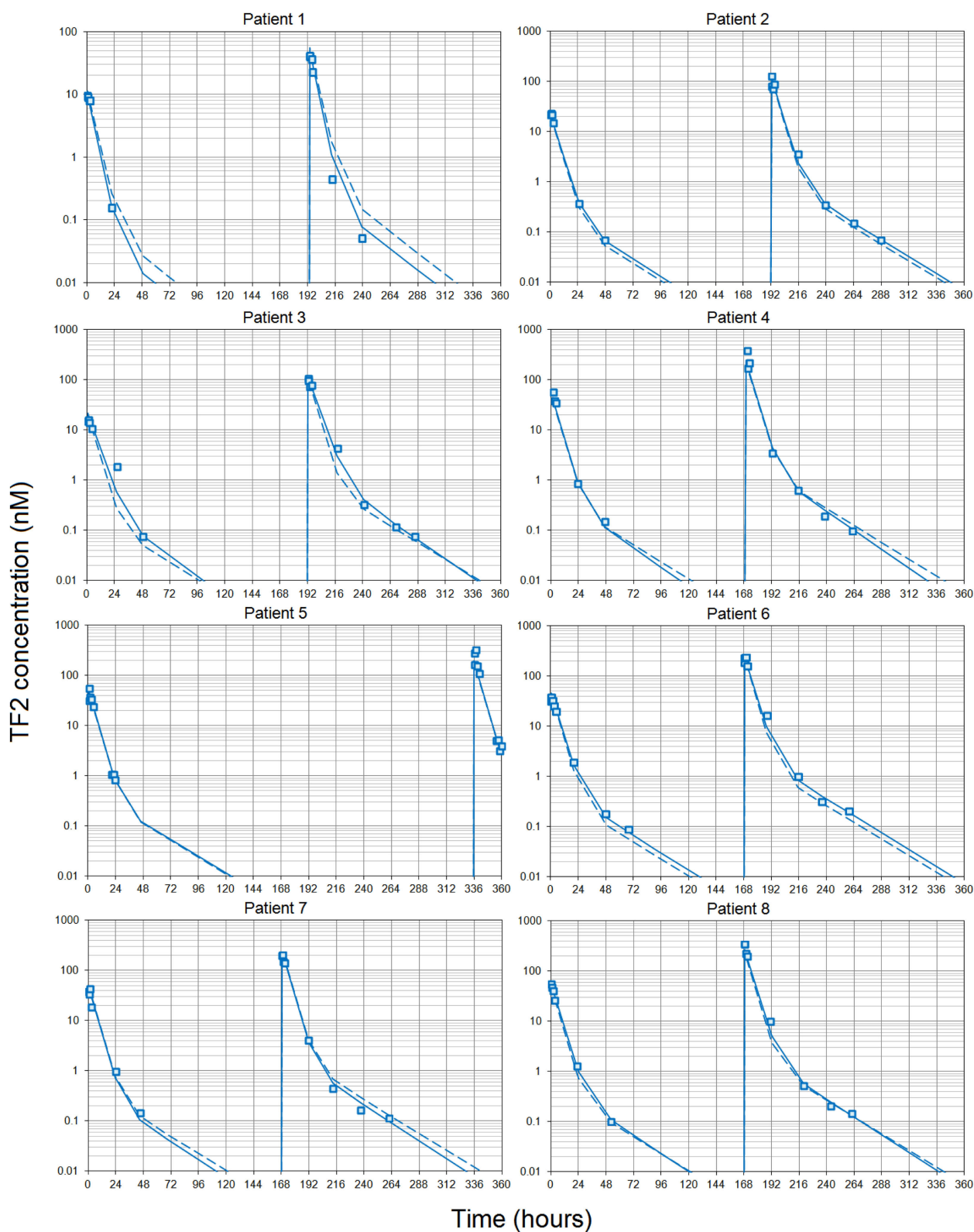


FIGURE 1 | Pharmacokinetics of the bispecific antibody TF2. Each patient received two infusions of TF2 at 7 or 8 days intervals (except patient 5). Blood samples were collected at selected time intervals during and after each infusion and centrifuges. TF2 concentrations were measured using a specific ELISA. The pharmacokinetics was then modeled using a two-compartment model and a population approach. Data collected after both infusions were fitted using a single set of parameters. Results (open squares) are plotted as a semilog plot with the population (dashed lines) and individual (solid lines) fitted curves.

Scintigraphy

All imaging centers were equipped with the same model of SPECT/CT gamma-camera (Symbia T/T2, Siemens). For pretherapeutic and therapeutic imaging sessions, three to five images were scheduled from 1 h to 7 days after radiopharmaceutical injection depending on the patient's ability to sustain imaging procedures. Each imaging session consisted of WB emission scan ($256 \times 1,024$ pixels) and tomographic acquisitions (128×128 pixels, 2×32 projections, and 30–45 s per projection). Each scans or tomographic acquisitions were performed using medium energy collimators. Due to expected low level of detected counts, especially at late time points, energy windows were centered on the two major peaks (15% width). In order to correct for Compton scattering (21), two energy windows (4% width) adjacent to each main peak were simultaneously acquired. CT scans (120 kVp, 100 mAs) were acquired in order to derive CT attenuation maps. Tomographic procedures consisted of two acquisitions to cover patients from lungs to pelvic area.

At an initial stage, as involved centers were equipped with thin ($3/8''$) or thick ($5/8''$) crystals, system planar sensitivity was evaluated for these two types of equipment for ^{111}In and ^{177}Lu sources of known activity (~ 200 and 900 MBq, respectively) poured in a thin cylinder plate (Table 2). As tomographic reconstructions accounted for point response function of the collimator, this feature was characterized by the full width of half-maximum of point source images at different distances from collimator plate. Gamma cameras and dose calibrator quality controls were performed in accordance to each institution procedures (no crosscalibration). Particular attention was given to patient alignment for each imaging session to help image registration during processing.

Dosimetry

Quantitative imaging was performed on tomographic reconstructions (OSEM 30 iterations, eight subsets) taking into account attenuation, Compton scattering (correction performed

on projections), and collimator response corrections as expressed in international guidelines (22). Initial estimated system sensitivity reported in Table 2 was used to translate detected count into activity for ^{111}In and ^{177}Lu acquisitions.

Patients' organ masses were derived from automatic or manual CT images segmentation performed with 3D Slicer (23) software. Trabecular bones in L2–L4 lumbar vertebrae were also segmented in order to evaluate bone marrow-absorbed dose (24). Tumor volumes were segmented on emission-reconstructed images and performed on images where the tumor-to-background ratio was visually designed as optimum. Tumor labeled volumes were subsequently exported as DICOM-RT structure set and integrated into the patient labeled-organs images after registration.

In order to obtain time–activity curves for volumes of interest, labeled images were registered against CT images performed at every imaging session using the MedInria software (25). Then, organ time–activity curves were adjusted with nls package of R software (26) using mono- or biexponential functions depending on the number of time points available to perform the regression analysis and submitted to a population PK analysis using the laboratory software package.

To estimate patient's organ-absorbed doses at pretherapeutic and therapeutic stages, MIRD S factors were scaled by patient organ masses. Time integration of fitted functions was calculated to derive cumulated activities at both sessions. Estimations at pretherapeutic were scaled to take into account the difference between physical half-lives of both radionuclides.

Statistics

Organ effective periods estimated at S1 and S2, as well as tumor- and organ-absorbed doses for each schedule, were compared using the Wilcoxon statistical test.

For each patient, Spearman statistical tests were conducted to evaluate whether S1-absorbed doses were able to predict absorbed doses during S2.

TABLE 4 | Two-compartment population analysis of TF2 pharmacokinetics.

Parameter ^a	$k_{2,1}$ (h^{-1})	$k_{1,2}$ (h^{-1})	k_{el} (h^{-1})	Volume/ m^2 (L/m^2)	Vc (L)	Clearance (L/h)
Population values						
Estimation	0.034	0.0075	0.182	1.86	NA	NA
SD	0.002	0.0005	0.003	0.04	NA	NA
Individual values						
Patient 1	0.033	0.0062	0.194	2.00	4.01	0.78
Patient 2	0.033	0.0080	0.177	1.82	2.71	0.48
Patient 3	0.036	0.0081	0.169	1.83	4.93	0.84
Patient 4	0.036	0.0071	0.182	1.80	3.33	0.61
Patient 5	0.034	0.0075	0.183	1.81	3.05	0.56
Patient 6	0.033	0.0085	0.174	1.84	3.20	0.56
Patient 7	0.035	0.0068	0.183	1.92	3.73	0.68
Patient 8	0.035	0.0073	0.177	1.77	3.45	0.61
Mean ^b	0.034	0.074	0.180	1.85	3.52	0.64
SD	0.001	0.001	0.007	0.07	0.69	0.12
CV (%)	5.5	14.5	9.0	7.7	21.4	20.1

^aThe transfer rates ($k_{2,1}$ and $k_{1,2}$), the elimination rate (k_{el}), and the central compartment volume per body surface area unit (m^2) were adjusted to a two-compartment model. The central compartment volume was a dependent parameter ($V_c = \text{volume}/\text{m}^2 \times \text{patient body surface area}$) as well as clearance ($\text{clearance} = V_c \times k_{el}$).

^bThe mean, SD, and CV for each parameter were calculated from individual estimations. Note the low interindividual variability and the lower CV of the adjusted volume per square meter compared to that of the actual central compartment volumes (V_c).

RESULTS

Patient Characteristics and Therapy Results

Ten patients were included in the study between June 2011 and September 2014 (one patient included in Brest, two patients in Angers, two patients in Nantes University Hospital, and five patients in Nantes ICO Cancer Centre) and nine were treated; one on the five patients included in Nantes ICO Cancer Centre died between the inclusion and the beginning of the study. Characteristics of the nine treated patients are summarized in **Table 3**. All patients received 185 MBq of ^{111}In -IMP288 for the pretherapeutic session S1 and a median activity of 2,147 MBq

(1,641–3,026 MBq) of ^{177}Lu -IMP288 for the therapeutic session S2, one or 2 weeks later. None of the nine patients experienced an anaphylactic reaction during TF2 or peptide infusion. One patient died 5 days after pRAIT (not considered treatment related) and was not evaluable for PK analysis, dosimetry, toxicity, or response assessment.

Bone marrow toxicity was mild in most patients (grade 1 thrombocytopenia in 2/9 patients). Only one patient experienced grade 2 anemia 3 months after ^{177}Lu administration. Three patients with liver metastases showed transaminase enzymes (AST and ALT) elevation during the follow-up, which was deemed to be disease-related, since the three patients had progression of liver metastases on CT and FDG-PET registered 4 weeks after pRAIT.

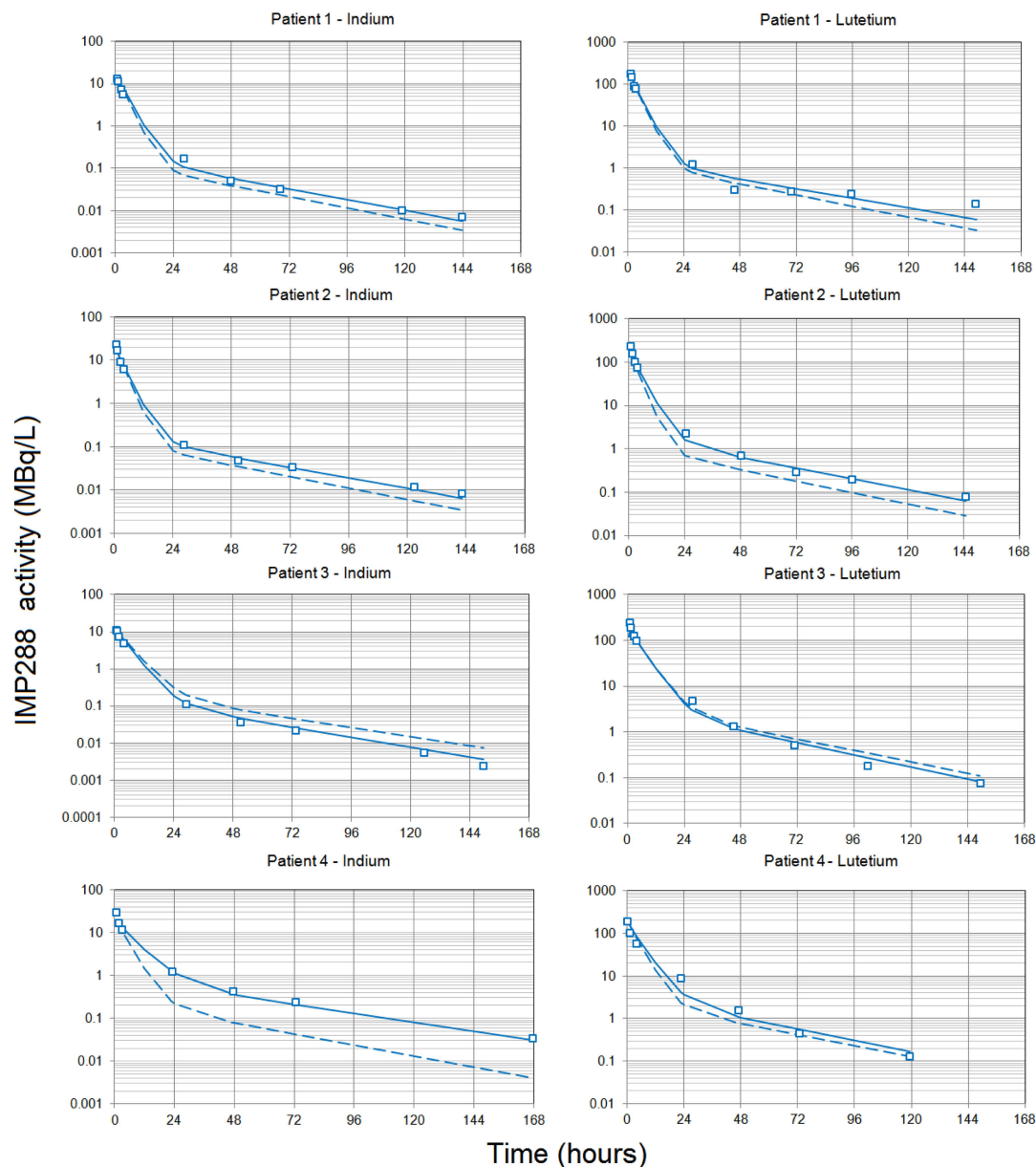


FIGURE 2 | Pharmacokinetics of the labeled hapten IMP288.

(Continued)

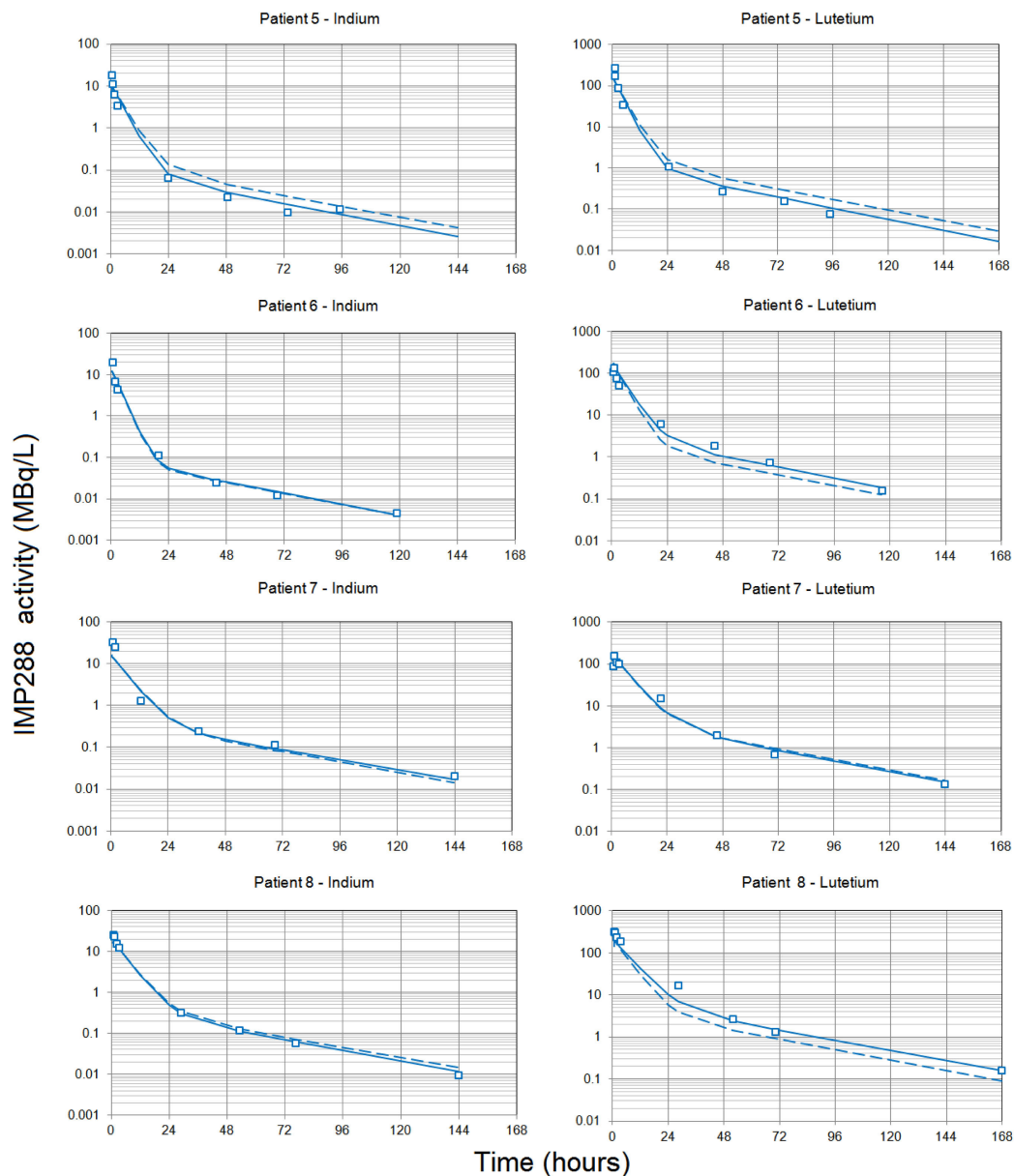


FIGURE 2 | Continued

Each patient received TF2 infusions then 24 or 48 h after each infusion, they received an infusion of IMP288 labeled with indium-111 after the first TF2 infusion or labeled with lutetium-177 after the second. Blood samples were collected at selected time intervals during and after each infusion, centrifuged, and counted. Indium-111 counts were corrected to match lutetium-177 radioactive half-life, and the figure shows IMP288 activity concentrations. The pharmacokinetics was modeled using a two-compartment model and a population approach. Results (open squares) are plotted as a semilog plot with the population (dashed lines) and individual (solid lines) fitted curves.

None of the patients showed biological signs or symptoms of renal toxicity.

According to RECIST criteria based on FDG-PET and CT data, two patients were considered as stable at 4 weeks post-pRAIT but progressive at 3 months. The six others patients were progressive as soon as 4 weeks after pRAIT.

Human antihuman antibody elevation was detected in 1/8 patients, 1 month after the second TF2 infusion, gradually decreasing from 2,966 ng/mL at 4 weeks to 969 ng/mL in the follow-up period of 3 months.

TF2 Pharmacokinetics

Simultaneous modeling of the two TF2 infusions for the eight patients who completed both S1 and S2 sessions using a two-compartment model showed that the PK was consistent between the two infusions, even if they were given at different TF2 molar doses (**Figure 1**). The use of population PK and the simultaneous modeling of the S1 and S2 TF2 infusions surmounted the problem of the limited sensitivity of the ELISA (**Table 4**). The small differences observed between the population and the individual fits showed that interindividual variability was quite

TABLE 5 | Two-compartment population analysis of IMP288 pharmacokinetics.

Parameter ^a	$k_{2,1}$ (h ⁻¹)	$k_{1,2}$ (h ⁻¹)	A_s	B_s	MR	k_{el} (h ⁻¹)	Volume/m ² (L/m ²)	Vc (L)	Clearance (L/h)
Population values									
Estimation	0.027	0.019	1.42	0.182	NA	NA	6.38	NA	NA
SD	0.001	0.002	0.07	0.012	NA	NA	0.27	NA	NA
Individual values									
Patient 1, indium	0.027	0.021	1.35	0.169	124.2	0.226	6.69	13.4	3.04
Patient 1, lutetium	0.024	0.021	1.37	0.172	125.5	0.241	6.50	13.1	3.15
Patient 2, indium	0.026	0.023	1.31	0.167	40.7	0.250	6.54	9.7	2.43
Patient 2, lutetium	0.027	0.022	1.22	0.156	40.1	0.219	6.63	9.9	2.16
Patient 3, indium	0.028	0.015	1.53	0.199	35.7	0.185	6.23	16.8	3.11
Patient 3, lutetium	0.028	0.017	1.43	0.183	37.8	0.165	6.25	16.8	2.78
Patient 4, indium	0.026	0.026	0.92	0.141	22.6	0.112	6.90	12.7	1.43
Patient 4, lutetium	0.029	0.019	1.29	0.167	22.0	0.173	6.78	12.5	2.17
Patient 5, indium	0.027	0.017	1.53	0.196	22.5	0.235	6.15	12.0	2.82
Patient 5, lutetium	0.028	0.017	1.52	0.196	31.1	0.249	6.13	11.9	2.97
Patient 6, indium	0.027	0.019	1.41	0.179	109.0	0.291	6.44	11.2	3.25
Patient 6, lutetium	0.028	0.021	1.31	0.170	18.8	0.179	6.93	12.0	2.15
Patient 7, indium	0.027	0.022	1.41	0.181	3.3	0.146	6.21	12.0	1.76
Patient 7, lutetium	0.028	0.018	1.41	0.181	3.2	0.137	6.54	12.7	1.74
Patient 8, indium	0.028	0.018	1.44	0.182	2.3	0.161	6.18	10.4	1.68
Patient 8, lutetium	0.028	0.020	1.16	0.174	2.5	0.124	6.49	10.9	1.36
Mean ^b	0.027	0.020	1.35	0.176		0.193	6.47	12.4	2.37
SD	0.001	0.003	0.16	0.015		0.052	0.27	2.0	0.65
CV (%)	4.5	14.3	11.5	8.6		27.0	4.1	16.4	27.5

^aThe transfer rates ($k_{2,1}$ and $k_{1,2}$), the central compartment volume per body surface area unit (m^2), and the two parameters A and B were adjusted using a two-compartment model. Estimations of the population adjusted parameters are given together with their estimated SD. The central compartment volume was a dependent parameter (V_c = volume/ m^2 × patient body surface area). Clearance was calculated as $A_s \times MR^{RS}$, MR being the ratio of the number of moles of injected IMP288 to the number of moles of TF2 present in the circulation at the time of IMP288 injection and the elimination constant k_{el} as clearance/ V_c .

^bThe mean, SD, and CV for each parameters were calculated from individual estimations.

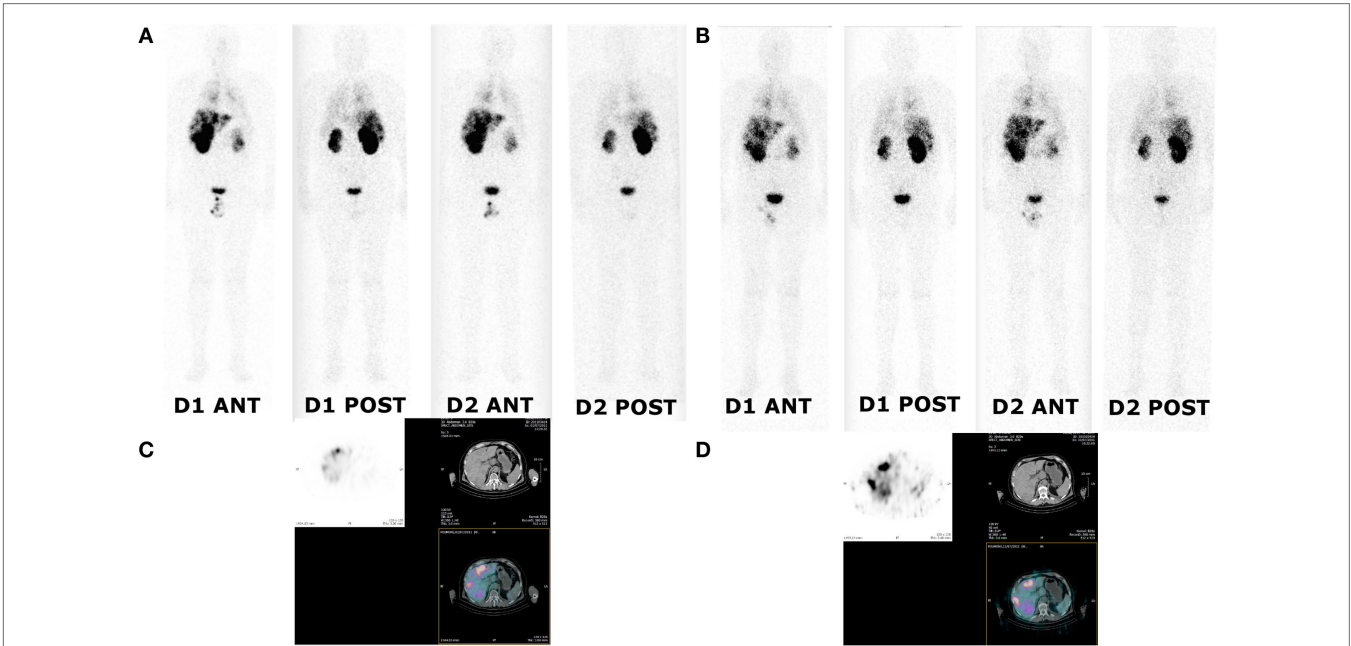


FIGURE 3 | Whole body and SPECT/CT images of patient 1 (cohort I). Whole body and SPECT/CT images were acquired 24 and 48 h after injection of ¹¹¹In-labeled IMP288 (A,C) and ¹⁷⁷Lu-labeled IMP288 (B,D). Patient 1 included in the first cohort had SCLC and a CEA level of 79 ng/mL. These images showed low tumor targeting in liver, mediastinum, and lung metastases.

small. The serum kinetics was rather fast with mean alpha half-lives of 3.7 ± 0.1 h and beta half-lives of 21.3 ± 0.7 h, with very low interindividual variability (3.2 and 3.3%, respectively). Mean serum clearance was 0.64 ± 0.12 L/h, and the use of BSA as a covariable (by setting $V_c = VBA \times BSA$) reduced the coefficient of variation of the V_c from 19 to 4.0% for the estimated parameter (VBA). This observation validates *a posteriori* the dosing scheme of the dose escalation on a BSA basis (44/88 nmol/m² for S1 and 240/480 nmol/m² for S2).

IMP288 Pharmacokinetics

Modeling the kinetics of the hapten was complicated by the necessity to take into account the effect of the residual bispecific antibody in serum at the time of hapten administration, which binds the hapten and modulates its clearance. To compare the PK of IMP288 labeled with indium-111 and with lutetium-177, indium activities were corrected for radioactive decay and transformed into equivalent lutetium-177 counts, assuming similar PK for IMP288 labeled with the two radionuclides (16). Then, the time-activity curves were fitted individually for all patients to a two-compartment model, which gave a good visual fit, not significantly improved by a third compartment according to the Akaike criterion (not shown). In a second step, the relationship between IMP288 PK and the pretargeting conditions was tested by plotting the estimated clearance or the V_c against the concentration of TF2 at the time of IMP288 injection (interpolated from the fitted TF2 concentration curves), or the amount of TF2 present in the circulation at the time of IMP288 (calculated as TF2 concentration \times TF2 V_c), or the molar ratio of injected IMP288 to the amount of TF2 in the circulation (MR). Indeed, in the circulation, TF2 binds the IMP288 hapten and slows its

clearance. It seems logical that the lower the excess of IMP288 relative to TF2, the larger the trapping of IMP288 in the circulation by the bispecific antibody, and hence, the slower its clearance. The correlation based on a power relationship was found to be better between clearance and MR, which was used thereafter as a covariable in the population analysis.

A population PK analysis was then performed on all 16 available kinetics, using BSA and MR as covariables. The larger interindividual variability in the IMP288 than in TF2 kinetics, with mean alpha half-lives of 3.4 ± 0.8 h and beta half-lives of 28.9 ± 2.1 h (corresponding to CV of 24 and 7.3%, respectively), could be explained in part by the influence of TF2 predose. The IMP288-indium-111 kinetics for patient 4 appeared as an outlier (**Figure 2**) but was not excluded from the analysis. The PK of the hapten is known to depend on the presence of TF2 in body fluids, and a strong correlation had been described earlier between IMP288 blood residence time and the concentration of TF2 blood concentrations at the time of peptide injection (16). Since the individual fitting analysis pointed to a relationship between hapten clearance and MR, MR was introduced in the population analysis as a covariable, and IMP288 clearance was calculated as $CI = A_b \times MR^{B_a}$ and k_{el} as clearance/ V_c (**Table 5**). Parameter adjustment finally gave clearance (L/h) = $1.33 \times MR^{0.18}$ ($R^2 = 0.66$). As expected, IMP288 clearance was higher than that of TF2, varying from 1.36 to 3.25 L/h, depending on MR, thus on the pretargeting conditions.

Since IMP288 kinetics were primarily driven by MR, and given the low interindividual variability of TF2 kinetics, pretargeting parameters (i.e., molar injected doses of TF2 and IMP288 and pretargeting delay) are expected to control the hapten kinetics. This means that the kinetics of the therapeutic session may be predicted

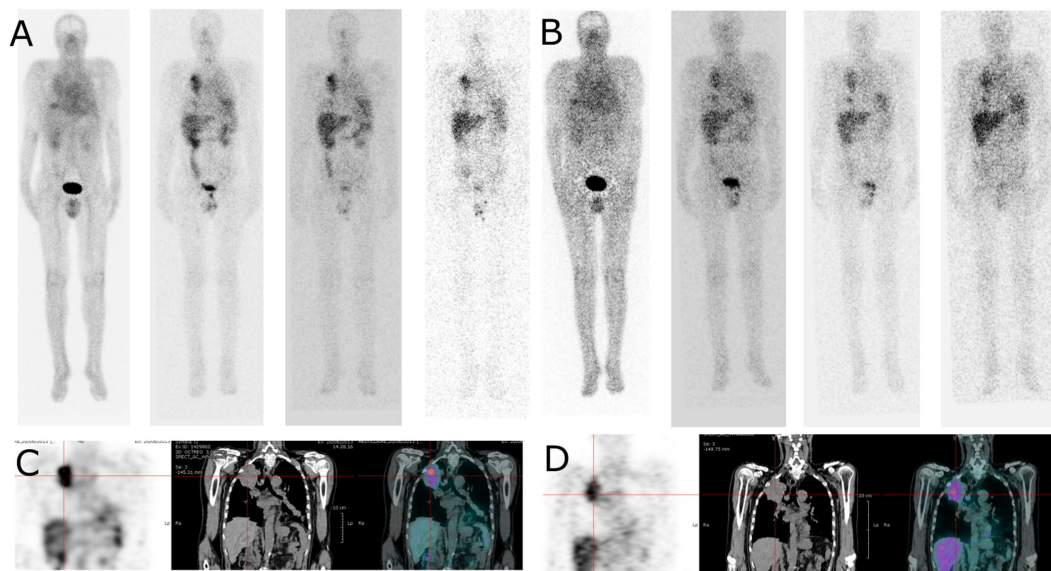


FIGURE 4 | Whole body and SPECT/CT images of patient 4 (cohort II). Whole body images (anterior view) were acquired 4, 24, 48, and 72 h after injection of ¹¹¹In-labelled IMP288 (**A**) and ¹⁷⁷Lu-labelled IMP288 (**B**). Patient 4, included in the cohort II, had NSCL and a CEA level of 275 ng/mL. These images clearly show lung tumor targeting in whole body and SPECT/CT images [(**C**) with ¹¹¹In-labelled IMP288 and (**D**) with ¹⁷⁷Lu-labelled IMP288]. According to RECIST criteria, the disease was considered as stable at 4 weeks, but progressive at 3 months. Patient 4 was the only patient with HAHA against TF2 > 50 ng/mL detected 1 month after the last TF2 injection.

TABLE 6 | Two-compartment population analysis of whole body IMP288 activity pharmacokinetics.

Parameter ^a	$k_{2,1}$ (h ⁻¹)	$k_{1,2}$ (h ⁻¹)	A_{WB}	B_{WB}	MR	k_{el} (h ⁻¹)
Population values						
Estimation	0.0163	0.0096	0.105	0.14	NA	NA
SD	0.0014	0.0009	0.004	0.01	NA	NA
Individual values						
Patient 1, indium	0.0152	0.0101	0.097	0.13	124.2	0.18
Patient 1, lutetium	0.0177	0.0094	0.110	0.15	125.5	0.23
Patient 2, indium	0.0126	0.0100	0.104	0.14	40.7	0.18
Patient 2, lutetium	0.0138	0.0101	0.115	0.16	40.1	0.21
Patient 3, indium	0.0178	0.0090	0.115	0.16	35.7	0.20
Patient 3, lutetium	0.0197	0.0085	0.121	0.17	37.8	0.23
Patient 4, indium	0.0136	0.0099	0.097	0.14	22.6	0.15
Patient 4, lutetium	0.0166	0.0099	0.089	0.13	22.0	0.13
Patient 5, indium	0.0146	0.0104	0.098	0.14	22.5	0.15
Patient 5, lutetium	0.0165	0.0102	0.083	0.12	31.1	0.13
Patient 6, indium	0.0141	0.0101	0.071	0.11	109.0	0.12
Patient 6, lutetium	0.0166	0.0098	0.091	0.13	18.8	0.13
Patient 7, indium	0.0143	0.0101	0.102	0.14	3.3	0.12
Patient 7, lutetium	0.0191	0.0090	0.070	0.13	3.2	0.08
Patient 8, indium	0.0141	0.0100	0.110	0.15	2.3	0.12
Patient 8, lutetium	0.0190	0.0090	0.098	0.14	2.5	0.11
Mean ^b	0.0160	0.0097	0.098	0.14		0.15
SD	0.0022	0.0006	0.015	0.02		0.04
CV (%)	13.9	5.8	15.2	11.6		29.0

^aWhole body (WB) activity kinetics was modeled as the sum of the activities in a central compartment and a distribution compartment with transfer rates ($k_{2,1}$ and $k_{1,2}$), and two parameters A and B as adjustable parameters; the elimination constant k_{el} was calculated as $k_{el} = k_{1,2} + k_{2,1} \cdot MR$, MR being the ratio of the number of moles of injected IMP288 to the number of moles of TF2 present in the circulation at the time of IMP288 injection. Estimations of the population adjusted parameters are given together with their estimated SD.

^bThe mean, SD, and CV for each parameter were calculated from individual estimations.

by the imaging session, in spite of the fact that absolute molar doses of the reagents are different, which will be confirmed hereafter.

Scintigraphy and Quantitative Analyses

Images registered after ¹¹¹In-labeled IMP288 showed targeting of all known tumors in all patients. WB scintigraphy and SPECT/CT images recorded after S1 and S2 were concordant (example of patients included in C1 and C2 are shown in **Figures 3** and **4**) even if tumor targeting visually appeared to be better in S2 than in S1 images, due to the higher levels of administered activity.

Reconstructed tomographic images were quantified and indium-111 counts were also corrected for radioactive decay to allow for comparison with the lutetium-177 data. A two-compartment model was used to describe the kinetics of WB counts (**Table 6**). The mean alpha half-life was 4.3 ± 1.1 h and beta half-life 80 ± 7 h, corresponding to a relatively large interindividual variability (25 and 9%, respectively).

The activity in the organs was modeled by a fraction of the activity in the central compartment plus an organ-specific distribution compartment, as described in the literature (27). Then the kinetics of activities in all regions of interest (WB, right and left lungs, liver, right and left kidneys, spleen, heart, whole aorta, and tumor), for all eight patients and for the two sessions, was fitted simultaneously by a population analysis. As in the serum kinetics analysis, the rate constant of elimination (k_{el}) from the central compartment was set as a power function of MR, and tissue weights were introduced in the analysis. A reasonable fit was

obtained, except for tumors, for which variations in on rates and off rates were too large to consider a population PK analysis and were thus adjusted individually. This analysis demonstrated the consistence of the measured activities and a relationship between WB clearance, and MR was again observed [k_{el} (1/h) = 0.095 MR^{0.15}], but with a lower correlation coefficient ($R^2 = 0.45$) than in the serum count analysis.

This analysis showed that tissue uptake, on an organ weight basis, as assessed by the organ compartment volume, was higher in kidneys and liver, as expected, intermediate in lungs and spleen, and lower in aorta and heart, whereas the fractions of activity in fast equilibrium with the central compartment was similar in all tissues, including tumors (**Table 7**). Tumor uptake was variable and higher in patients 4, 5, 6 (C1), and 7 (C2).

Dosimetry

The PK modeling of image data was completed by a classical dosimetry study performed as described in Section “Materials and Methods.” **Figures 5** and **6** present organ-absorbed doses normalized by injected activity estimated at S1 and S2. Considering cohort categorization, no significant differences in organ-absorbed doses estimated from both sessions were observed, as shown by Wilcoxon tests ($p > 0.05$). At the patient level, normalized organ-absorbed doses at S1 were also compared against those estimated at S2, using the Spearman test. Spearman's rho and corresponding p -value are reported in **Table 8** and showed a good correlation between organs-absorbed doses estimated at both sessions.

TABLE 7 | Population analysis of IMP288 activity distribution.

Parameter ^a	k_{on} (1/h $\times 10^3$)	k_{off} (1/h $\times 10^2$)	Fraction (L/kg $\times 10^2$)
Lung	1.06 \pm 0.06	1.17 \pm 0.06	3.38 \pm 0.19
Liver	1.45 \pm 0.11	1.14 \pm 0.08	2.33 \pm 0.21
Kidneys	4.35 \pm 0.28	2.22 \pm 0.08	5.91 \pm 0.37
Spleen	1.48 \pm 0.11	1.30 \pm 0.08	2.21 \pm 0.19
Heart	0.45 \pm 0.04	0.94 \pm 0.09	3.08 \pm 0.21
Aorta	0.61 \pm 0.05	1.04 \pm 0.09	3.66 \pm 0.26
Tumor			2.70 \pm 0.26

^aIMP288 distribution in tissues of interest was modeled using a tissue-specific distribution compartment and a fraction of the activity in the central compartment; the on and off rate constants, k_{on} and k_{off} , and the fraction of activity (fraction) were adjustable parameters using the central compartment of the whole body kinetics as the input function.

For all patients, 24 tumors were delineated on reconstructed SPECT or CT images. They were mostly located in lungs (37%) and liver (29%). Median tumor mass was 19.3 g (1.1–1,364 g). Median normalized tumor-absorbed doses in the three cohorts ranged from 0.05 to 0.25 mGy/MBq in S1 and from 0.10 to 0.54 mGy/MBq in S2. Extreme normalized tumor-absorbed doses for each cohort ranged from 0.02 to 0.12 mGy/MBq in S1 and from 0.52 to 1.08 mGy/MBq in S2. These absorbed doses not appeared to be significantly different as shown by a Wilcoxon test conducted on previous values ($p > 0.13$). Nevertheless, a Spearman test conducted on previous data showed a good correlation ($\rho = 0.85$, $p < 10^{-15}$) between tumor-absorbed doses estimated at both sessions.

Kruskal–Wallis tests were performed to compare organ-absorbed doses at each different dosage level and for both sessions. Statistical tests did not exhibit significant difference between groups for organs ($p > 0.07$). The same analysis was conducted on tumor-absorbed doses and showed significantly higher tumor-absorbed doses in patients included in cohort II or III than in cohort I ($p < 0.002$) as illustrated by **Figure 6**.

DISCUSSION

The main objectives of this study were to assess whether an imaging session may be predictive of absorbed doses in therapy (IMP288 labeled with indium-111 in the imaging session and with lutetium-177 in the therapy session) and to find the best pretargeting parameters (molar doses of TF2 and IMP288 and pretargeting delay) for cancer therapy. The imaging sessions were performed using molar doses 5.4 times lower than in the therapy session, to reduce exposure of the patients to the pretargeting reagents. This was assumed feasible without compromising the predictive character of the imaging session, based on the earlier preclinical assessment of the compounds and in view of the results obtained by Schoffelen et al. (16). It was, however, important to confirm this result in a different clinical setting.

To this end, PK modeling of TF2 serum concentration kinetics, IMP288 serum activity kinetics (adjusted to the physical half-life of lutetium-177 to allow comparisons), and of IMP288 activities measured by SPECT in WB and regions of interest corresponding to major tissues and tumors was performed using a population PK

modeling software developed in our laboratory (available upon request) that allowed for simultaneous multicompartment and multitissue analyses. The population approach allowed a more consistent modeling of data, ensuring convergence of parameter estimations even in cases where the number of data points was small due to assay sensitivity (TF2) or number of imaging sessions. In addition, the population approach allowed us to confirm that calculating individual TF2 or hapten doses on the basis of BSA reduced the variability of circulating TF2 concentrations and also allowed us to define a relationship between circulating TF2 concentrations at the time of hapten administration and the kinetics of the hapten. This relationship is complex, but it is expected that TF2 binds the hapten in the circulation and slows down its clearance, as already observed in many preclinical studies and in earlier clinical studies with chemically coupled bispecific antibodies (17).

The population PK analyses showed that molar ratios and time intervals must be kept constant, but that there is no need to perform the imaging and therapy sessions with the same molar doses, in order to obtain comparable hapten serum and tissue uptake kinetics in both imaging and therapy sessions. Indeed, quantitative assessment of the images showed that not only the serum kinetics, but also the distribution of activity in normal tissues and tumors in the therapy session may be predicted from the imaging session, as shown by the very high degree of correlation obtained. Being able to predict dosimetry, and avoiding treatment of patients whose tumor lesions do not bind the activity, using a low dose, pretherapy, imaging session, according to the theranostic approach, is a significant advantage in clinical practice.

The very different PK behavior of TF2 as compared to chemically coupled BsmAb requires pretargeting optimization studies. The pretargeting parameters must be finely tuned to avoid high circulating activities, detrimental to normal tissue dosimetry in therapy, and background in imaging, while keeping tumor uptake as high as possible. In this study, in spite of the small number of patients in each cohort, some conclusions can be drawn. In cohort I, comparatively low doses of TF2 were administered (7 and 37.5 mg/m²) with a delay of 48 h. This results in a fast clearance of the hapten and a low tumor uptake. In cohort II, the higher doses of TF2 (14 and 75 mg/m²) resulted in slower clearance of activity and significantly increased tumor uptake. Reduction of the delay to 24 h further increased the amount of TF2 present in the circulation and tissues at the time of hapten injection but did not significantly increased tumor uptake over cohort III, probably because of the high observed variability and because lutetium-177 data were available for only two patients.

Although serum and organ PK showed a correlation between MR and clearance, it must be noted that between cohort I and cohort III, clearance is only reduced by a factor of approximately two. In contrast, a significant difference in tumor-absorbed doses is found between cohort I and cohorts II and III, showing that increase of the TF2 dose and reduction of the pretargeting delay had a positive impact on tumor uptake without increasing significantly the doses delivered to normal tissues.

In line with the dosimetry assessment, hematological toxicity was quite limited, and non-hematological toxicity was observed only in liver involved with tumor in three cases. To further increase

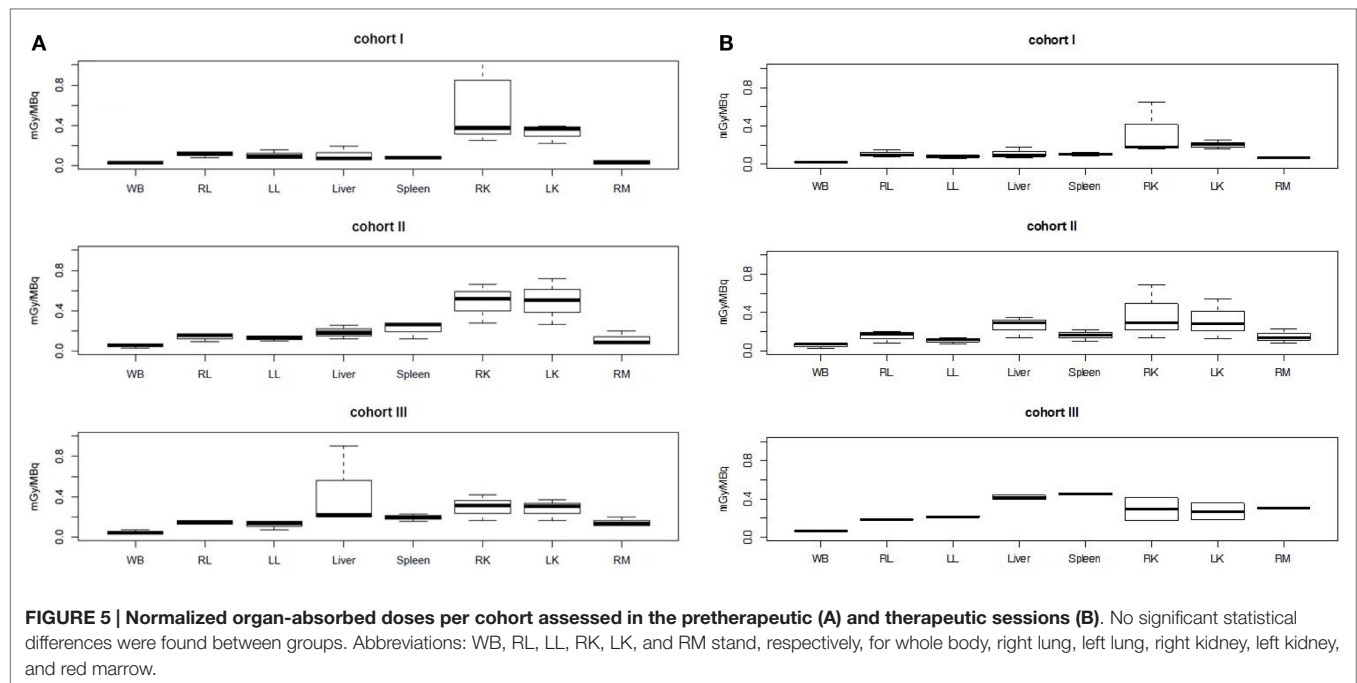


FIGURE 5 | Normalized organ-absorbed doses per cohort assessed in the pretherapeutic (A) and therapeutic sessions (B). No significant statistical differences were found between groups. Abbreviations: WB, RL, LL, RK, LK, and RM stand, respectively, for whole body, right lung, left lung, right kidney, left kidney, and red marrow.

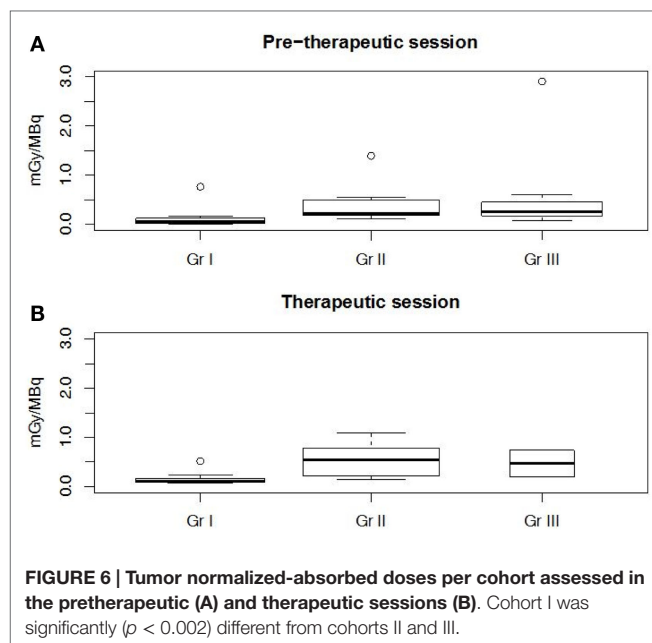


FIGURE 6 | Tumor normalized-absorbed doses per cohort assessed in the pretherapeutic (A) and therapeutic sessions (B). Cohort I was significantly ($p < 0.002$) different from cohorts II and III.

tumor-absorbed doses, the shorter pretargeting delay of 24 h thus appears superior to 48 h. Since in preclinical models (28), shorter delays started to increase the doses delivered to normal tissues, this 24-h delay may be considered optimal. On the other hand, increasing the administered amount of TF2 could be problematic in terms of cost, even if there is no indication of tumor binding site saturation. Thus, to improve treatment efficacy, which was minimal in this optimization study with only two cases of disease stabilization for short periods of time, the injected activity should

be increased for the second part of the study, which is planned with an activity escalation. Indeed, it was not expected that a single therapy cycle would be sufficient to deliver therapeutic doses that would show tumor shrinkage.

It has been shown that pretargeting performance strongly depends on the injected hapten to BsmAb molar ratio which should be kept as small as possible (1:20 or 1:40), as in this study. Then the hapten should be labeled to a high specific activity in order to target enough activity for therapy. This specific activity issue and the fact that tumor accretion is slower but significantly reversible make the use of shorter half-life and higher intrinsic toxicity radionuclides, such as yttrium-90, preferable to that of lutetium-177. The use of pairs of beta + /beta-emitting radionuclides (e.g., $^{86}\text{Y}/^{90}\text{Y}$) could also be a promising theragnostic approach with a same distribution both for dosimetry imaging using immunoPET and therapy. Short half-life alpha-emitting radionuclides, such as bismuth-213 or astatine-211, could also be considered.

Finally, the immune response and the number of patient developing human antibody against TF2 were lower than described previously by Schoffelen and coworkers (16) in a population of patients with CRCs, and grade 2 acute infusion reactions were observed in one-third (7/21) of the patients during the second TF2 infusion. These immune reactions were attenuated by adding antihistamine and corticosteroid premedications before the second TF2 infusion but did not disappear (immune response occurred in 2/5 premedicated patients). In our study, all patients were premedicated with an antihistamine and corticosteroid before each TF2 and peptide infusion, and none of them presented immune response symptoms. Moreover, Schoffelen and coworkers (16) described an immunization rate of 50% with HAA against TF2 detected in 11/21 patients as soon as 1 week after the

TABLE 8 | Spearman tests for the correlation between organ-absorbed doses estimated during pretherapeutic and therapeutic sessions^a.

Spearman test	1	2	3	4	5	6	7	8
Rho	0.986	0.827	0.904	0.725	0.918	0.836	0.891	0.727
p-Value	0.000	0.031	0.000	0.007	0.000	0.003	0.001	0.015

^aPatient 9 was not able to sustain therapeutic imaging session due to an altered condition.

second infusion gradually increasing in the follow-up period of 8 weeks. HAHA against TF2 > 50 ng/mL was detected in only one of our eight patients evaluated, starting 1 month after the second TF2 infusion and gradually decreasing in the follow-up period of 3 months. If the use of an antiallergic premedication partially explained the absence of immune reactions at the time of second injection of TF2 in our study, this did not explain the lower number of patients developing HAHA. The explanation did not come from the TF2 injection schemes which were identical or from the TF2 doses that were close. Our main hypothesis to explain this discrepancy could reside in the different histological types of tumors included in the two studies. While in the two studies, patients have already been treated with multiple lines of treatment, relapsing lung cancer is often more aggressive than relapsing CRC. This could explain poorer general conditions (7/9 patients died in the year following the study) and thus a more compromised immune system. It may also be that metastatic NSCLC patients are more heavily pretreated with cytotoxic chemotherapy than patients

with metastatic CRC, and this needs to be evaluated. In any case, the low immunogenicity and the low toxicity observed should offer the possibility of administering several courses of treatment to deliver tumor-killing irradiation levels.

ACKNOWLEDGMENTS

This work has been supported in part by grants from the French National Agency for Research, called “Investissements d’Avenir” IRON Labex n° ANR-11-LABX-0018-01 and ArronaxPlus Equipex n° ANR-11-EQPX-0004; the proprietary TF2 and IMP288 reagents were provided by Immunomedics, Inc., and IBC Pharmaceuticals, Inc.

SUPPLEMENTARY MATERIAL

The Supplementary Material for this article can be found online at <http://journal.frontiersin.org/article/10.3389/fmed.2015.00084>

REFERENCES

- Larson SM, Carrasquillo JA, Cheung NK, Press OW. Radioimmunotherapy of human tumours. *Nat Rev Cancer* (2015) 15(6):347–60. doi:10.1038/nrc3925
- Kraeber-Bodéré F, Bodet-Milin C, Rousseau C, Eugène T, Pallardy A, Frampas E, et al. Radioimmunoconjugates for the treatment of cancer. *Semin Oncol* (2014) 41(5):613–22. doi:10.1053/j.seminoncol.2014.07.004
- Barbet J, Kraeber-Bodéré F, Vuillez JP, Gautherot E, Rouvier E, Chatal JF. Pretargeting with the affinity enhancement system for radioimmunotherapy. *Cancer Biother Radiopharm* (1999) 14(3):153–66. doi:10.1089/cbr.1999.14.153
- Goldenberg DM, Sharkey RM, Paganelli G, Barbet J, Chatal JF. Antibody pretargeting advances cancer radioimmunodetection and radioimmunotherapy. *J Clin Oncol* (2006) 24(5):823–34. doi:10.1200/JCO.2005.03.8471
- Juweid M, Sharkey RM, Behr T, Swayne LC, Herskovic T, Pereira M, et al. Radioimmunotherapy of medullary thyroid cancer with iodine-131-labeled anti-CEA antibodies. *J Nucl Med* (1996) 37(6):905–11.
- Liersch T, Meller J, Kulle B, Behr TM, Markus P, Langer C, et al. Phase II trial of carcinoembryonic antigen radioimmunotherapy with ¹³¹I-labetuzumab after salvage resection of colorectal metastases in the liver: five-year safety and efficacy results. *J Clin Oncol* (2005) 23(27):6763–70. doi:10.1200/JCO.2005.18.622
- Kraeber-Bodéré F, Faivre-Chauvet A, Saï-Maurel C, Gautherot E, Fiche M, Campion L, et al. Bispecific antibody and bivalent hapten radioimmunotherapy in CEA-producing medullary thyroid cancer xenograft. *J Nucl Med* (1999) 40(1):198–204.
- Gautherot E, Rouvier E, Daniel L, Loucif E, Bouhou J, Manetti C, et al. Pretargeted radioimmunotherapy of human colorectal xenografts with bispecific antibody and ¹³¹I-labeled bivalent hapten. *J Nucl Med* (2000) 41(3):480–7.
- Kraeber-Bodéré F, Bardet S, Hoefnagel CA, Vieira MR, Vuillez JP, Murat A, et al. Radioimmunotherapy in medullary thyroid cancer using bispecific antibody and iodine 131-labeled bivalent hapten: preliminary results of a phase II clinical trial. *Clin Cancer Res* (1999) 5(10 Suppl):3190s–8s.
- Vuillez JP, Kraeber-Bodéré F, Moro D, Bardiès M, Douillard JY, Gautherot E, et al. Radioimmunotherapy of small cell lung carcinoma with the two-step method using a bispecific anti-carcinoembryonic antigen/anti-diethylenetriaminepentaacetic acid (DTPA) antibody and iodine-131 Di-DTPA hapten: results of a phase I/II trial. *Clin Cancer Res* (1999) 5(10 Suppl):3259s–67s.
- Chatal JF, Campion L, Kraeber-Bodéré F, Bardet S, Vuillez JP, Charbonnel B, et al. Survival improvement in patients with medullary thyroid carcinoma who undergo pretargeted anti-carcinoembryonic-antigen radioimmunotherapy: a collaborative study with the French endocrine tumor group. *J Clin Oncol* (2006) 24(11):1705–11. doi:10.1200/JCO.2005.04.4917
- Salaün PY, Campion L, Bournaud C, Faivre-Chauvet A, Vuillez JP, Taieb D, et al. Phase II trial of anticarcinoembryonic antigen pretargeted radioimmunotherapy in progressive metastatic medullary thyroid carcinoma: biomarker response and survival improvement. *J Nucl Med* (2012) 53(8):1185–92. doi:10.2967/jnumed.111.101865
- Rossi EA, Goldenberg DM, Cardillo TM, McBride WJ, Sharkey RM, Chang CH. Stably tethered multifunctional structures of defined composition made by the dock and lock method for use in cancer targeting. *Proc Natl Acad Sci U S A* (2006) 103(18):6841–6. doi:10.1073/pnas.0600982103
- Goldenberg DM, Rossi EA, Sharkey RM, McBride WJ, Chang CH. Multifunctional antibodies by the dock-and-lock method for improved cancer imaging and therapy by pretargeting. *J Nucl Med* (2008) 49(1):158–63. doi:10.2967/jnumed.107.046185
- Sharkey RM, Rossi EA, McBride WJ, Chang CH, Goldenberg DM. Recombinant bispecific monoclonal antibodies prepared by the dock-and-lock strategy for pretargeted radioimmunotherapy. *Semin Nucl Med* (2010) 40(3):190–203. doi:10.1053/j.semnuclmed.2009.12.002
- Schoffelen R, Woliner-van der Weg W, Visser EP, Goldenberg DM, Sharkey RM, McBride WJ, et al. Predictive patient-specific dosimetry and individualized dosing of pretargeted radioimmunotherapy in patients with advanced colorectal cancer. *Eur J Nucl Med Mol Imaging* (2014) 41(8):1593–602. doi:10.1007/s00259-014-2742-6
- Kraeber-Bodéré F, Faivre-Chauvet A, Ferrer L, Vuillez JP, Brard PY, Rousseau C, et al. Pharmacokinetics and dosimetry studies for optimization of

- anti-carcinoembryonic antigen x anti-hapten bispecific antibody-mediated pretargeting of Iodine-131-labeled hapten in a phase I radioimmunotherapy trial. *Clin Cancer Res* (2003) **9**(10 Pt 2):3973S–81S.
18. McBride WJ, Zanzonico P, Sharkey RM, Norén C, Karacay H, Rossi EA, et al. Bispecific antibody pretargeting PET (immunoPET) with an 124I-labeled hapten-peptide. *J Nucl Med* (2006) **47**(10):1678–88.
 19. Eisenhauer EA, Therasse P, Bogaerts J, Schwartz LH, Sargent D, Ford R, et al. New response evaluation criteria in solid tumours: revised RECIST guideline (version 1.1). *Eur J Cancer* (2009) **45**(2):228–47. doi:10.1016/j.ejca.2008.10.026
 20. Lavielle M, Mentré F. Estimation of population pharmacokinetic parameters of saquinavir in HIV patients with the MONOLIX software. *J Pharmacokinet Pharmacodyn* (2007) **34**(2):229–49. doi:10.1007/s10928-006-9043-z
 21. Ogawa K, Harata Y, Ichihara T, Kubo A, Hashimoto SA. Practical method for position-dependent Compton-scatter correction in single photon emission CT. *IEEE Trans Med Imaging* (1991) **10**:408–12. doi:10.1109/42.97591
 22. Dewaraja YK, Frey EC, Sgouros G, Brill AB, Roberson P, Zanzonico PB, et al. MIRD pamphlet No. 23: quantitative SPECT for patient-specific 3-dimensional dosimetry in internal radionuclide therapy. *J Nucl Med* (2012) **53**(8):1310–25. doi:10.2967/jnumed.111.100123
 23. Kikinis R, Pieper S. 3D Slicer as a tool for interactive brain tumor segmentation. *Conf Proc IEEE Eng Med Biol Soc* (2011) **2011**:6982–4. doi:10.1109/IEMBS.2011.6091765
 24. Ferrer L, Kraeber-Bodéré F, Bodet-Milin C, Rousseau C, Le Gouill S, Wegener WA, et al. Three methods assessing red marrow dosimetry in lymphoma patients treated with radioimmunotherapy. *Cancer* (2010) **116**(4 Suppl):1093–100. doi:10.1002/cncr.24797
 25. Toussaint N, Souplet J-C, Fillard P. MedINRIA: medical image navigation and research tool by INRIA. *Proc. of MICCAI '07 Workshop on Interaction in Medical Image Analysis and Visualization*. Brisbane, QLD (2007).
 26. R: A Language and Environment for Statistical Computing. R Foundation for Statistical Computing. Vienna. Available from: <http://www.R-project.org/>
 27. Lammertsma AA, Bench CJ, Hume SP, Osman S, Gunn K, Brooks DJ, et al. Comparison of methods for analysis of clinical [¹¹C]raclopride studies. *J Cereb Blood Flow Metab* (1996) **16**(1):42–52. doi:10.1097/00004647-199601000-00005
 28. Frampas E, Maurel C, Remaud-Le Saëc P, Mauxion T, Faivre-Chauvet A, Davodeau F, et al. Pretargeted radioimmunotherapy of colorectal cancer metastases: models and pharmacokinetics predict influence of the physical and radiochemical properties of the radionuclide. *Eur J Nucl Med Mol Imaging* (2011) **38**(12):2153–64. doi:10.1007/s00259-011-1903-0

Conflict of Interest Statement: The proprietary TF2 and IMP288 reagents were provided by Immunomedics, Inc., and IBC Pharmaceuticals, Inc. (Dr. David M. Goldenberg and Robert M. Sharkey).

Copyright © 2015 Bodet-Milin, Ferrer, Rauscher, Masson, Rbah-Vidal, Faivre-Chauvet, Cerato, Rousseau, Hureau, Couturier, Salatin, Goldenberg, Sharkey, Kraeber-Bodéré and Barbet. This is an open-access article distributed under the terms of the Creative Commons Attribution License (CC BY). The use, distribution or reproduction in other forums is permitted, provided the original author(s) or licensor are credited and that the original publication in this journal is cited, in accordance with accepted academic practice. No use, distribution or reproduction is permitted which does not comply with these terms.

Advantages of publishing in Frontiers



OPEN ACCESS

Articles are free to read,
for greatest visibility



COLLABORATIVE PEER-REVIEW

Designed to be rigorous
– yet also collaborative,
fair and constructive



FAST PUBLICATION

Average 85 days from
submission to publication
(across all journals)



COPYRIGHT TO AUTHORS

No limit to article
distribution and re-use



TRANSPARENT

Editors and reviewers
acknowledged by name
on published articles



SUPPORT

By our Swiss-based
editorial team



IMPACT METRICS

Advanced metrics
track your article's impact



GLOBAL SPREAD

5'100'000+ monthly
article views
and downloads



LOOP RESEARCH NETWORK

Our network
increases readership
for your article

Frontiers

EPFL Innovation Park, Building I • 1015 Lausanne • Switzerland
Tel +41 21 510 17 00 • Fax +41 21 510 17 01 • info@frontiersin.org
www.frontiersin.org

Find us on

